



**HAL**  
open science

# Design, synthesis and functionalization of ultrasmall nanoparticles for bioimaging

Nadia Licciardello

► **To cite this version:**

Nadia Licciardello. Design, synthesis and functionalization of ultrasmall nanoparticles for bioimaging. Other. Université de Strasbourg, 2015. English. NNT : 2015STRAF033 . tel-01552300v2

**HAL Id: tel-01552300**

**<https://theses.hal.science/tel-01552300v2>**

Submitted on 4 Jul 2017

**HAL** is a multi-disciplinary open access archive for the deposit and dissemination of scientific research documents, whether they are published or not. The documents may come from teaching and research institutions in France or abroad, or from public or private research centers.

L'archive ouverte pluridisciplinaire **HAL**, est destinée au dépôt et à la diffusion de documents scientifiques de niveau recherche, publiés ou non, émanant des établissements d'enseignement et de recherche français ou étrangers, des laboratoires publics ou privés.

**ÉCOLE DOCTORALE DES SCIENCES CHIMIQUES**

**Institut de science et d'ingénierie supramoléculaires**

**THÈSE** présentée par :

**Nadia LICCIARDELLO**

soutenue le : 11 **Septembre 2015**

pour obtenir le grade de : **Docteur de l'université de Strasbourg**

Discipline/ Spécialité : Chimie

**DESIGN, SYNTHESIS AND  
FUNCTIONALIZATION OF  
ULTRASMALL NANOPARTICLES FOR  
BIOIMAGING**

**THÈSE dirigée par :**

[Mme DE COLA Luisa]

Professeur, Université de Strasbourg

**RAPPORTEURS :**

[Mme PELLEGRINO Teresa]

[Mme GAZEAU Florence]

Tenured team leader, Istituto Italiano di Tecnologia, Genova  
CNRS research director, Université Paris 7

**AUTRES MEMBRES DU JURY :**

[M. PARAK Wolfgang]

[Mme BEGIN-COLIN Sylvie]

Professeur, University of Marburg

Professeur, Université de Strasbourg

*« [...] occorre diffidare del quasi-uguale,  
[...] del praticamente identico, del pressapoco,  
dell'oppure, di tutti i surrogati e di tutti i rappezzi.  
Le differenze possono essere piccole, ma portare  
a conseguenze radicalmente diverse,  
come gli aghi degli scambi;  
il mestiere del chimico consiste in buona parte  
nel guardarsi da queste differenze, nel conoscerle  
da vicino, nel prevenirne gli effetti.  
Non solo il mestiere del chimico. »*

Primo Levi, in *Il sistema periodico*, Einaudi Editore, **1975**, pag. 63

*« [...] one must distrust the almost-the-same,  
[...] the practically identical, the approximate,  
the or-even, all surrogates, and all patchwork.  
The differences can be small, but they can lead  
to radically different consequences,  
like a railroad's switch points;  
the chemist's trade consists in good part  
in being aware of these differences, knowing them  
close up, and foreseeing their effects.  
And not only the chemist's trade. »*

Primo Levi, in *The Periodic Table*, translation from Raymond Rosenthal, Schocken Books, **1984**, pag. 63

# TABLE OF CONTENTS

Rèsumé .....	v
Chapter 1: Introduction .....	1
1.1    Ultrasmall nanoparticles and their bioapplications .....	1
1.2    Multimodal imaging .....	6
1.3    Ultrasmall silicon nanoparticles .....	10
1.3.1    Why silicon nanoparticles? .....	10
1.3.2    Synthetic methods to produce silicon nanoparticles .....	11
1.3.3    On the origin of photoluminescence in silicon nanoparticles .....	20
1.3.4    Bioapplications of silicon nanoparticles .....	23
1.4    Carbon dots .....	28
1.4.1    Properties of carbon dots .....	28
1.4.2    Synthetic methods of preparation of carbon dots .....	30
1.4.3    Bioapplications of carbon dots .....	31
1.5    Ultrasmall cobalt nanoparticles .....	33
1.5.1    Properties of cobalt nanoparticles .....	33
1.5.2    Synthetic routes to prepare cobalt nanoparticles and their bioapplications .....	34
1.6    Aim of the thesis .....	36
1.7    References: .....	38
Chapter 2: Synthesis and characterization of ultrasmall silicon nanoparticles .....	47
2.1 Introduction .....	47
2.2 Amine-terminated silicon nanoparticles from microemulsion synthesis .....	48
2.2.1 Synthetic route .....	48
2.2.2 Characterization .....	51
2.3 Amine-terminated silicon nanoparticles prepared by hydrothermal synthesis .....	58
2.3.1 Synthetic route .....	58
2.3.2 Characterization .....	59
2.4 Conclusions .....	64
2.5 Experimental section: .....	65

2.6 References:.....	69
<b>Chapter 3: Functionalization of ultrasmall Si nanoparticles for bioimaging.....</b>	<b>71</b>
3.1 Introduction.....	71
3.2 Cytotoxicity of amine-terminated silicon nanoparticles .....	72
3.3 Surface functionalization of amine-terminated silicon nanoparticles.....	75
3.3.1 Coupling of amine-terminated Si NPs with the cyanine 5 dye.....	76
3.3.2 In vitro and in vivo experiments with Cy5-Si NPs.....	81
3.3.3 Coupling of Si NPs with <sup>64</sup> Cu complexes for <i>in vivo</i> PET imaging .....	86
3.4 Conclusions.....	92
3.5 Experimental section.....	93
3.6 References:.....	99
<b>Chapter 4: Functionalization of carbon dots for bioimaging .....</b>	<b>103</b>
4.1 Introduction.....	103
4.2 Preparation and characterization of CQDs .....	104
4.3 Surface modification of CQDs with cyanine 5 dye .....	107
4.4 <i>In vivo</i> positron emission tomography of CQDs.....	111
4.5 Conclusions.....	116
4.6 Experimental section.....	117
4.7 References:.....	122
<b>Chapter 5: Preparation, surface modification and characterization of silica-coated cobalt nanoparticles .....</b>	<b>123</b>
5.1 Introduction.....	123
5.2 Preparation of cobalt nanoparticles.....	124
5.2.1. Synthetic route and characterization .....	124
5.3 Preparation of silica-coated Co NPs .....	126
5.3.1 Synthetic route .....	126
5.3.2 Characterization .....	128
5.4 Surface modification of Co@SiO <sub>2</sub> NPs with amine-moieties and dyes .....	133
5.5 Conclusions.....	137
5.6 Experimental section .....	137
5.7 References.....	141

Chapter 6: Instrumental techniques .....	<b>143</b>
6.1 Transmission Electron Microscopy .....	143
6.2 Energy-Filtered Transmission Electron Microscopy .....	146
6.3 Energy dispersive X-ray spectroscopy .....	147
6.4 Emission and excitation spectroscopy .....	147
6.5 X-ray photoelectron spectroscopy .....	151
6.6 Positron emission tomography .....	153
6.7 References: .....	154
Summary .....	157
Acknowledgements .....	163



# Résumé

L'usage des nanoparticules (NPs) remonte à très longtemps dans l'histoire et les preuves de l'exploitation des propriétés optiques uniques des nanoparticules dans des objets antiques ont déjà été avancées dans la célèbre coupe de Lycurgue, conçue au 4<sup>ème</sup> siècle après J.-C.<sup>[1]</sup>. Cependant, le phénomène restait inexpliqué jusqu'à ce que le développement de la physique quantique clarifie la raison pour laquelle les propriétés des matériaux changent de façon aussi spectaculaire lorsque nous descendons à l'échelle nanométrique. Quand un objet est réduit à des dimensions nanométriques, nombreuses sont les propriétés qui changent par rapport à l'échelle macroscopique. Par exemple, dans le cas des « quantum dots » (points quantiques), apparaît le phénomène de fluorescence ou dans le cas des matériaux magnétiques, le phénomène de superparamagnétisme apparaît en dessous d'une taille critique. En 1960, Richard Feynman fut l'un des premiers à prédire le grand potentiel des nanosciences<sup>[2]</sup>. Il est inouï de constater qu'après plus de 50 ans, le “nanomonde” représente encore autant d'opportunités, que les nanosciences et la nanotechnologie représentent encore un domaine riche et encore à explorer. Les nanoparticules sont utilisées pour de nombreuses applications<sup>[3]</sup> allant de l'électronique à l'optoélectronique, et des senseurs à la médecine<sup>[4-5]</sup>. En particulier, la possibilité de concevoir et d'ajuster la taille, la fonctionnalisation et les propriétés des nanoparticules suscite de plus en plus l'intérêt dans le domaine de la nanomédecine<sup>[4, 6-9]</sup>, à la fois pour l'imagerie *in vitro* et *in vivo* <sup>[9-10]</sup>, mais également pour l'administration de médicaments<sup>[11]</sup>. La Figure 1 résume schématiquement les applications des nanoparticules en médecine.

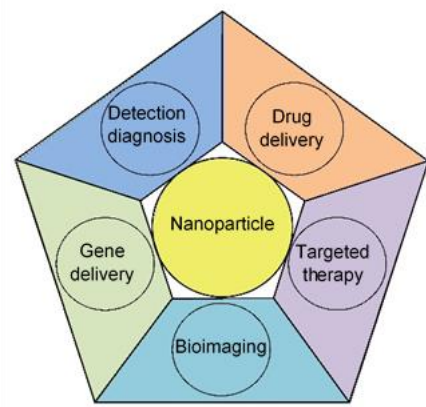


**Figure 1.** Applications les plus courantes des nanoparticules en médecine

En ce qui concerne l'imagerie, et en particulier pour la visualisation *in vivo* des organes et des tissus, il est important d'augmenter le plus possible la résolution, et récemment, l'imagerie multimodale, c'est-à-dire la combinaison de plusieurs techniques d'imagerie sur la même sonde<sup>[12]</sup>, a démontré d'intéressantes potentialités. En particulier, la combinaison de la tomographie par émission de positrons (PET), de l'imagerie optique et/ou de l'imagerie par résonance magnétique (IRM), a donné des résultats prometteurs dans la direction du régime de résolution submicronique. Pour ce concept, de nombreuses sondes multimodales ont été conçues en utilisant des systèmes dendritiques<sup>[13-15]</sup> où de grosses molécules dotées de différentes fonctionnalités. Mais la synthèse est souvent complexe et la purification est extrêmement difficile. Une voie alternative, qui peut offrir plusieurs avantages, est de développer des plateformes appropriées pour l'ancrage des différentes fonctionnalités nécessaires pour l'imagerie multimodale et, dans le même temps, assez petites pour être transportées et éliminées dans les organismes vivants. Les NPs, avec leur rapport surface/volume élevé et plusieurs de possibilités de fonctionnalisation, ont attiré l'attention dans ce domaine<sup>[16-18]</sup>. Les NPs permettent de combiner les propriétés du cœur<sup>[19]</sup>, telles que magnétisme ou photoluminescence, avec celles provenant de groupements fonctionnels qui peuvent être attachés à leur surface (par exemple des radiomarqueurs ou des agents ciblant). Bien que l'usage des nanoparticules soit très étendu, leur toxicité et leur accumulation dans les organes limite encore leurs applications *in vivo*<sup>[20-21]</sup>. En outre, parmi

les nanoparticules, beaucoup ne sont pas fonctionnalisées par liaison covalente, causant ainsi une éventuelle instabilité du système final *in vivo*<sup>[22]</sup>. Une autre question à considérer pour des applications *in vivo* est la capacité de passer à travers les barrières qui protègent certains organes, tels que la barrière hémato-encéphalique, qui doit être franchie afin de cibler les tumeurs cérébrales<sup>[23-24]</sup>. En fait, seuls les très petits objets correctement fonctionnalisés peuvent franchir cette barrière naturelle, et cela est l'une des raisons pour stimuler la recherche vers les NPs de très petite taille (<5 nm)<sup>[19]</sup>.

La thèse s'attaque à certaines de ces problématiques en préparant, caractérisant, fonctionnalisant et étudiant différents types de nanoparticules de très petite taille (NPs de silicium : Si NPs ; « carbon dots » : CQDs ; NPs de cobalt couvertes de silice : Co@SiO<sub>2</sub> NPs) dans le but final de proposer des sondes innovantes qui peuvent être utilisées, par exemple, dans l'imagerie multimodale et qui peuvent être facilement excrétées du corps. Quelques systèmes ont également été testés *in vitro* et *in vivo*.

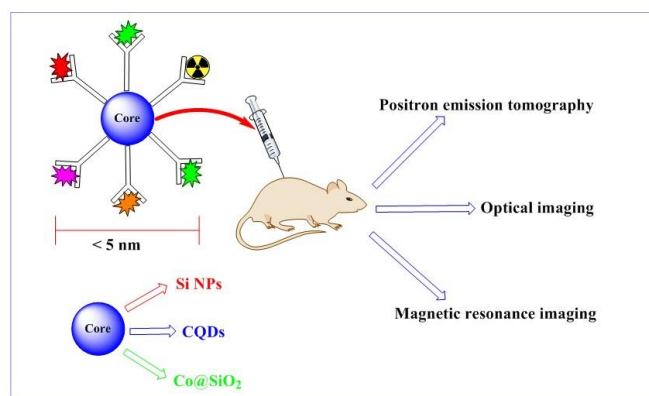


**Figure 2.** Représentation schématique d'une sonde multimodale. Dans cette étude, le cœur peut être une nanoparticule de silicium, de cobalt ou de carbone.

Comme on peut le constater sur la Figure 2, l'idée est de concevoir une sonde composée d'un cœur de très petite taille, dans notre cas à base de silicium, de cobalt ou de carbone, portant des groupes fonctionnels tels que des complexes radioactifs, des colorants ou/et des agents ciblant. Grâce aux différentes propriétés du cœur (luminescence pour les Si NPs et les CQDs, ou magnétisme

pour les Co@SiO<sub>2</sub> NPs) et aux groupes fonctionnels à la surface, on peut obtenir une sonde d'imagerie multimodale, soit pour la tomographie par émission de positrons, l'imagerie optique et/ou l'imagerie par résonance magnétique. Un point commun entre toutes les NPs étudiées, est la possibilité de fonctionnalisation à travers des liaisons covalentes. Les caractéristiques spécifiques des NPs sélectionnées sont mentionnées ci-dessous.

Les Si NPs offrent de nombreux avantages liés à : i) leur biocompatibilité, biodégradabilité et non-toxicité<sup>[25-28]</sup>; ii) leurs propriétés de photoluminescence qui sont fortement dépendantes à la fois des effets de fonctionnalisation de la surface et de confinement quantique<sup>[29]</sup>; iii) une excellente stabilité photophysique et chimique; iv) la possibilité de fonctionnaliser leur surface d'une manière covalente par des liaisons stables Si-C.

Les CQDs sont biocompatibles<sup>[30-31]</sup>, ils montrent une luminescence multicolore, dépendant à la fois des effets de confinement quantique et de fonctionnalisation de la surface. Ils possèdent également une stabilité photophysique et chimique élevées et sont préparés par synthèse très facilement. En outre, en raison des nombreuses similitudes, il est très intéressant de comparer le comportement *in vivo* des CQDs et des Si NPs.

Enfin, l'intérêt pour les nanoparticules de cobalt est principalement dû à leurs propriétés magnétiques. En effet, les Co NPs possèdent des valeurs de saturation de magnétisation plus élevées que celles composées d'oxydes métalliques comme l'oxyde de fer ou les ferrites<sup>[32]</sup>. Cette propriété permettrait d'introduire dans le corps une plus petite quantité de NPs, tout en conservant une réponse magnétique similaire, et donne des attentes prometteuses pour une utilisation future en IRM. De plus, tel que rapporté sur les NPs magnétiques<sup>[32-34]</sup>, les Co NPs ultrapetites peuvent avoir un comportement superparamagnétique<sup>[33, 35-36]</sup>. Cependant, la toxicité rapportée<sup>[37]</sup> de Co NPs doit être surmontée, au moyen d'une enveloppe protectrice<sup>[38-41]</sup>, avant de les utiliser *in vivo*. Pour cette raison, nous nous sommes concentrés sur la préparation d'une coquille mince de silice autour du cœur de cobalt, également

utile pour l'exploitation de la chimie de surface de la silice pour plus de fonctionnalisations de surface.

Après une introduction sur l'état de l'art sur les NPs de l'intérêt pour ce travail, la première partie de la thèse est consacrée aux Si NPs de très petite taille.

La préparation de Si NPs ultra-petites avec dispersion de taille étroite est toujours une tâche difficile, et en particulier la purification est difficile, avec un manque de méthodologies bien établies et claires. Les Si NPs peuvent être obtenues par des procédés chimiques ou physiques, impliquant soit des approches dites « bottom-up » ou « top-down ». Ici, nous nous sommes intéressés à des techniques « bottom-up » car le contrôle de la taille et de la terminaison à la surface des particules est beaucoup plus élevé avec ces méthodes.

Pour étudier les propriétés des nanoparticules de silicium, nous avons décidé de ne sélectionner qu'un type de fonctionnalisation (amine-terminaison) mais pour la synthèse des particules nous avons utilisé plusieurs approches afin de comprendre l'influence de la méthode de synthèse sur la taille, la luminescence, la structure, la composition et les effets biologiques. La terminaison amine a été choisie car notre but est d'obtenir des particules solubles dans l'eau et qui peuvent être facilement liés à d'autres molécules. Comme nous allons le constater, les groupements amines sont particulièrement indiqués dans ce but.

Les méthodes « bottom-up » discutées dans la thèse sont les méthodes de microémulsion et hydrothermale, toutes deux basées sur la réduction d'une source de silicium. Les techniques ont été optimisées pour obtenir de très petites NPs (de taille inférieure à 5 nm) avec une fonctionnalisation amine à la surface (amine-terminées Si NPs). Elles ont été caractérisées par plusieurs techniques, telles que la spectroscopie infrarouge (ATR/FTIR), la microscopie électronique en transmission à haute résolution (HR-TEM), la spectroscopie à rayons X à dispersion d'énergie (EDX), la spectroscopie photoélectronique aux rayons-X (XPS), l'analyse thermogravimétrique (TGA) et des mesures photophysiques. Une comparaison entre les propriétés des NPs obtenues par les

deux techniques a ensuite été effectuée afin d'étudier d'éventuelles différences, surtout de comportement dans l'imagerie *in vivo*.

Dans la méthode de microémulsion, les nanoparticules de silicium ont été préparées en utilisant une modification d'une méthode reportée<sup>[42-44]</sup> basée sur la réduction de tetraméthoxysilane ou de tetrachlorosilane avec de l'hydrure de lithium et d'aluminium (LiAlH<sub>4</sub>) et sur la réaction ultérieure (hydrosilylation) des nanoparticules obtenues (portantes la terminaison Si-H), avec de l'allylamine en présence du catalyseur H<sub>2</sub>PtCl<sub>6</sub>. La méthode de microémulsion est également appelée méthode de réduction en micelles inverses parce que la réaction a lieu dans des micelles de surfactant (tetraoctylammonium bromide, TOAB) qui nous permettent de contrôler la taille des NPs. Avec cette méthode, nous avons obtenu des nanoparticules très petites (environ 2 nm) avec la terminaison amine. Le schéma général de la méthode de microémulsion est présenté dans la Figure 3.

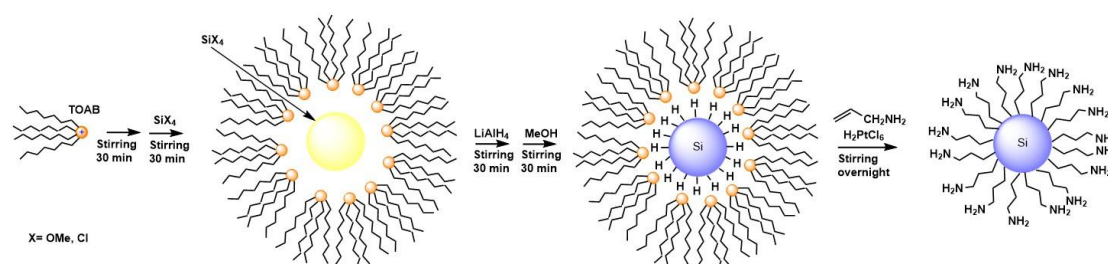


**Figure 3.** Méthode de synthèse, par réduction en micelles inverses, des Si NPs avec terminaison amine.

La purification a été une étape cruciale du travail. Enlever l'excès des réactifs et de surfactant après la synthèse, est très difficile parce que les NPs peuvent être facilement perdues au cours des étapes de purification conduisant à une diminution drastique du rendement global. Nous avons essayé plusieurs méthodes parmi lesquelles la dialyse et l'ultracentrifugation en gradient de densité, mais la chromatographie d'exclusion stérique fut la meilleure technique pour obtenir des Si NPs pures.

La Figure 4 présente des images HR-TEM montrant que les amine-terminées Si NPs obtenues avec la méthode de microémulsion sont très petites, avec une distribution de taille étroite (taille moyenne :  $2,5 \pm 0,6$  nm). De plus, dans le micrographe TEM reporté en Figure 4a, il est possible de voir le réseau cristallin du silicium. La distance entre deux franges est 0,2 nm ce qui coïncide avec la distance interplanaire des plans (220) du silicium cristallin.

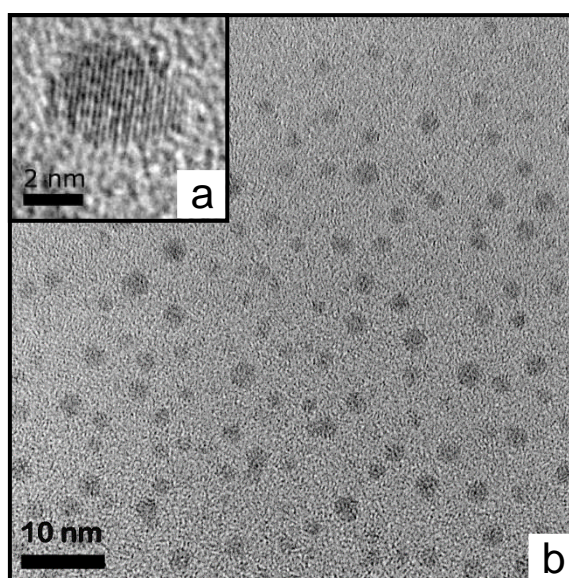


**Figure 4.** Images HR-TEM de Si NPs fonctionnalisées par un groupement amine, obtenues par la méthode de microémulsion ; a) nanoparticule isolée montrant les franges du réseau, caractéristiques des nanocristaux de silicium.

Le spectre d'absorption et d'émission dans l'eau (Figure 5a) montrent une émission dans la région du bleu du spectre électromagnétique. Selon le débat dans la littérature, cela est dû à un effet de taille ou de fonctionnalisation de la surface<sup>[29, 45-46]</sup>. Les photographies dans la Figure 5a montrent que la solution est transparente et jaune pâle sous la lumière ambiante et bleue sous irradiation UV. Si les spectres d'émission sont mesurés à différentes longueurs d'onde d'excitation, il est évident (Figure 5b) que le maximum d'émission est décalé vers le rouge lorsque l'on augmente la longueur d'onde d'excitation. Ce phénomène peut être lié à un « direct bandgap-like » comportement qui est induit par la présence des liaisons Si-C sur la surface des NPs<sup>[47]</sup>. Le rendement

quantique de photoluminescence (PLQY) est d'environ 2% à toutes les longueurs d'ondes d'excitation et, généralement, les durées de vie de luminescence peuvent être ajustées avec une décroissance tri-exponentielle en accord avec les résultats rapportés pour systèmes similaires<sup>[44, 48]</sup>.

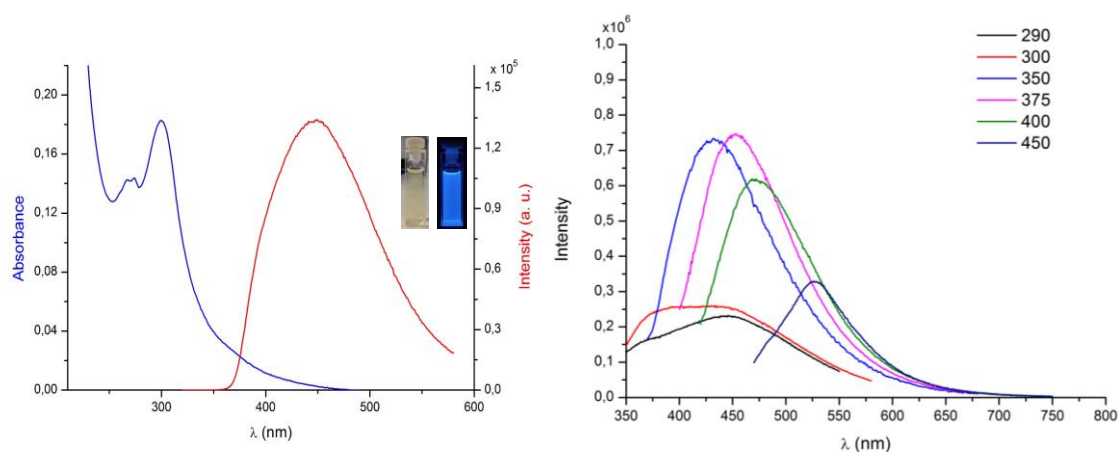


**Figure 5.** a) Spectres d'absorption (bleu) et d'émission (rouge), dans l'eau, des nanoparticules de silicium (méthode de microémulsion) avec une terminaison amine ( $\lambda_{exc} = 300$  nm; filtre 350 nm); encadré: photos de la solution dans des conditions ambiantes (à gauche) et sous irradiation UV (à droite); b) spectres d'émission à différentes longueurs d'ondes d'excitation de les mêmes Si NPs (les longueurs d'ondes d'excitation sont rapportées, en nm, en haut à droite)

Concernant la synthèse hydrothermale, les nanoparticules de silicium avec une terminaison amine ont été préparées selon la modification d'une méthode<sup>[49]</sup> basée sur le chauffage dans l'eau de (3-Aminopropyl)triméthoxysilane en présence de citrate de trisodium. Le procédé décrit dans la littérature est basé sur le chauffage par irradiation aux micro-ondes (15 min.), mais ici nous démontrons que, avec une durée de réaction plus longue (5 heures), les particules peuvent également être préparées dans un four conventionnel. L'avantage du chauffage conventionnel est la possibilité d'un écaillage facile à l'échelle industrielle. À l'échelle du laboratoire, chaque réaction peut produire jusqu'à 400 mg de Si NPs. Un schéma synthétique général pour cette méthode est reporté en figure 6.

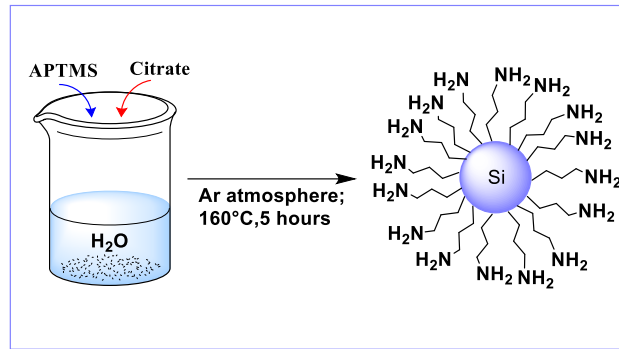


**Figure 6.** Approche synthétique pour la synthèse hydrothermale des nanoparticules de silicium terminées par un groupement amine; [APTMS = (3-aminopropyl)triméthoxysilane; citrate = Trisodium 2-hydroxypropane-1,2,3-tricarboxylate]

Les particules obtenues ont une taille légèrement plus grande (environ 4 nm) que celles obtenues par méthode de microémulsion. La synthèse donne moins d'impuretés car il y a seulement deux réactifs de départ, la purification est donc plus facile et la dialyse peut être utilisée. Cependant, les Si NPs faits par cette méthode contiennent une plus grande quantité de silicium oxydé par rapport à la méthode de microémulsion. Dans la Figure 7, les images typiques HR-TEM des Si NPs à terminaison amine, obtenus par la méthode hydrothermale, sont représentés (taille moyenne de  $4,3 \pm 1,3$  nm). En outre, sur la Figure 7b, on peut voir le réseau cristallin de silicium. La distance entre les franges est de 0,2 nm, comme pour la technique de microémulsion, ce qui est une valeur caractéristique de la distance entre les plans (220) de silicium cristallin.

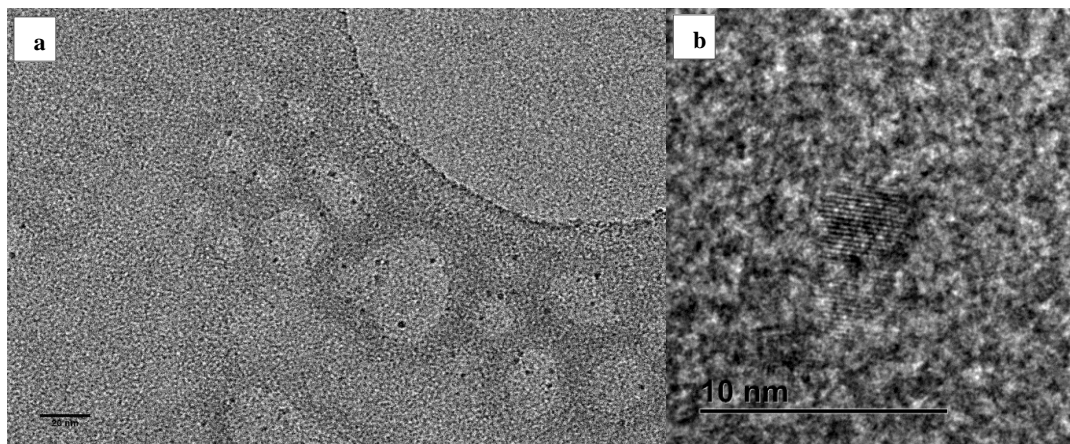


**Figure 7.** a) Images HR-TEM des Si NPs avec une terminaison amine obtenues par synthèse hydrothermale ; b) une nanoparticule montrant les franges cristallines du silicium.

Des spectres caractéristiques UV-vis et d'émission dans l'eau (Figure 8a) montrent que les particules émettent aussi dans la région du bleu lorsqu'elles sont préparées par la méthode hydrothermale. Dans ce cas également, si les spectres d'émission sont mesurés à différentes longueurs d'onde d'excitation, le maximum d'émission est décalé vers le rouge lorsque l'on augmente la longueur d'onde d'excitation (Figure 8b). Ce phénomène est moins prononcé qu'avec la méthode de microémulsion, ce qui peut être expliqué par des différences de composition superficielle entre les deux types des NPs, selon le débat dans la littérature<sup>[29, 47]</sup>. Le rendement quantique de photoluminescence des Si NPs préparés par méthode hydrothermale dépend de la longueur d'onde d'excitation et il peut être plus élevé (avec une valeur maximale de 13%) que celui des NPs préparé par le procédé de microémulsion. Les durées de vie de luminescence peuvent être ajustées avec une décroissance tri-exponentielle, comme rapporté dans la littérature<sup>[44]</sup>.

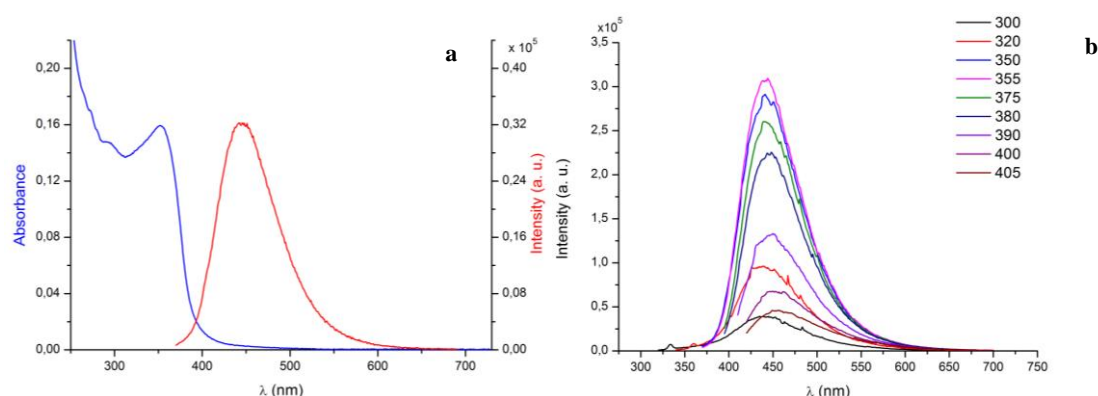


**Figure 8. a)** Spectres d'absorption (bleu) et d'émission (rouge) des Si NPs avec une terminaison amine (méthode hydrothermale) dans l'eau ( $\lambda_{exc} = 355$  nm) ; **b)** spectres d'émission à différentes longueurs d'ondes d'excitation de les mêmes Si NPs (les longueurs d'ondes d'excitation sont rapportées, en nm, en haut à droite)

Les particules préparées par ces deux méthodes ont été comparées également en termes de composition, de degré de fonctionnalisation et de stabilité de luminescence dans le temps. A partir des données XPS et IR, il en résulte que les NPs obtenues par procédé hydrothermale contient une teneur légèrement plus élevée de liaisons Si-O. A partir des données XPS et TGA, il était

également possible d'estimer pour les deux types de particules que la quantité de groupes amine par particule est de l'ordre de quelques centaines.

Afin de tester la stabilité à long terme de la photoluminescence des particules préparées par les deux méthodes, des mesures d'émissions ont été répétées après 18 semaines de stockage à l'abri de la lumière. Les deux types des NPs montrent une diminution de l'intensité d'émission. Cependant, alors que pour les NPs préparées par microémulsion, l'intensité d'émission devient environ 60% de la valeur initiale, dans le cas de la synthèse hydrothermale, il descend à environ 10% de la valeur initiale.

Une fois les propriétés comparées, les deux types des Si NPs avec terminaison amine ont été testés *in vitro* en utilisant des lignées de cellules A549 (cellules cancéreuses du poumon). Les NPs montrent une faible toxicité dans la gamme de concentrations généralement utilisés pour des tests *in vivo* (1-10 µg/mL), mais celles faites par synthèse hydrothermale montrent une viabilité cellulaire très élevée même lorsque des concentrations allant jusqu'à 1 mg/mL sont utilisées.

En conclusion, les deux méthodes conduisent avec succès à la formation des Si NPs de très petite taille à terminaison amine. Avec la méthode de microémulsion, des particules moins oxydées, plus petites (taille moyenne : 2,5 nm) et avec une stabilité d'émission plus élevée dans le temps peuvent être obtenues. D'autre part, la méthode hydrothermale permet d'obtenir des nanoparticules légèrement plus grosses (taille moyenne de 4,3 nm) dans de plus grandes quantités avec une biocompatibilité supérieure.

Le deuxième type de NPs étudiées, afin de comparer leur comportement *in vivo* avec les Si NPs, sont les CQDs. Ils ont été préparés par traitement par micro-ondes d'une solution aqueuse de chlorhydrate de L-arginine (2M) et d'éthylènediamine (2M)<sup>[51]</sup>. Dans la littérature, les CQDs sont décrits sous forme de particules quasi-sphériques ou des structures nanométriques plates de graphène avec plusieurs multifonctionnalités sur la surface<sup>[30, 52-53]</sup>. La méthode synthétique utilisée dans ce travail est connue pour entraîner une surface riche en groupements amines, carboxyliques et hydroxyles, qui contribuent de

différentes manières, selon les discussions dans la littérature, à la luminescence des CQDs. La Figure 9a rapporte une image typique HR-TEM, montrant la présence de nanoparticules avec une taille moyenne d'environ 3 nm.

Comme représenté sur la microphotographie à grossissement élevé d'une seule particule, rapportée dans l'encadré, ces CQDs sont cristallins avec une distance interplanaire de 2,1 Å, conformément à l'espacement indiqué dans le graphène<sup>[50]</sup> et le plan basal (0001) de la graphite<sup>[51]</sup>.

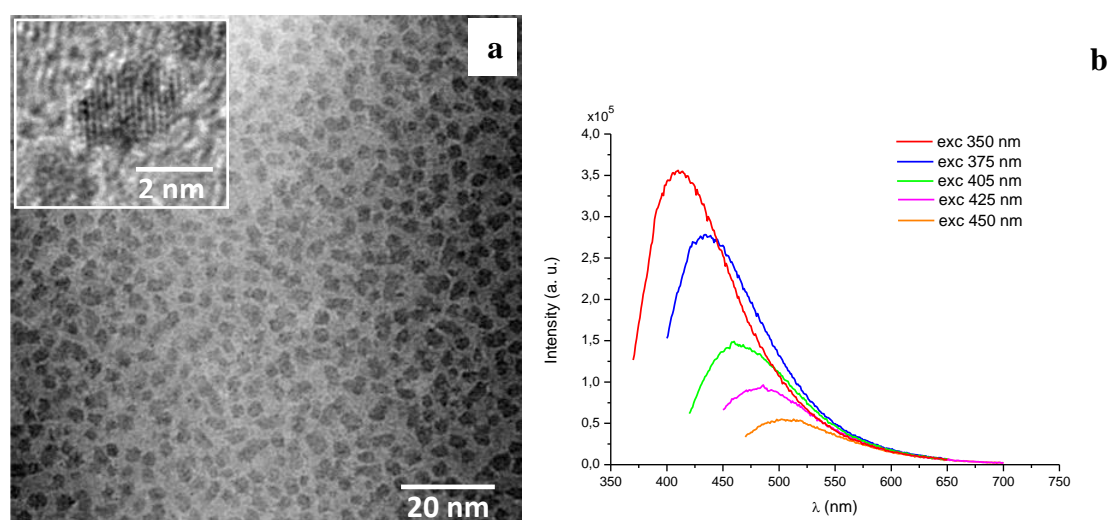


**Figure 9. a)** Images HR-TEM de CQDs; l'encadré montre une image à grossissement élevé d'une seule particule ; **b)** spectres d'émission de CQDs dans l'éthanol à différentes longueurs d'onde d'excitation (les longueurs d'ondes d'excitation sont rapportées en haut à droite).

Sur la Figure 9b, les spectres d'émission obtenus dans l'éthanol à différentes longueurs d'onde d'excitation sont rapportés, montrant que les propriétés de photoluminescence dépendent de la longueur d'onde d'excitation comme cela est indiqué généralement dans les données de la littérature<sup>[30, 51, 54-56]</sup>. Le PLQY pour les CQDs dans l'éthanol est de 7-8% à toutes les longueurs d'onde d'excitation utilisées et la durée de vie est ajustée avec une décroissance bi-exponentielle, ce qui est également rapporté pour des nanoparticules similaires<sup>[57]</sup>.

Les Si NPs et CQDs ont été, ensuite, étudiés *in vivo* et leur comportement a été comparé. Avant les expériences de bio-imagerie, les Si NPs et les CQDs ont été

fonctionnalisés avec un seul type de marqueur (soit un colorant ou un radiotracer), mais il sera montré que les résultats obtenus sont prometteurs pour une future sonde avec des multifonctionnalités sur la même particule. Les Si NPs avec terminaison amine et les CQDs ont été fonctionnalisés avec le colorant cyanine 5 ou avec des complexes de  $^{64}\text{Cu}$ . La raison pour fonctionnaliser les NPs avec le colorant cyanine est d'obtenir d'émission dans la région spectrale du rouge lointain, utile pour effectuer imagerie optique *in vivo*. En effet la radiation rouge est plus pénétrante dans les tissus et, par conséquent, elle peut être détectée même lorsque les particules atteignent les organes internes tels que le foie, les poumons et les reins. Le complexe de  $^{64}\text{Cu}$  permet de réaliser la tomographie par émission de positrons en raison des propriétés de désintégration radioactive de l'isotope de cuivre.  $^{64}\text{Cu}$  a une demi-vie d'environ 12 heures et, en certain pourcentage, il se désintègre en  $^{64}\text{Ni}$  par émission des positrons. Cette émission est utilisée comme un marqueur en médecine nucléaire. Les [Cy5 couplées-] et [ $^{64}\text{Cu}$  complexe couplées-] NPs ont été caractérisées montrant que leur taille est encore très petite et la cytotoxicité a été évaluée *in vitro*, confirmant leur biocompatibilité. Par conséquent, des expériences d'imagerie optique et de PET *in vivo* ont été effectuées. Dans les expériences d'imagerie optique, les Si NPs couplées avec la sulfo-cyanine 5 (s-Cy5-Si NPs) ont été injectés, à travers la veine de la queue, dans NMRI nu/nu souris femelles. A partir des images en Figure 10, il est clair que, 50 minutes après l'injection, la plupart des particules est dans la vessie.



**Figure 10.** Images optiques de NMRI nu/nu souris à 0, 5, 20, 50 minutes après l'injection de s-Cy5-Si NPs ; le point lumineux sur la partie supérieure de chaque image est une solution de s-Cy5-Si NPs avec la même concentration que la solution injectée.

Des expériences de biodistribution ont montré que, bien que certaines des nanoparticules s'accumulent dans l'intestin, elles sont très prometteuses pour une future sonde multimodale, puisque la majorité des NPs est déjà excrétée à 50 minutes après l'injection. Dans des expériences d'imagerie PET *in vivo*, les deux types de Si NPs ont été comparés entre eux et par rapport aux CQDs. Comme on peut le voir sur la Figure 11, les Si NPs préparées par la méthode hydrothermale et marquées avec le complexe de  $^{64}\text{Cu}$  [ $^{64}\text{Cu}$ -NOTA-Si NPs (hydro)] sont toutes dans la vessie 50 minutes après l'injection. Les Si NPs préparées par microémulsion et aussi marquées avec l'isotope radioactif de cuivre [ $^{64}\text{Cu}$ -NOTA-Si NPs (micro)] vont également à la vessie, mais, à un certain pourcentage, restent dans l'intestin. Enfin, l'activité des CQDs marqués avec le complexe du  $^{64}\text{Cu}$  ( $^{64}\text{Cu}$ -NOTA-CQDs) est principalement dans la vessie 50 minutes après l'injection, mais une petite quantité reste dans la vésicule biliaire et dans l'intestin.

Des expériences de biodistribution ont montré que, 60 minutes post-injection, les CQDs sont principalement excrétés dans l'urine, mais une quantité appréciable est toujours présente dans le foie et dans l'intestin. Les mêmes études de biodistribution pour les deux types de Si NPs montrent qu'ils sont principalement excrétés dans l'urine, mais les [ $^{64}\text{Cu}$ -NOTA Si NPs (micro)] s'accumulent également, dans un certain pourcentage, dans l'intestin comme déjà vu dans les images PET. Le comportement observé pour les CQDs est similaire à celui observé pour les  $^{64}\text{Cu}$ -NOTA-Si NPs préparées par microémulsion, mais la quantité de matière qui reste dans le corps et qui s'accumule dans les organes est plus élevée pour les CQDs que dans le cas des Si NPs. En fait, les courbes en bas de la Figure 11 montrent que tous les types de nanoparticules s'accumulent principalement dans la vessie pour être, par la suite, excrétés mais, 50 minutes après l'injection, le pourcentage de la dose injectée (% ID) présent dans la vessie pour les CQDs est inférieur (environ 40 %) à celui pour les Si NPs (environ 60 %).

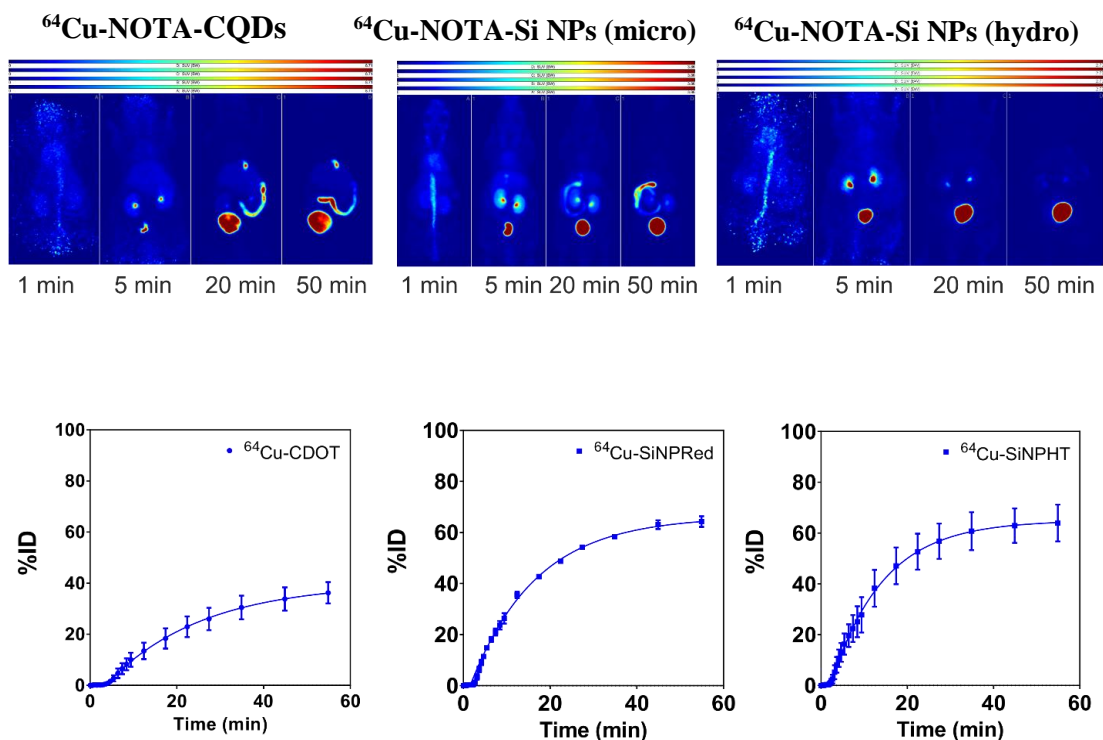


**Figure 11.** Images de tomographie par émission de positrons, à différents moments après l'injection, de NMRI nu/nu souris injectés avec  $^{64}\text{Cu-NOTA-CQDs}$  (en haut à gauche) et [ $^{64}\text{Cu-NOTA-Si NPs}$ ] faite par microémulsion (haut milieu) ou méthode hydrothermale (en haut à droite) ; pourcentage de la dose injectée en fonction du temps post-injection dans la vessie des souris injectés avec  $^{64}\text{Cu-NOTA-CQDs}$ , en bas à gauche, [ $^{64}\text{Cu-NOTA-Si NPs (micro)}$ ], au milieu, ou avec [ $^{64}\text{Cu-NOTA-Si NPs (hydro)}$ ], en bas à droite.

Il est très intéressant de comparer les mécanismes d'excrétion, rénale et hépatobiliaire, pour les trois types de particules. En fait, le mécanisme d'excrétion rénal, c'est-à-dire par les reins et la vessie, est le plus préférable comme rapporté dans la littérature<sup>[20-21]</sup>.

En Figure 12, il est évident que [ $^{64}\text{Cu-NOTA Si NPs (hydro)}$ ] sont les matériaux les plus prometteurs entre les trois types de particules parce que ces NPs sont éliminées, presque entièrement, par l'excrétion rénale. [ $^{64}\text{Cu-NOTA-Si NPs (micro)}$ ] et CQDs suivent, au contraire, tous les deux mécanismes d'excrétion, rénale et hépatobiliaire (c'est à dire à travers le foie et l'intestin). En conclusion, les trois types de NPs présentent quelques différences dans le

comportement *in vivo*, mais tous sont principalement excrétés très rapidement de l'organisme grâce à leur très petite taille.

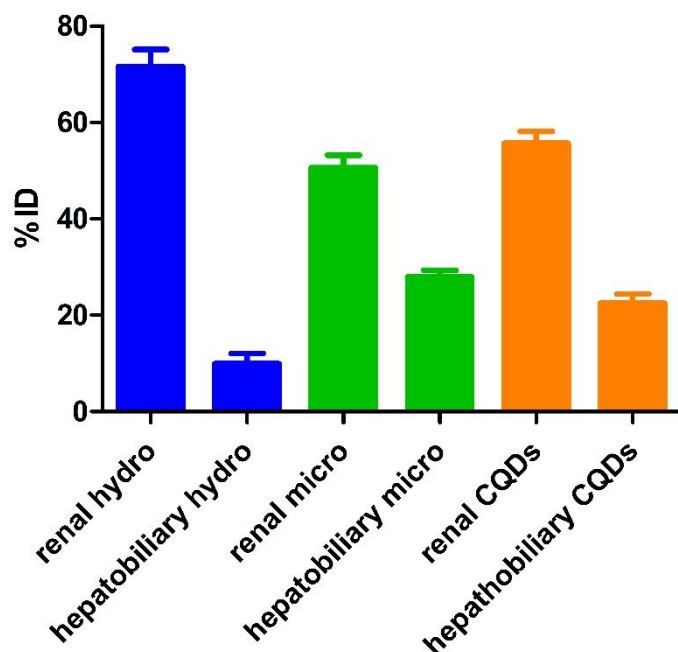


**Figure 12.** Histogramme montrant le rapport entre le mécanisme rénal et hépatobiliaire d'excrétion du [ $^{64}\text{Cu}$ -NOTA-Si NPs (hydro)] (bleu), [ $^{64}\text{Cu}$ -NOTA-Si NPs (micro)] (vert) et [ $^{64}\text{Cu}$ -NOTA-CQDs] (orange)

Étant donné que le seul papier disponible<sup>[16]</sup> sur la biodistribution par PET de Si NPs de très petite taille (préparés par une méthode différente) rapporte qu'elles s'accumulent dans le foie, les résultats obtenus dans cette thèse sont très encourageants. En fait les deux types de Si NPs étudiées, ne montrent pas d'accumulation dans le foie donnant ainsi des attentes prometteuses pour une future application dans l'imagerie multimodale.

Le dernier exemple de nanoparticules de très petite taille étudié dans cette thèse, concerne les nanoparticules de cobalt avec une coquille de silice (Co@SiO<sub>2</sub> NPs). Les nanoparticules de cobalt (Co NPs) sont préparées selon une méthode basée sur la décomposition thermique de Co<sub>2</sub>(CO)<sub>8</sub>, en présence de composés alkyliques d'aluminium<sup>[58-60]</sup>. Cette technique permet de produire des nanoparticules de cobalt stables à l'air grâce à une étape d'oxydation douce ce qui crée une coquille mince d'oxyde de cobalt autour des particules,

empêchant une oxydation supplémentaire. Les Co NPs utilisées pour le revêtement de silice ont une taille moyenne de  $7,3 \pm 1,5$  nm. Beaucoup de publications rapportent sur la création d'une coquille de silice autour des particules magnétiques<sup>[61-66]</sup>, y compris sur le cobalt<sup>[38-41]</sup> ; mais seulement quelques-uns<sup>[67-68]</sup> rapportent sur des petites Co NPs avec une coquille très mince de silice. Nous avons optimisé une stratégie de synthèse à température ambiante pour préparer des NPs cœur/coquille de très petite taille (taille totale d'environ 10 nm) avec une très mince coquille de silice (environ 2 nm). Obtenir une coquille très mince de silice est très difficile et, parfois, nous avons obtenu des nanoparticules d'oxyde de silicium isolées ou des Co NPs encapsulés dans une matrice de silice plutôt que des particules cœur/coquille isolées. Après plusieurs essais, nous avons optimisé la synthèse et contrôlé la croissance de silice en utilisant la stratégie présentée dans la Figure 13.

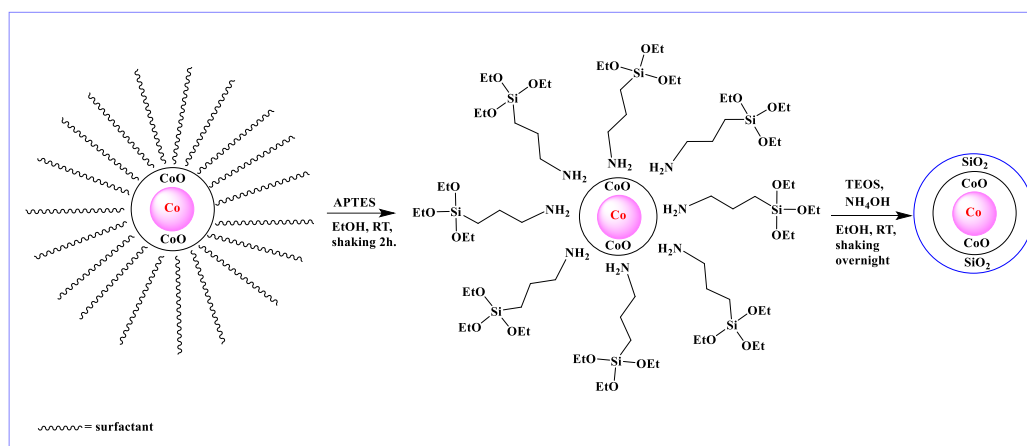


**Figure 13.** Schème de synthèse de nanoparticules de cobalt avec une coquille de silice.

Les Co@SiO<sub>2</sub> NPs ont été caractérisées par HR-TEM, EDX, XPS et par microscopie électronique en transmission filtrée en énergie (EFTEM).

La taille moyenne des NPs est de  $8,5 \text{ nm} \pm 1,5 \text{ nm}$ , donc en dessous de 10 nm, même après revêtement avec silice. Les images HR-TEM à grossissement élevé et les spectres EDX confirment la présence d'une très mince coquille de silice. Une autre preuve de la formation de la coquille de silice autour des Co NPs sont les images EFTEM. En particulier, la Figure 14 rapporte une image TEM conventionnelle de les Co@SiO<sub>2</sub> NPs (a) et les distributions EFTEM de cobalt

(b) et de l'oxygène (c). Toutes les images se rapportent à la même zone d'intérêt. Les distributions élémentaires sont obtenues à partir des spectres de perte d'énergie du faisceau d'électrons de la TEM. L'image en d) est la superposition des deux distributions élémentaires (cobalt en vert et oxygène en rouge). La superposition confirme que le cœur de cobalt est entouré par une peau d'oxyde de cobalt couverte par une autre coquille où l'oxygène est seul, c'est-à-dire la coquille de silice obtenue. Ceci est plus évident dans la Figure 14e, où un zoom sur une particule individuelle est rapporté.

Les Co@SiO<sub>2</sub> NPs ont été fonctionnalisées avec des groupements amines et caractérisées par XPS. Quelques premières tentatives pour fonctionnaliser ces amine-terminées Co@SiO<sub>2</sub> NPs avec des colorants, comme ATTO 655 et la rhodamine B, ont été réalisées avec succès, même si les intensités d'émission du système final étaient trop faibles pour réaliser des expériences *in vitro*. Néanmoins, ces résultats préliminaires montrent qu'il est possible de modifier la surface des Co@SiO<sub>2</sub> NPs avec des molécules souhaitées. La fonctionnalisation des NPs avec des groupements amines laisse ouverte la possibilité de coupler les NPs avec d'autres molécules, comme par exemple des ligands pour des radio-isotopes, afin d'effectuer d'imagerie PET, ou des agents pour cibler les cellules cancéreuses.

En conclusion, cette thèse montre que des NPs très petites, telles que Si NPs, CQDs et Co@SiO<sub>2</sub> NPs peuvent être préparées, caractérisées et fonctionnalisées, par des liaisons covalentes stables, avec des colorants ou des radiotraceurs pour étudier leurs comportement *in vitro* et *in vivo*.

Les NPs exhibent les propriétés attendues et, lorsqu'elles sont testées *in vitro*, elles ont montré une très faible cytotoxicité. Des résultats prometteurs ont été obtenus dans les expériences *in vivo* depuis les Si NPS et les CQDs ont été excrétés par le corps en temps très courts (50 minutes).

En outre, les Si NPs, obtenues par la méthode hydrothermale, ont donné le meilleur résultat dans l'imagerie PET *in vivo*, étant excrétées

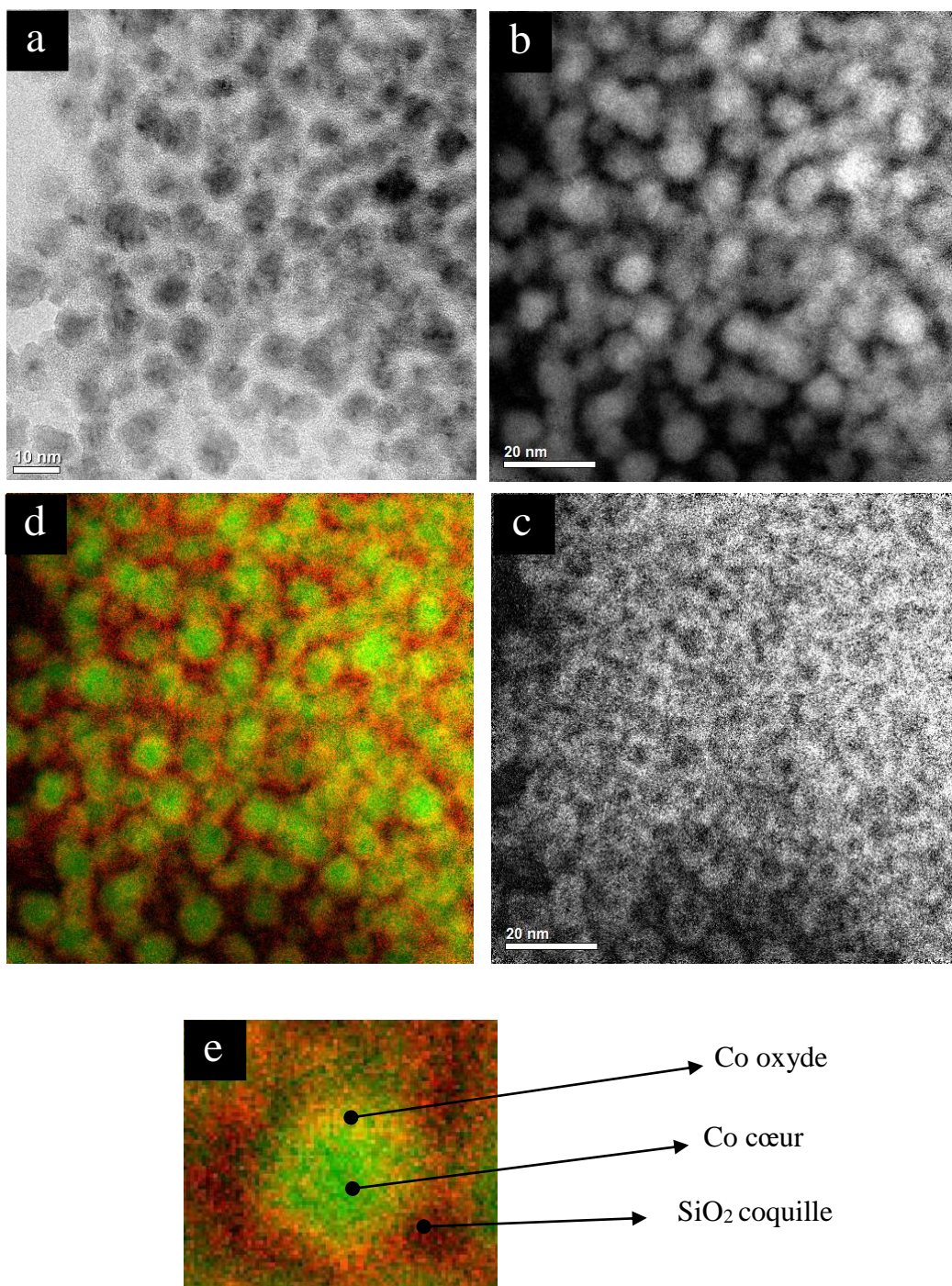


**Figure 14.** a) Image HR-TEM de Co@SiO<sub>2</sub> NPs ; distribution EFTEM de cobalt (b) et d'oxygène (c) ; superposition (d) des images (b) et (c) ; e) zoom de l'image (d) sur une seule particule

seulement 50 minutes après l'injection dans le corps et montrant aucune accumulation dans les organes.

Enfin, Co@SiO<sub>2</sub> NPs ont été préparés avec succès et leur surface a été fonctionnalisée avec des groupements amine appropriés pour des subséquentes conjugaisons. Les couplages avec des colorants indiquent la disponibilité des restants groupements amine pour d'éventuels autres couplages pour une future application dans des sondes magnétiques multimodales.

## References :

- [1] J. Estelrich, M. Quesada-Pérez, J. Forcada, J. Callejas-Fernández, in *Soft Nanoparticles for Biomedical Applications* (Ed.: J. E. José Callejas-Fernández, Manuel Quesada-Pérez, Jacqueline Forcada), RSC Nanoscience & Nanotechnology, **2014**, pp. 1-17.
- [2] R. P. Feynman, *Engineering and Science* **1960**, *23*, 22-36.
- [3] M. Hosokawa (editor), K. Nogi (editor), M. Naito (editor), T. Yokoyama (editor), *Nanoparticle Technology Handbook*, Elsevier, **2012**.
- [4] B. Pelaz, S. Jaber, D. J. de Aberasturi, V. Wulf, T. Aida, J. M. de la Fuente, J. Feldmann, H. E. Gaub, L. Josephson, C. R. Kagan, N. A. Kotov, L. M. Liz-Marzán, H. Mattoussi, P. Mulvaney, C. B. Murray, A. L. Rogach, P. S. Weiss, I. Willner, W. J. Parak, *ACS Nano* **2012**, *6*, 8468-8483.
- [5] M. V. Kovalenko, L. Manna, A. Cabot, Z. Hens, D. V. Talapin, C. R. Kagan, V. I. Klimov, A. L. Rogach, P. Reiss, D. J. Milliron, P. Guyot-Sionnest, G. Konstantatos, W. J. Parak, T. Hyeon, B. A. Korgel, C. B. Murray, W. Heiss, *ACS Nano* **2015**.
- [6] K. L. Viola, J. Sbarboro, R. Sureka, M. De, M. A. Bicca, J. Wang, S. Vasavada, S. Satpathy, S. Wu, H. Joshi, P. T. Velasco, K. MacRenaris, E. A. Waters, C. Lu, J. Phan, P. Lacor, P. Prasad, V. P. Dravid, W. L. Klein, *Nat Nano* **2015**, *10*, 91-98.
- [7] S. Marchesan, M. Prato, *ACS Medicinal Chemistry Letters* **2013**, *4*, 147-149.
- [8] J. Callejas-Fernández, J. Estelrich, M. Quesada-Pérez, J. Forcada, *Soft Nanoparticles for Biomedical Applications*, Royal Society of Chemistry, **2014**.
- [9] O. S. Wolfbeis, *Chemical Society Reviews* **2015**, *44*, 4743-4768.
- [10] S. Kunjachan, J. Ehling, G. Storm, F. Kiessling, T. Lammers, *Chemical Reviews* **2015**.
- [11] J. Liu, C. Detrembleur, S. Mornet, C. Jerome, E. Duguet, *Journal of Materials Chemistry B* **2015**, *3*, 6117-6147.
- [12] L. Martí-Bonmatí, R. Sopena, P. Bartumeus, P. Sopena, *Contrast Media & Molecular Imaging* **2010**, *5*, 180-189.
- [13] N. R. B. Boase, I. Blakey, B. E. Rolfe, K. Mardon, K. J. Thurecht, *Polymer Chemistry* **2014**, *5*, 4450-4458.

- [14] H. Kobayashi, Y. Koyama, T. Barrett, Y. Hama, C. A. S. Regino, I. S. Shin, B.-S. Jang, N. Le, C. H. Paik, P. L. Choyke, Y. Urano, *ACS Nano* **2007**, *1*, 258-264.
- [15] L.-p. Wu, M. Ficker, J. B. Christensen, P. N. Trohopoulos, S. M. Moghimi, *Bioconjugate Chemistry* **2015**.
- [16] C. Tu, X. Ma, A. House, S. M. Kauzlarich, A. Y. Louie, *ACS Medicinal Chemistry Letters* **2011**, *2*, 285-288.
- [17] L. Jing, K. Ding, S. V. Kershaw, I. M. Kempson, A. L. Rogach, M. Gao, *Advanced Materials* **2014**, *26*, 6367-6386.
- [18] T. Liu, S. Shi, C. Liang, S. Shen, L. Cheng, C. Wang, X. Song, S. Goel, T. E. Barnhart, W. Cai, Z. Liu, *ACS Nano* **2015**, *9*, 950-960.
- [19] B. H. Kim, M. J. Hackett, J. Park, T. Hyeon, *Chemistry of Materials* **2014**, *26*, 59-71.
- [20] H. Soo Choi, W. Liu, P. Misra, E. Tanaka, J. P. Zimmer, B. Itty Ipe, M. G. Bawendi, J. V. Frangioni, *Nat Biotech* **2007**, *25*, 1165-1170.
- [21] X.-D. Zhang, J. Yang, S.-S. Song, W. Long, J. Chen, X. Shen, H. Wang, Y.-M. Sun, P.-X. Liu, S. Fan, *International Journal of Nanomedicine* **2014**, *9*, 2069-2072.
- [22] W. G. Kreyling, A. M. Abdelmonem, Z. Ali, F. Alves, M. Geiser, N. Haberl, R. Hartmann, S. Hirn, D. J. de Aberasturi, K. Kantner, G. Khadem-Saba, J.-M. Montenegro, J. Rejman, T. Rojo, I. R. de Larramendi, R. Ufartes, A. Wenk, W. J. Parak, *Nat Nano* **2015**, *10*, 619-623.
- [23] T. D. Farr, C.-H. Lai, D. Grünstein, G. Orts-Gil, C.-C. Wang, P. Boehm-Sturm, P. H. Seeberger, C. Harms, *Nano Letters* **2014**, *14*, 2130-2134.
- [24] H. Yamamoto, in *Nanoparticle Technology Handbook (Second Edition)* (Ed.: M. H. N. N. Yokoyama), Elsevier, Amsterdam, **2012**, pp. 543-546.
- [25] F. Peng, Y. Su, Y. Zhong, C. Fan, S.-T. Lee, Y. He, *Accounts of Chemical Research* **2014**, *47*, 612-623.
- [26] J.-H. Park, L. Gu, G. von Maltzahn, E. Ruoslahti, S. N. Bhatia, M. J. Sailor, *Nat Mater* **2009**, *8*, 331-336.
- [27] L. T. Canham, *Advanced Materials* **1995**, *7*, 1033-1037.
- [28] N. K. Hon, Z. Shaposhnik, E. D. Diebold, F. Tamanoi, B. Jalali, *Journal of Biomedical Materials Research Part A* **2012**, *100A*, 3416-3421.
- [29] M. Dasog, Z. Yang, S. Regli, T. M. Atkins, A. Faramus, M. P. Singh, E. Muthuswamy, S. M. Kauzlarich, R. D. Tilley, J. G. C. Veinot, *ACS Nano* **2013**, *7*, 2676-2685.
- [30] G. Hong, S. Diao, A. L. Antaris, H. Dai, *Chemical Reviews* **2015**.
- [31] S.-T. Yang, L. Cao, P. G. Luo, F. Lu, X. Wang, H. Wang, M. J. Mezziani, Y. Liu, G. Qi, Y.-P. Sun, *Journal of the American Chemical Society* **2009**, *131*, 11308-11309.
- [32] L.-Y. Lu, L.-N. Yu, X.-G. Xu, Y. Jiang, *Rare Met.* **2013**, *32*, 323-331.
- [33] J. P. Chen, C. M. Sorensen, K. J. Klabunde, G. C. Hadjipanayis, *Journal of Applied Physics* **1994**, *76*, 6316-6318.
- [34] C. N. R. Rao, G. U. Kulkarni, P. J. Thomas, in *Nanocrystals: Synthesis, Properties and Applications*, Springer-Verlag, **2007**, pp. 1-23.
- [35] S. N. Khanna, S. Linderoth, *Physical Review Letters* **1991**, *67*, 742-745.
- [36] L. M. Parkes, R. Hodgson, L. T. Lu, L. D. Tung, I. Robinson, D. G. Fernig, N. T. K. Thanh, *Contrast Media & Molecular Imaging* **2008**, *3*, 150-156.
- [37] J. Sengupta, S. Ghosh, P. Datta, A. Gomes, A. Gomes, *Journal of Nanoscience and Nanotechnology* **2014**, *14*, 990-1006.

- [38] Y. Kobayashi, M. Horie, M. Konno, B. Rodríguez-González, L. M. Liz-Marzán, *The Journal of Physical Chemistry B* **2003**, *107*, 7420-7425.
- [39] N. Batail, I. Cléménçon, C. Legens, A. Chaumonnot, D. Uzio, *European Journal of Inorganic Chemistry* **2013**, *2013*, 1258-1264.
- [40] V. Salgueiriño-Maceira, M. A. Correa-Duarte, M. Farle, M. A. López-Quintela, K. Sieradzki, R. Diaz, *Langmuir* **2006**, *22*, 1455-1458.
- [41] V. Salgueiriño-Maceira, M. Spasova, M. Farle, *Advanced Functional Materials* **2005**, *15*, 1036-1040.
- [42] M. Rosso-Vasic, E. Spruijt, B. van Lagen, L. De Cola, H. Zuilhof, *Small* **2008**, *4*, 1835-1841.
- [43] J. H. Warner, A. Hoshino, K. Yamamoto, R. D. Tilley, *Angewandte Chemie International Edition* **2005**, *44*, 4550-4554.
- [44] M. Rosso-Vasic, E. Spruijt, Z. Popovic, K. Overgaag, B. van Lagen, B. Grandidier, D. Vanmaekelbergh, D. Dominguez-Gutierrez, L. De Cola, H. Zuilhof, *Journal of Materials Chemistry* **2009**, *19*, 5926-5933.
- [45] J. Thomas, S. Ashby, F. Huld, T. Pennycook, Y. Chao, *J Nanopart Res* **2015**, *17*, 1-8.
- [46] J. J. Romero, M. J. Llansola-Portolés, M. L. Dell'Arciprete, H. B. Rodríguez, A. L. Moore, M. C. Gonzalez, *Chemistry of Materials* **2013**, *25*, 3488-3498.
- [47] K. Dohnalova, A. N. Poddubny, A. A. Prokofiev, W. D. A. M. de Boer, C. P. Umesh, J. M. J. Paulusse, H. Zuilhof, T. Gregorkiewicz, *Light Sci Appl* **2013**, *2*, e47.
- [48] J. R. Siekierzycka, M. Rosso-Vasic, H. Zuilhof, A. M. Brouwer, *The Journal of Physical Chemistry C* **2011**, *115*, 20888-20895.
- [49] Y. Zhong, F. Peng, F. Bao, S. Wang, X. Ji, L. Yang, Y. Su, S.-T. Lee, Y. He, *Journal of the American Chemical Society* **2013**, *135*, 8350-8356.
- [50] L. Wang, Y. Wang, T. Xu, H. Liao, C. Yao, Y. Liu, Z. Li, Z. Chen, D. Pan, L. Sun, M. Wu, *Nat Commun* **2014**, *5*.
- [51] D. Mazzier, M. Favaro, S. Agnoli, S. Silvestrini, G. Granozzi, M. Maggini, A. Moretto, *Chemical Communications* **2014**, *50*, 6592-6595.
- [52] X. T. Zheng, A. Ananthanarayanan, K. Q. Luo, P. Chen, *Small* **2015**, *11*, 1620-1636.
- [53] H. Li, Z. Kang, Y. Liu, S.-T. Lee, *Journal of Materials Chemistry* **2012**, *22*, 24230-24253.
- [54] S. N. Baker, G. A. Baker, *Angewandte Chemie International Edition* **2010**, *49*, 6726-6744.
- [55] M. Bhaisare, A. Talib, M. S. Khan, S. Pandey, H.-F. Wu, *Microchim Acta* **2015**, 1-9.
- [56] Z. Fan, S. Li, F. Yuan, L. Fan, *RSC Advances* **2015**, *5*, 19773-19789.
- [57] L. Wang, S.-J. Zhu, H.-Y. Wang, S.-N. Qu, Y.-L. Zhang, J.-H. Zhang, Q.-D. Chen, H.-L. Xu, W. Han, B. Yang, H.-B. Sun, *ACS Nano* **2014**, *8*, 2541-2547.
- [58] H. Bönemann, W. Brijoux, R. Brinkmann, N. Matoussevitch, N. Waldöfner, N. Palina, H. Modrow, *Inorganica Chimica Acta* **2003**, *350*, 617-624.
- [59] H. Bönemann, W. Brijoux, R. Brinkmann, N. Matoussevitch, W. Norbert, *Vol. WO/2004/001776 Germany*, **2003**.
- [60] S. Behrens, H. Bönemann, N. Matoussevitch, E. Dinjus, H. Modrow, N. Palina, M. Frerichs, V. Kempter, W. Maus-Friedrichs, A. Heinemann, M. Kammel, A. Wiedenmann, L. Pop, S. Odenbach, E. Uhlmann, N. Bayat, J. Hesselbach, J. M. Guldbakke, *Z. Phys. Chem.* **2006**, *220*, 3-40.

- [61] N. Hong, A. T. Raghavender, O. Ciftja, M. H. Phan, K. Stojak, H. Srikanth, Y. Zhang, *Appl. Phys. A* **2013**, *112*, 323-327.
- [62] Q. Dai, M. Lam, S. Swanson, R.-H. R. Yu, D. J. Milliron, T. Topuria, P.-O. Jubert, A. Nelson, *Langmuir* **2010**, *26*, 17546-17551.
- [63] C. Cannas, A. Musinu, A. Ardu, F. Orrù, D. Peddis, M. Casu, R. Sanna, F. Angius, G. Diaz, G. Piccaluga, *Chemistry of Materials* **2010**, *22*, 3353-3361.
- [64] G. Ennas, A. Falqui, S. Marras, C. Sangregorio, G. Marongiu, *Chemistry of Materials* **2004**, *16*, 5659-5663.
- [65] A. B. Dávila-Ibáñez, R. Mariño-Fernández, M. Maceira-Campos, A. García-Lorenzo, V. Martínez-Zorzano, V. Salgueiriño, *The Journal of Physical Chemistry C* **2014**, *118*, 28266-28273.
- [66] J. H. Jang, H. B. Lim, *Microchemical Journal* **2010**, *94*, 148-158.
- [67] S. Behrens, H. Bönnemann, N. Matoussevitch, A. Gorschinski, E. Dinjus, W. Habicht, J. Bolle, S. Zinoveva, N. Palina, J. Hormes, H. Modrow, S. Bahr, V. Kempter, *Journal of Physics: Condensed Matter* **2006**, *18*, S2543.
- [68] N. Matoussevitch, A. Gorschinski, W. Habicht, J. Bolle, E. Dinjus, H. Bönnemann, S. Behrens, *Journal of Magnetism and Magnetic Materials* **2007**, *311*, 92-96.



# Chapter 1

## Introduction

### Abstract

This Chapter, after a brief introduction on nanoparticles and their applications in medicine, introduces the advantages and opportunities offered by ultras-small (< 5 nm) nanoparticles in bioimaging with particular attention to multimodal imaging. The second part of the chapter gives an overview on the state-of-art on properties, methods of preparation, functionalization, *in vitro* and *in vivo* applications of ultras-small silicon nanoparticles, carbon dots and cobalt based nanoparticles that will be the object of this thesis.

### 1.1 Ultras-small nanoparticles and their bioapplications

The use of nanoparticles (NPs) has a long history and their unique optical properties were already exploited in ancient objects and paintings such as the famous Lycurgus cup, manufactured in the fourth century AD<sup>[1]</sup>. This cup displays different colors depending if it is irradiated from the exterior or the interior, being red or green depending on the direction of the incident light. This is due to the presence of NPs in the material composing the cup. However, the phenomenon remained unexplained until the development of quantum physics, which clarified why properties of materials change dramatically when the size goes down to the nanoscale. In 1960 Richard Feynman was one of the first to predict the great potentialities of nanoscience<sup>[2]</sup>. It is amazing to see that, after more than 50 years, the « nanoworld » is still full of opportunities and

nanoscience and nanotechnology represent a wide and rich field to explore. Nanoparticles are used in many applications<sup>[3]</sup> ranging from electronics, photonics, photovoltaics to sensing and medicine<sup>[4-5]</sup>. In particular, the possibility to design and tune size, functionalization and properties of NPs is attracting increasing interest in the field of nanomedicine<sup>[4,6-9]</sup>, both for *in vitro* and *in vivo* imaging<sup>[9-10]</sup> as well as for drug delivery<sup>[11]</sup>. Figure 1.1 tries to summarize, schematically, the applications of nanoparticles in medicine.

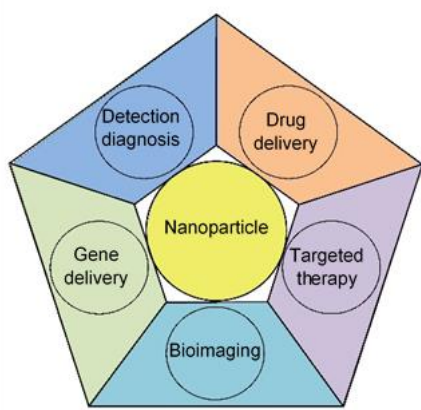


**Figure 1.1.** Some of the most common applications of nanoparticles in medicine

For these applications several kinds of NPs can be used<sup>[12]</sup>. Actually the field is very broad and a comprehensive overview is difficult and beyond the scope of this thesis. Limiting the attention to inorganic NPs, noble metal<sup>[13]</sup> and oxide-based ones<sup>[14]</sup> are very popular, but many other systems can be employed, depending on the specific application.

Concerning imaging applications and, in particular, *in vivo* visualization of organs and tissues, an increasing resolution is desired. In this respect, the new frontier of diagnostics is multimodal imaging that combines several imaging techniques on the same probe<sup>[15]</sup>. More precisely, the combination of positron emission tomography (PET), optical imaging and/or magnetic resonance imaging (MRI) has given promising results in the direction of the submicron resolution regime. For this concept, many multimodal probes have been designed using dendritic systems<sup>[16-18]</sup> or large molecules with different functionalities. However, the synthesis is often complex and purification is extremely difficult.

An alternative route, that can offer several advantages, is that of developing small "platforms" suitable for the anchoring of the different functionalities needed for multimodal imaging and, at the same time, small enough to be transported and eliminated by living organisms. Nanoparticles, with their high surface area and easy functionalization, have indeed attracted large attention in this field<sup>[19-21]</sup>. NPs allow combining the properties of their core<sup>[22]</sup> (e.g., magnetism or photoluminescence) with those deriving from the functional groups present on their surface (e. g., radioactivity).

Although the use of NPs is wide, toxicity and accumulation in organs still limit their *in vivo* applications. Also, in many cases, the functionalization does not occur through covalent bonds, and this can lead to a decomposition of the system *in vivo*<sup>[23]</sup>. Another issue to be considered for *in vivo* applications is the ability to pass through the barriers that protect certain organs, such as the blood-brain barrier (BBB) that must be crossed in order to target brain tumors<sup>[24-25]</sup>. Actually, only extremely small objects, properly functionalized, can cross this natural barrier, and this is one of the reasons for boosting research towards ultrasmall sized (< 5 nm) NPs<sup>[22]</sup>. For these reasons, the type of the materials and the size of nanoparticles are a crucial issue. Ultrasmall NPs tackle some of the issues discussed above since, due to their size, they have intermediate properties between molecules and larger particles and they possess a very large surface area. The great advantage offered by ultrasmall NPs is that they can be excreted easily from the body reducing accumulation in organs and, as mentioned before, they could be exploited to cross barriers in the body, e.g. the BBB. In addition, when shrinking the size to small and, in particular, to ultrasmall dimensions, many are the properties that change compared to the corresponding bulk materials. For example, in the case of magnetic materials, superparamagnetism starts to occur below a certain size and, in the case of quantum dots, fluorescence properties arise. Such kind of size-depending properties are very useful in order to achieve bioimaging of cells, tissues and organs and this is another reason why ultrasmall nanoparticles are very promising in the field of nanomedicine.

For the reasons illustrated above, i.e. the properties deriving from ultrasmall dimensions, the possibility to functionalize the surface *via* stable covalent bonds and also for the specific features that will be outlined in the following paragraphs, the aim of this thesis is the synthesis, characterization, functionalization and *in vitro* and *in vivo* applications of three kinds of ultrasmall nanoparticles: silicon NPs (Si NPs), carbon dots (CQDs) and silica coated cobalt NPs (Co@SiO<sub>2</sub> NPs). They show the properties of ultrasmall NPs, but they are also characterized by a very stable surface functionalization since the desired groups are anchored on their surface by covalent Si-C or C-C bonds.

The idea is to design innovative probes for multimodal imaging, which are non-toxic and can be easily excreted from the body. The probe is composed of an ultrasmall core, in our case a silicon, carbon or silica coated cobalt based one, properly functionalized, e.g. with radiolabels, dyes and/or targeting agents as sketched in Figure 1.2. Due to the different properties of the core (luminescence for Si NPs and CQDs or magnetism for Co@SiO<sub>2</sub> NPs) and the functional groups on the surface (for instance radioactivity), a multimodal probe, either for positron emission tomography, optical imaging and/or magnetic resonance imaging, can be obtained. If the particles are functionalized also with targeting agents, they could selectively reach e.g. tumour tissues in the body.

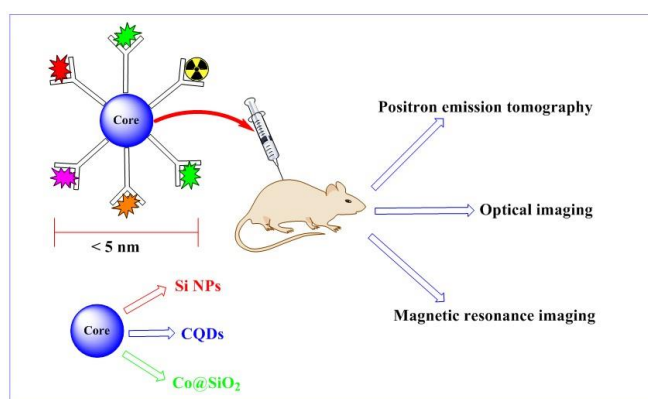


**Figure 1.2.** Schematic representation of a multimodal probe. In this study, the core can be silicon, cobalt or carbon nanoparticles.

The choice of the core material is dictated by different advantages we can gain from its specific properties, but an important feature common to all the NPs

investigated is that their surface can be functionalized through stable covalent bonds.

The specific characteristics of the selected NPs can be outlined as follows.

Silicon nanoparticles offer many advantages connected with: their biocompatibility, biodegradability and non-toxicity<sup>[26-29]</sup>; photoluminescence properties that are strongly dependent both from quantum confinement and surface functionalization effects<sup>[30]</sup>; an excellent photophysical and chemical stability; the possibility to functionalize their surface in a covalent way through stable Si-C bonds.

Carbon dots are biocompatible<sup>[31-32]</sup>, show a bright multi-coloured luminescence, dependent on both quantum confinement and surface functionalization effects, possess a high photophysical and chemical stability and are prepared through very facile one-step synthesis. However, it is more difficult to control their size, their shape and their surface chemistry. In view of the several similar properties, it is very interesting to compare the behavior *in vivo* of CQDs and Si NPs.

Finally, the interest for cobalt nanoparticles is mainly in their magnetic properties. Indeed, Co NPs possess higher values of saturation magnetization than the ones composed of metal oxides such as ferrite or iron oxides<sup>[33]</sup>. This property would allow to introduce in the body a smaller quantity of NPs while retaining a similar magnetic response, and gives promising expectations for a future use in MRI. In addition, as reported for other magnetic NPs<sup>[33-35]</sup>, ultrasmall Co NPs can display superparamagnetic behaviour<sup>[34, 36-37]</sup>. However, the reported toxicity<sup>[38]</sup> of Co NPs must be overcome, by means of a protecting shell<sup>[39-42]</sup> before using them *in vivo*. Also, the synthetic methods to obtain Co NPs have been well established and it is possible to obtain very stable and quite monodisperse particles.

Since these NPs are good candidates as cores for multimodal probes, this chapter continues with a brief introduction on multimodal imaging, followed by an overview on the preparation, functionalization and bioapplications of these three kinds of ultrasmall NPs.

## 1.2 Multimodal imaging

Bioimaging is an important tool for non-invasive detection of tumour or disease in the body. Nowadays, MRI, PET and optical imaging techniques are widely used in the hospitals for bioimaging. The new frontier of diagnostics is multimodal imaging that combines several techniques using an unique probe. The combination of these multiple informations can be reached either acquiring the images at the same time (synchronous) and merging them automatically, or at different times (asynchronous) and fusing them, afterwards, by digital manipulation techniques.<sup>[15]</sup> In order to make multimodal imaging working in an appropriate way, it is necessary to use probes that can give detectable signals and that are highly specific for the desired target. NPs are very useful in this respect both for their special properties deriving from their “nano-size” and for their large surface area that can be functionalized with different biomolecules and/or specific targeting agents.

In 1966 Kuhl et al.<sup>[43]</sup> were the first to use a prototype of SPECT-CT (Single photon emission computed tomography-computed tomography), a multimodal technique, to obtain thoracic images of a patient. In diagnostics, nowadays, the most used multimodal techniques are SPECT-CT and positron emission tomography-computed tomography (PET-CT). More recently, positron emission tomography combined with magnetic resonance (PET-MR) started to have an increased use. Indeed MR imaging has several advantages vs the most common X-ray detection, like high soft-tissue contrast, and allows to obtain multidimensional, morphological, structural, and functional informations.

Regarding the probes, a great research effort is directed towards the design and preparation of nanoparticles possessing more than one detectable property to exploit multimodal imaging<sup>[9, 12]</sup>, which is still a rather new and exciting field of research. For example, Fan et al.<sup>[44]</sup> reported on magnetite nanorings decorated with semiconductor quantum dots, namely CdSe/ZnS nanoparticles. The particles were functionalized with polyethylenimine (PEI) and then grafted on the surface of magnetite nanorings that were modified with citric acid. The final

system, as can be seen in Figure 1.3, is a dual-modality magnetic-fluorescent nanoprobe, with a size of 100-200 nm, which is uptaken by MGH bladder cancer cells.

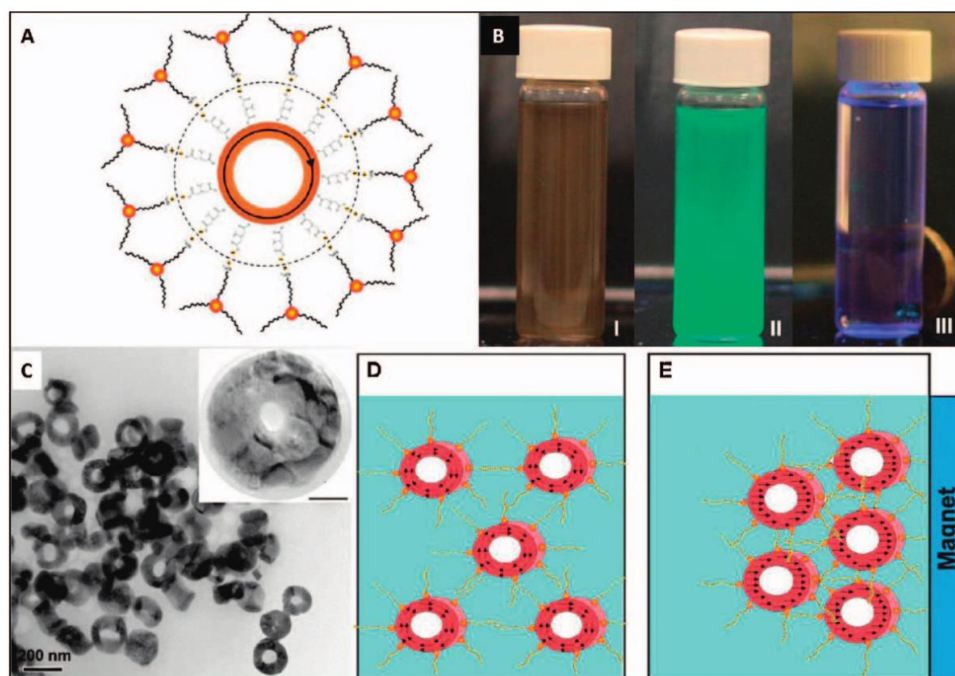


**Figure 1.3.** A) Model of a fluorescent magnetic nanoring; B) pictures of the magnetic-fluorescent nanorings in water in: I) ambient conditions; II) under UV-irradiation; III) under UV irradiation and applied magnetic field; C) Transmission electron micrographs of the fluorescent-magnetic nanorings; D-E) model of fluorescent-magnetic nanorings in solution (D) and under applied magnetic field. Reprinted from ref<sup>[12]</sup>, adapted from ref<sup>[44]</sup>

In another example, Sun et al.<sup>[45]</sup> report on NaYF:Yb, Tm@NaGdF upconversion nanoparticles (UCNPs), that were coated with mesoporous silica (mSiO<sub>2</sub>). Afterwards, the silica surface was functionalized with lanthanide (Eu, Sm, Er, Nd, Yb)  $\beta$ -diketonate derivatives through the use of alkoxysilane-modified dibenzoylmethane (dbm-Si). The final system UCNPs@mSiO<sub>2</sub>-Ln(dbm)<sub>4</sub>, with a size of 95-110 nm, show low toxicity and high biocompatibility and can give both down-conversion and up-conversion luminescence showing a multi-coloured emission (from 450 to 1700 nm). Up-conversion is suitable for performing *in vivo* studies, while down-conversion is appropriate for *in vitro*

tests. Furthermore, the presence of Gd (III) in the particles, allows their use also as contrast agents in magnetic resonance imaging. Therefore these particles are another promising example of bimodal imaging. In Figure 1.4, a schematic model of the above mentioned particles and of their applications in imaging are shown.

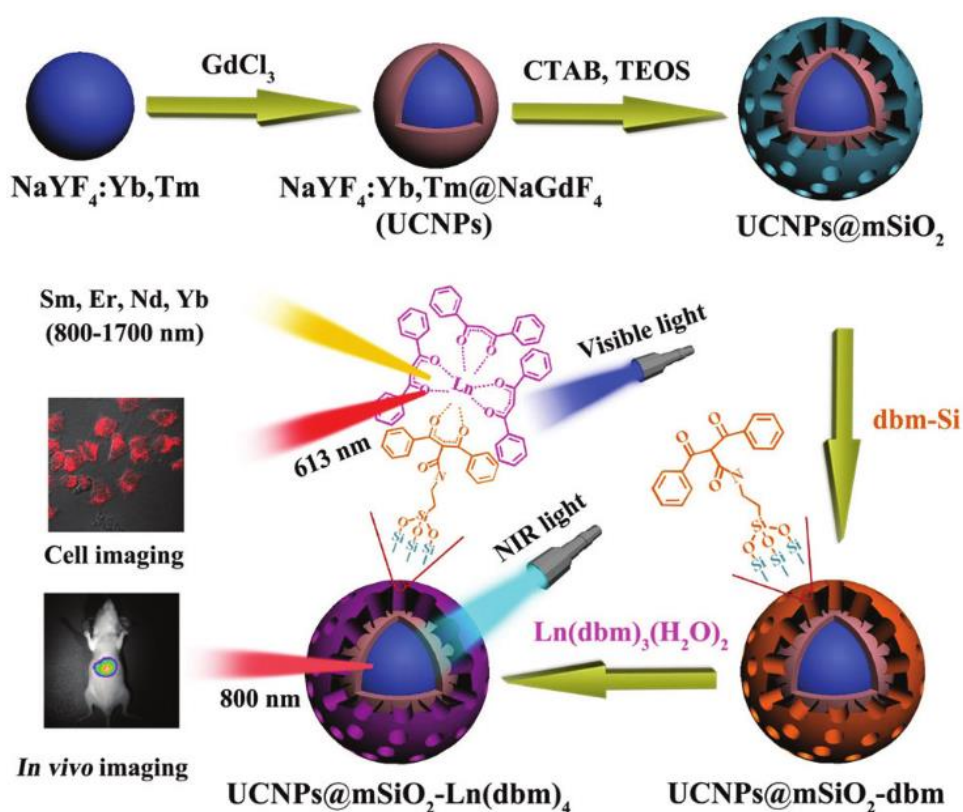


**Figure 1.4.** Scheme of the preparation of  $\text{UCNPs}@m\text{SiO}_2\text{Ln}(\text{dbm})_4$  and their applications in imaging (*in vitro* and *in vivo*); Ln = Eu, Sm, Er, Nd, Yb). Reprinted from ref<sup>[45]</sup>

A more relevant example is the work of Kauzlarich group<sup>[19]</sup> (Figure 1.5). They were the first to perform *in vivo* biodistribution experiments with ultrasmall silicon nanoparticles (Si NPs) radiolabelled with a  $^{64}\text{Cu}$  complex. The  $^{64}\text{Cu}$  complex allows to perform positron emission tomography due to the presence of the copper isotope that has interesting radioactive decay properties.  $^{64}\text{Cu}$  has a half-life of about 12 hours and a certain percentage of it decays, by positron emission, to  $^{64}\text{Ni}$ . The positron emission is then used in nuclear medicine as a

label. Kauzlarich, therefore, reports on PET of mice using dextran-coated manganese doped silicon nanoparticles that are functionalized with a  $^{64}\text{Cu}$  complex (final average hydrodynamic radius 15.1 nm). The manganese doping is, probably, done in the perspective of a future use of these NPs in multimodal imaging since the same authors reported in another contribution about the appearance of magnetic properties in Mn doped Si NPs<sup>[46-48]</sup>. The particles are rapidly excreted by renal filtration, but they also accumulate in the liver. This could be due to the distribution of sizes, with smaller particles being rapidly excreted and bigger ones accumulating in the liver. Nevertheless, this is an important example of biocompatible NPs that possess multiple properties (in this case, the photoluminescence of the ultrasmall silicon core, the radioactivity of the surface functional groups and the magnetic properties deriving from the manganese doping) and, therefore, an interesting strategy of possible multimodal probe with ultrasmall Si NPs.

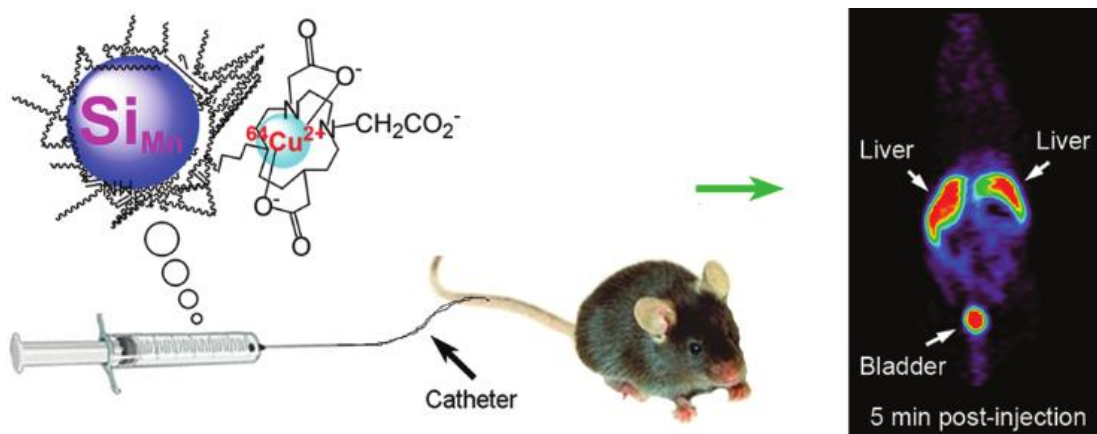


**Figure 1.5.** A schematic representation of dextran coated manganese doped silicon nanoparticles that are functionalized with a  $^{64}\text{Cu}$  complex and PET image at 5 minutes post-injection in mice, showing that particles are already in the bladder, but start to accumulate also in the liver. Reprinted from<sup>[19]</sup>

## 1.3 Ultrasmall silicon nanoparticles

### 1.3.1 Why silicon nanoparticles?

Silicon is one of the most abundant materials on Earth. It has been widely used in several applications thanks to its semiconductor properties and low toxicity. In the last 50 years, the technological applications and, parallel, the research on silicon increased enormously, mostly in connection with microelectronics applications<sup>[49-50]</sup>. In the field of nanoscience and nanotechnology, silicon-based materials are of large interest, also in view of the new properties that appear when size shrinks to the nanoscale. Silicon nanoparticles (Si NPs) are applied in several fields ranging from light emitting devices (LEDs) <sup>[51-54]</sup> to solar cells <sup>[55-61]</sup> to biological fluorescence imaging<sup>[19, 62-80]</sup>. Silicon NPs are particularly interesting for different reasons and, among these, the possibility to tune and control particle size down to ultrasmall dimensions (< 5 nm), as well as their luminescent properties that are dependent both on size (due to quantum confinement effects) and on surface functionalization. Silicon nanoparticles are characterized also by an excellent photophysical and chemical stability, once their surface is properly capped. Also, they are very versatile since they can be easily functionalized with various groups thanks to the well-known chemistry of silicon surfaces and the formation of stable Si-C bonds. To be used in bioimaging, it is essential that nanoparticles are non-toxic and extremely biocompatible. It has been already reported<sup>[26-27, 81]</sup> that porous silicon nanoparticles (mean size: 126 nm) are biodegradable and the degradation products are easily cleared through the kidneys in mice. Actually silicon already exists in mammals [humans] as a trace element and the biodegradation product of silicon nanomaterials is the highly biocompatible orthosilicic acid. For their properties, silicon nanoparticles can be included in the bigger family of semiconductor quantum dots. For long time, classical semiconductor quantum dots, such as CdSe, CdS or ZnS, have been proposed as an alternative to organic

dyes for the labelling in bioimaging due to their higher resistance against photo-bleaching and the intense and narrow emission spectra. But it is well known<sup>[82]</sup> that these nanoparticles show a quite high cytotoxicity, and therefore their use *in vivo* has been limited to fluorescence driven surgery<sup>[83]</sup>. Si NPs are therefore a good alternative since they retain the properties of semiconductors, bright tunable luminescence and high resistance against photobleaching. In addition, contrary to classical quantum dots, they are highly biocompatible and non-toxic. Finally, for the possibility to obtain different functionalizations on their surface, Si NPs can be used as a modifiable platform on which to perform specific bioconjugations.

### **1.3.2 Synthetic methods to produce silicon nanoparticles**

The preparation of ultrasmall silicon nanoparticles with narrow size dispersion is still a challenging task, and, in particular, the purification is tedious and difficult, with a lack of well-established and clear methodologies. In this section we focus on the different synthetic methods<sup>[84-85]</sup> to produce non porous silicon nanoparticles, with special attention to the preparation of ultrasmall NPs.

Si NPs can be obtained by chemical or physical methods, involving either bottom-up or top-down approaches. A non-exhaustive sketch, trying to summarize the most common methods, is reported in Figure 1.6.

Usually top-down techniques can produce very clean particles, but, with chemical bottom-up methods the control of the size and the surface termination of the particles is much higher. Typical physical or physico-chemical techniques to produce silicon nanoparticles include top-down techniques such as ball milling<sup>[86-87]</sup>, electrochemical etching, laser ablation as well as gas phase reactions (including chemical vapour deposition and plasma methods) and pyrolysis methods<sup>[85, 88-89]</sup>.

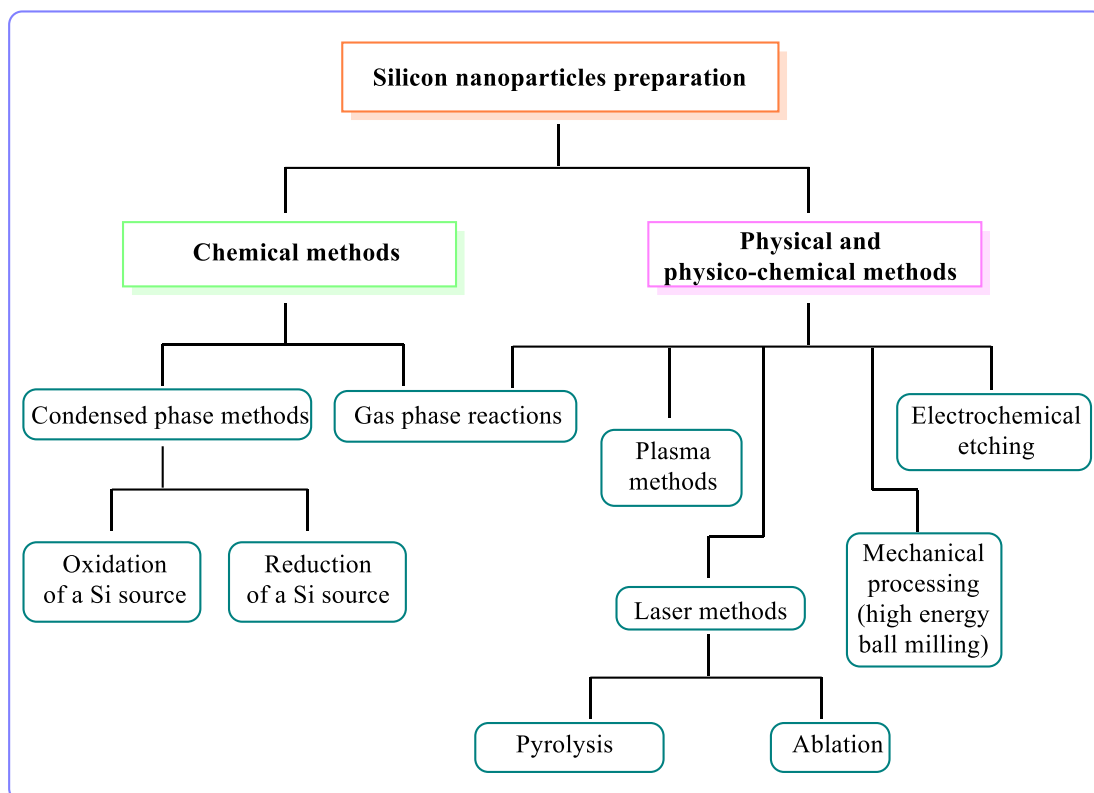


**Figure 1.6.** Scheme of the main synthetic routes for the preparation of silicon nanoparticles

In the last years, several bottom-up chemical techniques have been developed allowing a quite precise control of the size and the surface termination of silicon nanoparticles.

These techniques can be roughly divided in a few main categories: i) reduction or ii) oxidation of a silicon precursor, iii) microwave-assisted reductions or oxidations and iv) high temperature thermal reduction of silsesquioxanes. In the following paragraphs we will describe in details these bottom-up chemical approaches.

### 1.3.2.1 Reduction of a silicon precursor

In Figure 1.7, a general scheme for the production of silicon nanoparticles through the reduction of a silicon precursor is reported. One of the first reactions in this direction was reported by Heath<sup>[90]</sup>, but the harsh reaction conditions limited the use of this method. Indeed Heath method is based on the simultaneous

reduction of  $\text{SiCl}_4$  and  $\text{RSiCl}_3$  ( $\text{R} = \text{H}$ , octyl) by means of sodium in a non-polar solvent (pentane or hexane) under inert atmosphere at high temperature ( $385\text{ }^\circ\text{C}$ ) and pressure ( $> 100\text{ atm}$ ) for 3-7 days. The use of different organic chains ( $\text{R}$ ) in  $\text{RSiCl}_3$  allows a control on the size of the final particles and, indeed, when  $\text{R} = \text{H}$ , there is no control on the size of particles, but when  $\text{R} = \text{octyl}$ , the mean particle size is  $5.5\text{ nm} \pm 2.5\text{ nm}$ . Later on, several syntheses, carried out under much milder conditions, have been established as can be seen in Figure 1.7. All these syntheses are performed under strict inert atmosphere and are based on the reduction of a silicon precursor. They can be divided in three typologies: microemulsion method, simple reduction without surfactants and metathesis reactions with Zintl salts. In the case of the microemulsion method, the reduction of the silicon precursor happens inside reverse micelles of a surfactant to produce H-terminated Si NPs that are further functionalized through a hydrosilylation step catalyzed either by a Pt catalyst or by UV irradiation. Both the surfactant and/or the reducing agent used influence dramatically the final size obtained, but the use of micelles as “nano-reactors” allows a quite precise control of the size with a low degree of polydispersion. The scheme in Figure 1.7, takes into account the variations on this method reported from different authors. Wilcoxon et al.<sup>[91]</sup> were the first to report this kind of reaction, but they stopped at the production of H-terminated NPs without further functionalization. The particles produced by Wilcoxon have a size between 1.8 and 10 nm and they were separated in two smaller distributions of sizes using high-pressure liquid chromatography (HPLC). These H-terminated Si NPs show luminescence in all the range 350 - 700 nm with the most intense emission situated in the blue region of the spectrum (365 nm). Tilley et al.<sup>[63,92]</sup> used both  $\text{SiCl}_4$  and  $\text{SiBr}_4$  as precursors and tetraoctyl ammonium bromide (TOAB) or pentaethylene glycol monododecyl ether ( $\text{C}_{12}\text{E}_5$ ) as surfactants. They studied the influence, on the size and properties of the particles, of different reducing agents and methods of capping (Pt catalyst or UV irradiation). By changing reducing agent, they

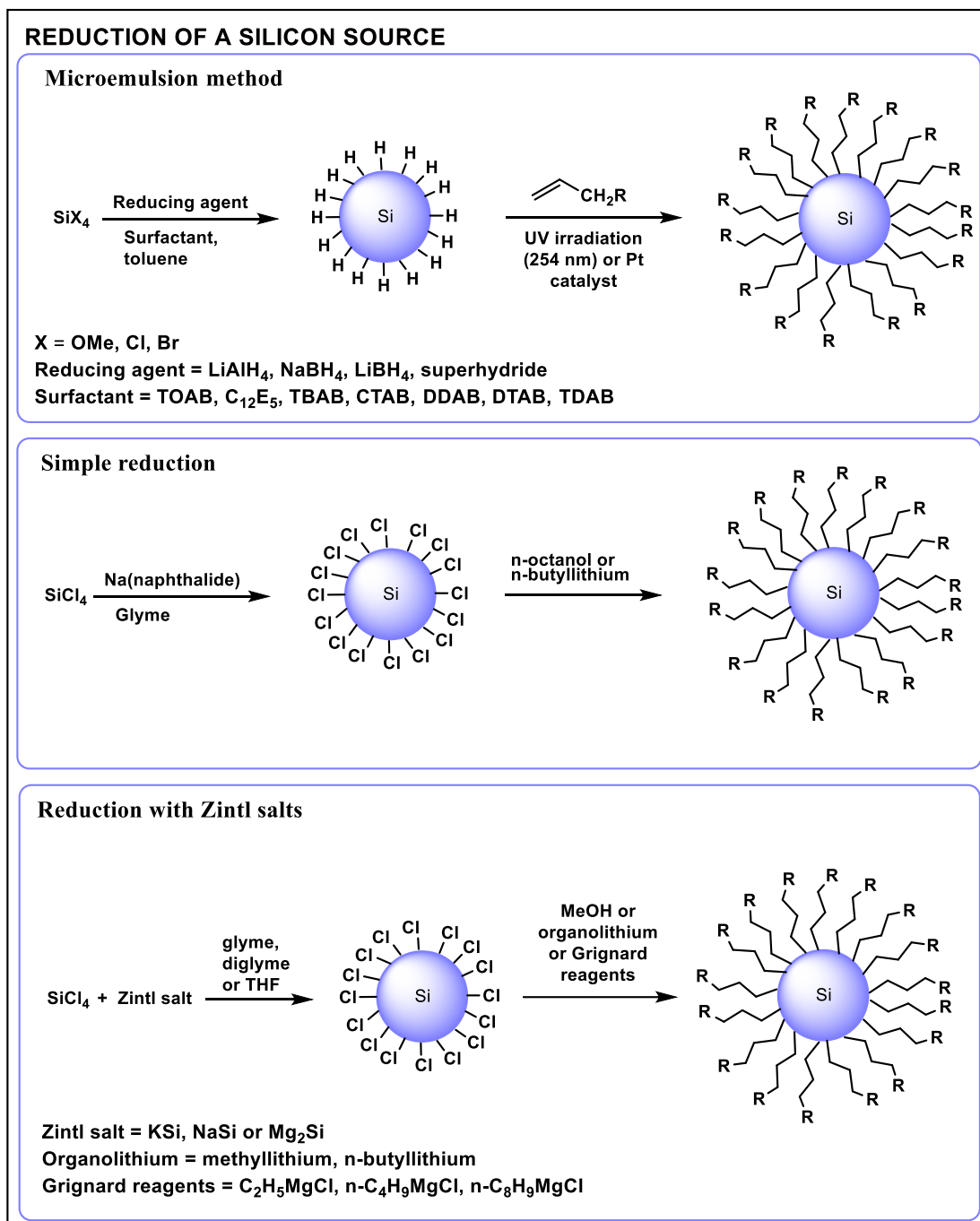


**Figure 1.7.** General scheme of the methods based on the reduction of a silicon source (R = alkyl-, alkenyl-, amine-, epoxy-, alkoxy-, azide-groups, etc.)

could tune the size from  $1.6 \text{ nm} \pm 0.4 \text{ nm}$  in the case of the strongest reducing agent ( $\text{LiAlH}_4$ ) to  $2.5 \text{ nm} \pm 1.0 \text{ nm}$  in the case of the weakest reducing agent ( $\text{NaBH}_4$ ). All the particles prepared by this method emit in the blue region of the spectrum, and a slight red shift was observed for the biggest particles. Rosso-Vasic et al.<sup>[64, 93]</sup> used always  $\text{Si}(\text{OMe})_4$  as a silicon precursor and TOAB as a

surfactant, but several different kinds of capping agents (mean size of the particles: 1.6 nm) and, also in this case, the particles emit in the blue region of the electromagnetic spectrum. Doyle et al.<sup>[94]</sup> changed various surfactants such as TOAB, tetrabutyl ammonium bromide (TBAB), cetyltrimethyl ammonium bromide (CTAB), didodecyldimethyl ammonium bromide (DDAB), dodecyltrimethyl ammonium bromide (DTAB), tetradodecyl ammonium bromide (TDAB) to show how size of the final particles is affected by the different micelles that act as “nano-reactors”. The smallest size is obtained with TOAB ( $\approx 2.0$  nm) and they can tune the size up to 6.0 nm with the other surfactants.

The second possible kind of reaction (simple reduction) was reported by Kauzlarich et al.<sup>[95]</sup>. They reduced  $\text{SiCl}_4$  using sodium naphthalide in 1,2-dimethoxyethane (glyme) to obtain Cl-terminated particles that were then capped with n-octanol. They did not use any surfactant to control the growth of the NPs and the mean particle size, in this case, was  $5.2 \text{ nm} \pm 1.9 \text{ nm}$  with a high polydispersion due to the absence of the template. The photoluminescence of the particles is still in the blue region of the electromagnetic spectrum.

Kauzlarich et al. also reported<sup>[96-98]</sup> the reduction of  $\text{SiCl}_4$  by means of Zintl salts. The reaction produces Cl-terminated Si NPs that can be functionalized in different ways using methanol for example to obtain methoxy-terminated particles or organolithium or Grignard reagents to get different alkyl chains on the surface. Depending on the functionalization, the size of the particles can change, but all Si NPs produced are in the range 2.0 - 5.0 nm and they emit in the range 315 – 520 nm depending on the excitation wavelengths.

### **1.3.2.2 Oxidation of a silicon precursor**

In Figure 1.8, a general scheme for the production of Si NPs through the oxidation of a silicon precursor is reported. This method is based on the use of Zintl salts that can be oxidized either by bromine or by ammonium halide. Also in this case, all the reactions are performed in strict inert atmosphere to avoid

oxidation of Si NPs. The first report in this direction is from the group of Kauzlarich et al.<sup>[99]</sup> in which they prepare H-terminated Si NPs through oxidation of Mg<sub>2</sub>Si by means of bromine and subsequent treatment of the obtained Br-terminated particles, with LiAlH<sub>4</sub>. NPs were characterized only by FT-IR spectroscopy and photophysical measurements that show photoluminescence in the blue region of the electromagnetic

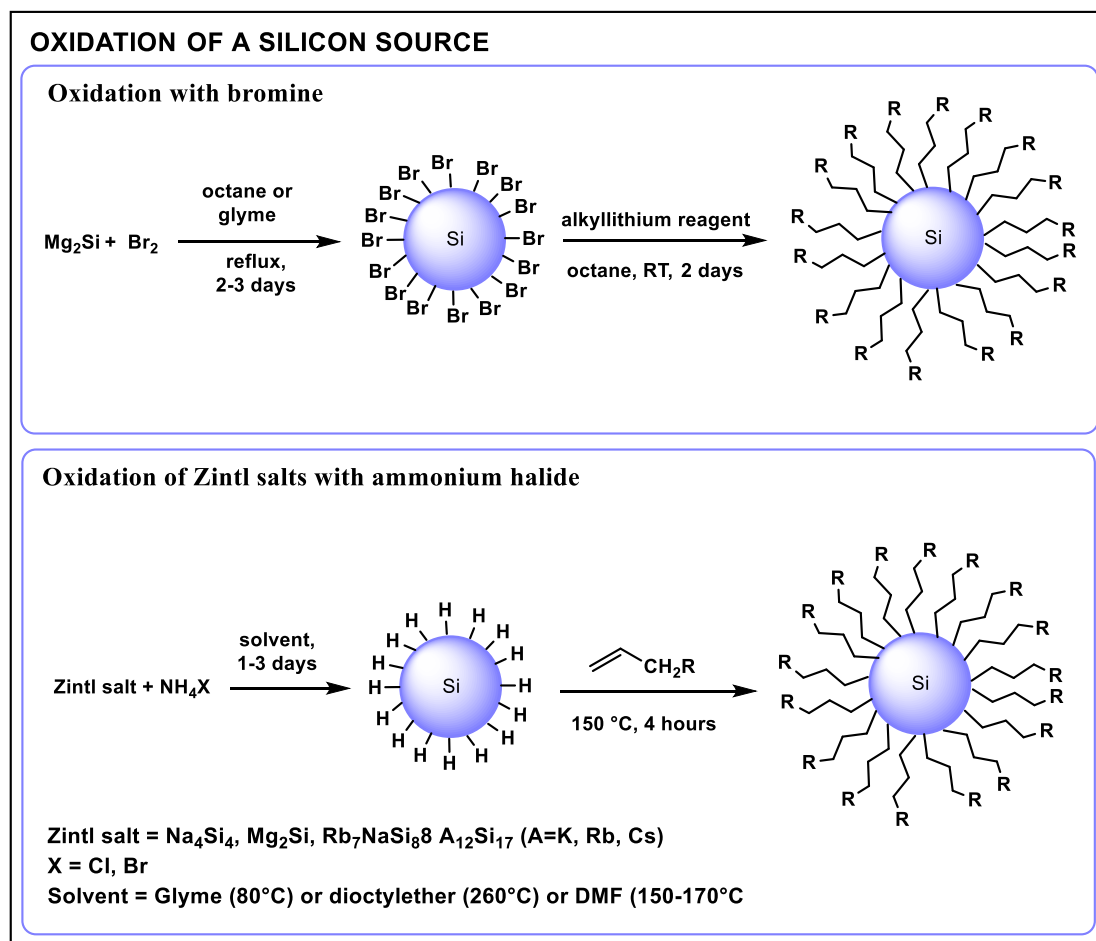


**Figure 1.8.** Oxidation of a silicon source (R = alkyl-, alkenyl-, amine-, epoxy-, alkoxy-, azide-groups, etc.)

spectrum. In 2003<sup>[100]</sup> the same author reported an optimized method to obtain alkyl/alkoxy-capped Si NPs through the oxidation of Mg<sub>2</sub>Si with bromine and subsequent treatment with alkyllithium reagents. The oxidation of Zintl salts by means of ammonium halides have been reported both by the group of Kauzlarich<sup>[101-102]</sup> and Cho et al.<sup>[103]</sup>. In the first reports, the particles obtained were H-terminated and they were not further functionalized. The size of Si NPs

was  $\approx 4.0$  nm and the photoluminescence, also in this case, is in the blue region of the electromagnetic spectrum. In the most recent report by Kauzlarich<sup>[102]</sup>, different Zintl salts have been explored and the size and emission of particles can be slightly tuned from 3.1 nm to 4.5 nm, depending on the alkali metal cation of the Zintl salt used (increasing size of the cation usually leads to bigger particles).

### 1.3.2.3 Microwave-assisted synthesis

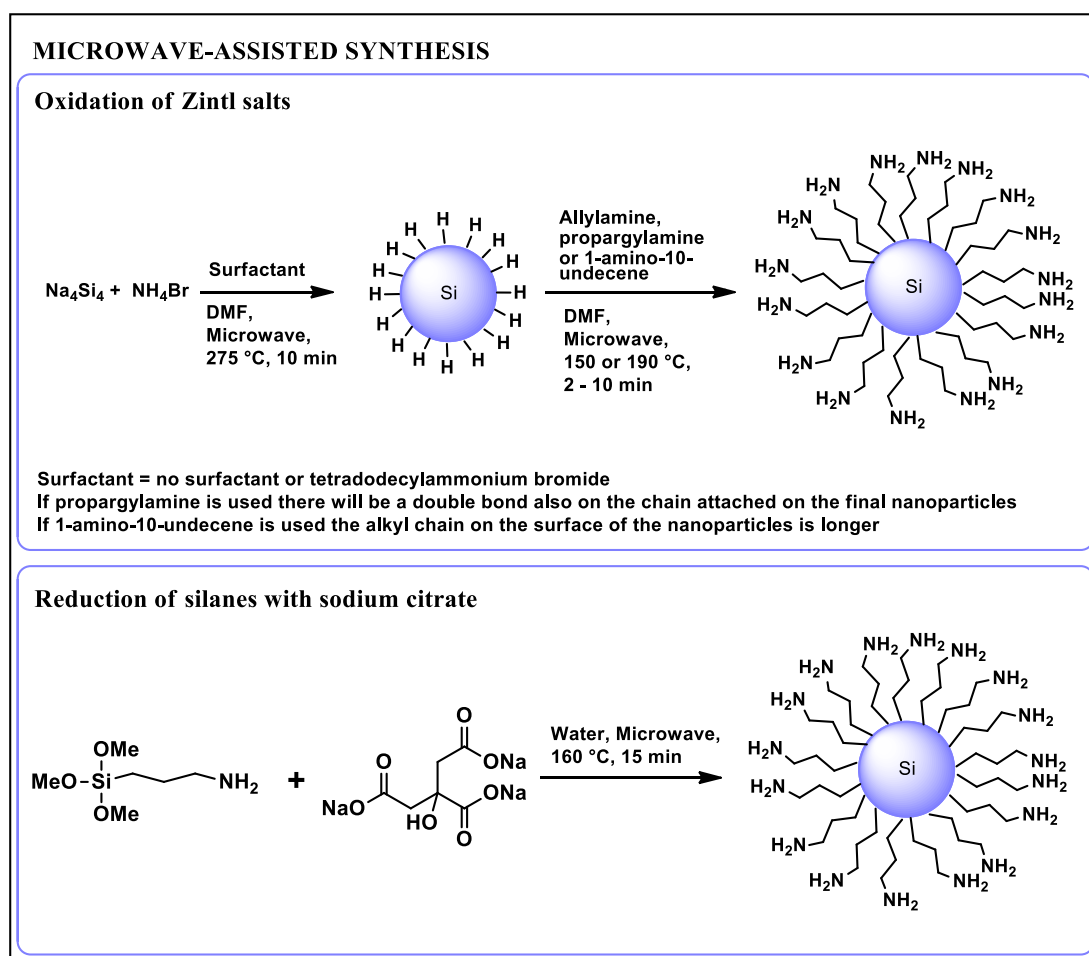


**Figure 1.9.** Microwave-assisted synthesis of silicon nanoparticles

In Figure 1.9, is summarized a general scheme for the production of Si NPs *via* the microwave-assisted oxidation or reduction of a silicon precursor.

Kauzlarich et al.<sup>[104-105]</sup> reported a method in which the oxidation of a Zintl salt, by means of ammonium bromide, is assisted by microwave heating under inert

atmosphere. In the first report, the reaction goes through the formation of H-terminated Si NPs that are further functionalized with terminal amine-groups through a second step of heating in the microwave. Otherwise, H-terminated Si NPs were embedded in silica formed by a base-catalyzed Stoeber method. Amine-terminated Si NPs prepared in this way, possess a size of  $3.4 \text{ nm} \pm 0.7 \text{ nm}$  and both amine-terminated and silica-encapsulated Si NPs show a blue photoluminescence. In the second report, Kauzlarich et al.<sup>[104-105]</sup> obtain amine-terminated Si NPs through a single step reaction in the microwave oven in the presence of a surfactant. They compared the two-steps and one-step syntheses finding out that the one-pot, two-steps method is the best for the production of Si NPs.

He et al.<sup>[70]</sup> reported the reduction, in aqueous solution, of (3-aminopropyl)trimethoxysilane by means of trisodium citrate under microwave heating. The synthesis is only one-step and it produces amine-terminated Si NPs with a size of  $\approx 2.2 \text{ nm}$  and showing blue photoluminescence as well.

#### **1.3.2.4 Thermal decomposition of hydrogen silsesquioxane**

In Figure 1.10, a general scheme for the production of silicon nanoparticles through the high temperature reduction of hydrogen silsesquioxane is reported. Veinot et al.<sup>[106-107]</sup> report the synthesis, by means of hydrogen silsesquioxane or other silsesquioxanes, of Si NPs embedded in silica and the subsequent production of H-terminated particles by etching with hydrofluoric acid. The particles obtained have a diameter of  $\approx 3.4 \text{ nm}$  and, after etching, they emit in the visible and near-infrared region of the electromagnetic spectrum. Later on, Veinot et al.<sup>[108]</sup> reported also the functionalization of the obtained H-terminated Si NPs through a thermally or photochemically activated hydrosilylation step and they showed that nanoparticles with different sizes react differently in the hydrosilylation step. Ozin et al.<sup>[109-111]</sup> and Kauzlarich and Tilley et al.<sup>[30]</sup> reported about the synthesis of capped Si NPs through thermal reduction of

silsesquioxanes and subsequent functionalization through thermal activated hydrosilylation. Indeed, H-terminated nanoparticles obtained during the reduction of silsesquioxanes, are etched from the silica and functionalized with organic moieties thanks to a thermally activated hydrosilylation step. Even in this case, particle size is quite small (around 2.0 nm), but Si NPs emit in the red region of the electromagnetic spectrum in contrast with the blue emission predicted by the quantum confinement model. Indeed, this is another piece of the puzzle in the wide debate in literature regarding the photoluminescence of silicon nanoparticles and which are the factors that influence it.

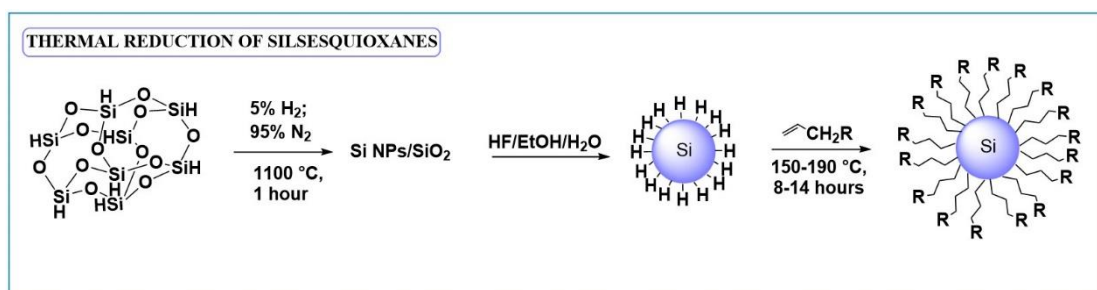


**Figure 1.10.** Thermal reduction of silsesquioxanes for the production of silicon nanoparticles (R = alkyl-, alkenyl-, amine-, epoxy-, alkoxy-, azide-groups, etc.)

In conclusion, bottom-up techniques give the opportunity to functionalize the surface of the particles with several different groups going, e.g., from alkyl or alkenyl chains to amine-, epoxy-, alkoxy-, azide-groups. Usually the size of the particles obtained is very small and the emission properties can change from blue to red according to the synthetic method used.

### 1.3.3 On the origin of photoluminescence in silicon nanoparticles

It is worth to have a deeper look at the photoluminescence properties of silicon nanoparticles and discuss about their origin. Silicon nanoparticles belong to the bigger family of semiconductor quantum dots, called in this way to underline the appearance of quantum effects as consequence of their “nano-size”. As all semiconductors, silicon possesses a characteristic energy gap ( $E_g$ ) between the conduction and the valence band. For bulk silicon,  $E_g$  corresponds to 1.12 eV. The particularity of silicon is that this energy band gap is indirect, that means the top energy level in the valence band and the bottom one in the conduction band do not correspond to the same value of momentum  $k$ . The structure of the energy gap in bulk silicon is shown in Figure 1.11.

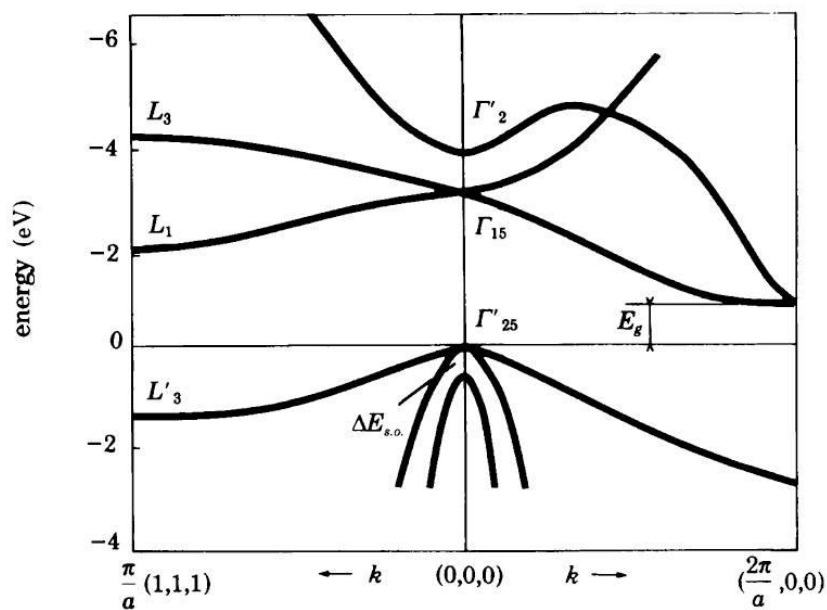


**Figure 1.11.** Energy band structure of bulk silicon. Reproduced with permission from<sup>[112]</sup>

Due to the indirect energy gap, bulk silicon does not show any emission because the transition from the conduction to the valence band is electronically forbidden. When the size is reduced to the nanoscale, many events that are negligible in the “macro-world” start to occur influencing dramatically the properties of

materials. Photoluminescence properties in silicon nanomaterials and, in particular, red emission in silicon nanowires have been observed for the first time in 1990<sup>[113]</sup>. It was the first proof that silicon could emit if its size shrinks to the nanoscale. Since that moment, many efforts have been done to understand deeply the nature of this luminescence and it seems that several are the factors that contribute to the expression and the modulation of emission properties in silicon nanoparticles. Indeed the most accepted theory of the emission of Si NPs is related to the quantum confinement effect. In this paragraph, it will be explained how luminescence of the particles can be also influenced by defects in the structure of the particles, by surface functionalization effects and by the method of preparation.

From the point of view of the electronic structure, nanoparticles behaviour can be described with the quantum-mechanic model of “particle in a box”. In particular, in semiconductor quantum dots, the energy levels of the valence and conductance band become discrete and the energy gap between the two bands is inversely proportional to the size of the particles. This means that smaller particles will show a higher energy gap and therefore their emission will be more blue-shifted. A schematic view of this size-dependent effect on photoluminescence is shown in Figure 1.12<sup>[114]</sup>.

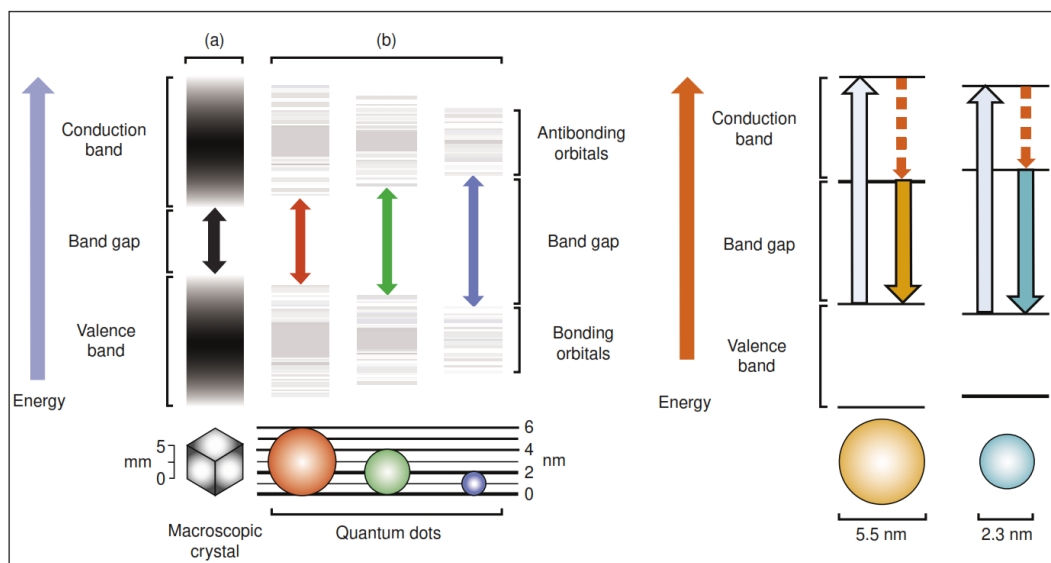


**Figure 1.12.** Quantum confinement effects on the photoluminescence of semiconductor quantum dots. Reproduced with permission from<sup>[114]</sup>.

In the case of silicon nanoparticles, it seems that the indirect band gap undergoes to changes and transformations that bring to a transition from indirect to direct energy gap<sup>[115-116]</sup>. Nevertheless, photoluminescence in Si NPs is not easily explained and many factors are influencing it. Recently, it has been also shown how the emission properties of silicon nanoparticles can be tuned by introducing defects in the structure, for example by doping with boron and phosphorus atoms<sup>[117-118]</sup>. The particles obtained by this method are very small ( $\approx 3$  nm), but they emit in the near-infrared region in contrast with the model of “particle in a box”. It seems that the co-doping with boron and phosphorus brings to the formation of donor and acceptor states in the band gap of silicon, similarly to what happens in doped bulk silicon, and this allows to tune the photoluminescence properties.

Also the synthetic route strongly influences the photoluminescence of silicon nanoparticles. Indeed the groups of Kauzlarich and Tilley reported how the luminescence of Si NPs shifts to the blue in the presence of nitrogen and oxygen-containing chemicals used during the synthetic procedure<sup>[30]</sup>. They compared dodecyl-terminated Si NPs made by three different methods: thermal reduction of hydrogen silsesquioxane (HSQ) followed by hydrosilylation; oxidation of Zintl salt by means of ammonium bromide; reduction of  $\text{SiCl}_4$  with hydrides in the presence of the surfactant tetraoctylammonium bromide (TOAB). All the obtained particles emit in the blue region of the electromagnetic spectrum except the ones made by reduction of HSQ that emit in the red. Even the excited state lifetimes are quite different, being longer in the case of the synthesis starting from HSQ. To prove that nitrogen- and oxygen-rich environments can shift the photoluminescence in the blue, red-emitting H-terminated Si NPs made by HSQ reduction were reacted with TOAB and ammonium bromide. At increasing concentrations of nitrogen-containing reagents, the emission of the particles shifts to the blue, but if the reaction is made in inert atmosphere, the shift in the emission does not occur showing that it is fundamental the contemporary presence of nitrogen and oxygen to have blue emission. All these findings support the idea that emission in silicon nanoparticles is not only due to quantum

confinement effects, but is highly influenced also by surface properties, defects in the structure and synthetic route.

Also Zuilhof et al.<sup>[119-120]</sup> studied the photophysics of Si NPs and they reported that, when the surface of silicon nanoparticles is capped with carbon-containing groups, changes and transformations in the band gap occur bringing to a more direct-like energy gap transition. However if oxygen is present on the surface of the particles, the emission is shifted more to the red.

Gonzalez et al.<sup>[121-122]</sup> demonstrated that is indeed the functionalization on the Si surface responsible for the different emission of the particles since when a small layer of Si-O-Si bonds is present on the Si surface the emission properties are not influenced by the synthetic route or by the functionalization.

In literature, the debate on the emission properties of Si NPs is still open and many are the factors that influence the photophysics of such material making more complicated a deeper understanding.

### **1.3.4 Bioapplications of silicon nanoparticles**

The first authors to test ultrasmall Si NPs *in vitro* are Ruckenstein et al.<sup>[62]</sup> and Tilley et al.<sup>[63]</sup> who reported, respectively, that polyacrylic acid coated red-emitting Si NPs are uptaken on the surface of Chinese hamster ovary (CHO) cells and that blue-emitting amine-terminated Si NPs are uptaken by HeLa cells and distributed uniformly inside the cytosol. Rosso-Vasic et al.<sup>[64]</sup> incubated blue-emitting amine-terminated Si NPs with different amine-length chains in murine cell line BV2 and particles accumulate in the cell cytosol showing very low cytotoxicity. Si NPs were, later on, tested through MTT (3-(4,5-dimethylthiazol-2-yl)2,5-diphenyl tetrazolium bromide) assay<sup>[65-67]</sup> to show how different surface functionalizations can influence the cytotoxicity of these nanoparticles. In these studies, it has been found that amine-terminated Si NPs, that are usually positively charged, are quite toxic, if compared, e.g., with their neutral and carboxylic-terminated analogues. Swihart et al.<sup>[68]</sup> and Ozin et al.<sup>[69]</sup> reported about small (4 nm) and bigger (100 nm) Si NPs encapsulated either in

phospholipid or solid lipid micelles. The particles are highly uptaken by pancreatic cancer cells or human breast cancer cells and show very low cytotoxicity. He et al.<sup>[70-71]</sup> reported that amine-terminated Si NPs, made by two different methods, conjugated with the goat anti-mouse IgG antibody are a very suitable probe for long-term imaging of cells. Indeed, the antibody-conjugated NPs have been incubated with HeLa cells and they stain either the nuclei or the microtubules, showing stable photoluminescence up to 2 hours of continuous observation. Yamaguchi et al.<sup>[72]</sup> reported that aggregates of Si NPs with a size of 20 - 40 nm, coated with a block polymer (Pluronic F127), selectively label the endoplasmic reticulum of human umbilical vein endothelial cells (HUVECs). In a later work, Yamaguchi et al.<sup>[73]</sup> show how internalization in cells is influenced by surface functionalization and size of Si NPs. Two kinds of functionalization (allylamine and block copolymer Pluronic F127) and two different sizes (few tens of nanometers and > 100 nm) of Si NPs were incubated in live and fixed HUVECs cells. In Figure 1.13, an experiment of co-localization with Lyso-tracker that labels selectively lysosomes is shown. From the figure, it is clear that amine-terminated NPs are always aggregating selectively in

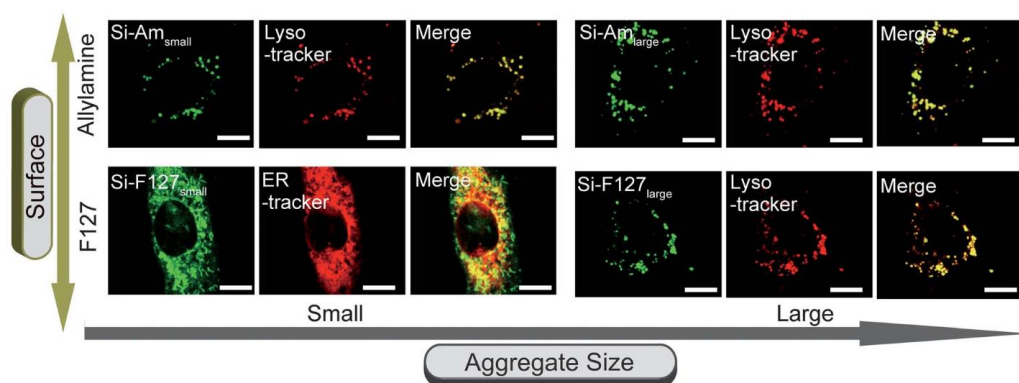


**Figure 1.13.** Confocal microscopic images of live HUVECs incubated with small and large amine-terminated (Si-Am<sub>small</sub> and Si-Am<sub>large</sub> respectively) and F127-functionalized Si NPs (Si-F127<sub>small</sub> and Si-F127<sub>large</sub> respectively). HUVECs were also labeled with Lyso-Tracker/ER tracker to do the co-localization experiment. Left and central columns are the fluorescent images of Si NPs and Lyso-Tracker/ER-tracker respectively. The right columns are the superimposed images. Scale bar is 10  $\mu$ m. Reproduced with permission from<sup>[73]</sup>

lysosomes independently from their size. Instead, F127-functionalized Si NPs label selectively the endoplasmatic reticulum (ER) when they are small and the lysosomes when they are bigger.

Klein et al.<sup>[74]</sup> reported on the possible use of silicon nanoparticles for radiosensitization of cancer and tissue cells. They incubated uncapped and amino-silanized oxidized silicon nanoparticles with human breast cancer cells (MCF-7) and mouse fibroblast healthy cells (3T3). The cells were, then, exposed to X-rays and only amine-terminated Si NPs increase the production of reactive oxygen species (ROS) resulting in higher cytotoxicity for the cancer cells in respect to the healthy ones. Zuilhof et al.<sup>[123]</sup>, Intartaglia et al.<sup>[124]</sup> and Wang et al.<sup>[125]</sup> reported on the coupling of Si NPs with single-strand DNA for further possible bioapplications. Erogbogbo et al.<sup>[75]</sup> showed that folic acid-functionalized Si NPs are uptaken by human pancreatic cancer cells (Panc-1), while the same particles without folic acid on the surface are not internalized. Ahire et al.<sup>[76]</sup> coupled amine-terminated ultrasmall porous Si NPs with different kinds of sugars. Sugar-terminated Si NPs exhibit very low cytotoxicity in comparison with amine-terminated Si NPs and are more readily uptaken by cancer cells than by healthy cells. Kauzlarich et al.<sup>[19, 77-78]</sup> doped Si NPs with iron or manganese to obtain a multimodal agent both for magnetic and optical imaging. The iron doped NPs show very low toxicity when incubated in HepG2 liver cells and the manganese doped ones functionalized with dextran can be used as contrast agents for MRI and near-infrared excited two-photons imaging. Manganese doped Si NPs functionalized with dextran are non-toxic for mammalian cells and accumulate, in specific way, in the macrophages. This is an important result since atherosclerotic plaques that are vulnerable to rupture are usually associated with a high density of macrophages and these particles represent a good alternative for the multimodal imaging. In addition the group of Kauzlarich<sup>[19]</sup> was the first to perform *in vivo* biodistribution experiments on ultrasmall Si NPs. Indeed, they reported PET imaging of mice using dextran coated manganese doped Si NPs that are functionalized with a <sup>64</sup>Cu complex (final average hydrodynamic radius 15.1 nm). Most of the particles are rapidly

excreted by renal filtration, but some also accumulate in the liver. This is maybe due to the distribution of sizes, smaller particles are rapidly excreted and bigger ones accumulate in the liver.

Erogbogbo et al.<sup>[79]</sup> describe a system in which Si NPs (4 nm) and iron oxide nanoparticles (7 nm) are co-encapsulated in phospholipid-polyethyleneglycol (DSPE-PEG) micelles to obtain a multimodal imaging probe, both fluorescent and magnetic with an average size of 50 nm. These systems were incubated with macrophage RAW cells both in the absence and in the presence of a magnetic field. When the magnetic field is applied, the uptake of the particles is increased and can be detected through fluorescence. Then, particles were tested *in vivo* being injected directly in tumour xenograft of a tumour-bearing mouse and at 24 hours post-injection, they still show bright luminescence proving that, if particles are targeted to the tumour, their stability can be enhanced (usually reported luminescence stability of quantum dots in tumour site is around 6-8 hours). In another report, Erogbogbo et al.<sup>[80]</sup> prepared Si NPs by laser pyrolysis of silanes and subsequent etching and functionalization obtaining particles with different sizes (from 2 to 8 nm) and a range of photoluminescence wavelengths from 450 to 900 nm.

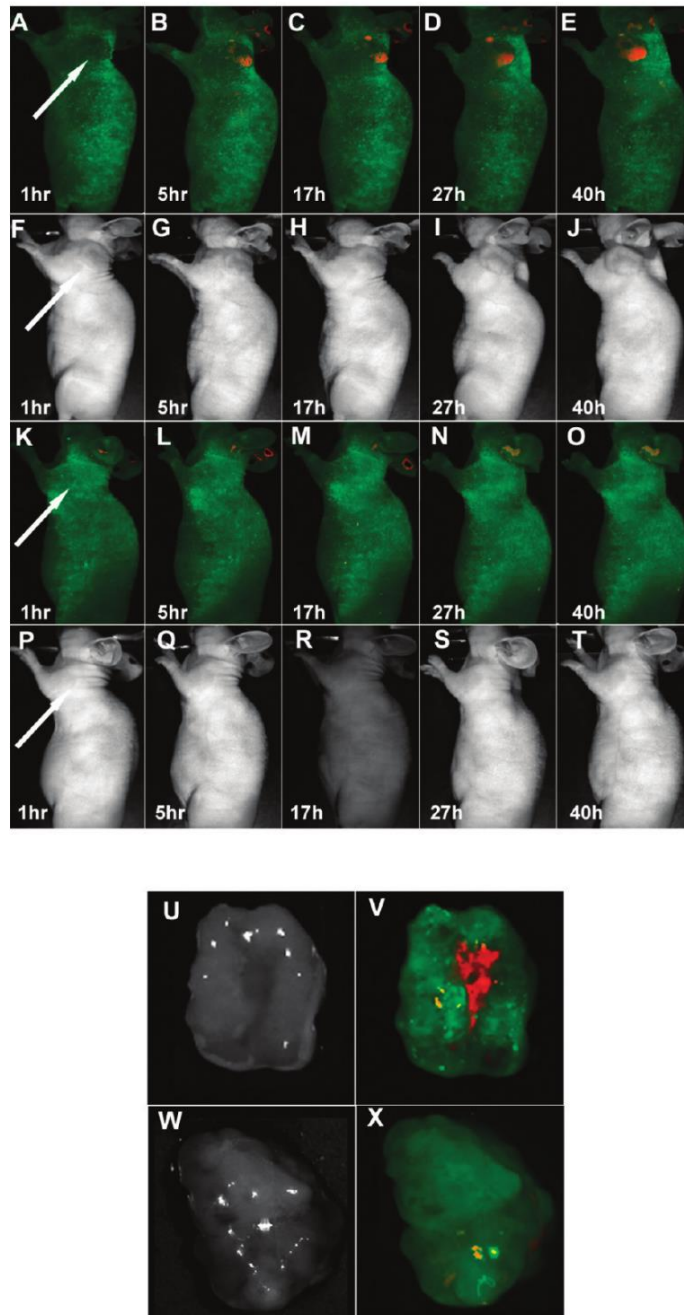


**Figure 1.14.** *In vivo* luminescence imaging, at different times post-injection, of Panc-1 tumor bearing mice (the tumor is on the left shoulder and it is indicated with white arrows) injected with 5 mg of micelle-encapsulated RGD-Si NPs (A-E) and of micelle-encapsulated Si NPs (K-O). The autofluorescence and the Si NPs signals are in green and red respectively. Images F-J and images P-T correspond to the luminescence images A-E and K-O, respectively. In U,W *ex vivo* images and in V,X luminescence images of tumours at 40 hours post-injection in mice treated with micelle-encapsulated RGD-Si NPs (U,V) or with micelle-encapsulated Si NPs (W,X). Reproduced with permission<sup>[80]</sup>

Si NPs were, then, encapsulated in phospholipidic micelles and conjugated with RGD peptides which are highly specific for integrins overexpressed in the tumour vasculature. Micelle-encapsulated RGD-Si NPs and micelle-encapsulated Si NPs were injected, through the tail vein, in tumour bearing mice and the *in vivo* fluorescence imaging, at different post-injection times, is shown in Figure 1.14. The luminescence intensity in the tumour site increases with time when RGD-particles are used, but in the case of particles without RGD functionalization, no uptake was observed. With the same kind of particles, the authors were able also to perform mapping of sentinel lymph nodes and multicolor near-infrared imaging in live mice. In conclusion, ultrasmall Si NPs have been already widely explored *in vitro* and *in vivo*, but more knowledge must be acquired on the behaviour *in vivo*.

## **1.4 Carbon dots**

### **1.4.1 Properties of carbon dots**

Since the discovery of the Buckminsterfullerene in 1985<sup>[126]</sup>, carbon based nanomaterials have attracted increasing interest in many fields of science. Amongst them, carbon quantum dots are very interesting for their relatively easy synthesis and for their luminescence properties that are dependent on their size and on their surface functionalization as in the case of silicon nanoparticles. In Figure 1.15, the different structures of some of the most used carbon based nanomaterials are shown<sup>[31]</sup>.

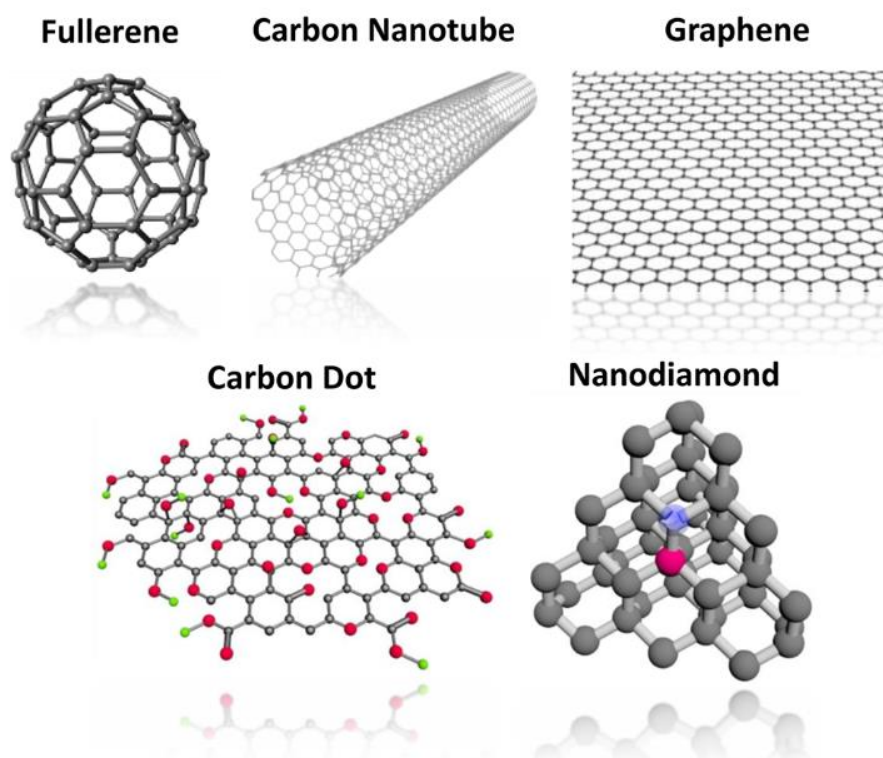


**Figure 1.15.** Most common carbon based nanomaterials: fullerene, carbon nanotubes, graphene, carbon dots and nanodiamonds. Reproduced with permission from<sup>[31]</sup>

Fluorescent carbon quantum dots were discovered quite recently in 2004 almost accidentally during the electrophoretic purification of single-walled carbon nanotubes (SWNTs) obtained by arc-discharge<sup>[127]</sup>. On the structural organization and shape of carbon dots there is still an open discussion, but they are mostly described as nanosized graphene ( $< 10 \text{ nm}$ )<sup>[31]</sup>. In reality, some authors divide carbon quantum dots in two kinds of materials: carbon dots (CQDs or C-dots) and graphene quantum dots (GQDs). They describe CQDs as quasi-spherical nanoparticles with a diameter smaller than 10 nm and GQDs as a single or a-few layered nanosized graphene (size can reach up to 60 nm)<sup>[128-129]</sup>. One of the most interesting features of carbon dots is their photoluminescence that can cover all the visible electromagnetic spectrum from 400 until 750 nm. The emission peaks usually shift according to the excitation wavelength used and this is due to the heterogeneity of sizes and composition in carbon dots samples. The photoluminescence properties are still under

investigation but it seems that, in addition to the size confinement effect, they are due to a variety of composition (surface and inner structure) effects. Indeed carbon dots have usually a multifunctional surface with different groups that are excited with different excitation wavelengths. The strong, stable and multi-coloured emission of carbon dots together with their biocompatibility make this kind of material an appealing alternative for bioapplications.

### **1.4.2 Synthetic methods of preparation of carbon dots**

Many are the methods to produce carbon dots and both top-down and bottom-up techniques are used<sup>[31, 128, 130]</sup>. Top-down techniques includes arc-discharge, laser ablation or electrochemical oxidation of graphitic bulk materials. Bottom-up techniques include several methods such as thermal decomposition of organic compounds, template-assisted synthesis, hydrothermal, solvothermal or microwave-assisted treatment of amino-acids, organosilanes, polymers and many natural compounds<sup>[131]</sup>. The most widely used methods are the hydrothermal and microwave-assisted syntheses<sup>[132]</sup>. In Figure 1.16, one example of hydrothermal<sup>[133]</sup> and microwave-assisted synthesis<sup>[134-135]</sup> are shown. In the hydrothermal synthesis reported by Zhu et al.<sup>[133]</sup>, citric acid is heated up at high temperatures for several hours in water in the presence of 1,2-ethylendiamine. The obtained particles have a size of 2 - 6 nm and contain mostly  $sp^2$  - hybridized carbon atoms, some  $sp^3$  - hybridized carbon atoms and also amide and carboxylic groups. Jiang et al.<sup>[134]</sup> and Mazzier et al.<sup>[135]</sup> report, instead the preparation of CQDs by microwave-assisted synthesis in which an amino-acid is heated for few minutes in a domestic microwave oven in the presence of 1,2-ethylendiamine in water. With this method, particle size is in the range 1 - 4 nm and particles contain both carboxylic, amide and amine groups on their surface.

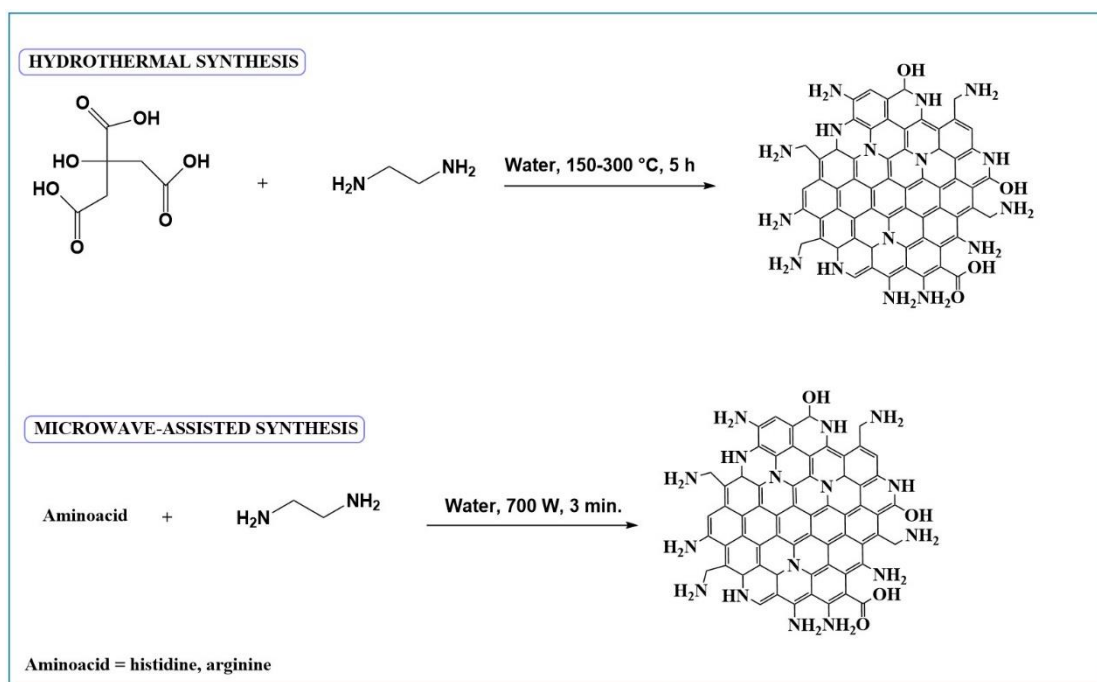


**Figure 1.16.** Two examples of hydrothermal and microwave assisted synthesis for the preparation of carbon dots

### 1.4.3 Bioapplications of carbon dots

Due to their biocompatibility, their bright multi-colored emission and their stability against photobleaching, carbon dots are promising materials for bioimaging. Indeed, they have already been tested both *in vitro* and *in vivo*. Yang et al.<sup>[32]</sup>, in 2009, reported the first example of *in vivo* experiments using carbon dots. They showed that CQDs remain strongly emissive also *in vivo*, opening many applications for imaging with these nanoparticles. Ruan et al.<sup>[136]</sup>, e. g., report of the use of carbon dots to detect glioma, a malignant tumour present in 80% of brain tumours. CQDs were incubated *in vitro* with C6 glioma cells showing that they are uptaken by cells with a mechanism mediated by endosomes. Then CQDs were tested *in vivo* in glioma bearing mice and it was found that they accumulate more where the glioma is located than in normal brain tissue. In Figure 1.17, *in vivo* images of glioma bearing mice at different times after injection of carbon dots are shown. CQDs were injected through the

tail vein and, as it can be seen, the intensity of emission, at 5 minutes post-injection, is higher in the brain where the glioma is located. In addition the emission intensity decreases in time showing that particles are excreted quite quickly. The 3-D reconstruction of the distribution of CQDs into the brain after 2 hours from CQDs injection together with the *ex vivo* images show that CQDs are localized in the glioma.

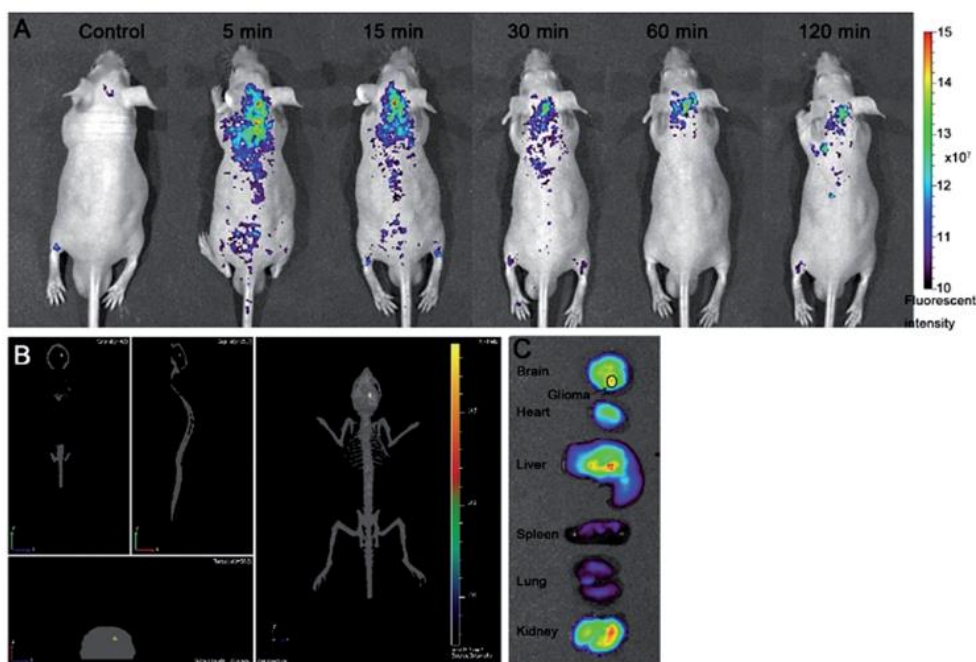


**Figure 1.17.** **A)** *In vivo* images, at different times post-injection of CQDs, of glioma bearing mice; **B)** 3-D reconstruction of the distribution of CQDs inside the brain at 2 hours post-injection; **C)** *ex vivo* images of tissues at 2 hours post-injection of CQDs. Reprinted with permission from<sup>[136]</sup>

## 1.5 Ultrasmall cobalt nanoparticles

### 1.5.1 Properties of cobalt nanoparticles

Magnetic nanoparticles have attracted increasing interest due to the wide range of applications they might be used for. Indeed they are used for magnetic inks<sup>[137-138]</sup>, recording media<sup>[139]</sup>, sensors<sup>[140]</sup> and, more recently, also for bioapplications<sup>[141-145]</sup> in magnetic resonance imaging<sup>[146-147]</sup>, drug delivery<sup>[148]</sup> or hyperthermia therapy<sup>[149-151]</sup>. For biomedical applications, magnetic metallic nanoparticles, such as cobalt, nickel, iron and their alloys, are very interesting because they usually possess higher saturation magnetization than metal oxides such as ferrite or iron oxides<sup>[33]</sup>. This property would allow to introduce in the body a smaller quantity of NPs while retaining a similar magnetic response, and gives promising expectations for a future use in MRI. When the particle size shrinks to the nanoscale and reach a critical value, which may change for each material, magnetic particles can show a superparamagnetic behaviour<sup>[33-35]</sup>. This means that the magnetic moments will be randomized and can be easily manipulated with an external magnetic field. This property becomes very interesting for bioapplications such as magnetic resonance imaging and hyperthermia therapy. Cobalt has a ferromagnetic behaviour, but it is reported that ultrasmall cobalt nanoparticles can have superparamagnetic properties<sup>[34, 36-37]</sup>. Cobalt has a very important role in biological systems. Indeed, it is a constituent of cobalamin, the vitamin B, which is involved in the formation of blood and in the normal operation of brain and nervous system. In addition, cobalt is present in several other vitamins<sup>[152]</sup>. However, toxicity and instability have limited the use of cobalt nanoparticles in the past. It has been shown<sup>[38]</sup> that cobalt nanoparticles have a quite high toxicological effect in many cell lines *in vitro*. In particular, cell sensitivity to Co NPs increases in the following way for some cell lines: A549 = MDCK = NCIH441 = Caco-2 > DCs > HepG2. Al

Samri et al.<sup>[153]</sup> showed that C/Co/SiO<sub>2</sub> and C/Co<sub>3</sub>O<sub>4</sub>/SiO<sub>2</sub> NPs increase caspase activity and alter the structure of lungs, but the presence of a silica shell could improve the biocompatibility of Co NPs. For this reason, recent research focused on the surface modification of cobalt nanoparticles with a silica shell<sup>[39-40]</sup> to render them less toxic and to facilitate surface functionalization.

## 1.5.2 Synthetic routes to prepare cobalt nanoparticles and their bioapplications

Ultrasmall cobalt nanoparticles can be prepared by several bottom-up methods and, playing with parameters of the reaction, it is possible to tune particles size, shape and composition. Usually high temperatures and inert atmosphere are necessary conditions. In Figure 1.18, four examples of bottom-up synthesis are reported. Cobalt nanoparticles can be obtained by three main different typologies of reaction<sup>[33, 154]</sup>: high temperature liquid phase synthesis; reduction, at room temperature, of cobalt salts in reverse micelles<sup>[34, 155]</sup>; reduction or thermal decomposition of cobalt salts using templates<sup>[156-157]</sup>. The high temperature liquid phase synthesis includes either the thermal decomposition of Co<sub>2</sub>(CO)<sub>8</sub> in organic solvents in the presence of a polymer, a peptide or an aluminium alkyl compound<sup>[158-159]</sup>, or the reduction of cobalt salts by means of superhydrides or polyalcohols in the presence of a trialkylphosphine<sup>[160-161]</sup>. One of the challenges of the preparation of Co NPs is to avoid the formation of cobalt oxide, to tune particle size and to stabilize the final particles. In this direction, the group of Boennemann et al.<sup>[162-164]</sup> reported on the synthesis of Co NPs (size 5 to 10 nm) by thermal decomposition of Co<sub>2</sub>(CO)<sub>8</sub> in the presence of aluminium alkyl compounds (AlR<sub>3</sub>). This technique produces long-time air-stable cobalt nanoparticles due to the step of smooth oxidation, which creates a thin cobalt oxide layer around particles preventing further oxidation. Particles size can be tuned changing the length of the alkyl chain in the AlR<sub>3</sub> compound or the molar ratio between Co<sub>2</sub>(CO)<sub>8</sub> and AlR<sub>3</sub>. As an example of reduction of cobalt salts by

poyalcohols, Murray et al.<sup>[165]</sup> use long chain 1,2-diols as reducing agents instead of the common used ethylene glycol or glycerol and this procedure helps to disperse well the precursors during particles growth. Also in this kind of synthesis, the use of different lengths for the alkyl chain of the trialkylphosphine, helps to tune particle size (usually a longer chain brings to the formation of smaller particles). Sorensen et al.<sup>[34]</sup> reported, instead, on the synthesis of Co NPs reducing  $\text{CoCl}_2$  with  $\text{NaBH}_4$ , under inert atmosphere, in toluene inside reverse micelles of the surfactant didodecyldimethyl ammonium bromide (DDAB) obtaining particles with a size of 1.8 - 4.4 nm. As an example of synthesis of Co NPs inside templates, Escalera et al.<sup>[156]</sup> described the synthesis of Co NPs (2 - 4 nm) made by the reduction of a cobalt salt with  $\text{NaBH}_4$  inside the pores of mesoporous silica nanoparticles, that act as a template. Once Co NPs are formed, silica NPs are removed by dissolution with  $\text{NaOH}$ .

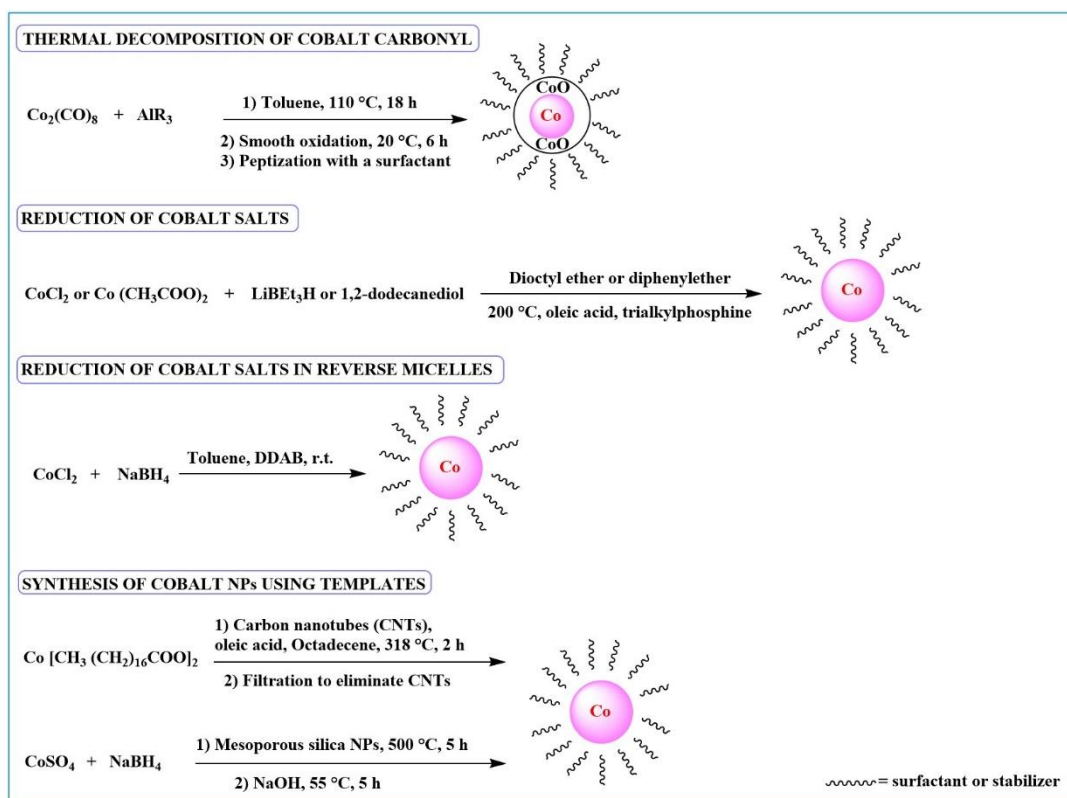


**Figure 1.18.** Four examples of bottom-up synthesis of ultrasmall cobalt nanoparticles (R =  $\text{CH}_3$ ,  $\text{C}_2\text{H}_5$ ,  $\text{C}_8\text{H}_{17}$ ; trialkylphosphine = tributyl- or trioctylphosphine; DDAB = didodecyldimethyl ammonium bromide)

As it is described in literature<sup>[166-168]</sup>, cobalt ferrites, cobalt complexes, cobalt doped iron oxide and mixed cobalt/metal nanoparticles find several applications in magnetic resonance imaging, but for pure cobalt nanoparticles, coated with carbon or silica, few applications are shown till now. Hwang et al.<sup>[169]</sup> reported on the toxicity of cobalt ferrite and silica coated cobalt ferrite NPs showing that the coated ones show an increased biocompatibility. Indeed, due to the toxicity of cobalt and on the few reports, at date, on the preparation of silica or carbon coated metallic cobalt nanoparticles, there are still only a couple of tests *in vitro* and *in vivo*, except the ones assessing their cytotoxicity in various cell lines or the penetration in human skin<sup>[153, 170-172]</sup>. For example Balla et al.<sup>[173]</sup> report of carbon coated Co NPs ( $\approx 30$  nm) conjugated with the  $\beta$ -cell-specific single-chain antibody fragment, SCA B1, as a new contrast agent for magnetic resonance imaging (MRI). In particular, they successfully performed *in vivo* visualization of single native pancreatic islets, the sites of insulin production, in the pancreas of mice using MRI, but excretion is still an issue because the particles used, accumulate in the liver and in the spleen due to their rather large (30 - 40 nm) size.

## 1.6 Aim of the thesis

The aim of this thesis is the synthesis, characterization, functionalization and *in vitro* and *in vivo* investigation of different kinds of ultras-small nanoparticles, which are good candidates for the design of innovative multimodal imaging probes. We focused on silicon NPs, carbon dots and silica-coated cobalt NPs. This choice was dictated by the unique properties deriving from both the ultras-small size and the nature of the material, as outlined previously in this chapter. The goal is to combine the properties of the core with the ones of the molecules (e.g. radiotracers or dyes) that can be covalently anchored to the surface in order to perform *in vivo* imaging and to compare the behaviour of different ultras-small NPs.

The thesis is divided in 6 chapters.

Chapter 1, after a brief introduction to multimodal imaging, gives an overview of the state of art on properties, methods of preparation, functionalization, characterization and bioapplications of ultrasmall silicon, carbon and cobalt NPs.

Chapter 2 focuses on the preparation, *via* two different approaches, of ultrasmall amine-terminated Si NPs and on their characterization and comparison.

Chapter 3 discusses the further surface modification of these NPs with functional molecules suitable for bioimaging and reports on the results of *in vitro* and *in vivo* experiments.

Chapter 4 deals with the preparation, characterization, surface functionalization and *in vivo* experiments of carbon dots with the aim to compare the behaviour of such material to silicon NPs.

In Chapter 5, the preparation, characterization and surface modification of silica-coated cobalt NPs will be discussed, in the perspective of a future *in vivo* use of this material.

Finally, Chapter 6 gives a short overview of the main instrumental techniques used during the thesis work.

## 1.7 References:

- [1] J. Estelrich, M. Quesada-Pérez, J. Forcada, J. Callejas-Fernández, in *Soft Nanoparticles for Biomedical Applications* (Ed.: J. E. José Callejas-Fernández, Manuel Quesada-Pérez, Jacqueline Forcada), RSC Nanoscience & Nanotechnology, **2014**, pp. 1-17.
- [2] R. P. Feynman, *Engineering and Science* **1960**, *23*, 22-36.
- [3] M. Hosokawa (editor), K. Nogi (editor), M. Naito (editor), T. Yokoyama (editor), *Nanoparticle Technology Handbook*, Elsevier, **2012**.
- [4] B. Pelaz, S. Jaber, D. J. de Aberasturi, V. Wulf, T. Aida, J. M. de la Fuente, J. Feldmann, H. E. Gaub, L. Josephson, C. R. Kagan, N. A. Kotov, L. M. Liz-Marzán, H. Mattoussi, P. Mulvaney, C. B. Murray, A. L. Rogach, P. S. Weiss, I. Willner, W. J. Parak, *ACS Nano* **2012**, *6*, 8468-8483.
- [5] M. V. Kovalenko, L. Manna, A. Cabot, Z. Hens, D. V. Talapin, C. R. Kagan, V. I. Klimov, A. L. Rogach, P. Reiss, D. J. Milliron, P. Guyot-Sionnest, G. Konstantatos, W. J. Parak, T. Hyeon, B. A. Korgel, C. B. Murray, W. Heiss, *ACS Nano* **2015**.
- [6] K. L. Viola, J. Sbarboro, R. Sureka, M. De, M. A. Bicca, J. Wang, S. Vasavada, S. Satpathy, S. Wu, H. Joshi, P. T. Velasco, K. MacRenaris, E. A. Waters, C. Lu, J. Phan, P. Lacor, P. Prasad, V. P. Dravid, W. L. Klein, *Nat Nano* **2015**, *10*, 91-98.
- [7] S. Marchesan, M. Prato, *ACS Medicinal Chemistry Letters* **2013**, *4*, 147-149.
- [8] J. Callejas-Fernández, J. Estelrich, M. Quesada-Pérez, J. Forcada, *Soft Nanoparticles for Biomedical Applications*, Royal Society of Chemistry, **2014**.
- [9] O. S. Wolfbeis, *Chemical Society Reviews* **2015**, *44*, 4743-4768.
- [10] S. Kunjachan, J. Ehling, G. Storm, F. Kiessling, T. Lammers, *Chemical Reviews* **2015**.
- [11] J. Liu, C. Detrembleur, S. Mornet, C. Jerome, E. Duguet, *Journal of Materials Chemistry B* **2015**, *3*, 6117-6147.
- [12] N. C. Bigall, W. J. Parak, D. Dorfs, *Nano Today* **2012**, *7*, 282-296.
- [13] P. K. Jain, X. Huang, I. H. El-Sayed, M. A. El-Sayed, *Accounts of Chemical Research* **2008**, *41*, 1578-1586.
- [14] A. K. Gupta, M. Gupta, *Biomaterials* **2005**, *26*, 3995-4021.
- [15] L. Martí-Bonmatí, R. Sopena, P. Bartumeus, P. Sopena, *Contrast Media & Molecular Imaging* **2010**, *5*, 180-189.
- [16] N. R. B. Boase, I. Blakey, B. E. Rolfe, K. Mardon, K. J. Thurecht, *Polymer Chemistry* **2014**, *5*, 4450-4458.
- [17] H. Kobayashi, Y. Koyama, T. Barrett, Y. Hama, C. A. S. Regino, I. S. Shin, B.-S. Jang, N. Le, C. H. Paik, P. L. Choyke, Y. Urano, *ACS Nano* **2007**, *1*, 258-264.
- [18] L.-p. Wu, M. Ficker, J. B. Christensen, P. N. Trohopoulos, S. M. Moghimi, *Bioconjugate Chemistry* **2015**.
- [19] C. Tu, X. Ma, A. House, S. M. Kauzlarich, A. Y. Louie, *ACS Medicinal Chemistry Letters* **2011**, *2*, 285-288.
- [20] L. Jing, K. Ding, S. V. Kershaw, I. M. Kempson, A. L. Rogach, M. Gao, *Advanced Materials* **2014**, *26*, 6367-6386.

- [21] T. Liu, S. Shi, C. Liang, S. Shen, L. Cheng, C. Wang, X. Song, S. Goel, T. E. Barnhart, W. Cai, Z. Liu, *ACS Nano* **2015**, *9*, 950-960.
- [22] B. H. Kim, M. J. Hackett, J. Park, T. Hyeon, *Chemistry of Materials* **2014**, *26*, 59-71.
- [23] W. G. Kreyling, A. M. Abdelmonem, Z. Ali, F. Alves, M. Geiser, N. Haberl, R. Hartmann, S. Hirn, D. J. de Aberasturi, K. Kantner, G. Khadem-Saba, J.-M. Montenegro, J. Rejman, T. Rojo, I. R. de Larramendi, R. Ufartes, A. Wenk, W. J. Parak, *Nat Nano* **2015**, *10*, 619-623.
- [24] T. D. Farr, C.-H. Lai, D. Grünstein, G. Orts-Gil, C.-C. Wang, P. Boehm-Sturm, P. H. Seeberger, C. Harms, *Nano Letters* **2014**, *14*, 2130-2134.
- [25] H. Yamamoto, in *Nanoparticle Technology Handbook (Second Edition)* (Ed.: M. H. N. N. Yokoyama), Elsevier, Amsterdam, **2012**, pp. 543-546.
- [26] F. Peng, Y. Su, Y. Zhong, C. Fan, S.-T. Lee, Y. He, *Accounts of Chemical Research* **2014**, *47*, 612-623.
- [27] J.-H. Park, L. Gu, G. von Maltzahn, E. Ruoslahti, S. N. Bhatia, M. J. Sailor, *Nat Mater* **2009**, *8*, 331-336.
- [28] L. T. Canham, *Advanced Materials* **1995**, *7*, 1033-1037.
- [29] N. K. Hon, Z. Shaposhnik, E. D. Diebold, F. Tamanoi, B. Jalali, *Journal of Biomedical Materials Research Part A* **2012**, *100A*, 3416-3421.
- [30] M. Dasog, Z. Yang, S. Regli, T. M. Atkins, A. Faramus, M. P. Singh, E. Muthuswamy, S. M. Kauzlarich, R. D. Tilley, J. G. C. Veinot, *ACS Nano* **2013**, *7*, 2676-2685.
- [31] G. Hong, S. Diao, A. L. Antaris, H. Dai, *Chemical Reviews* **2015**.
- [32] S.-T. Yang, L. Cao, P. G. Luo, F. Lu, X. Wang, H. Wang, M. J. Mezziani, Y. Liu, G. Qi, Y.-P. Sun, *Journal of the American Chemical Society* **2009**, *131*, 11308-11309.
- [33] L.-Y. Lu, L.-N. Yu, X.-G. Xu, Y. Jiang, *Rare Met.* **2013**, *32*, 323-331.
- [34] J. P. Chen, C. M. Sorensen, K. J. Klabunde, G. C. Hadjipanayis, *Journal of Applied Physics* **1994**, *76*, 6316-6318.
- [35] C. N. R. Rao, G. U. Kulkarni, P. J. Thomas, in *Nanocrystals: Synthesis, Properties and Applications*, Springer-Verlag, **2007**, pp. 1-23.
- [36] S. N. Khanna, S. Linderoth, *Physical Review Letters* **1991**, *67*, 742-745.
- [37] L. M. Parkes, R. Hodgson, L. T. Lu, L. D. Tung, I. Robinson, D. G. Fernig, N. T. K. Thanh, *Contrast Media & Molecular Imaging* **2008**, *3*, 150-156.
- [38] J. Sengupta, S. Ghosh, P. Datta, A. Gomes, A. Gomes, *Journal of Nanoscience and Nanotechnology* **2014**, *14*, 990-1006.
- [39] Y. Kobayashi, M. Horie, M. Konno, B. Rodríguez-González, L. M. Liz-Marzán, *The Journal of Physical Chemistry B* **2003**, *107*, 7420-7425.
- [40] N. Batail, I. Cléménçon, C. Legens, A. Chaumonnot, D. Uzio, *European Journal of Inorganic Chemistry* **2013**, *2013*, 1258-1264.
- [41] V. Salgueiriño-Maceira, M. A. Correa-Duarte, M. Farle, M. A. López-Quintela, K. Sieradzki, R. Diaz, *Langmuir* **2006**, *22*, 1455-1458.
- [42] V. Salgueiriño-Maceira, M. Spasova, M. Farle, *Advanced Functional Materials* **2005**, *15*, 1036-1040.
- [43] D. E. Kuhl, J. Hale, W. L. Eaton, *Radiology* **1966**, *87*, 278-284.
- [44] H.-M. Fan, M. Olivo, B. Shuter, J.-B. Yi, R. Bhuvanewari, H.-R. Tan, G.-C. Xing, C.-T. Ng, L. Liu, S. S. Lucky, B.-H. Bay, J. Ding, *Journal of the American Chemical Society* **2010**, *132*, 14803-14811.
- [45] L. Sun, X. Ge, J. Liu, Y. Qiu, Z. Wei, B. Tian, L. Shi, *Nanoscale* **2014**, *6*, 13242-13252.

- [46] X. Ma, C. Tu, A. Y. Louie, S. M. Kauzlarich, American Chemical Society, **2009**, pp. INOR-737.
- [47] X. Zhang, M. Brynda, R. D. Britt, E. C. Carroll, D. S. Larsen, A. Y. Louie, S. M. Kauzlarich, *J. Am. Chem. Soc.* **2007**, *129*, 10668-10669.
- [48] J. Tam, T. M. Atkins, A. Louie, S. M. Kauzlarich, American Chemical Society, **2010**, pp. INOR-272.
- [49] J. D. Cressler, *SILICON EARTH, Introduction to the Microelectronics and Nanotechnology Revolution*, Cambridge University Press, **2009**.
- [50] W. C. O'Mara, R. B. Herring, L. P. Hunt, *Handbook of Semiconductor Silicon Technology*, Noyes Publications, **1990**.
- [51] D. P. Puzzo, E. J. Henderson, M. G. Helander, Z. Wang, G. A. Ozin, Z. Lu, *Nano Letters* **2011**, *11*, 1585-1590.
- [52] F. Maier-Flaig, J. Rinck, M. Stephan, T. Bocksrocker, M. Bruns, C. Kübel, A. K. Powell, G. A. Ozin, U. Lemmer, *Nano Letters* **2013**, *13*, 475-480.
- [53] K.-Y. Cheng, R. Anthony, U. R. Kortshagen, R. J. Holmes, *Nano Letters* **2010**, *10*, 1154-1157.
- [54] K.-Y. Cheng, R. Anthony, U. R. Kortshagen, R. J. Holmes, *Nano Letters* **2011**, *11*, 1952-1956.
- [55] G. Conibeer, M. Green, R. Corkish, Y. Cho, E.-C. Cho, C.-W. Jiang, T. Fangsuwannarak, E. Pink, Y. Huang, T. Puzzer, T. Trupke, B. Richards, A. Shalay, K.-l. Lin, *Thin Solid Films* **2006**, *511-512*, 654-662.
- [56] D. Timmerman, I. Izeddin, P. Stallinga, I. N. Yassievich, T. Gregorkiewicz, *Nat Photon* **2008**, *2*, 105-109.
- [57] G. Conibeer, M. Green, E.-C. Cho, D. König, Y.-H. Cho, T. Fangsuwannarak, G. Scardera, E. Pink, Y. Huang, T. Puzzer, S. Huang, D. Song, C. Flynn, S. Park, X. Hao, D. Mansfield, *Thin Solid Films* **2008**, *516*, 6748-6756.
- [58] H. Shujuan, C. Gavin, *Journal of Physics D: Applied Physics* **2013**, *46*, 024003.
- [59] C.-Y. Liu, Z. C. Holman, U. R. Kortshagen, *Nano Letters* **2009**, *9*, 449-452.
- [60] S. Sivasubramaniam, A. Faramus, R. D. Tilley, M. M. Alkaisi, *Journal of Renewable and Sustainable Energy* **2014**, *6*, 011204.
- [61] S. Perraud, E. Quesnel, S. Parola, J. Barbé, V. Muffato, P. Faucherand, C. Morin, K. Jarolimek, R. A. C. M. M. Van Swaaij, M. Zeman, S. Richards, A. Kingsley, H. Doyle, K. Linehan, S. O'Brien, I. M. Povey, M. E. Pemble, L. Xie, K. Leifer, K. Makasheva, B. Despax, *physica status solidi (a)* **2013**, *210*, 649-657.
- [62] Z. F. Li, E. Ruckenstein, *Nano Letters* **2004**, *4*, 1463-1467.
- [63] J. H. Warner, A. Hoshino, K. Yamamoto, R. D. Tilley, *Angewandte Chemie International Edition* **2005**, *44*, 4550-4554.
- [64] M. Rosso-Vasic, E. Spruijt, Z. Popovic, K. Overgaag, B. van Lagen, B. Grandidier, D. Vanmaekelbergh, D. Dominguez-Gutierrez, L. De Cola, H. Zuilhof, *Journal of Materials Chemistry* **2009**, *19*, 5926-5933.
- [65] L. Ruizendaal, S. Bhattacharjee, K. Pournazari, M. Rosso-Vasic, L. H. J. de Haan, G. M. Alink, A. T. M. Marcelis, H. Zuilhof, *Nanotoxicology* **2009**, *3*, 339-347.
- [66] S. Bhattacharjee, L. de Haan, N. Evers, X. Jiang, A. Marcelis, H. Zuilhof, I. Rietjens, G. Alink, *Particle and Fibre Toxicology* **2010**, *7*, 25.
- [67] S. Bhattacharjee, I. M. Rietjens, M. P. Singh, T. M. Atkins, T. K. Purkait, Z. Xu, S. Regli, A. Shukaliak, R. J. Clark, B. S. Mitchell, G. M. Alink, A. T.

- Marcelis, M. J. Fink, J. G. Veinot, S. M. Kauzlarich, H. Zuilhof, *Nanoscale* **2013**, *5*, 4870-4883.
- [68] F. Erogbogbo, K.-T. Yong, I. Roy, G. Xu, P. N. Prasad, M. T. Swihart, *ACS Nano* **2008**, *2*, 873-878.
- [69] E. J. Henderson, A. J. Shuhendler, P. Prasad, V. Baumann, F. Maier-Flaig, D. O. Faulkner, U. Lemmer, X. Y. Wu, G. A. Ozin, *Small* **2011**, *7*, 2507-2516.
- [70] Y. Zhong, F. Peng, F. Bao, S. Wang, X. Ji, L. Yang, Y. Su, S.-T. Lee, Y. He, *Journal of the American Chemical Society* **2013**, *135*, 8350-8356.
- [71] Y. Zhong, X. Sun, S. Wang, F. Peng, F. Bao, Y. Su, Y. Li, S.-T. Lee, Y. He, *ACS Nano* **2015**, *9*, 5958-5967.
- [72] P. Shen, S. Ohta, S. Inasawa, Y. Yamaguchi, *Chemical Communications* **2011**, *47*, 8409-8411.
- [73] S. Ohta, P. Shen, S. Inasawa, Y. Yamaguchi, *Journal of Materials Chemistry* **2012**, *22*, 10631-10638.
- [74] S. Klein, M. L. Dell'Arciprete, M. Wegmann, L. V. R. Distel, W. Neuhuber, M. C. Gonzalez, C. Kryschi, *Biochemical and Biophysical Research Communications* **2013**, *434*, 217-222.
- [75] F. Erogbogbo, M. T. Swihart, *AIP Conference Proceedings* **2010**, *1275*, 35-39.
- [76] J. H. Ahire, M. Behray, C. A. Webster, Q. Wang, V. Sherwood, N. Saengkrit, U. Ruktanonchai, N. Woramongkolchai, Y. Chao, *Advanced Healthcare Materials* **2015**, n/a-n/a.
- [77] M. P. Singh, T. M. Atkins, E. Muthuswamy, S. Kamali, C. Tu, A. Y. Louie, S. M. Kauzlarich, *ACS Nano* **2012**, *6*, 5596-5604.
- [78] C. Tu, X. Ma, P. Pantazis, S. M. Kauzlarich, A. Y. Louie, *Journal of the American Chemical Society* **2010**, *132*, 2016-2023.
- [79] F. Erogbogbo, K.-T. Yong, R. Hu, W.-C. Law, H. Ding, C.-W. Chang, P. N. Prasad, M. T. Swihart, *ACS Nano* **2010**, *4*, 5131-5138.
- [80] F. Erogbogbo, K.-T. Yong, I. Roy, R. Hu, W.-C. Law, W. Zhao, H. Ding, F. Wu, R. Kumar, M. T. Swihart, P. N. Prasad, *ACS Nano* **2011**, *5*, 413-423.
- [81] E. Tasciotti, X. Liu, R. Bhavane, K. Plant, A. D. Leonard, B. K. Price, M. M.-C. Cheng, P. Decuzzi, J. M. Tour, F. Robertson, M. Ferrari, *Nat Nano* **2008**, *3*, 151-157.
- [82] A. M. Derfus, W. C. W. Chan, S. N. Bhatia, *Nano Letters* **2004**, *4*, 11-18.
- [83] S. Kim, Y. T. Lim, E. G. Soltész, A. M. De Grand, J. Lee, A. Nakayama, J. A. Parker, T. Mihaljevic, R. G. Laurence, D. M. Dor, L. H. Cohn, M. G. Bawendi, J. V. Frangioni, *Nat Biotech* **2004**, *22*, 93-97.
- [84] Z. Kang, Y. Liu, S.-T. Lee, *Nanoscale* **2011**, *3*, 777-791.
- [85] J. G. C. Veinot, *Chemical Communications* **2006**, 4160-4168.
- [86] H. Sun, S. Miyazaki, H. Tamamitsu, K.-i. Saitow, *Chemical Communications* **2013**, *49*, 10302-10304.
- [87] A. S. Heintz, M. J. Fink, B. S. Mitchell, *Applied Organometallic Chemistry* **2010**, *24*, 236-240.
- [88] S. Chinnathambi, S. Chen, S. Ganesan, N. Hanagata, *Advanced Healthcare Materials* **2014**, *3*, 10-29.
- [89] H. M. R. Gonçalves, J. C. G. Esteves da Silva, *Current Analytical Chemistry* **2012**, *8*, 67-77.
- [90] J. R. Heath, *Science* **1992**, *258*, 1131-1133.
- [91] J. P. Wilcoxon, G. A. Samara, P. N. Provencio, *Physical Review B* **1999**, *60*, 2704-2714.

- [92] A. Shiohara, S. Prabakar, A. Faramus, C.-Y. Hsu, P.-S. Lai, P. T. Northcote, R. D. Tilley, *Nanoscale* **2011**, *3*, 3364-3370.
- [93] M. Rosso-Vasic, E. Spruijt, B. van Lagen, L. De Cola, H. Zuilhof, *Small* **2008**, *4*, 1835-1841.
- [94] K. Linehan, H. Doyle, *Small* **2014**, *10*, 584-590.
- [95] R. K. Baldwin, K. A. Pettigrew, E. Ratai, M. P. Augustine, S. M. Kauzlarich, *Chem. Commun. (Cambridge, U. K.)* **2002**, 1822-1823.
- [96] R. A. Bley, S. M. Kauzlarich, *Journal of the American Chemical Society* **1996**, *118*, 12461-12462.
- [97] C.-S. Yang, R. A. Bley, S. M. Kauzlarich, H. W. H. Lee, G. R. Delgado, *Journal of the American Chemical Society* **1999**, *121*, 5191-5195.
- [98] R. K. Baldwin, K. A. Pettigrew, J. C. Garno, P. P. Power, G.-y. Liu, S. M. Kauzlarich, *Journal of the American Chemical Society* **2002**, *124*, 1150-1151.
- [99] Q. Liu, S. M. Kauzlarich, *Mater. Sci. Eng., B* **2002**, *B96*, 72-75.
- [100] K. A. Pettigrew, Q. Liu, P. P. Power, S. M. Kauzlarich, *Chem. Mater.* **2003**, *15*, 4005-4011.
- [101] D. Neiner, H. W. Chiu, S. M. Kauzlarich, *J. Am. Chem. Soc.* **2006**, *128*, 11016-11017.
- [102] B. M. Nolan, T. Henneberger, M. Waibel, T. F. Fässler, S. M. Kauzlarich, *Inorganic Chemistry* **2015**, *54*, 396-401.
- [103] B. Cho, S. Baek, H.-G. Woo, H. Sohn, *Journal of Nanoscience and Nanotechnology* **2014**, *14*, 5868-5872.
- [104] T. M. Atkins, A. Thibert, D. S. Larsen, S. Dey, N. D. Browning, S. M. Kauzlarich, *Journal of the American Chemical Society* **2011**, *133*, 20664-20667.
- [105] T. M. Atkins, A. Y. Louie, S. M. Kauzlarich, *Nanotechnology* **2012**, *23*, 294006/294001-294006/294009.
- [106] C. M. Hessel, E. J. Henderson, J. G. C. Veinot, *Chemistry of Materials* **2006**, *18*, 6139-6146.
- [107] E. J. Henderson, J. A. Kelly, J. G. C. Veinot, *Chemistry of Materials* **2009**, *21*, 5426-5434.
- [108] J. A. Kelly, A. M. Shukaliak, M. D. Fleischauer, J. G. C. Veinot, *Journal of the American Chemical Society* **2011**, *133*, 9564-9571.
- [109] M. L. Mastronardi, F. Hennrich, E. J. Henderson, F. Maier-Flaig, C. Blum, J. Reichenbach, U. Lemmer, C. Kübel, D. Wang, M. M. Kappes, G. A. Ozin, *Journal of the American Chemical Society* **2011**, *133*, 11928-11931.
- [110] M. L. Mastronardi, F. Maier-Flaig, D. Faulkner, E. J. Henderson, C. Kübel, U. Lemmer, G. A. Ozin, *Nano Letters* **2012**, *12*, 337-342.
- [111] M. L. Mastronardi, E. J. Henderson, D. P. Puzzo, G. A. Ozin, *Advanced Materials* **2012**, *24*, 5890-5898.
- [112] B. Sapoval, C. Hermann, in *Physics of Semiconductors*, Springer-Verlag, New York, **1995**, p. 42.
- [113] L. T. Canham, *Applied Physics Letters* **1990**, *57*, 1046-1048.
- [114] D. Ioannou, D. K. Griffin, *Nano Reviews* **2010**, *1*, 10.3402/nano.v3401i3400.5117.
- [115] T. Takagahara, K. Takeda, *Physical Review B* **1992**, *46*, 15578-15581.
- [116] V. Kocovski, O. Eriksson, J. Ruzs, *Physical Review B* **2013**, *87*, 245401.
- [117] H. Sugimoto, M. Fujii, K. Imakita, S. Hayashi, K. Akamatsu, *The Journal of Physical Chemistry C* **2012**, *116*, 17969-17974.

- [118] H. Sugimoto, M. Fujii, K. Imakita, S. Hayashi, K. Akamatsu, *The Journal of Physical Chemistry C* **2013**, *117*, 11850-11857.
- [119] K. Dohnalova, A. N. Poddubny, A. A. Prokofiev, W. D. A. M. de Boer, C. P. Umesh, J. M. J. Paulusse, H. Zuilhof, T. Gregorkiewicz, *Light Sci Appl* **2013**, *2*, e47.
- [120] J. R. Siekierzycka, M. Rosso-Vasic, H. Zuilhof, A. M. Brouwer, *The Journal of Physical Chemistry C* **2011**, *115*, 20888-20895.
- [121] M. J. Llansola Portolés, R. Pis Diez, M. L. Dell’Arciprete, P. Caregnato, J. J. Romero, D. O. Mártire, O. Azzaroni, M. Ceolín, M. C. Gonzalez, *The Journal of Physical Chemistry C* **2012**, *116*, 11315-11325.
- [122] J. J. Romero, M. J. Llansola-Portolés, M. L. Dell’Arciprete, H. B. Rodríguez, A. L. Moore, M. C. Gonzalez, *Chemistry of Materials* **2013**, *25*, 3488-3498.
- [123] L. Ruizendaal, S. P. Pujari, V. Gevaerts, J. M. J. Paulusse, H. Zuilhof, *Chemistry – An Asian Journal* **2011**, *6*, 2776-2786.
- [124] R. Intartaglia, A. Barchanski, K. Bagga, A. Genovese, G. Das, P. Wagener, E. Di Fabrizio, A. Diaspro, F. Brandi, S. Barcikowski, *Nanoscale* **2012**, *4*, 1271-1274.
- [125] L. Wang, V. Reipa, J. Blasic, *Bioconjugate Chemistry* **2004**, *15*, 409-412.
- [126] H. W. Kroto, J. R. Heath, S. C. O'Brien, R. F. Curl, R. E. Smalley, *Nature* **1985**, *318*, 162-163.
- [127] X. Xu, R. Ray, Y. Gu, H. J. Ploehn, L. Gearheart, K. Raker, W. A. Scrivens, *Journal of the American Chemical Society* **2004**, *126*, 12736-12737.
- [128] X. T. Zheng, A. Ananthanarayanan, K. Q. Luo, P. Chen, *Small* **2015**, *11*, 1620-1636.
- [129] H. Li, Z. Kang, Y. Liu, S.-T. Lee, *Journal of Materials Chemistry* **2012**, *22*, 24230-24253.
- [130] S. N. Baker, G. A. Baker, *Angewandte Chemie International Edition* **2010**, *49*, 6726-6744.
- [131] V. Georgakilas, J. A. Perman, J. Tucek, R. Zboril, *Chemical Reviews* **2015**, *115*, 4744-4822.
- [132] Z. Yang, Z. Li, M. Xu, Y. Ma, J. Zhang, Y. Su, F. Gao, H. Wei, L. Zhang, *Nano-Micro Lett.* **2013**, *5*, 247-259.
- [133] S. Zhu, Q. Meng, L. Wang, J. Zhang, Y. Song, H. Jin, K. Zhang, H. Sun, H. Wang, B. Yang, *Angewandte Chemie International Edition* **2013**, *52*, 3953-3957.
- [134] J. Jiang, Y. He, S. Li, H. Cui, *Chemical Communications* **2012**, *48*, 9634-9636.
- [135] D. Mazzier, M. Favaro, S. Agnoli, S. Silvestrini, G. Granozzi, M. Maggini, A. Moretto, *Chemical Communications* **2014**, *50*, 6592-6595.
- [136] S. Ruan, J. Qian, S. Shen, J. Zhu, X. Jiang, Q. He, H. Gao, *Nanoscale* **2014**, *6*, 10040-10047.
- [137] B. Basly, T. Alnasser, K. Aissou, G. Fleury, G. Pecastaings, G. Hadziioannou, E. Duguet, G. Goglio, S. Mornet, *Langmuir* **2015**, *31*, 6675-6680.
- [138] N. Marjanović, A. Chiolerio, M. Kus, F. Ozel, S. Tilki, N. Ivanović, Z. Rakočević, V. Andrić, T. Barudžija, R. R. Baumann, *Thin Solid Films* **2014**, *570, Part A*, 38-44.
- [139] H. Sato, T. Homma, *Journal of Nanoscience and Nanotechnology* **2007**, *7*, 225-231.
- [140] K. Bagga, D. F. Brougham, T. E. Keyes, D. Brabazon, *Physical Chemistry Chemical Physics* **2015**.

- [141] T.-J. Yoon, K. N. Yu, E. Kim, J. S. Kim, B. G. Kim, S.-H. Yun, B.-H. Sohn, M.-H. Cho, J.-K. Lee, S. B. Park, *Small* **2006**, *2*, 209-215.
- [142] C. Alexiou, R. Schmid, R. Jurgons, M. Kremer, G. Wanner, C. Bergemann, E. Huenges, T. Nawroth, W. Arnold, F. Parak, *Eur Biophys J* **2006**, *35*, 446-450.
- [143] K. McNamara, S. A. M. Tofail, *Physical Chemistry Chemical Physics* **2015**.
- [144] C. Ghobril, G. Popa, A. Parat, C. Billotey, J. Taleb, P. Bonazza, S. Begin-Colin, D. Felder-Flesch, *Chemical Communications* **2013**, *49*, 9158-9160.
- [145] S. Lesieur, F. Gazeau, N. Luciani, C. Menager, C. Wilhelm, *Journal of Materials Chemistry* **2011**, *21*, 14387-14393.
- [146] L. Lartigue, P. Hugounenq, D. Alloyeau, S. P. Clarke, M. Lévy, J.-C. Bacri, R. Bazzi, D. F. Brougham, C. Wilhelm, F. Gazeau, *ACS Nano* **2012**, *6*, 10935-10949.
- [147] H. B. Na, I. C. Song, T. Hyeon, *Advanced Materials* **2009**, *21*, 2133-2148.
- [148] A. Riedinger, P. Guardia, A. Curcio, M. A. Garcia, R. Cingolani, L. Manna, T. Pellegrino, *Nano Letters* **2013**, *13*, 2399-2406.
- [149] A. Walter, C. Billotey, A. Garofalo, C. Ulhaq-Bouillet, C. Lefèvre, J. Taleb, S. Laurent, L. Vander Elst, R. N. Muller, L. Lartigue, F. Gazeau, D. Felder-Flesch, S. Begin-Colin, *Chemistry of Materials* **2014**, *26*, 5252-5264.
- [150] J. Kolosnjaj-Tabi, R. Di Corato, L. Lartigue, I. Marangon, P. Guardia, A. K. A. Silva, N. Luciani, O. Clément, P. Flaud, J. V. Singh, P. Decuzzi, T. Pellegrino, C. Wilhelm, F. Gazeau, *ACS Nano* **2014**, *8*, 4268-4283.
- [151] C. Wilhelm, F. Gazeau, *Journal of Magnetism and Magnetic Materials* **2009**, *321*, 671-674.
- [152] M. Kobayashi, S. Shimizu, *European Journal of Biochemistry* **1999**, *261*, 1-9.
- [153] M. T. Al Samri, R. Silva, S. Almarzooqi, A. Albawardi, A. R. D. Othman, R. S. M. S. Al Hanjeri, S. K. M. Al Dawaar, S. Tariq, A.-K. Soud, T. Asefa, *International Journal of Nanomedicine* **2013**, *8*, 1223-1244.
- [154] S. Zhang, J. Lee, S. Sun, *The Open Surface Science Journal* **2012**, *4*, 26-34.
- [155] H. T. Yang, C. M. Shen, Y. K. Su, T. Z. Yang, H. J. Gao, Y. G. Wang, *Applied Physics Letters* **2003**, *82*, 4729-4731.
- [156] E. Escalera, M. A. Ballem, J. M. Córdoba, M.-L. Antti, M. Odén, *Powder Technology* **2012**, *221*, 359-364.
- [157] W. Baaziz, I. Florea, S. Moldovan, V. Papaefthimiou, S. Zafeiratos, S. Begin-Colin, D. Begin, O. Ersen, C. Pham-Huu, *Journal of Materials Chemistry A* **2015**, *3*, 11203-11214.
- [158] N. T. K. Thanh, V. F. Puentes, L. D. Tung, D. G. Fernig, *Journal of Physics: Conference Series* **2005**, *17*, 70.
- [159] J. R. Thomas, *Journal of Applied Physics* **1966**, *37*, 2914-2915.
- [160] S. Sun, C. B. Murray, *Journal of Applied Physics* **1999**, *85*, 4325-4330.
- [161] C. Osorio-Cantillo, A. N. Santiago-Miranda, O. Perales-Perez, Y. Xin, *Journal of Applied Physics* **2012**, *111*, 07B324.
- [162] H. Bönemann, W. Brijoux, R. Brinkmann, N. Matoussevitch, N. Waldöfner, N. Palina, H. Modrow, *Inorganica Chimica Acta* **2003**, *350*, 617-624.
- [163] H. Bönemann, W. Brijoux, R. Brinkmann, N. Matoussevitch, W. Norbert, *Vol. WO/2004/001776 Germany*, **2003**.
- [164] S. Behrens, H. Bönemann, N. Matoussevitch, E. Dinjus, H. Modrow, N. Palina, M. Frerichs, V. Kempter, W. Maus-Friedrichs, A. Heinemann, M. Kammel, A. Wiedenmann, L. Pop, S. Odenbach, E. Uhlmann, N. Bayat, J. Hesselbach, J. M. Guldbakke, *Z. Phys. Chem.* **2006**, *220*, 3-40.
- [165] C. B. Murray, S. Sun, H. Doyle, T. Betley, *MRS Bulletin* **2001**, *26*, 985-991.

- [166] J. Klostergaard, C. E. Seeney, *Nanomedicine: Nanotechnology, Biology and Medicine* **2012**, *8*, Supplement 1, S37-S50.
- [167] K. E. Scarberry, E. B. Dickerson, J. F. McDonald, Z. J. Zhang, *Journal of the American Chemical Society* **2008**, *130*, 10258-10262.
- [168] E. Fantechi, C. Innocenti, M. Zanardelli, M. Fittipaldi, E. Falvo, M. Carbo, V. Shullani, L. Di Cesare Mannelli, C. Ghelardini, A. M. Ferretti, A. Ponti, C. Sangregorio, P. Ceci, *ACS Nano* **2014**, *8*, 4705-4719.
- [169] D. W. Hwang, D. S. Lee, S. Kim, *Journal of Nuclear Medicine* **2012**, *53*, 106-112.
- [170] J. Ponti, E. Sabbioni, B. Munaro, F. Broggi, P. Marmorato, F. Franchini, R. Colognato, F. Rossi, *Mutagenesis* **2009**, *24*, 439-445.
- [171] F. Larese Filon, M. Crosera, E. Timeus, G. Adami, M. Bovenzi, J. Ponti, G. Maina, *Toxicology in Vitro* **2013**, *27*, 121-127.
- [172] R. Colognato, A. Bonelli, J. Ponti, M. Farina, E. Bergamaschi, E. Sabbioni, L. Migliore, *Mutagenesis* **2008**, *23*, 377-382.
- [173] D. Z. Balla, S. Gottschalk, G. Shajan, S. Ueberberg, S. Schneider, M. Hardtke-Wolenski, E. Jaeckel, V. Hoerr, C. Faber, K. Scheffler, R. Pohmann, J. Engelmann, *Contrast Media & Molecular Imaging* **2013**, *8*, 495-504.



# Chapter 2

## Synthesis and characterization of ultrasmall silicon nanoparticles

### Abstract

This Chapter focuses on the preparation, *via* two different bottom-up approaches, of ultrasmall water-soluble amine-terminated silicon nanoparticles and on their characterization from the morphological, compositional and photophysical point of view. Differences and similarities in size, polydispersity, core and surface composition and photoluminescence properties of the NPs are discussed in the perspective of their use as platforms for further functionalizations.

### 2.1 Introduction

The development of multimodal probes that are non-toxic and can be applied for *in vivo* imaging, is the main challenge of this thesis. Amongst the possibilities, we have chosen ultrasmall silicon nanoparticles (Si NPs) because of the many advantages, connected with their biocompatibility and non-toxicity<sup>[1-2]</sup>, the tunable luminescence properties and, not least, the possibility to functionalize their surface in a covalent way. We decided to investigate the properties of silicon nanoparticles, by focusing our attention on a single kind of initial surface functionalization, namely the amine termination, and to explore different routes of preparation in order to understand how the synthetic route can influence size, emission, structure, composition and biological effects. The amine-termination has been chosen because the aim is to obtain water-soluble particles that can

easily undergo further functionalization (e.g. with labels or targeting agents), and amine groups are particularly well suited to this goal.

In this Chapter, we report on the wet-chemistry methods we used for preparing the amine-terminated Si NPs. These bottom-up techniques, namely microemulsion and hydrothermal syntheses - both based on the reduction of a silicon source - were optimized for obtaining ultrasmall (< 5 nm) amine-terminated Si NPs. The NPs were then characterized by means of several techniques, including attenuated total reflectance infrared spectroscopy (ATR-FTIR), high-resolution transmission electron microscopy (HR-TEM), energy dispersive X-ray emission analysis (EDX), X-ray photoelectron spectroscopy (XPS) and photophysical measurements.

## **2.2 Amine-terminated silicon nanoparticles from microemulsion synthesis**

### **2.2.1 Synthetic route**

In the microemulsion synthesis, silicon nanoparticles were prepared using a modification of a reported method<sup>[3-5]</sup> based on the reduction of either  $\text{Si}(\text{OCH}_3)_4$  or  $\text{SiCl}_4$  with  $\text{LiAlH}_4$ , followed by a hydrosilylation reaction of the obtained Si-H terminated NPs with allylamine in the presence of the catalyst  $\text{H}_2\text{PtCl}_6$ . This method is also known as “reduction in reverse micelles,” since the reaction takes place inside micelles of the surfactant tetraoctylammonium bromide (TOAB) that allow to control the growth of the particles. With this synthesis we obtain ultrasmall amine-terminated silicon NPs (size: 1.5 - 3 nm). All reactions were performed under strictly controlled oxygen and water free atmosphere (glove box,  $\text{pO}_2 < 0.1$  ppm,  $\text{pH}_2\text{O} < 0.1$  ppm) in order to prevent oxidation of the NPs.

The general scheme of the microemulsion synthesis of amine-terminated Si NPs is shown in Figure 2.1.

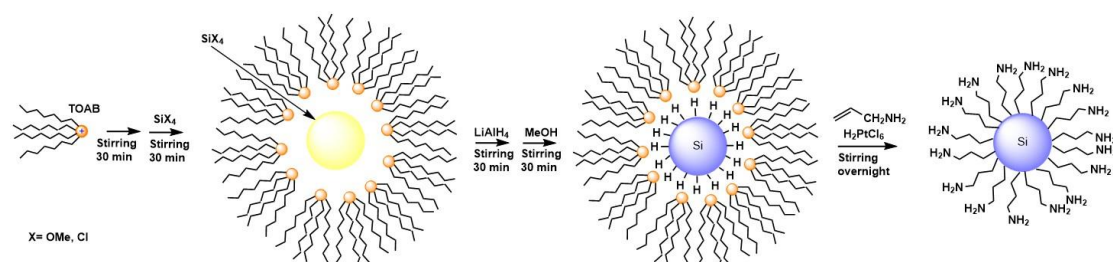


**Figure 2.1** General reaction scheme for the preparation of amine-terminated Si NPs via microemulsion synthesis

Table 1 reports a summary scheme of the different reaction conditions used in this thesis. Several parameters, such as the silicon source, reaction time and temperature of the hydrosilylation step were changed, with the aim to establish a reproducible and scalable procedure for obtaining amine-terminated Si NPs.

**Table 1.** Summary of the different reaction schemes performed by changing different parameters (capping agent is allylamine for all reactions)

Silicon precursor	Time of hydrosilylation	Temperature during hydrosilylation
Si (OCH <sub>3</sub> ) <sub>4</sub>	1 hour	room temp.
Si (OCH <sub>3</sub> ) <sub>4</sub>	Overnight	70 °C
SiCl <sub>4</sub>	Overnight	room temp.
Si (OCH <sub>3</sub> ) <sub>4</sub>	Overnight	room temp.

The best results, in terms of photophysical and morphological properties of Si NPs, were obtained at room temperature with a prolonged (overnight) hydrosilylation step, which yielded properties comparable with the highest standards reported in the literature.

Purification has been an important and crucial part of the work. The removal of the excess of capping agent and surfactant from the particles is a non-trivial task since the nanoparticles can be easily lost during the purification steps due to their ultrasmall size. This can lead to a drastic decrease of the overall yield. We explored several methods including dialysis and density gradient

ultracentrifugation (DGU), but size exclusion chromatography turned out to be the best technique to obtain clean ultrasmall Si NPs. Dialysis purification methods led to the loss of large fractions of particles through the membrane pores (even when using the smallest available molecular weight cut-off, such as 1KDa) and, in addition, they leave some surfactant impurities in the sample. Centrifugation methods are often used for NPs purification, but Si NPs have low density (e.g., compared to other NPs) and very small size. Therefore, satisfactory separation cannot be obtained by conventional centrifugation methods.

Inspired by a recent paper<sup>[6]</sup> in which different sizes of Si NPs were separated by DGU, we attempted to use this method for separating Si NPs from unreacted reagents, surfactant and reaction by-products.

As can be seen in Figure 2.2, we succeeded in separating different fractions. The ones containing our particles are easily distinguished due to their blue luminescence under UV light. Although effective in separation, the DGU method is not suitable for the purification because it introduces the density



**Figure 2.2.** Different fractions of Si NPs separated by DGU under UV irradiation (the blue emission comes from the fractions containing the nanoparticles)

gradient medium itself (Iodixanol solution) as an impurity. A high content of iodine was found in the samples when they were analyzed by XPS (Figure 2.3). This impurity is not easily removed and it is non-compatible with further bioapplications of the particles.

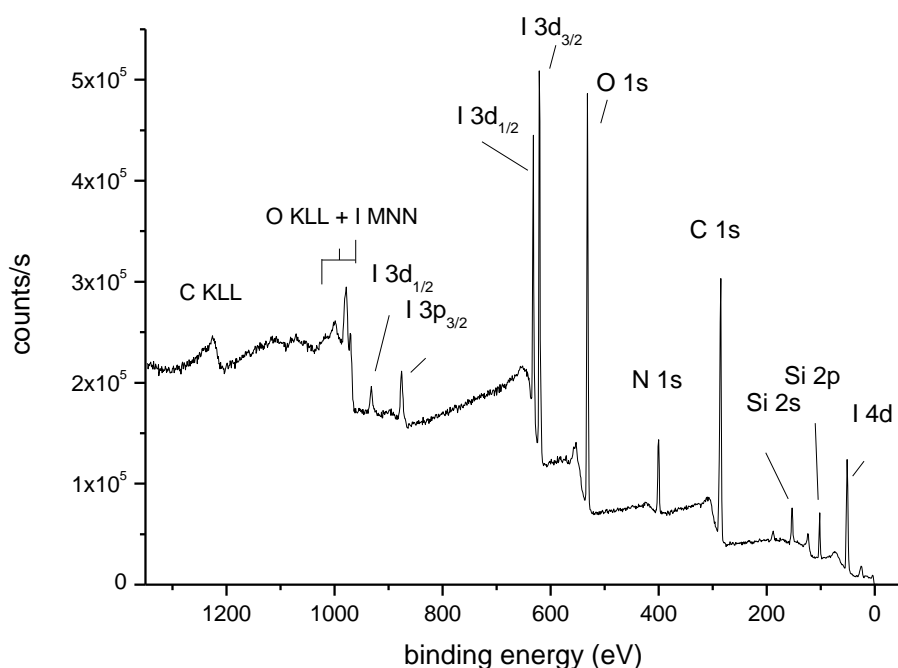


**Figure 2.3.** Survey XPS spectrum of a DGU fraction containing the blue emitting Si NPs. Note the massive presence of iodine coming from the density gradient medium.

To our knowledge the best purification technique is size exclusion chromatography (Sephadex LH-20; eluent: methanol) as it has been shown also in literature<sup>[7]</sup>. In particular, the best results are obtained if the column is repeated several times, being the first fraction that comes out the cleanest, as verified by the absence of impurities in thin-layer chromatography.

## 2.2.2 Characterization

After purification, an extensive characterization of amine-terminated Si NPs has been carried out to determine size, crystallinity, photoluminescence (PL) properties and degree of functionalization.

Typical HR-TEM images of amine-terminated Si NPs obtained by microemulsion method (Figures 2.4a and 2.4b), show that the particles are ultrasmall. In Figure 2.4c, a typical size distribution histogram shows that the particles have an average size of  $2.5 \pm 0.6$  nm. In addition, in the TEM

micrograph reported in Figure 2.4a it is possible to see the crystal lattice of silicon. The distance between fringes is 0.2 nm, characteristic value for the lattice spacing of the (220) planes of crystalline silicon.

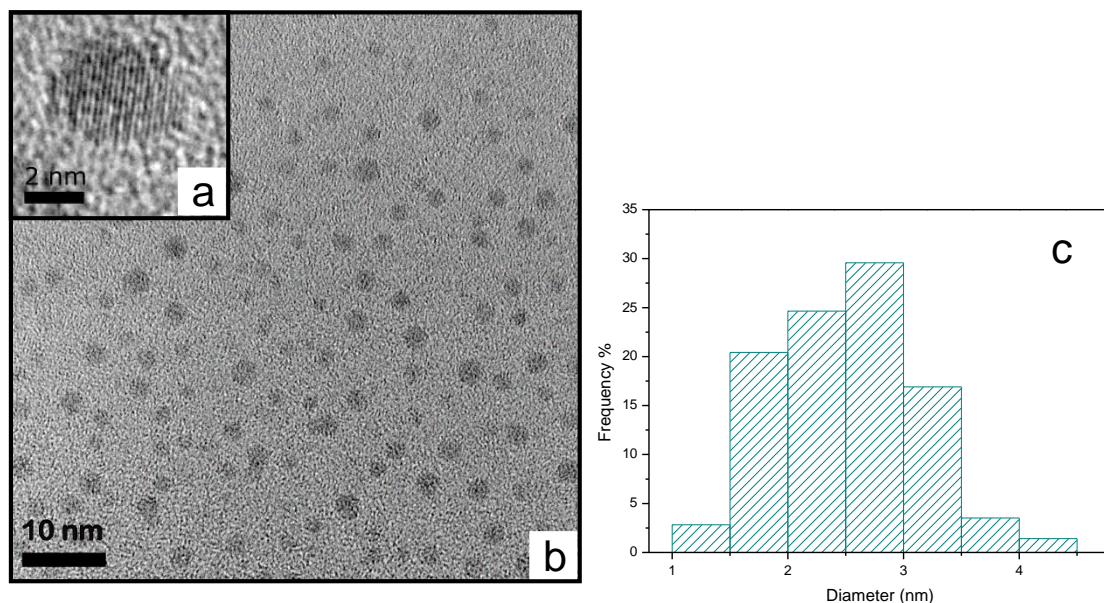


**Figure 2.4.** a), b) HR-TEM images of amine-terminated silicon nanoparticles obtained by microemulsion synthesis; in a): the crystal fringes of silicon are clearly visible; c) size distribution graph (average size  $2.5 \pm 0.6$  nm)

In the same HR-TEM microscope, it is also possible to perform energy dispersive X-ray (EDX) analysis. In Figure 2.5, a typical EDX spectrum for amine-terminated Si NPs is reported. As can be seen, the characteristic peak (1.75 keV) of the silicon  $K\alpha$  radiation confirms the NPs composition and does not reveal the presence of major impurities. The signals of copper, carbon and oxygen are due to the copper-coated carbon grids used to support the sample.



maximum when exciting at  $\lambda_{\text{exc}} = 300$  nm is centered at 449 nm. In Figure 2.6b it is shown a typical excitation spectrum ( $\lambda_{\text{em}} = 449$  nm) in water of amine-terminated Si NPs prepared by microemulsion method. The spectrum shows two features: a first peak close to the peak in absorption (290 nm) and a second more intense peak at 360 nm, which is not visible in the absorption spectrum. In literature, the excitation spectra of Si NPs are often missing but, when shown, they do not correspond to the absorption spectra<sup>[9, 11]</sup>.

Figure 2.7 reports the effect of the excitation wavelength on the emission spectra. The position of the emission maximum is not constant, and in particular, it red-shifts at increasing excitation wavelengths. This effect is attributed to a direct bandgap-like behaviour induced by the presence of Si-C bonds at the NPs surface<sup>[12]</sup>.

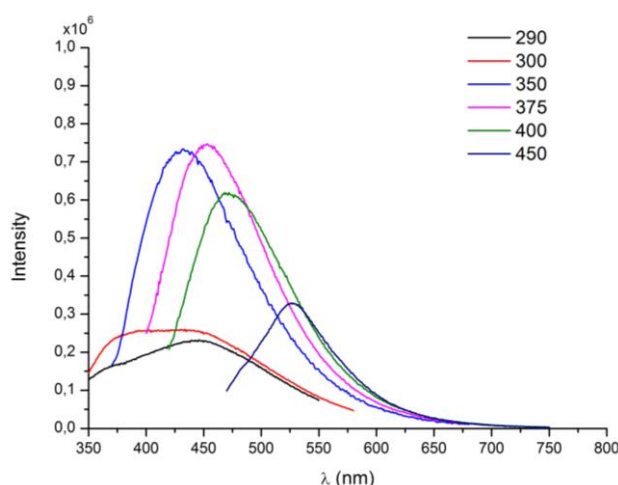


**Figure 2.7.** Emission spectra at various excitation wavelengths of amine-terminated Si NPs (microemulsion method) in ethanol (the excitation wavelengths, in nm, are reported on the top right)

On a different perspective, the intensity of emission is higher when we are exciting at 375 nm, confirming that the species that mostly contributes to the emission, features larger absorption in this spectral region.

The photoluminescence quantum yield (PLQY) was measured by integrating sphere (for details see page 148) and it is around 2% at all excitation wavelengths and the PL lifetime was measured at  $\lambda_{\text{em}} = 450$  nm, exciting at 290 nm (maximum value in absorption) and at 375 nm (in the region of the maximum intensity in

emission). Both lifetimes can be fitted with a three-exponential decay (Table 2) in agreement with the findings for similar systems<sup>[5, 13]</sup>.

<b>Table 2.</b> Photoluminescence lifetimes (and relative contributions) of amine-terminated silicon nanoparticles in ethanol		
	<b>Lifetime</b> ( $\lambda_{exc} = 290 \text{ nm}$ ; $\lambda_{em} = 450 \text{ nm}$ )	<b>Lifetime</b> ( $\lambda_{exc} = 375 \text{ nm}$ ; $\lambda_{em} = 450 \text{ nm}$ )
<b>NH<sub>2</sub>-Si NPs</b>	$\tau_1$ : <b>4.8 ns (35 %)</b> $\tau_2$ : <b>11.8 ns (13 %)</b> $\tau_3$ : <b>1.1 ns (52 %)</b>	$\tau_1$ : <b>4.4 ns (46 %)</b> $\tau_2$ : <b>10.5 ns (14 %)</b> $\tau_3$ : <b>1.1 ns (40 %)</b>

The full excitation versus emission wavelength map is shown in Figure 2.8. The intensity, given in color scale, shows that the most intense emission takes place at excitation wavelength values of 350 - 390 nm. The black dots in the figure represent the measured position of photoluminescence maxima at each excitation wavelength. In order to estimate NPs size from the emission spectra, we determined the photoluminescence peak maximum under UV excitation (290 nm) and at the excitation maximum. According to a theoretical model<sup>[12]</sup>, we can estimate the average NPs size and we found that the amine-terminated Si NPs have an average diameter of <1.9 nm. This value is in good agreement with the HR-TEM data, showing sizes in the range of 1.5 - 3.0 nm.

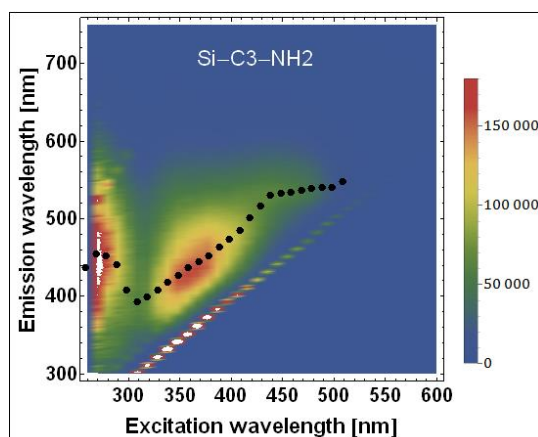


**Figure 2.8.** Emission versus excitation wavelengths map: intensity is given by color scale. Black dots indicate position of PL maximum at different excitation wavelengths.

The long-term stability of PL was checked by measuring the emission of NPs after 18 weeks of storage in the dark. The NPs display good stability, since their emission is still more than 60% of the initial value.

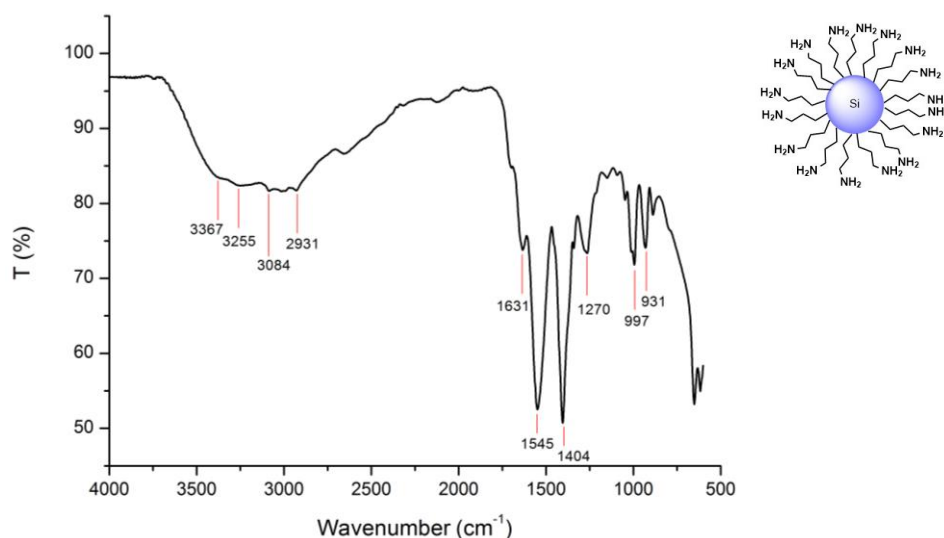


**Figure 2.9.** ATR-FTIR spectrum of amine-terminated Si NPs (microemulsion method); top right: model of a single nanoparticle. Peaks are assigned according to literature and IR tables<sup>[4, 14-16]</sup>

The attenuated total reflectance FTIR (ATR-FTIR) spectrum of amine-terminated Si NPs (Figure 2.9) confirms the surface composition of the particles. The region of the spectrum from 3367 to 2931  $\text{cm}^{-1}$  contains both, the C-H stretching (3084 and 2931  $\text{cm}^{-1}$ ) and the N-H asymmetric (3367  $\text{cm}^{-1}$ ) and

symmetric ( $3255\text{ cm}^{-1}$ ) stretching of the  $\text{-NH}_2$  group of the protecting propylaminic chain. The peak at  $1631\text{ cm}^{-1}$  is associated to the bending of the  $\text{NH}_2$  bond. The peak at  $1545\text{ cm}^{-1}$  is probably associated to a deformation mode of H-bonded amine groups (as reported<sup>[17]</sup> in similar systems) due to interactions of the shells of adjacent NPs or between the shell and some residual free allylamine hydrogen-bonded to the shell. The peaks at  $1404$  and  $1270\text{ cm}^{-1}$  are related to the vibrational modes of the  $\text{Si-CH}_2$  bond, confirming the successful attachment of the propylaminic chain to the silicon surface. The absence of peaks in the region  $1100 - 1000\text{ cm}^{-1}$  confirms that the particles do not contain appreciable amounts of silicon oxide.

Further information on the prepared NPs was obtained from XPS measurements. Figure 2.10 reports the  $\text{Si}2\text{p}$ ,  $\text{C}1\text{s}$  and  $\text{N}1\text{s}$  regions of the XPS spectrum of Si NPs.

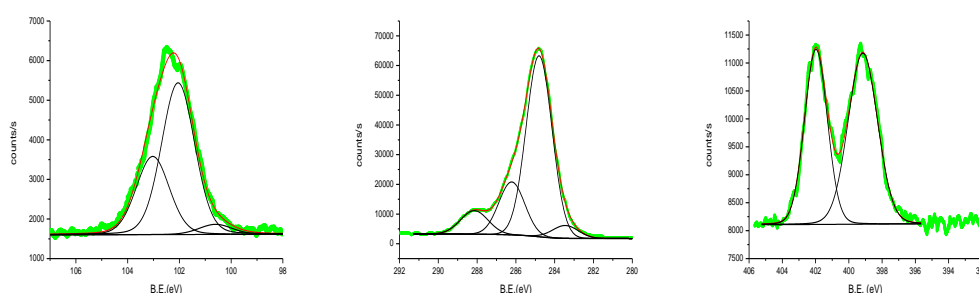


**Figure 2.10.** From left to right:  $\text{Si}2\text{p}$ ,  $\text{C}1\text{s}$  and  $\text{N}1\text{s}$  high resolution regions of XPS spectrum of amine-terminated Si NPs made by the microemulsion technique. Experimental data are in green. The results of curve resolution are reported in red (resulting curve) and black (individual components).

The silicon peak can be resolved in three bands at  $\sim 100.5\text{ eV}$ ,  $\sim 102.0\text{ eV}$ ,  $\sim 103.0\text{ eV}$ , assigned respectively to  $\text{Si-C}$  bonds, to silicon bound to only one oxygen (most probably  $\text{O-Si-Si}$ ) and to more oxidized silicon species<sup>[18]</sup>. The elemental silicon component does not display appreciable intensity. To the best of our knowledge, elemental silicon signals, are only reported for particles with bigger size<sup>[8]</sup>, where the ratio between surface and bulk silicon atoms is lower than in the case of ultrasmall nanoparticles. The low-oxidation fraction of silicon atoms (with B.E.s up to  $102.0\text{ eV}$ ) represents about 70% of the total. The presence of higher BE component can be explained either by the presence of

unreacted tetramethyl orthosilicate or by some oxidation occurred during the storage of the sample before XPS analysis. The presence of Si-C bond is confirmed by a small, but significant, low binding energy component of C1s at about 283.5 eV. Finally, N1s peak features two components, the one at lower binding energy being assigned to free amine moieties, while the higher binding energy one is compatible with protonated amino groups. From the atomic ratios obtained from the XPS peak areas by standard procedures, we estimated the average number of amine functionalities per Si NP, as detailed in the experimental part. The calculation yields an average value of about 200 amines per Si NP. From geometrical considerations, we can estimate that a 2.5 nm-sized NP contains about 400 silicon atoms,  $\approx 65\%$  of them being surface atoms. We can estimate that a large fraction of the surface silicon atoms are bound to amine molecules.

The above evaluation was compared with independent thermogravimetric analysis (TGA) measurements, performed under nitrogen atmosphere. The estimation was made by entirely attributing the weight loss above 200°C to the loss of the organic molecules covalently bound to silicon, according to literature data on similar systems<sup>[19-21]</sup>. This gives a value of  $\approx 100$  amine molecules per NP, again indicating that a large fraction of the surface silicon atoms are bound to the amine.

## **2.3 Amine-terminated silicon nanoparticles prepared by hydrothermal synthesis**

### **2.3.1 Synthetic route**

In the hydrothermal synthesis, amine-terminated Si NPs were prepared according to a modification of a reported method<sup>[22]</sup> based on microwave heating of an aqueous solution of (3-Aminopropyl)trimethoxysilane in the presence of

trisodium citrate. Here we demonstrate that with a longer reaction time (5 hours), the particles can be prepared also in a conventional oven inside Teflon pressure-resistant vessels. The advantage of using a conventional heating is that the synthesis can be easily scaled up at an industrial level. At laboratory scale, each run can yield up to 400 mg of Si NPs.

A general synthetic scheme for the hydrothermal method is depicted in Figure 2.11.

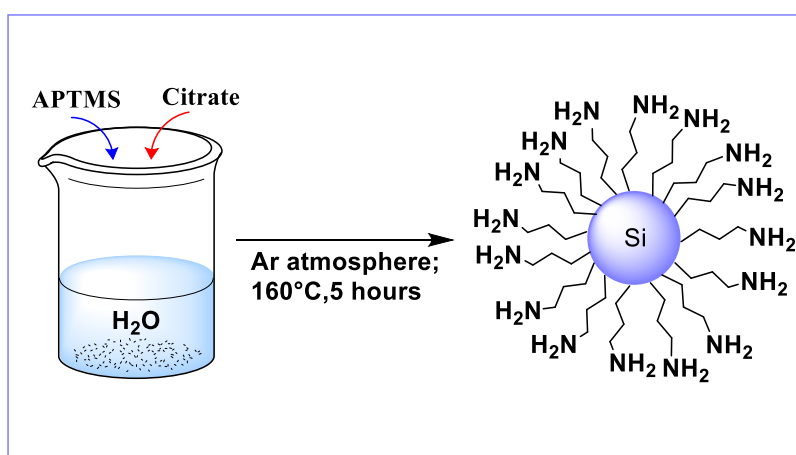


**Figure 2.11.** Schematic hydrothermal synthesis route for the preparation of amine terminated silicon nanoparticles. [APTMS = (3-aminopropyl) trimethoxysilane; citrate = Trisodium 2-hydroxypropane-1,2,3-tricarboxylate]

As shown in the following, the particles obtained by this method are typically slightly bigger than the ones obtained by microemulsion method. The synthesis is much cleaner since there are only two starting reagents, making the purification easier and the use of dialysis affordable. However, we will show that Si NPs made by this method contain a higher amount of oxidized silicon compared to the microemulsion method.

### 2.3.2 Characterization

In Figure 2.12 and 2.13 the typical HR-TEM images of amine-terminated Si NPs, obtained by the hydrothermal method, and a typical size distribution graph are

shown. Figure 2.13 shows that average size of the particles is  $4.3 \pm 1.3$  nm. In addition, in Figure 2.12b it is possible to observe the crystal lattice of silicon. The distance between fringes is of 0.2 nm, which is a characteristic value for the lattice spacing of the (220) planes of crystalline silicon.

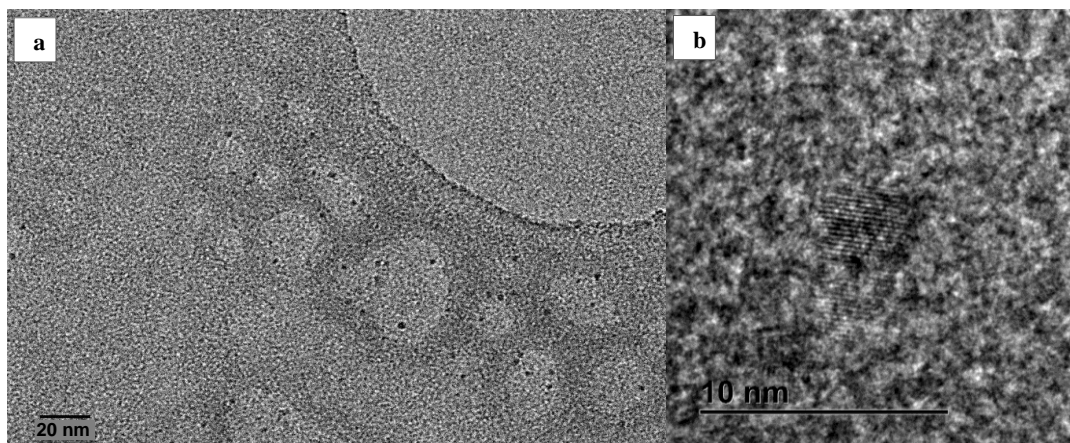


**Figure 2.12.** HR-TEM images of amine-terminated silicon nanoparticles obtained by hydrothermal synthesis; **15b**: an isolated NP presenting the crystal fringes of silicon.

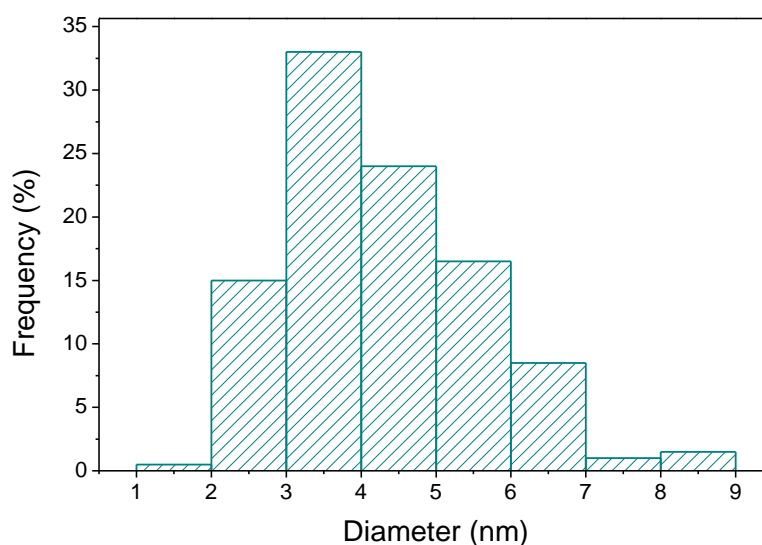


**Figure 2.13.** Size distribution histogram of amine-terminated Si NPs obtained by hydrothermal method (average size  $4.3 \pm 1.3$  nm)

In Figure 2.14, the EDX spectrum for amine-terminated Si NPs obtained by hydrothermal technique is reported. As can be seen, the characteristic silicon  $K\alpha$

peak (1.75 keV) confirms the composition of the particles. Copper, carbon and oxygen peaks are due to the copper-coated carbon grid supporting the sample.

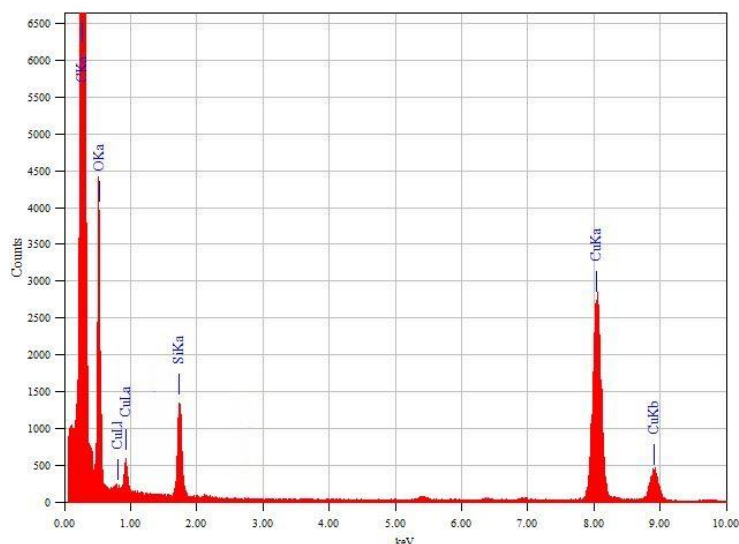


**Figure 2.14.** EDX spectrum of amine-terminated silicon nanoparticles prepared by hydrothermal method.

The typical UV-vis and emission spectra in water of these amine-terminated Si NPs (Figure 2.15a) show that they emit in the blue region of the electromagnetic spectrum also in this case.

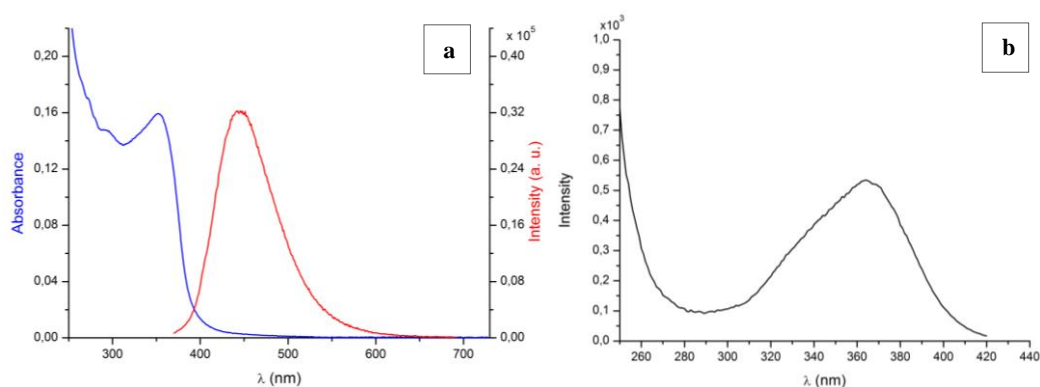


**Figure 2.15.** **a)** Absorption (blue) and emission (red) spectra of amine-terminated Si NPs (hydrothermal method) in water ( $\lambda_{exc} = 355$  nm); **b)** excitation spectrum in water ( $\lambda_{em} = 446$  nm).

The emission maximum when exciting at  $\lambda_{exc} = 355$  nm is centered at 446 nm. In Figure 2.15b a typical excitation spectrum ( $\lambda_{em} = 446$  nm) in water is reported.

The excitation spectrum shows a peak at 365 nm. This value does not correspond to the maximum in the absorption spectrum (353 nm).

When the emission spectra are measured at different excitation wavelengths (Figure 2.16), the maximum is red-shifted when increasing the excitation wavelength, but in less extent than in the microemulsion prepared NPs. This could be ascribed to some differences in surface composition of the two kinds of NPs, according to the literature debate<sup>[8, 12]</sup>. Also in this case, the highest intensity in the emission is located at excitation wavelengths close to the value of the maximum in the excitation spectrum.

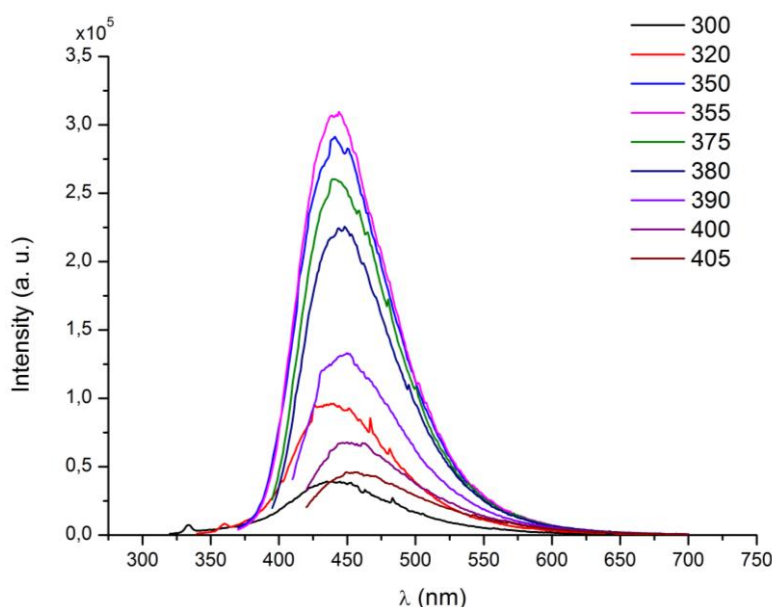


**Figure 2.16.** Emission spectra at various excitation wavelengths of amine-terminated Si NPs (hydrothermal method) in water (the excitation wavelengths, in nm, are reported on the top right)

The PLQY, measured also in this case by integrating sphere, ranges from 2 % to 13 % when exciting from 290 nm to 390 nm, and decreases again at higher excitation wavelengths. The maximum value of PLQY of Si NPs prepared by hydrothermal method is higher than the one of the NPs prepared by the microemulsion method. Lifetimes can be fitted also in this case with a three-exponential decay (with corresponding contributions) being  $\tau_1$ : 7.5 ns (54 %),  $\tau_2$ : 2.5 ns (22 %) and  $\tau_3$ : 15.9 ns (24 %).

On the other hand, after 18 weeks of storage in the dark, the emission of the NPs decreased to less than 10% of its initial value.

The attenuated total reflectance FTIR (ATR-FTIR) spectrum of amine-terminated Si NPs is reported in Figure 2.17. In general, it is similar to the spectrum obtained for Si NPs made by the microemulsion technique, but indicates also the presence of Si-O bonds.

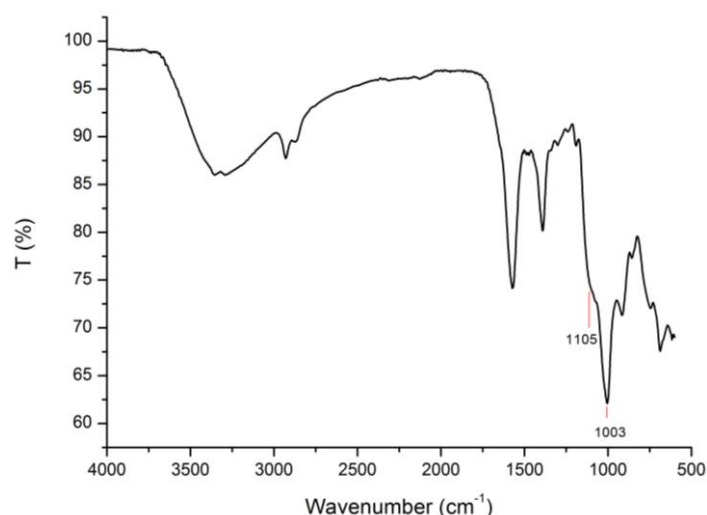


**Figure 2.17.** ATR-FTIR spectrum of amine-terminated Si NPs (hydrothermal method)

In detail, peaks are assigned according to reported values for amine-terminated silicon nanoparticles and IR tables<sup>[4, 14-16]</sup>. The region of the spectrum from 3360 to 2930  $\text{cm}^{-1}$  contains both, the C-H stretching and the N-H asymmetric and symmetric stretching of the  $-\text{NH}_2$  group of the propylaminic chain attached on the surface of the silicon NPs. The peaks in the range of 1600-1550  $\text{cm}^{-1}$  are associated to the bending of the amine group and to the H-bonded amine as explained for the microemulsion method. The peaks in the region 1400-1270  $\text{cm}^{-1}$  are related to the vibrational modes of the Si- $\text{CH}_2$  bond. The two peaks at 1105 and 1003  $\text{cm}^{-1}$  (marked in Figure 2.17) are characteristic of the silicon oxide vibration modes.

The relevant spectral regions of the XPS spectra for amine-terminated Si NPs prepared via hydrothermal method, are shown in Figure 2.18.

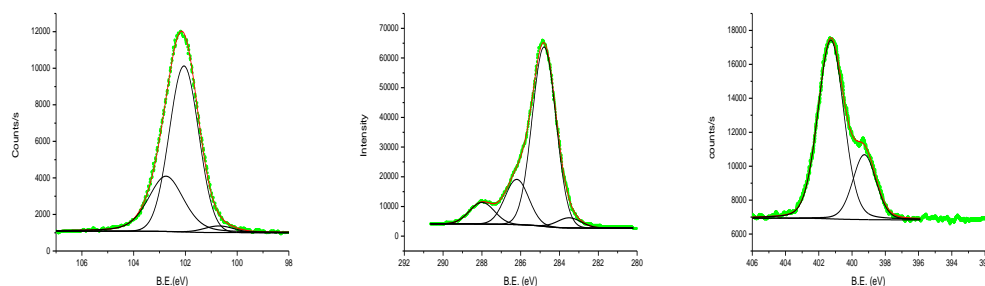


**Figure 2.18.** From left to right: Si2p, C1s and N1s high resolution regions of XPS spectrum of amine-terminated Si NPs made by hydrothermal synthesis. Experimental data in green, fitted spectrum in red, fit components in black.

The overall appearance of the spectra is similar to those obtained for particles prepared by the microemulsion method. There are again three components in Si2p, four components in C1s and two components in N1s peak. In particular, the presence of Si-C moieties was again observed, but they are less abundant (by a factor 0.5-0.6) of those present on the samples prepared by microemulsion. This is consistent with a slightly different surface composition of NPs obtained via the two synthetic routes and in particular, with a higher quantity of oxygen at the surface of NPs from the hydrothermal method.

The number of amine groups per Si NP was estimated from XPS intensities and from TGA measurements, following the same procedure reported in section 2.2.2. From both the measurements, a value of 500 ÷ 600 amine molecules per particle was obtained, indicating that a large fraction of surfaces silicon atoms are bound to the amine-terminated chain.

## 2.4 Conclusions

In this Chapter, two different methods (microemulsion and hydrothermal) have been explored to prepare ultrasmall amine-terminated Si NPs. The obtained NPs were characterized from the morphological, compositional and photophysical point of view by several techniques and the two types of particles compared to each other. From the data illustrated and discussed in the Chapter, it is possible

to draw some conclusions on the differences, advantages and disadvantages of the two preparation methods.

The great advantage of the microemulsion reaction procedure is that it can lead to ultrasmall silicon nanoparticles with stable photoluminescence properties on a time scale of several months. Also, the NPs produced with this method contain a lower amount of oxidized species than the ones prepared by the hydrothermal method. The average size of NPs is smaller (2.5 nm) than the hydrothermal one (4.3 nm) and the emission maximum can be tuned by changing the excitation wavelength. A disadvantage of the method is the need of complex purification procedures. On the other hand, the synthesis by hydrothermal method is cleaner, requires less purification efforts and can be easily scaled-up. From the point of view of the PL properties, hydrothermally prepared Si NPs are less stable and the emission wavelength is less tunable, but their initial PLQY can reach values much higher than those measured for the NPs generated via microemulsion synthesis (up to 13 % vs 2%).

In conclusion, both methods lead successfully to the formation of ultrasmall water-soluble amine-terminated NPs suitable for further functionalization, e.g. for bioapplications. Therefore, depending on the desired properties and application, it results more convenient to use one or the other kind of NPs prepared. The comparison of the behaviour in *in vitro* and *in vivo* experiments of these two typologies of NPs will be the object of Chapter 3.

## **2.5 Experimental section:**

### **2.5.1 Microemulsion method**

#### ***Materials***

All chemicals were purchased from Sigma-Aldrich and used without further purification, unless specified differently. Tetraoctylammonium bromide was purchased from Merck. Toluene (extra dry over molecular sieve 99.85%, AcroSeal®) was purchased from Acros and was deaerated by constant bubbling

of argon inside the bottle for 20-30 minutes. Methanol was deaerated before use. Allylamine was dried over  $\text{CaCl}_2$  overnight, distilled and deaerated before use.

### ***Synthetic procedure***

Silicon nanoparticles (Si NPs) were prepared using a modification of a reported method.<sup>[3-5]</sup> The reaction is performed in a nitrogen glove box ( $\text{H}_2\text{O}$  and  $\text{O}_2$  levels < 0.1 ppm). 7.5 g of tetraoctylammonium bromide was mixed with 100 ml of dry toluene and the mixture was stirred for 30 min. 0.5 ml of  $\text{Si}(\text{OCH}_3)_4$  or  $\text{SiCl}_4$  was added and stirring was continued for 30 min allowing the silicon precursor to enter the micelles. Subsequently, 7 ml of  $\text{LiAlH}_4$  (1 M in THF) was added in order to reduce the silicon precursor and form hydrogen-terminated Si NPs. After 30 min of stirring, dry and deaerated methanol (3.2 ml) was added to quench the excess of  $\text{LiAlH}_4$ . The quantity of MeOH was reduced in respect to reported methods to avoid the formation of methoxy-terminated nanoparticles. The final amine-terminated NPs were obtained adding distilled and degassed allylamine (13 ml) to the flask containing hydrogen-terminated Si NPs in the glove box, in the presence of 0.2 ml of  $\text{H}_2\text{PtCl}_6$  catalyst (0.05 M in MeOH). After overnight stirring, 3-aminopropyl Si NPs were extracted with water, washed with ethyl acetate and filtered twice through syringe membrane filters (Millex, Millipore, PVDF, 0.45  $\mu\text{m}$ ). The resulting Si NPs were further purified by size exclusion chromatography (Sephadex LH-20) against MeOH.

## **2.5.2 Hydrothermal method**

### ***Materials***

All chemicals were purchased from Sigma-Aldrich and were used without further purification. Milli-Q water (Millipore) has been used as the solvent. High pressure resistant Teflon vessels were used for the reaction.

### ***Synthetic procedure***

Amine-terminated nanoparticles were prepared modifying a reported method<sup>[22]</sup>. 0.8211 g of  $\text{C}_6\text{H}_5\text{Na}_3\text{O}_7$  (trisodium citrate) were added to 20 ml of Ar-saturated Milli-Q water. After stirring and bubbling with Ar for 15 minutes, 5.0 ml of

$\text{NH}_2(\text{CH}_2)_3\text{Si}(\text{OMe})_3$  (APTMS) were added to the solution of citrate and stirred under Ar for other 15 minutes. This starting mixture was transferred into a Teflon vessel while constantly bubbling Ar. The precursor solution was heated at 160 °C for 5 hours in a conventional oven. After cooling down to room temperature, the sample was purified by dialysis against water (MWCO: 1 KDa; Spectra/Por® 7 dialysis tubing).

### 2.5.3 Characterization

#### *XPS*

XPS analysis has performed by using a K-Alpha™ X-ray Photoelectron Spectrometer system from Thermo Scientific. Al  $\text{K}\alpha$  X-radiation was used (15kV, 72 W, 200  $\mu\text{m}$  spot diameter). The transmission function of the analyzer had been calibrated using a standard argon ion etched copper sample. Spectra were measured using a pass energy of 200 eV for survey spectra and 50 eV for core level spectra. For XPS measurements, a dispersion of Si NPs in ethanol or water is deposited on a gold or aluminium support and allowed to dry overnight in a low-vacuum chamber before the introduction in the ultra-high vacuum chamber of the XPS system. Binding energies were calibrated using as reference the hydrocarbon C1s peak at 284.8 eV. Curve resolution was performed either with the proprietary Thermo Advantage data evaluation software or by means of the public domain software XPS peak developed by Prof. R. W.M. Kwok, The Chinese University of Hong Kong. Quantitative information about the surface composition is calculated from peak intensities using standard sensitivity factors. The number of amine groups per Si atom in the sample has been estimated from the N/Si ratio and from the C/Si ratio (considering only the C component bound to silicon). The calculation neglects any possible effect of photoelectron attenuation, and this tends to overestimate the contribution of atoms that are closer to the outer surface with respect to those located in inner layers. The obtained estimation of the amine molecules per silicon atom was then converted into amines/NP by using the average size of the particles obtained from TEM

size distribution histograms and assuming that the NPs have a spherical shape and the same atomic density of bulk silicon.

### ***HR-TEM***

Samples for HR-TEM and EDX were prepared drop-casting an ethanolic solution of the sample on carbon coated copper grids (Quantifoil, GmbH). The analysis were performed using a FEI Titan 80-300 transmission electron microscope operated at 300 KV. Size distribution histograms were built counting 200 nanoparticles.

### ***Photophysical measurements***

Absorption spectra were acquired using a double-beam Shimadzu UV-3600 UV-Vis-NIR spectrophotometer.

Steady-state emission spectra were recorded on a HORIBA Jobin-Yvon IBH FL-322 Fluorolog 3 spectrometer equipped with a 450 W xenon arc lamp, as the excitation source, and a TBX-4-X single-photon-counting device as the detector. Emission and excitation spectra were corrected for source intensity (lamp and grating) and emission spectral response (detector and grating) by standard correction curves.

Time-resolved measurements were performed on FluoTime 300 “Easy Tau” spectrometer (PicoQuant) equipped with subnanoseconds LDH sources powered by a PicoQuant PDL 820 variable (0.2-80 MHz) pulsed power supply. Measurements were performed using a PicoHarp TCSPC (Time-Correlated Single Photon Countings) module. The decays were fitted by means of PicoQuant FluoFit Global Fluorescence Analysis Software (PicoQuant GmbH, Germany).

PLQY were measured on a Hamamatsu Quantaaurus-QY integrating sphere equipped with a 150 W CW Xenon source.

## **ATR-FTIR**

FT-IR spectra were acquired on a Shimadzu IRAffinity-1 spectrometer used in attenuated total reflectance (ATR) mode.

## **TGA**

Measurements were performed, under nitrogen atmosphere, on a STA 449 F1 (Netzsch) instrument. At least 3 mg of the waxy sample were put in an aluminium oxide crucible. Samples were heated to 120 °C (with a speed of 20 K/min) and an isothermal step was performed for 20 minutes in order to remove any traces of solvent remained in the sample. Then samples were heated up to 600 °C (with a speed of 5 K/min).

## **2.6 References:**

- [1] F. Peng, Y. Su, Y. Zhong, C. Fan, S.-T. Lee, Y. He, *Accounts of Chemical Research* **2014**, *47*, 612-623.
- [2] J.-H. Park, L. Gu, G. von Maltzahn, E. Ruoslahti, S. N. Bhatia, M. J. Sailor, *Nat Mater* **2009**, *8*, 331-336.
- [3] M. Rosso-Vasic, E. Spruijt, B. van Lagen, L. De Cola, H. Zuilhof, *Small* **2008**, *4*, 1835-1841.
- [4] J. H. Warner, A. Hoshino, K. Yamamoto, R. D. Tilley, *Angewandte Chemie International Edition* **2005**, *44*, 4550-4554.
- [5] M. Rosso-Vasic, E. Spruijt, Z. Popovic, K. Overgaag, B. van Lagen, B. Grandidier, D. Vanmaekelbergh, D. Dominguez-Gutierrez, L. De Cola, H. Zuilhof, *Journal of Materials Chemistry* **2009**, *19*, 5926-5933.
- [6] M. L. Mastronardi, F. Hennrich, E. J. Henderson, F. Maier-Flaig, C. Blum, J. Reichenbach, U. Lemmer, C. Kübel, D. Wang, M. M. Kappes, G. A. Ozin, *Journal of the American Chemical Society* **2011**, *133*, 11928-11931.
- [7] A. Shiohara, S. Prabakar, A. Faramus, C.-Y. Hsu, P.-S. Lai, P. T. Northcote, R. D. Tilley, *Nanoscale* **2011**, *3*, 3364-3370.
- [8] M. Dasog, Z. Yang, S. Regli, T. M. Atkins, A. Faramus, M. P. Singh, E. Muthuswamy, S. M. Kauzlarich, R. D. Tilley, J. G. C. Veinot, *ACS Nano* **2013**, *7*, 2676-2685.
- [9] J. Thomas, S. Ashby, F. Huld, T. Pennycook, Y. Chao, *J Nanopart Res* **2015**, *17*, 1-8.
- [10] J. J. Romero, M. J. Llansola-Portolés, M. L. Dell'Arciprete, H. B. Rodriguez, A. L. Moore, M. C. Gonzalez, *Chemistry of Materials* **2013**, *25*, 3488-3498.
- [11] K. A. Pettigrew, Q. Liu, P. P. Power, S. M. Kauzlarich, *Chem. Mater.* **2003**, *15*, 4005-4011.

- [12] K. Dohnalova, A. N. Poddubny, A. A. Prokofiev, W. D. A. M. de Boer, C. P. Umesh, J. M. J. Paulusse, H. Zuilhof, T. Gregorkiewicz, *Light Sci Appl* **2013**, 2, e47.
- [13] J. R. Siekierzycka, M. Rosso-Vasic, H. Zuilhof, A. M. Brouwer, *The Journal of Physical Chemistry C* **2011**, 115, 20888-20895.
- [14] A. Shiohara, S. Hanada, S. Prabakar, K. Fujioka, T. H. Lim, K. Yamamoto, P. T. Northcote, R. D. Tilley, *Journal of the American Chemical Society* **2010**, 132, 248-253.
- [15] D. L. Pavia, G. M. Lampman, G. S. Kriz, *Introduction to spectroscopy*, third ed., Brooks/Cole Thomson learning, **2001**.
- [16] G. Socrates, *Infrared and Raman Characteristic Group Frequencies, Tables and charts*, John Wiley and Sons, LTD, **2001**.
- [17] C. Weigel, R. Kellner, *Z. Anal. Chem.* **1989**, 335, 663-668.
- [18] G. F. Cerofolini, C. Galati, S. Reina, L. Renna, G. G. Condorelli, I. L. Fragalà, G. Giorgi, A. Sgamellotti, N. Re, *Applied Surface Science* **2005**, 246, 52-67.
- [19] S. P. Ashby, J. A. Thomas, J. Garcia-Canadas, G. Min, J. Corps, A. V. Powell, H. Xu, W. Shen, Y. Chao, *Faraday Discussions* **2014**, 176, 349-361.
- [20] J. Nelles, D. Sendor, M. Bertmer, A. Ebbers, F.-M. Petrat, U. Simon, *Journal of Nanoscience and Nanotechnology* **2007**, 7, 2818-2822.
- [21] P. Das, A. Saha, A. R. Maity, S. C. Ray, N. R. Jana, *Nanoscale* **2013**, 5, 5732-5737.
- [22] Y. Zhong, F. Peng, F. Bao, S. Wang, X. Ji, L. Yang, Y. Su, S.-T. Lee, Y. He, *Journal of the American Chemical Society* **2013**, 135, 8350-8356.

# Chapter 3

## Functionalization of ultrasmall Si NPs for bioimaging

### Abstract

This Chapter deals with the surface modification of amine-terminated silicon nanoparticles with molecules, such as dyes or radiotracers, suitable for optical or positron emission tomography imaging. NPs are studied *in vitro* to assess their cytotoxicity and their *in vivo* behavior is investigated in order to compare NPs made by the two different syntheses reported in Chapter 2. Experiments of *in vivo* PET imaging and biodistribution will show that NPs are excreted very quickly from the body and some of them show no accumulation in organs giving promising expectation for future multimodal imaging.

### 3.1 Introduction

As mentioned in Chapter 1, ultrasmall Si NPs showed promising results in *in vitro*<sup>[1-18]</sup> and *in vivo*<sup>[17, 19-20]</sup> experiments. Some authors reported already about the possibility to use Si NPs in multimodal imaging.<sup>[17, 21]</sup> Nevertheless, to date, there is only one report on *in vivo* positron emission tomography (PET) with ultrasmall Si NPs and, in that case, NPs accumulate in the liver<sup>[17]</sup>.

In this thesis, we propose to use Si NPs as a platform for multimodal imaging. For this purpose, it is important to engineer the surface of the particles with desired imaging labels. This Chapter deals with the functionalization of ultrasmall Si NPs, prepared by the methods already described in Chapter 2, with

different molecules, such as dyes or radiolabels. After proper surface modification, *in vitro* and *in vivo* experiments were performed. In particular, we will report on *in vitro* cytotoxicity tests and *in vivo* PET imaging experiments performed with Si NPs prepared both by microemulsion and by hydrothermal methods. Experiments of optical imaging on properly functionalized Si NPs will be also described. The results achieved demonstrate the feasibility of the use of ultrasmall Si NPs as core components of a multimodal probe.

### **3.2 Cytotoxicity of amine-terminated silicon nanoparticles**

In order to use Si NPs, or any type of nanoparticle, in bioimaging, it is essential to test the cytotoxicity *in vitro* before moving to *in vivo* experiments. Therefore, the *in vitro* experiments for amine-terminated Si NPs will be shown in this Chapter.

In literature, the toxicity of ultrasmall amine-terminated Si NPs has previously been tested *in vitro* through MTT (3-(4,5-dimethylthiazol-2-yl)2,5-diphenyl tetrazolium bromide) cell viability assays<sup>[4-6]</sup>. In the studies reported, amine-terminated Si NPs, that are usually positively charged, resulted to be quite toxic if compared to their neutral and carboxylic-terminated analogues. In addition, it was shown that the toxicity of ultrasmall amine-terminated Si NPs increases in the presence of serum<sup>[4]</sup> and this has been ascribed to the fact that the proteins contained in the serum may interact with NPs allowing an easier cellular uptake causing higher toxicity effects.

In this thesis, amine-terminated Si NPs prepared by both, microemulsion method and by hydrothermal synthesis were tested *in vitro* in A549 cell lines (adenocarcinomic human alveolar basal epithelial cells) to assess their cytotoxicity. Cellular viability is determined using MTS (3-(4,5dimethylthiazol-2-yl)-5-(3-carboxymethoxyphenyl)-2-(4-sulfophenyl)-

2H-tetrazolium) assay (similar to MTT assays previously reported), which is based on the measurement of the absorbance of the formazan molecule produced after the reduction of MTS operated by mitochondria in viable cells.

Therefore, lower absorbance in the MTS assay indicates a reduction in the metabolic activity of the cells, which in turn can be interpreted as a reduction in cell viability. Figure 3.1 shows the results of the MTS assays performed after incubation of silicon nanoparticles for 24 hours in A549 cell lines in cell culture medium supplemented with increasing concentrations of fetal bovine serum (FBS). The study has been performed varying serum concentration because it has been shown that serum drastically influences the cellular uptake of larger NPs and, in particular, it is reported that increasing serum concentration interferes with the overall uptake of larger NPs decreasing the toxicity<sup>[22]</sup>.

Amine-terminated Si NPs prepared by microemulsion method and by hydrothermal synthesis were compared to each other and to a positive control (amine-modified polystyrene nanoparticles with a size of 50 nm). It is well known<sup>[23-27]</sup> that amine-modified polystyrene NPs in this size range are quite toxic, inducing cell death by apoptosis. However, it has been reported<sup>[22]</sup> that the toxicity of these nanoparticles can be reduced by increasing the amount of serum. These reported results are in stark contrast to those reported for smaller nanoparticles. Indeed in the case of larger particles, the presence of high concentrations of proteins (serum) reduces the overall uptake of the NPs reducing the toxicity as explained above<sup>[22]</sup>. As can be seen in Figure 3.1a, the positive control (50 nm amine-modified polystyrene nanoparticles) shows the expected behaviour with a strong decrease of toxicity in the presence of high levels of serum. In the same figure, it is shown that the toxicity of amine-terminated Si NPs prepared by both methods (microemulsion and hydrothermal synthesis) seems not to be dramatically influenced by the quantity of FBS present in the system. Actually, a careful examination of the plots reveals a slight increase, although not very pronounced, of toxicity at higher amounts of FBS in contrast to what happens in the case of the positive control.

This could be interpreted in terms of a different uptake mechanism for ultrasmall NPs compared to the bigger ones. In addition, interesting differences are found between amine-terminated particles obtained by the two different synthetic routes. Amine-terminated Si NPs made by the hydrothermal method (Figure 3.1c) exhibit very low levels of toxicity even at concentrations as high as 1 mg/mL. Instead, amine-terminated Si NPs made by microemulsion method, show higher toxicity when using high NPs concentration. Nevertheless, the particles exhibit low levels of cytotoxicity in the range of concentrations typically used for *in vivo* tests (1-10  $\mu\text{g/mL}$ ). A possible explanation for the different *in vitro* behaviour (at higher NPs concentration) could be related to a

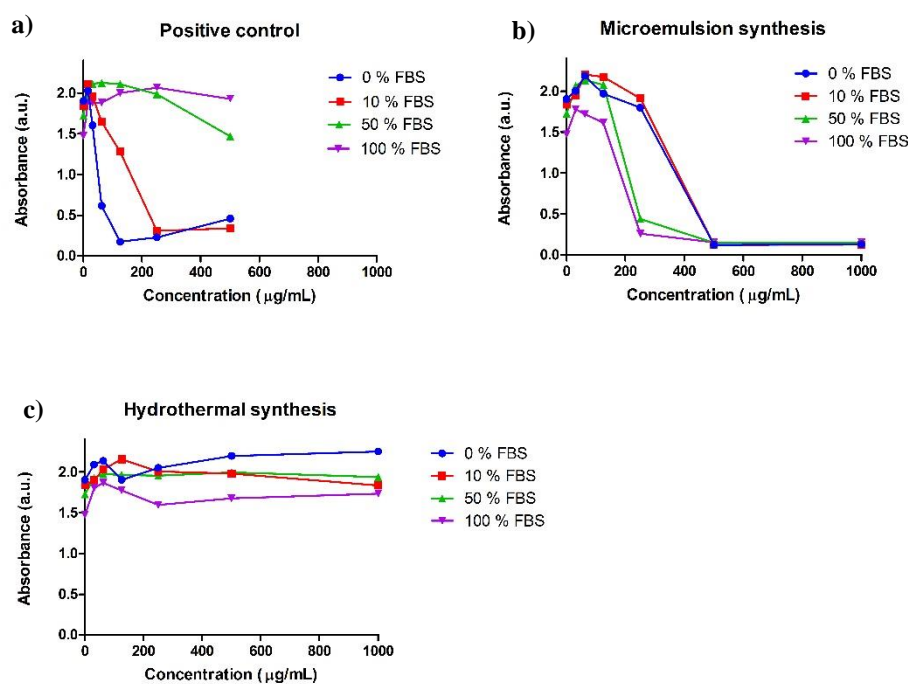


**Figure 3.1.** MTS cytotoxicity assay after incubation of three different kinds of particles in A549 cell lines for 24 hours in cell culture medium containing increasing amounts of fetal bovine serum (FBS): **a)** positive control, amine modified polystyrene (PS-NH<sub>2</sub>) nanoparticles with a size of 50 nm; **b)** amine-terminated silicon nanoparticles prepared by microemulsion technique (average size: 2.5 nm); **c)** amine-terminated Si NPs prepared by hydrothermal synthesis (average size: 4.3 nm)

higher content of amino-groups in the microemulsion prepared particles (as indicated by XPS data discussed in the previous Chapter) and/or to the possible presence of surfactant traces that remained adsorbed on the microemulsion prepared NPs even after several purification cycles.

### **3.3 Surface functionalization of amine-terminated silicon nanoparticles**

In this section, the coupling of different molecules with Si NPs will be described. Prior to bioimaging experiments, Si NPs have been functionalized with a single kind of label, either a dye or a radiolabel, but it will be shown that the results achieved are promising to obtain a future multifunctional NP probe.

More precisely, amine-terminated Si NPs have been functionalized with dyes, such as cyanine 5 and with radiotracers, such as  $^{64}\text{Cu}$  complexes. In the case of the cyanine 5-modified particles, the size of Si NPs remains in the ultrasmall range even after coupling ( $< 10$  nm). The reason for functionalizing the NPs with a cyanine dye is to obtain emission in the far-red region of the electromagnetic spectrum, which is useful to perform *in vivo* experiments and optical detection. The red emission has deeper penetration length into tissues allowing detection when the particles reach internal organs such as liver, lungs and kidneys.

The  $^{64}\text{Cu}$  complex instead, allows us to perform *in vivo* PET imaging in virtue of the decay properties of the  $^{64}\text{Cu}$  isotope. This radioisotope has a half-life of about 12 hours and in a certain percentage decays to  $^{64}\text{Ni}$  by positron emission. This emission is used in nuclear medicine as a label.

In the perspective of a future multimodal probe, NPs could also be functionalized with targeting agents, e.g. with specific peptides that selectively recognize cancer cells. A general scheme of multi-functionalized Si NPs is shown in Figure 3.2. As said before, we will limit mostly to the conjugation to a single kind of label each time (e.g.,  $^{64}\text{Cu}$  complex or dye), but the scheme gives an idea of the future probe in which multi-functionalization will be carried on.

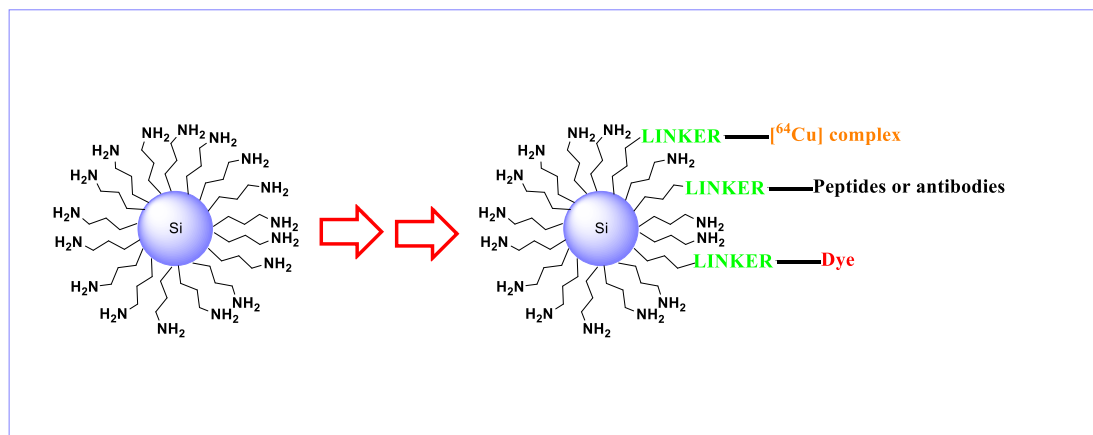


**Figure 3.2.** Schematic representation of some possible multi-functionalizations that can be carried on amine-terminated Si NPs

### 3.3.1 Coupling of amine-terminated Si NPs with the cyanine 5 dye

Amine-terminated Si NPs were coupled to the commercial N-hydroxysuccinimide ester of the dye cyanine 5 and to its water-soluble analogue (sulfo-cyanine 5). A simple scheme for the reaction is reported in Figure 3.3.

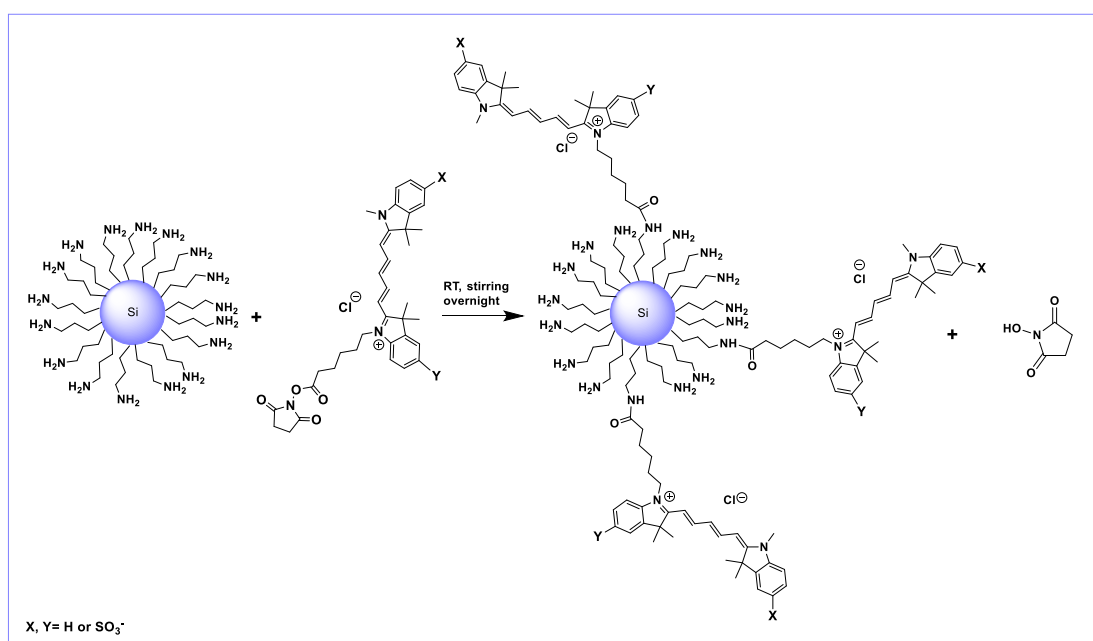


**Figure 3.3.** Synthetic route for the coupling of amine-terminated Si NPs with the dye cyanine 5 (X, Y= H) or its water-soluble analogue sulfo-cyanine 5 (X, Y = SO<sub>3</sub><sup>-</sup>)

The coupling is based on the formation of an amide bond between the amine groups on the particles and the succinimidic ester on the cyanine 5. After the reaction is completed, cyanine 5- or sulfo-cyanine 5-modified Si NPs (respectively Cy5-Si NPs or s-Cy5-Si NPs) were purified from unreacted dye by dialysis against water until UV-Vis spectra did not show any presence of the dye in the external water. This step is necessary, but causes a large loss of NPs. After purification, Cy5-Si NPs and s-Cy5-Si NPs were investigated by HR-TEM, complete photophysical characterization and XPS. In Figure 3.4, a typical HR-TEM image shows that particles do not change morphology after coupling with the dye and that there are no significant changes in the particles core dimension, being the mean size 2.5 or 4.3 nm depending on the NPs synthetic method, microemulsion or hydrothermal.

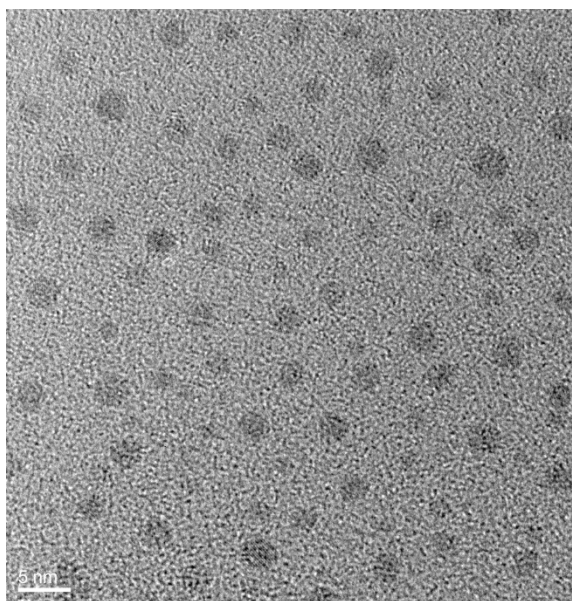


**Figure 3.4.** HR-TEM image of cyanine 5-modified Si NPs

In Figure 3.5a, typical UV-vis spectra in ethanol of Cy5-Si NPs, amine-terminated Si NPs and free cyanine 5 are compared. Sample Cy5-Si NPs features contributions from both Si NPs and Cy5, as clearly visible from the absorbance in the region 200 - 350 nm and from the peak at 650 nm, respectively. The contribution from Si NPs is rather low and the peak at 300 nm is not clearly visible. This might be due to the dialysis step used for purification, which leads

to some loss of NPs. In Figure 3.5b, the emission spectra in ethanol of Cy5-Si NPs, amine-terminated Si NPs and free cyanine 5 are also compared. In the spectrum of Cy5-Si NPs both, the peak of the NPs and the one of the dye are present, indicating that the coupling has occurred since all the free dye has been removed by dialysis. In addition, another indication that the coupling has occurred is suggested by a slight red-shift of the emission maximum of the NPs in sample Cy5-Si NPs. When exciting both samples at 375 nm, Cy5-Si NPs have an emission maximum centered at 460 nm, while the free amine-terminated Si NPs show the emission maximum at 450 nm. The part of the spectrum due to the emission of cyanine 5 does not show appreciable differences between sample Cy5-Si NPs and the free dye.

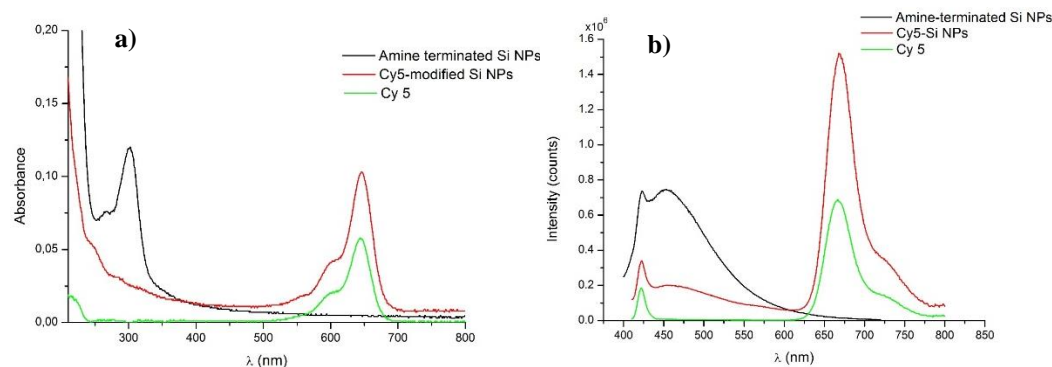


**Figure 3.5.** a) UV-vis and b) emission spectra ( $\lambda_{exc} = 375$  nm; filter 400 nm) in ethanol of a typical sample of amine-terminated Si NPs (black), Cy5-Si NPs (red) and of the free dye Cy5 (green)

As can be seen in Table 1, lifetimes are not particularly influenced by the coupling and they can be fitted with a mono-exponential decay when looking at the emission wavelength of the dye and with the typical three-exponential decay when looking at the emission wavelength of the particles.

<b>Table 1.</b> Photoluminescence lifetimes (and relative contributions) of amine-terminated Si NPs, Cy5-Si NPs and free dye Cy5 in ethanol.		
	<b>Lifetime</b> ( $\lambda_{exc} = 375 \text{ nm}$ ; $\lambda_{em} = 668 \text{ nm}$ )	<b>Lifetime</b> ( $\lambda_{exc} = 375 \text{ nm}$ ; $\lambda_{em} = 450 \text{ nm}$ )
<b>Cy5</b>	$\tau_1 = 0.9 \text{ ns}$ (100%)	
<b>Amine-terminated Si NPs</b>		$\tau_1 : 4.4 \text{ ns}$ (46 %) $\tau_2 : 10.5 \text{ ns}$ (14 %) $\tau_3 : 1.1 \text{ ns}$ (40 %)
<b>Cy5-Si NPs</b>	$\tau_1 = 1.1 \text{ ns}$ (100%)	$\tau_1 = 3.5 \text{ ns}$ (41.7 %) $\tau_2 = 9.9 \text{ ns}$ (4.7 %) $\tau_3 = 1.1 \text{ ns}$ (53.6 %)

In sample Cy5-Si NPs, the photoluminescence quantum yield (PLQY) increases in both the emission window of the dye and in the one of the particles, if compared to the free dye and free particles respectively. When exciting at 630 nm, the PLQY of sample Cy5-Si NPs is 24 % instead of 17% as in the free dye solution, and when exciting at 375 nm, PLQY is 3% instead of 1% as in the free amine-terminated Si NPs dispersion. A crucial information for the *in vivo* experiments is to know how many cyanine-5 molecules per particle are present in sample Cy5-Si NPs. It is still challenging to get this information and also in literature, no reports describe the quantification of the number of groups on silicon nanoparticles. The concentration of dye in Cy5-Si NPs samples was estimated from a calibration curve built measuring absorbance of the free dye at different concentrations. This estimation is based on the assumptions that, after purification, all the remaining dye is bound to the NPs and that the absorption coefficient of the dye is not changed after coupling. Knowing from independent estimation, the concentration (w/V) of NPs in the sample after coupling, and knowing the average size of the NPs, it is possible to estimate the average number of dye molecules bound to one NP. In the case of the samples used for *in vitro* and *in vivo* studies, the above estimation gives an average of ~ 0.5 dye molecules per nanoparticle. This estimated value is in the same order of magnitude of the ideal 1:1 ratio that one would like to obtain in order to have all the particles labelled with the dye and still susceptible to be further

functionalized with additional label molecules. In any case, even if not all the particles are functionalized with the dye, the functionalized fraction obtained is sufficient to perform optical imaging *in vivo*, and leaves open the opportunity to add other molecules, e.g. targeting agents or/and radiotracers, on the NPs surface. Figure 3.6 reports the survey XPS spectrum of the sulfo-Cy5-Si NPs deposited on an aluminium substrate. The presence of sulfur, (originating from the sulfonic functional groups present in the dye), suggests that cyanine is present at the sample surface.

The nitrogen to sulfur atomic ratio, calculated from the intensities of N1s and S2p, gives a value of  $\approx 2.5$ , which is higher than that expected from the 1:1 obtained from the stoichiometry of the dye. The excess of nitrogen is interpreted in terms of free amines still present at the surface of the NPs, giving a qualitative confirmation that many amine groups remain free after the coupling with the cyanine dye.

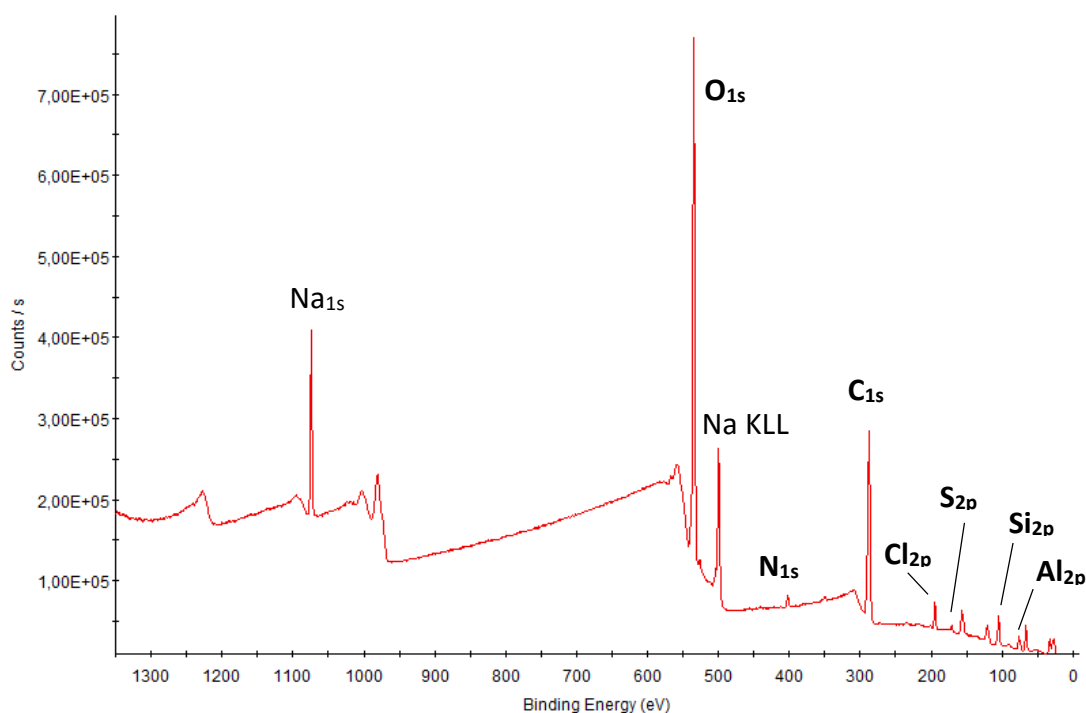


**Figure 3.6.** Survey XPS spectrum of s-Cy5-Si NPs.

### 3.3.2 In vitro and in vivo experiments with Cy5-Si NPs

Prior to *in vivo* experiments, Cy5-Si NPs were tested *in vitro* to assess any change in cytotoxicity after functionalization of the particles with the dye. The cellular uptake mechanism of such particles was also investigated. In this paragraph, the results obtained with sulfo-cyanine 5 modified Si NPs (s-Cy5-Si NPs) will be shown. Figure 3.7 shows the result of MTS assays performed after incubation of s-Cy5-Si NPs for 24 hours in A549 cell lines in cell culture medium containing increasing amounts of fetal bovine serum (FBS), i.e. in the same experimental conditions used for the amine-terminated NPs not coupled with the dye. The behaviour of the s-Cy5-Si NPs is compared to a positive control (50 nm amine modified polystyrene nanoparticles) in the same cell line.

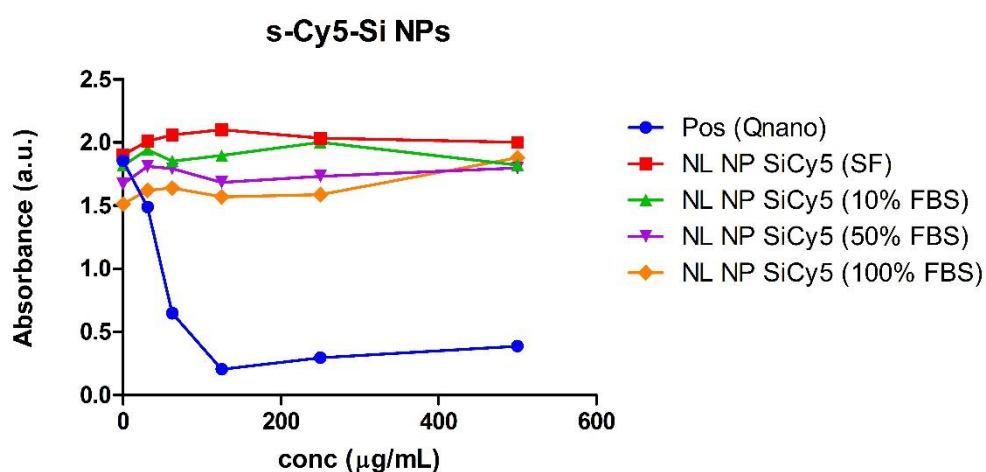


**Figure 3.7.** MTS assay after 24 hours incubation in A549 cell lines of sulfo-cyanine 5-modified silicon nanoparticles (s-Cy5-Si NPs) in cell culture medium containing increasing amounts of fetal bovine serum (FBS); Pos (Qnano) are the positive control NPs [amine modified polystyrene (PS-NH<sub>2</sub>) nanoparticles with a size of 50 nm] incubated in the same cells; SF = serum free

As can be seen in Figure 3.7, s-Cy5-Si NPs show still a very low cytotoxicity as in the case of amine-terminated Si NPs checked previously. Also in this case, there appears to be a slight decrease in cell viability when the amount of serum is higher. This could be explained as in the previous Chapter by the NPs size,

which remains in the ultrasmall range after functionalization. However, it is worth noting that the A549 cell line was optimised to be cultured in 10% FBS. Cell metabolism (especially over 24 hours as is the exposure in this experiment) can greatly change with higher serum concentrations. Therefore the lower MTS readouts observed from cells culture in 100% FBS compared to 10% FBS, could be due to the cells having lower metabolism.

To understand the mechanism of cell uptake for s-Cy5-Si NPs, some experiments of flow cytometry have been carried out. Indeed, while most nanoparticles are believed to enter cells by energy-mediated processes such as endocytosis, it is possible that ultrasmall particles may passively diffuse through the cell membrane (similarly to the behaviour of small molecules). To investigate which of these two mechanisms s-Cy5-Si NPs are uptaken by cells, we incubated the particles in A549 cell line for 7 hours at 37 °C, and in systems where we purposely reduce energy mediated processes (i.e. using 4 °C or adding NaN<sub>3</sub>). The same experiment was also repeated in cell culture medium containing different concentrations of fetal bovine serum (FBS). The fluorescence histograms obtained are shown in Figure 3.8.

The histograms represent the frequency distribution of the fluorescence signal recorded for >15,000 single cell events when analysed using 633 nm excitation and an emission window of 675 ± 12.5 nm. The curve in all cases appears to be mostly symmetrical indicating that the data is normally distributed. When the particles are incubated with the cells at 37 °C, there is an overall increase in the population of cells to higher fluorescent intensities. As Cy5 is active under these optical settings, we can assume that the increase in fluorescence of the cells is due to internalisation of the particles. (NB all efforts are made to minimise the number of particles stuck to the cell surfaces so that measurements reflect internalised particles only – the efficiency of this will be monitored by confocal microscopy). No difference is observed between the populations incubated in cell culture medium containing different concentrations of serum proteins – suggesting that the proteins do not have an effect on uptake. When energy is removed from the incubation scenario (i.e. reducing the temperature to 4 °C or

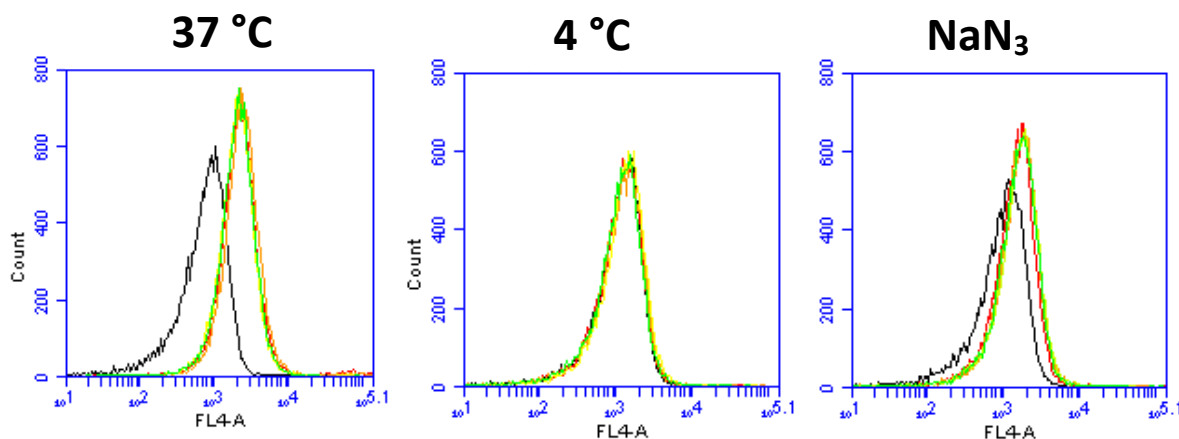


**Figure 3.8.** Fluorescence histograms acquired by flow cytometry of s-Cy5-Si NPs incubated for 7 hours with A549 cells in cell culture medium containing different serum concentrations at 37 °C and in reduced energy systems (4 °C and in the presence of NaN<sub>3</sub>) (SF = serum free; FBS = fetal bovine serum); black traces represent untreated cells; red traces represent cells incubated with s-Cy5-Si NPs in SF conditions; orange traces represent cells incubated with s-Cy5-Si NPs in 10% FBS v/v; yellow traces represent cells incubated with s-Cy5-Si NPs in 50% FBS v/v; green traces represent cells incubated with s-Cy5-Si NPs in 100 % FBS v/v;  $\lambda_{exc} = 633$  nm and emission window = 662.5 - 687.5 nm

using NaN<sub>3</sub> (which affects mitochondrial oxidative phosphorylation, to achieve ATP depletion) there is a smaller shift in the population from the fluorescent distribution of the cells in absence of particles (black trace) when compared to the cells incubated at 37 °C. This suggests that the uptake of s-Cy5-Si NPs is reduced when the energy of the cells is reduced, implying that the particles mostly enter via energy dependent mechanisms, such as endocytosis (as opposed to diffusion which is a passive process). Again, even in reduced energy exposure conditions, the concentration of serum proteins in the exposure medium has no significant effect on uptake. This could be due to a different uptake mechanism for ultrasmall NPs in comparison with bigger particles (as increasing concentrations of serum usually decrease the number of particles taken up by cells)<sup>[22]</sup>.

To complete the *in vitro* study, confocal microscopy imaging was performed on fixed samples of A549 cells incubated for 7 hours at 37 °C with s-Cy5-Si NPs (Figure 3.9). The particles (red spots in the image) are taken up by cells and co-localized with lysosomes (green colour in the image). This confirms that the

particles enter the cell through an energy dependent process such as endocytosis with final destination in lysosomes (particles that enter through passive diffusion, such as small molecules are found throughout the whole cytosol and not localised in acidified compartments like lysosomes).

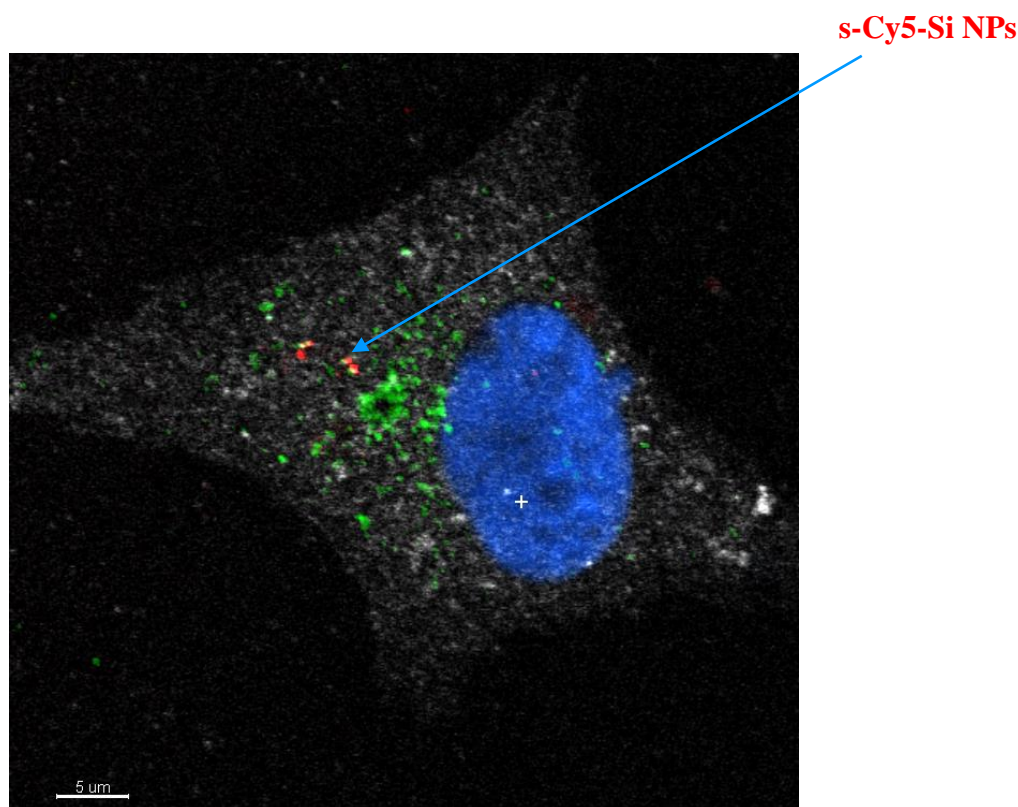


**Figure 3.9.** Confocal microscopy of s-Cy5-Si NPs incubated in A549 cell line for 7 hours (nucleus is stained with DAPI, blue colour; lysosomes are stained with LAMP-1 primary antibody, green colour; EGFR is stained in white; s-Cy5-Si NPs are represented in red)

Since *in vitro* tests showed that the particles have very low cytotoxicity, *in vivo* optical imaging using Cy5-modified Si NPs were performed. s-Cy5-Si NPs were injected through the tail vein in female NMRI nu/nu mice. The animals were irradiated with 650 nm light and the signals at 700 nm were collected in time. The emission intensity, which is connected to the distribution of particles in the blood and in the bladder are showed in Figure 3.10. As can be seen, already at 10 minutes post-injection many of the particles are in the bladder.

In Figure 3.11, the optical images of mice at different times post-injection are shown. They are compared to a standard placed close to the mouse and consisting

in the same solution of s-Cy5-Si NPs injected in the mice. From the images, it is clear that, at time zero, only the tail is fluorescent because particles are being injected through the tail vein. Then particles start to diffuse in all the body, starting to reach the bladder where all NPs accumulate at 50 minutes post-injection.

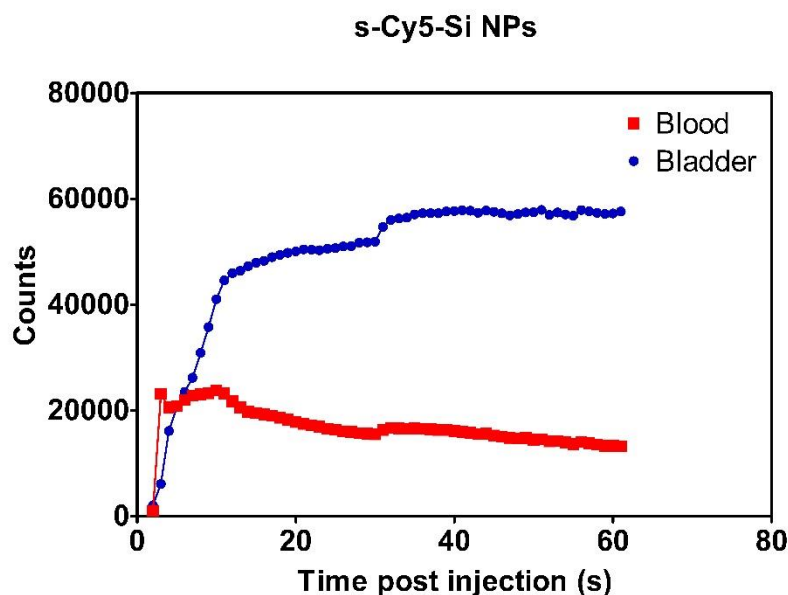


**Figure 3.10.** Biodistribution of s-Cy5-Si NPs in the blood (red curve) and in the bladder (blue curve) of NMRI nu/nu mice



**Figure 3.11.** Optical images of NMRI nu/nu mice at 0, 5, 20, 50 (going from left to right) minutes post-injection of s-Cy5-Si NPs; the bright spot on the top is a solution of s-Cy5-Si NPs with the same concentration of the solution injected

Figure 3.12 shows the biodistribution in organs after mice sacrifice. As it can be seen, the majority of the particles are in the bladder and in the intestine. The accumulation in intestine suggests that s-Cy5-Si NPs are following both of the two possible excretion pathways for NPs, i.e. renal excretion, through kidneys and bladder, and hepatobiliary excretion through the liver and the intestine.

Although the system can be improved reducing accumulation in the intestine, the result obtained is very promising for a future multimodal probe since particles do not accumulate in other organs and the majority of them are excreted already at 50 minutes post-injection.

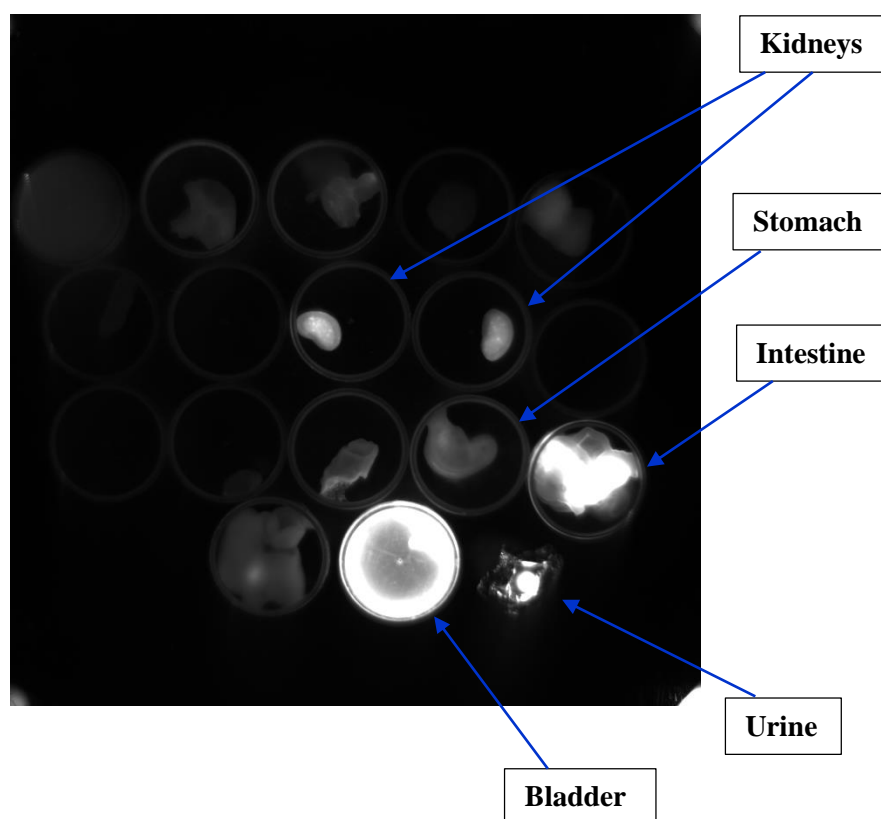


**Figure 3.12.** Biodistribution by optical imaging in organs of sacrificed mice after injection of s-Cy-Si NPs.

### 3.3.3 Coupling of Si NPs with $^{64}\text{Cu}$ complexes for *in vivo* PET imaging

In literature, to date, there is only one example of *in vivo* PET imaging with ultrasmall Si NPs<sup>[17]</sup> and in this experiment, NPs accumulate in the liver. Therefore, it results interesting to compare the *in vivo* behaviour of the two kinds of ultrasmall Si NPs prepared, by performing PET imaging.

Si NPs, prepared both by microemulsion and hydrothermal method were coupled to the commercially available S-2-(4-Isothiocyanatobenzyl)-1,4,7-triazacyclononane-1,4,7-triacetic acid (p-SCN-Bn-NOTA), a common ligand for copper. The coupling happens between the isothiocyanate moiety of the ligand and the amino groups on the Si NPs surface to form a thiourea bond in the final NOTA-Si NPs (Figure 3.13).

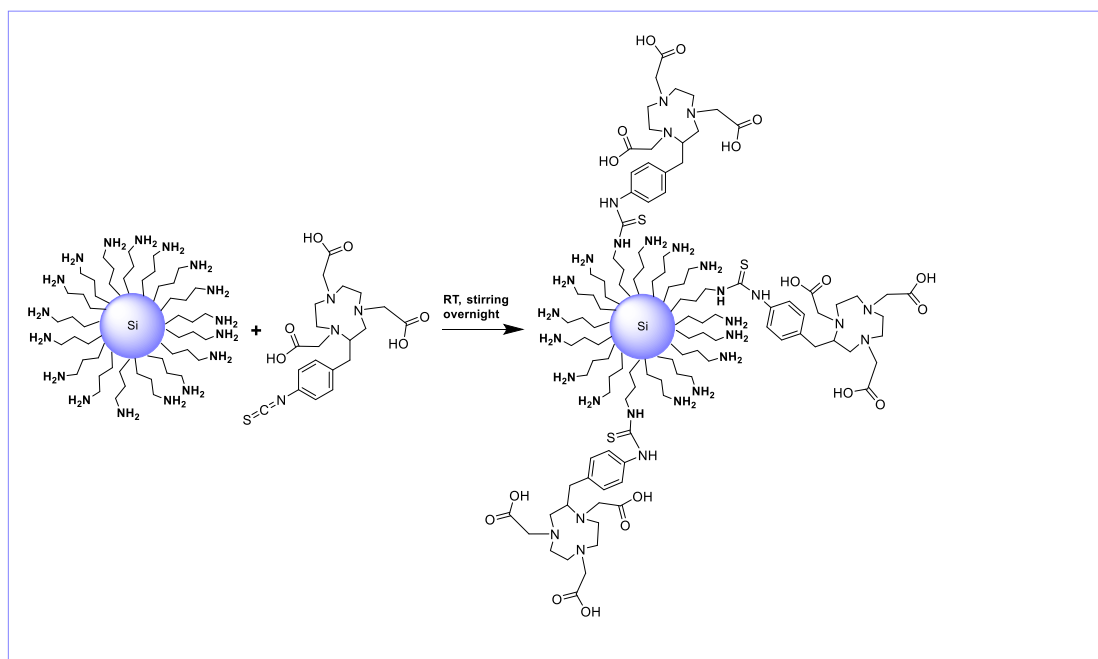


**Figure 3.13.** Reaction scheme of Si NPs coupling with p-SCN-Bn-NOTA ligand

After the reaction is completed, NOTA-Si NPs are purified from unreacted ligand by dialysis against water. Subsequently, the particles were mixed with a  $[^{64}\text{Cu}]\text{CuCl}_2$  solution to complex them with the radionuclide  $^{64}\text{Cu}$  in order to perform PET. The  $[^{64}\text{Cu}\text{-NOTA-Si NPs}]$  obtained in this way, were injected through the tail vein in male Wistar rats to perform biodistribution studies and in female NMRI nu/nu squamous cell carcinoma (A431) tumour bearing mice to perform *in vivo* PET imaging. In Figure 3.14, the comparison between PET images obtained for  $[^{64}\text{Cu}\text{-NOTA-Si NPs}]$  prepared by microemulsion,  $[^{64}\text{Cu}\text{-NOTA-Si NPs (micro)}]$ , and hydrothermal,  $[^{64}\text{Cu}\text{-NOTA-Si NPs (hydro)}]$ , method is shown. As can be seen from this Figure,  $[^{64}\text{Cu}\text{-NOTA-Si NPs (hydro)}]$  accumulate in the bladder at 50 minutes post-injection while  $[^{64}\text{Cu}\text{-NOTA-Si}$

NPs (micro)] accumulate in the bladder too, but a certain percentage remains also in the intestine at 50 minutes post-injection.

The two curves in the lower part of Figure 3.14 represent the activity, expressed as percentage of injected dose, present in the bladder versus time post-injection. The curves grow in time showing that the particles are accumulating in the bladder to be subsequently, excreted. The mice used bear a tumour, in the back or right hind leg, but no accumulation of particles in the tumour site was observed. This can be due to the lack of any cancer-specific targeting agent and because the NPs are too small to show enhanced permeability and retention effect (EPR effect). EPR is the effect by which particles tend to accumulate in higher concentrations in cancer tissues in respect to healthy tissues<sup>[28-30]</sup>. Indeed, the tumour microvascular endothelium exhibits a higher permeability to particles or bigger macromolecules in respect to healthy ones<sup>[30]</sup>. Our hypothesis is that

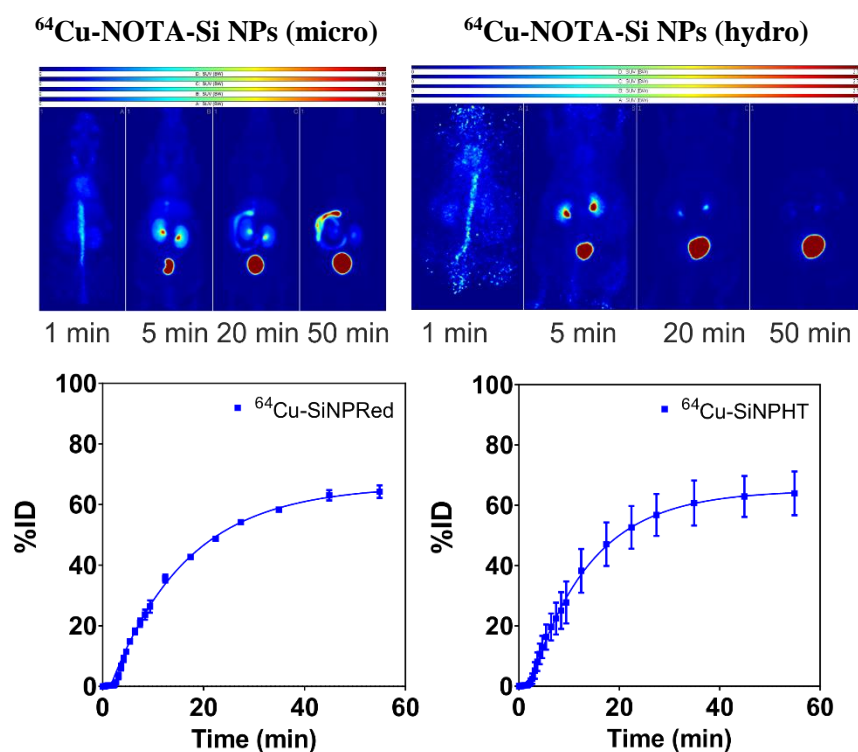


**Figure 3.14.** PET images at different times post-injection of NMRI nu/nu mice injected with [ $^{64}\text{Cu-NOTA-Si NPs}$ ] made by microemulsion (top left) or hydrothermal (top right) method; percentage of injected dose versus time post-injection in the bladder of mice injected with [ $^{64}\text{Cu-NOTA-Si NPs (micro)}$ ], bottom left, or with [ $^{64}\text{Cu-NOTA-Si NPs (hydro)}$ ], bottom right

ultrasmall Si NPs possess a too small dimension to show EPR effect, so they have to be properly engineered to target cancer cells.

As mentioned before, only one example of *in vivo* PET imaging of ultrasmall Si NPs, namely dextran-coated manganese-doped Si NPs, has been reported so far<sup>[17]</sup> and, in this experiment, it was found that NPs accumulate in the liver. NPs can be eliminated by renal clearance, i.e. through kidneys and bladder, or by hepatobiliary excretion, i.e. through liver and intestine, or by a combination of the two excretion mechanisms. Renal clearance is a highly desirable trait for diagnostic nanoparticles in order to reduce retention in non-targeted tissue, to observe efficient excretion of unbound probes from the body and to minimize nanoparticle toxicity<sup>[31]</sup>. As it has been proposed in literature<sup>[32]</sup>, NPs that can have a future in theranostics should have a hydrodynamic radius  $\leq 5.5$  nm and non-toxic components that, preferably, could be biodegraded into clearable components. All the NPs, studied in this thesis, meet these requirements and our results are very promising since both kinds of Si NPs do not accumulate in the liver. In particular, Si NPs made by the hydrothermal method accumulate only in the bladder, being completely excreted.

To deeply investigate the behaviour of the two types of Si NPs, biodistribution experiments were performed. For these studies, rats were sacrificed at specific times post-injection, organs were weighed and the activity present in the organs was measured.

In Figures 3.15 and 3.16 the biodistribution experiments reported both as percentage of injected dose (% ID) and as standardized uptake value [SUV = (activity/g tissue)/(injected activity/body weight)] are shown.

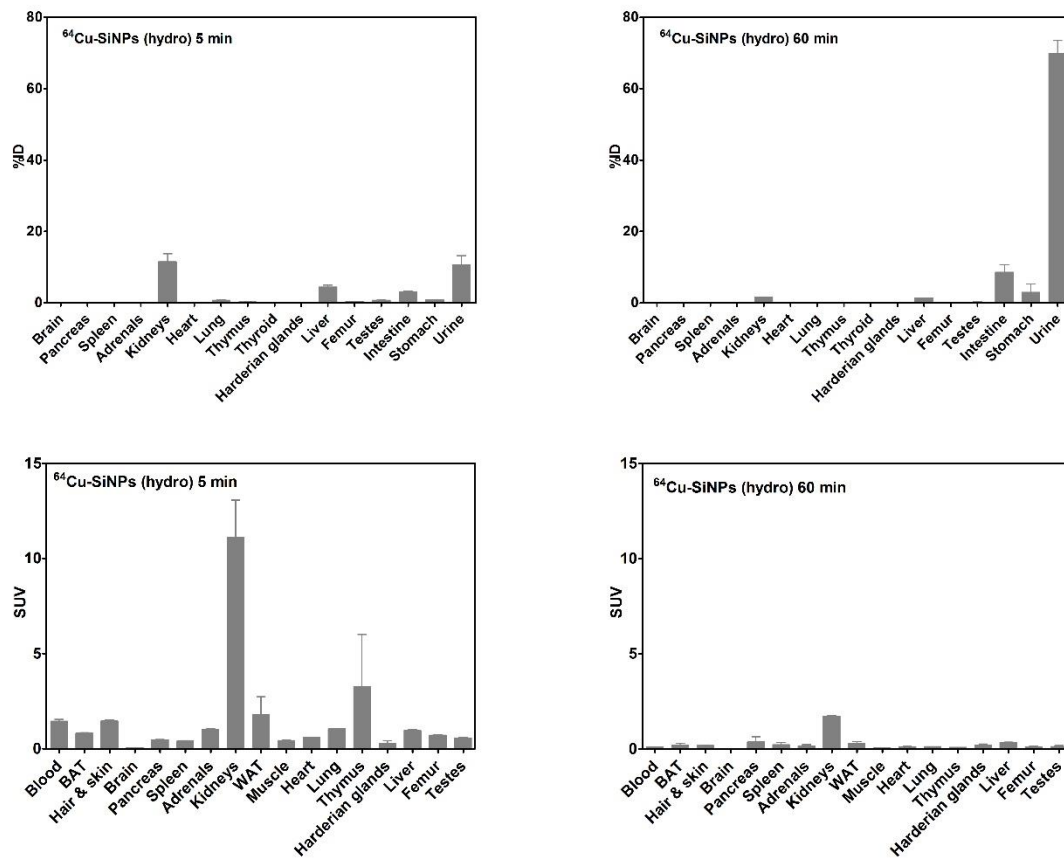


**Figure 3.15.** Biodistribution of [ $^{64}\text{Cu}$ -NOTA-Si NPs (hydro)], expressed as % ID (upper figures) and SUV (bottom figures), at 5 and 60 minutes post-injection in male Wistar rats.

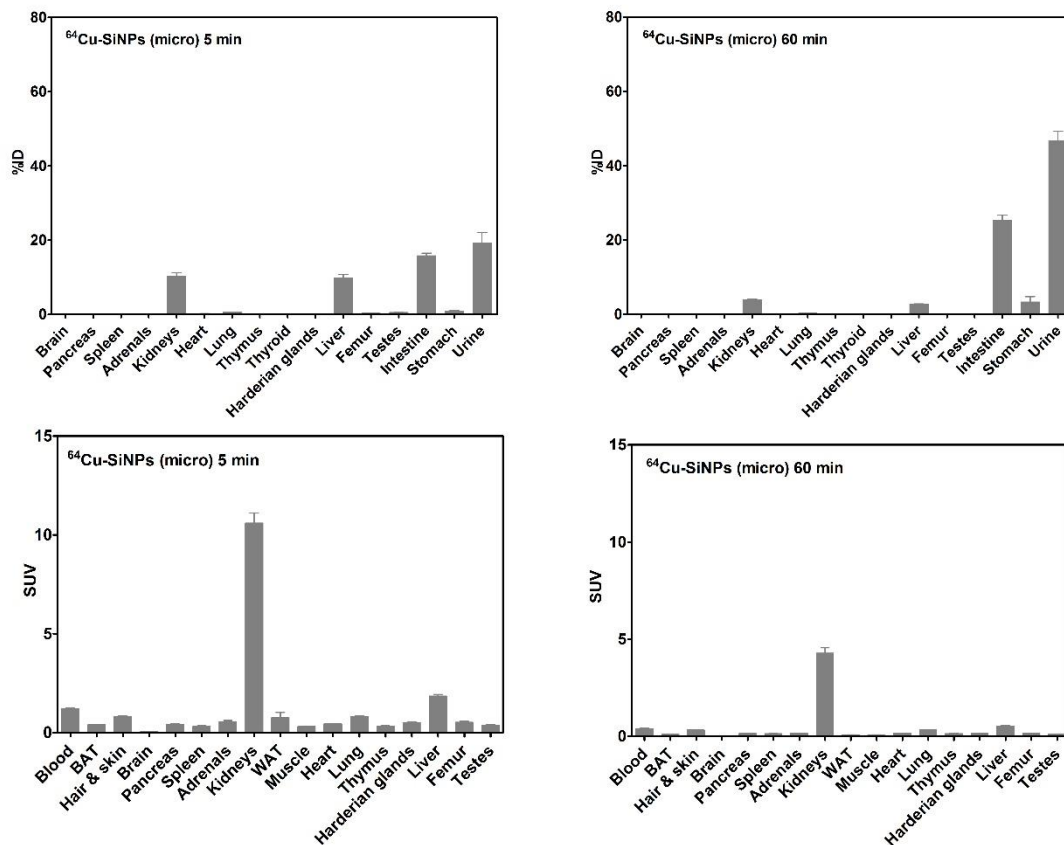


**Figure 3.16.** Biodistribution of [ $^{64}\text{Cu}$ -NOTA-Si NPs (micro)], expressed as % ID (upper figures) and SUV (bottom figures), at 5 and 60 minutes post-injection in male Wistar rats.

From Figures 3.15 and 3.16, it is evident that after 60 minutes, both kinds of Si NPs are mainly excreted through urine, but [ $^{64}\text{Cu}$ -NOTA-Si NPs (micro)] accumulate in some percentage in the intestine as already discussed before in this Chapter. In Figure 3.17, a histogram shows the ratios between renal and hepatobiliary excretion for both kinds of Si NPs used.

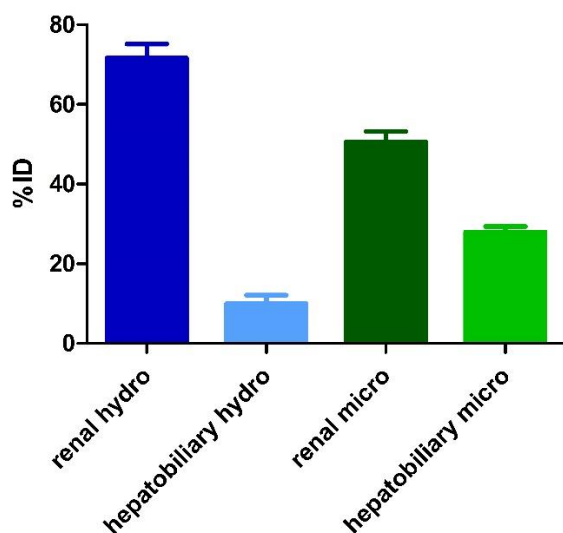


**Figure 3.17.** Histogram showing the ratio between renal and hepatobiliary mechanism of excretion for [ $^{64}\text{Cu}$ -NOTA-Si NPs (hydro)] and [ $^{64}\text{Cu}$ -NOTA-Si NPs (micro)]

[ $^{64}\text{Cu}$ -NOTA-Si NPs (hydro)] follow mainly a renal mechanism of excretion while [ $^{64}\text{Cu}$ -NOTA-Si NPs (micro)] follow both mechanisms (renal and hepatobiliary). In both cases, NPs do not accumulate in other organs and therefore, they represent a very promising platform for future multimodal imaging. In addition, [ $^{64}\text{Cu}$ -NOTA-Si NPs (hydro)] behave in a very ideal way as they accumulate directly in the bladder, which represent the preferred excretion pathway for NPs as mentioned before<sup>[31-32]</sup>.

### 3.4 Conclusions

In this Chapter, Si NPs made by the two different methods discussed in Chapter 2, were tested *in vitro* to assess their cytotoxicity and, subsequently, functionalized with a dye or a radiotracer to study their behavior *in vitro* and *in vivo*. In *in vitro* tests, NPs made by microemulsion method, although not too toxic at low concentrations, show higher cytotoxicity than hydrothermal-prepared ones that, in contrast, show very high cell viability even at concentration as high as 1 mg/mL confirming the high biocompatibility of this system. Cy5-Si NPs were characterized and it was found that they show both the emission properties of Si NPs and of the dye. In addition, their surface is still

available for further couplings showing the presence of free amine-groups on the surface after the functionalization with the dye. Cy5-Si NPs showed a very low cytotoxicity and, from flow cytometry measurements, it resulted that NPs are, most probably, uptaken by cells through an endocytosis mechanism. Confocal microscopy seems to confirm this mechanism of uptake since NPs are co-localized with lysosomes. *In vivo* optical imaging experiments showed that Cy5-NPs are excreted very fast, being already in the bladder at 50 minutes post-injection, but some accumulation in the intestine was also observed. Finally, both kinds of amine-terminated Si NPs were coupled to a  $^{64}\text{Cu}$  complex and their behavior in *in vivo* PET imaging was compared. Both kinds of NPs are mostly excreted through renal clearance, but NPs made by microemulsion method, follow also the hepatobiliary mechanism of excretion showing some accumulation in the intestine. Hydrothermal prepared-Si NPs behave in an ideal way as they are entirely excreted through the bladder already at 50 minutes post-injection. The slightly different behaviour, both *in vitro* and *in vivo*, of the two kinds of NPs could be ascribed to the slightly different composition and properties of the NPs, as explained in Chapter 2. The results achieved are promising for the future application of these NPs in multimodal imaging.

## **3.5 Experimental section**

### **3.5.1 Coupling of Si NPs with cyanine 5**

#### ***Materials***

Cyanine 5 NHS ester and its water soluble analogue, sulfo-Cyanine 5 NHS ester were purchased from Lumiprobe.

#### ***Synthetic procedure***

Cy5- and sulfo-Cy5-modified Si NPs (Cy5-Si NPs and s-Cy5-Si NPs) were prepared simply mixing the particles with the desired NHS ester of the dye. In a typical experiment, 100 mg of amine-terminated Si NPs (either prepared by microemulsion or

by hydrothermal method) were dispersed in 4.0 mL of absolute ethanol. Then 0.4 to 0.6 mg of Cy5- or s-Cy5-NHS ester is added. The final solution is shaken for 12 hours in the dark. After reaction is completed, the sample was purified by dialysis against water (MWCO: 1 KDa; Spectra/Por® 7 dialysis tubing) for several days until the external water does not contain free dye.

### **3.5.2 *In vitro* experiments**

#### ***Cell culture***

Tissue culture reagents were purchased from GIBCO Invitrogen Corporation/Life technologies Life Sciences unless otherwise specified. The adherent human tumour cell lines A549 (ATCC-CCL-185) were maintained as monolayer cultures in MEM supplemented with 10% Fetal Bovine Serum (FBS) at 37 °C and 5% CO<sub>2</sub>. All cell lines were confirmed to be mycoplasma negative using the LookOut mycoplasma PCR detection kit (Sigma-Aldrich) and were tested monthly.

#### ***MTS assays***

Cellular viability was determined by the MTS assay, which measures the reduction of 3-(4,5-dimethylthiazol-2-yl)-5-(3-carboxymethoxyphenyl)-2-(4-sulfophenyl)-2H-tetrazolium (MTS) to formazan by mitochondria in viable cells. 10 000 cells were seeded in each well of a 96-well plate (Greiner) and incubated for 24 hours before exposing to nanoparticles. The medium was replaced by nanoparticle dispersions, freshly prepared by diluting the nanoparticle stock in serum-free MEM, or medium supplemented with different concentration of FBS. The nanomaterials to be tested were added to the wells at the following doses: 15.62 µg/ml, 31.35 µg/ml, 62.5 µg/ml, 125 µg/ml, 250 µg/ml and 500 µg/ml. After the incubation period (24 hours) the cell culture media was removed from each well. The CellTiter 96 AQueous One Solution Reagent (Promega) was added to each well of the 96 well plate. The plate was incubated with the MTS reagent for 60 minutes at 37 °C in a humidified, 5% CO<sub>2</sub> atmosphere. Formazan absorbance was measured at 490 nm using a microtiter plate reader (Varioskan Flash, Thermo Scientific, MA, USA). Recorded data were processed as follows: the average background level was subtracted from each well. The resulting absorbance from each dosing well was normalized to the absorbance value of untreated cells. Additional control experiments, namely the MTS reagent mixed with

nanoparticles only, were performed to assess potential interference of the nanoparticles, and did not reveal any interference of the NPs used with the MTS assay.

### ***Flow cytometry***

A total of 100 000 cells were seeded in 24 well plates (Greiner), and incubated for 24 h before exposing to nanoparticles. The medium was then replaced by the nanoparticle dispersions, freshly prepared by diluting the nanoparticle stock to a concentration of 250 µg/mL in serum-free MEM, or medium supplemented with different concentration of FBS, for 7 hours. For flow cytometry, cells were washed once with MEM supplement with 10% FBS and twice with PBS and harvested with trypsin. Cell pellets were then fixed at room temperature with 4 % formalin (Sigma-Aldrich) for 20 min, and resuspended in PBS before cell-associated fluorescence (15 000 cells per sample) was measured using an Accuri C6 reader (BD Accuri Cytometers). The results are reported as the median of the distribution of cell fluorescence intensity, averaged over three independent replicates.

### ***Confocal microscopy***

For confocal microscopy, 100000 cells were seeded onto 35 mm plates with 15 mm diameter glass coverslips and grown for 24 h prior to exposure to nanoparticles. Cell were exposed to nanoparticles at a concentration of 250 µg/ mL for 7 hr. For organelle and protein staining, samples were then washed three times with 1mL PBS, fixed for 20 min with 1mL of 4 % formalin at room temperature. The cell-membrane was permeabilised using 1 mL of 0.1 % saponin (Sigma Aldrich) solution for 5 min at room temperature and cell were then incubated for 30 min at room temperature with a blocking solution of 1 % bovine serum albumin fraction V (Sigma Aldrich) in PBS–Tween to prevent antibody non-specific binding. Samples were then incubated for 1 h at room temperature with a primary antibody 1 : 200 rabbit polyclonal to LAMP-1 (Abcam) and with a primary antibody 1 : 200 mouse monoclonal antibody to EGFR (Abcam, to aid visualization of the cell under the microscope), washed three times with 1 mL PBS, and then incubated at room temperature for 1 h with 1 : 400 dilution of Alexa Fluor® 488 goat anti-rabbit IgG and with 1 : 400 dilution of Alexa Fluor® 647 goat anti-mouse IgG as secondary antibodies (Molecular Probes, Life Technologies). Samples were washed three times with 1 mL PBS and incubated for 5 min with DAPI (Sigma Aldrich) before mounting with MOWIOL (Polysciences Inc.) on slides for

imaging. The cells were observed using a Carl Zeiss LSM 510 Meta laser scanning confocal microscope with lasers at 364 nm and long pass filter LP 385 nm (DAPI), 488 nm and band pass filter 505–530 nm (LAMP-1 antibody), 543 nm and band pass filter 558–612 nm (EGFR antibody) and 633 nm and band pass filter 644–719 nm (nanoparticles).

### 3.5.3 Coupling of Si NPs with NOTA ligand

#### *Materials*

S-2-(4-Isothiocyanatobenzyl)-1,4,7-triazacyclononane-1,4,7-triacetic acid (SCN-Bn-NOTA; #B-605) was purchased from Macrocyclics.

#### *Synthetic procedure*

[NOTA-Si NPs (micro)] and [NOTA-Si NPs (hydro)] were prepared dispersing 1 mg of amine-terminated Si NPs (either prepared by microemulsion or by hydrothermal method) in 150  $\mu$ L of deionized water and placed in a 1.5 mL low protein binding Eppendorf-tube. A specific amount of SCN-Bn-NOTA (0.1 or 0.8  $\mu$ mol/mg - according to the used amount of nanoparticles) was dissolved in 100  $\mu$ L of deionized water and, then, added to the NPs dispersion. The final dispersion was then shaken on a thermo-mixer (Eppendorf) at 750 rpm for 16 h at 25 °C. All samples, which were used for *in vivo* experiments, have been purified by dialysis against deionized water (MWCO 500 – 1000 Da, Spectra Por Float-A-Lyzer G2, 1 mL). Afterwards a defined aliquot was freeze-dried to obtain the final concentration of particles.

### 3.5.4 Radiolabeling of [NOTA-Si NPs (micro)] and [NOTA-Si NPs (hydro)]

The production of  $^{64}\text{Cu}$  was performed at Cyclone® 18/9 (Helmholtz-Zentrum Dresden-Rossendorf) in a  $^{64}\text{Ni}(p,n)^{64}\text{Cu}$  nuclear reaction with specific activities of 150–250 GBq  $\mu\text{mol}^{-1}$  Cu diluted in HCl (10 mM).<sup>[33]</sup> An aliquot of [ $^{64}\text{Cu}$ ]CuCl<sub>2</sub> solution (20–100 MBq) was buffered with MES (2-(N-morpholino)ethanesulfonic acid)/NaOH-buffer (0.1 M; pH 6). Typically, a specific amount of nanoparticles, up to 10  $\mu\text{g}$ , was mixed in a 1.5 mL low protein binding Eppendorf-tube with a specific aliquot of

[<sup>64</sup>Cu]Cu(II)-solution (varying up to 40 MBq) and addition of MES/NaOH buffer (0.1 M; pH 6) up to a final volume in the range of 150-200 µL. The particles have been labelled by means of mechanical shaking for 30 min at 25 °C. To check the full labeling, a 5.0 µL aliquot of the reaction was combined with 2.0 nmol EDTA (pH 7.0) and the labeling process of the nanoparticles ( $R_f = 0$ ) was monitored by radio-TLC using ITLC-SA plates (Merck Millipore) in combination with a mobile phase of 0.9% NaCl in dH<sub>2</sub>O. As control, separate radio-TLC analysis of [<sup>64</sup>Cu]Cu-EDTA ( $R_f = 0.9$ ) was performed in the same mobile phase. Evaluation of radio-TLC was carried out using a radioactivity thin layer analyser (Rita Star, Raytest).

### 3.5.5 Animal experiments

All animal experiments were carried out according to the German regulations on animal welfare (approved by Landesdirektion Dresden, 24-9168.21-4/2004-1). Male Wistar rats (aged 7-9 weeks; Harlan Winkelmann GmbH, Borchon, Germany) and female NMRI nu/nu mice (aged 7-14 weeks; Technische Universität Dresden, Oncoray, Germany) were housed under standard conditions with free access to standard food and tap water. For PET experiments in tumour-bearing mice, about  $2 \times 10^6$  A431 cells were injected subcutaneously in the back or right hind leg of NMRI nu/nu mice according to the protocol published elsewhere.

### 3.5.6 Biodistribution

Two groups of four rats (5 and 60 min) were intravenously injected into a lateral tail vein with 0.5–5.0 MBq of <sup>64</sup>Cu-labeled nanoparticles, which were dissolved in 0.5 mL of electrolyte solution E-153 (Serumwerk Bernburg, Germany) at pH 7.2. The specific activity ranged from 5.0 to 30 GBq/µmol at the time of injection. Animals were sacrificed at 5 and 60 min post injection. Blood and the major organs were collected, weighed, and counted in a Wallac WIZARD automatic  $\gamma$ -counter (PerkinElmer, Germany). The activity of the tissue samples was decay-corrected and calibrated by comparing the counts in tissue with the counts in aliquots of the injected tracer that had been measured in the  $\gamma$ -counter at the same time. The activity amount in the selected tissues and organs was expressed as percent of injected dose (% ID). The activity concentration in the biodistribution measurements were calculated as SUV [SUV =

(activity/g tissue)/(injected activity/body weight)] and expressed as means  $\pm$  standard deviation (mean  $\pm$  SD) for each group of four animals.

### **3.5.7 *In vivo* small animal positron emission tomography (PET)**

Rats or mice were anesthetized (Desfluran in oxygen/air (30 %)), positioned and immobilized prone with their medial axis parallel to the axial axis of the scanners (NanoScan PET/CT, Mediso, microPET® P4, Siemens preclinical solutions). The radiotracer was administered intravenously as an infusion using a syringe pump over one minute (Harvard Apparatus, flow rate: injection volume as mL/min) through a needle catheter into a lateral tail vein. The standardized uptake values (SUV) were calculated from the ROI as the ratio of activity concentration (Bq/mL) at time  $t$  and injected dose (Bq) at the time of injection ( $t_0$ ) divided by body weight (g). For the demonstration of the increasing activity uptake, the early (midframe time 3 min post injection) images were subtracted from the late image (midframe time 50 min post injection).

### **3.5.8 Characterization**

#### ***HR-TEM***

Samples for HR-TEM were prepared drop-casting an ethanolic solution of the sample on carbon coated copper grids (Quantifoil, GmbH). The analysis were performed using a FEI Titan 80-300 transmission electron microscope operated at 300 KV.

#### ***XPS***

For XPS measurements, a dispersion of Si NPs in ethanol or water is deposited on aluminium support and allowed to dry overnight in a low-vacuum chamber before the introduction in the ultra-high vacuum chamber of the XPS system. Other experimental details as in Chapter 2.

### ***Photophysical measurements***

Absorption spectra were acquired using a double-beam Shimadzu UV-3600 UV-Vis-NIR spectrophotometer.

Steady-state emission spectra were recorded on a HORIBA Jobin-Yvon IBH FL-322 Fluorolog 3 spectrometer equipped with a 450 W xenon arc lamp, as the excitation source, and a TBX-4-X single-photon-counting device as the detector. Emission and excitation spectra were corrected for source intensity (lamp and grating) and emission spectral response (detector and grating) by standard correction curves.

Time-resolved measurements were performed on FluoTime 300 “Easy Tau” spectrometer (PicoQuant) equipped with subnanoseconds LDH sources powered by a PicoQuant PDL 820 variable (0.2-80 MHz) pulsed power supply. Measurements were performed using a PicoHarp TCSPC (Time-Correlated Single Photon Countings) module. The decays were fitted by means of PicoQuant FluoFit Global Fluorescence Analysis Software (PicoQuant GmbH, Germany).

PLQY were measured on a Hamamatsu Quantaaurus-QY integrating sphere equipped with a 150 W CW Xenon source.

## **3.6 References:**

- [1] Z. F. Li, E. Ruckenstein, *Nano Letters* **2004**, *4*, 1463-1467.
- [2] J. H. Warner, A. Hoshino, K. Yamamoto, R. D. Tilley, *Angewandte Chemie International Edition* **2005**, *44*, 4550-4554.
- [3] M. Rosso-Vasic, E. Spruijt, Z. Popovic, K. Overgaag, B. van Lagen, B. Grandidier, D. Vanmaekelbergh, D. Dominguez-Gutierrez, L. De Cola, H. Zuilhof, *Journal of Materials Chemistry* **2009**, *19*, 5926-5933.
- [4] L. Ruizendaal, S. Bhattacharjee, K. Pournazari, M. Rosso-Vasic, L. H. J. de Haan, G. M. Alink, A. T. M. Marcelis, H. Zuilhof, *Nanotoxicology* **2009**, *3*, 339-347.
- [5] S. Bhattacharjee, L. de Haan, N. Evers, X. Jiang, A. Marcelis, H. Zuilhof, I. Rietjens, G. Alink, *Particle and Fibre Toxicology* **2010**, *7*, 25.

- [6] S. Bhattacharjee, I. M. Rietjens, M. P. Singh, T. M. Atkins, T. K. Purkait, Z. Xu, S. Regli, A. Shukaliak, R. J. Clark, B. S. Mitchell, G. M. Alink, A. T. Marcelis, M. J. Fink, J. G. Veinot, S. M. Kauzlarich, H. Zuilhof, *Nanoscale* **2013**, *5*, 4870-4883.
- [7] F. Erogbogbo, K.-T. Yong, I. Roy, G. Xu, P. N. Prasad, M. T. Swihart, *ACS Nano* **2008**, *2*, 873-878.
- [8] E. J. Henderson, A. J. Shuhendler, P. Prasad, V. Baumann, F. Maier-Flaig, D. O. Faulkner, U. Lemmer, X. Y. Wu, G. A. Ozin, *Small* **2011**, *7*, 2507-2516.
- [9] Y. Zhong, F. Peng, F. Bao, S. Wang, X. Ji, L. Yang, Y. Su, S.-T. Lee, Y. He, *Journal of the American Chemical Society* **2013**, *135*, 8350-8356.
- [10] Y. Zhong, X. Sun, S. Wang, F. Peng, F. Bao, Y. Su, Y. Li, S.-T. Lee, Y. He, *ACS Nano* **2015**, *9*, 5958-5967.
- [11] P. Shen, S. Ohta, S. Inasawa, Y. Yamaguchi, *Chemical Communications* **2011**, *47*, 8409-8411.
- [12] S. Ohta, P. Shen, S. Inasawa, Y. Yamaguchi, *Journal of Materials Chemistry* **2012**, *22*, 10631-10638.
- [13] S. Klein, M. L. Dell'Arciprete, M. Wegmann, L. V. R. Distel, W. Neuhuber, M. C. Gonzalez, C. Krysch, *Biochemical and Biophysical Research Communications* **2013**, *434*, 217-222.
- [14] F. Erogbogbo, M. T. Swihart, *AIP Conference Proceedings* **2010**, *1275*, 35-39.
- [15] J. H. Ahire, M. Behray, C. A. Webster, Q. Wang, V. Sherwood, N. Saengkrit, U. Ruktanonchai, N. Woramongkolchai, Y. Chao, *Advanced Healthcare Materials* **2015**, n/a-n/a.
- [16] M. P. Singh, T. M. Atkins, E. Muthuswamy, S. Kamali, C. Tu, A. Y. Louie, S. M. Kauzlarich, *ACS Nano* **2012**, *6*, 5596-5604.
- [17] C. Tu, X. Ma, A. House, S. M. Kauzlarich, A. Y. Louie, *ACS Medicinal Chemistry Letters* **2011**, *2*, 285-288.
- [18] C. Tu, X. Ma, P. Pantazis, S. M. Kauzlarich, A. Y. Louie, *Journal of the American Chemical Society* **2010**, *132*, 2016-2023.
- [19] F. Erogbogbo, K.-T. Yong, R. Hu, W.-C. Law, H. Ding, C.-W. Chang, P. N. Prasad, M. T. Swihart, *ACS Nano* **2010**, *4*, 5131-5138.
- [20] F. Erogbogbo, K.-T. Yong, I. Roy, R. Hu, W.-C. Law, W. Zhao, H. Ding, F. Wu, R. Kumar, M. T. Swihart, P. N. Prasad, *ACS Nano* **2011**, *5*, 413-423.
- [21] T. M. Atkins, M. P. Singh, A. Louie, S. M. Kauzlarich, American Chemical Society, **2011**, pp. INOR-513.
- [22] J. A. Kim, A. Salvati, C. Aberg, K. A. Dawson, *Nanoscale* **2014**, *6*, 14180-14184.
- [23] M. G. Bexiga, J. A. Varela, F. Wang, F. Fenaroli, A. Salvati, I. Lynch, J. C. Simpson, K. A. Dawson, *Nanotoxicology* **2011**, *5*, 557-567.
- [24] P. Ruenraroengsak, P. Novak, D. Berhanu, A. J. Thorley, E. Valsami-Jones, J. Gorelik, Y. E. Korchev, T. D. Tetley, *Nanotoxicology* **2012**, *6*, 94-108.
- [25] T. Xia, M. Kovoichich, M. Liong, J. I. Zink, A. E. Nel, *ACS Nano* **2008**, *2*, 85-96.
- [26] F. Wang, L. Yu, M. P. Monopoli, P. Sandin, E. Mahon, A. Salvati, K. A. Dawson, *Nanomedicine: Nanotechnology, Biology and Medicine* **2013**, *9*, 1159-1168.
- [27] F. Wang, M. G. Bexiga, S. Anguissola, P. Boya, J. C. Simpson, A. Salvati, K. A. Dawson, *Nanoscale* **2013**, *5*, 10868-10876.
- [28] Y. Matsumura, H. Maeda, *Cancer Research* **1986**, *46*, 6387-6392.
- [29] H. Maeda, *Journal of Controlled Release* **2012**, *164*, 138-144.

- [30] F. Yamashita, M. Hashida, *Advanced Drug Delivery Reviews* **2013**, *65*, 139-147.
- [31] X.-D. Zhang, J. Yang, S.-S. Song, W. Long, J. Chen, X. Shen, H. Wang, Y.-M. Sun, P.-X. Liu, S. Fan, *International Journal of Nanomedicine* **2014**, *9*, 2069-2072.
- [32] H. Soo Choi, W. Liu, P. Misra, E. Tanaka, J. P. Zimmer, B. Itty Ipe, M. G. Bawendi, J. V. Frangioni, *Nat Biotech* **2007**, *25*, 1165-1170.
- [33] S. Thieme, M. Walther, H. J. Pietzsch, J. Henniger, S. Preusche, P. Mäding, J. Steinbach, *Applied Radiation and Isotopes* **2012**, *70*, 602-608.



# Chapter 4

## Functionalization of carbon dots for bioimaging

### Abstract

This Chapter is dedicated mainly to the functionalization of carbon dots with a dye or a radiotracer and to the *in vivo* experiments in order to make a comparison with the behaviour of silicon nanoparticles. The ultrasmall carbon dots (3 nm size), displaying multi-coloured emission, were surface-modified with the same dye or  $^{64}\text{Cu}$  complex used for Si NPs and their behaviour in *in vivo* PET imaging experiments was studied and compared with that of the ultrasmall Si NPs.

### 4.1 Introduction

Thanks to their biocompatibility, bright multi-coloured emission and stability against photobleaching, carbon quantum dots (CQDs) are promising materials for bioimaging<sup>[1-2]</sup>. CQDs can be prepared through facile one-step synthesis. However, it is more difficult to control their size, their shape and their surface chemistry. The structure of CQDs is still object of research but, in contrast to Si NPs, their shape cannot be approximated to a spherical particle. As discussed in Chapter 1, CQDs have been already widely used in bioimaging although they were discovered only ten years ago<sup>[3]</sup>. In this thesis, we want to compare CQDs to Si NPs as materials for bioimaging. Indeed, silicon and carbon possess many similar properties and it is very interesting to compare the *in vivo* behavior of ultrasmall NPs made by these two elements. In this part of the

thesis, we studied the photoluminescence properties of CQDs and we coupled them with the dye cyanine 5 in order to make a comparison with Cy5-modified Si NPs. Furthermore, CQDs have been tested in *in vivo* PET imaging and the results compared to those obtained in analogous tests done with Si NPs.

## 4.2 Preparation and characterization of CQDs

CQDs were prepared according to a reported procedure<sup>[4]</sup> by microwave treatment of an aqueous solution of L-arginine hydrochloride (2M) and ethylenediamine (2M). Starting materials were processed in a common kitchen microwave oven operated at a nominal power of 700 W for 3 minutes. The reaction took place at ambient pressure and temperature was not monitored. Figure 4.1 shows the scheme of the synthetic route followed for the production of carbon dots.

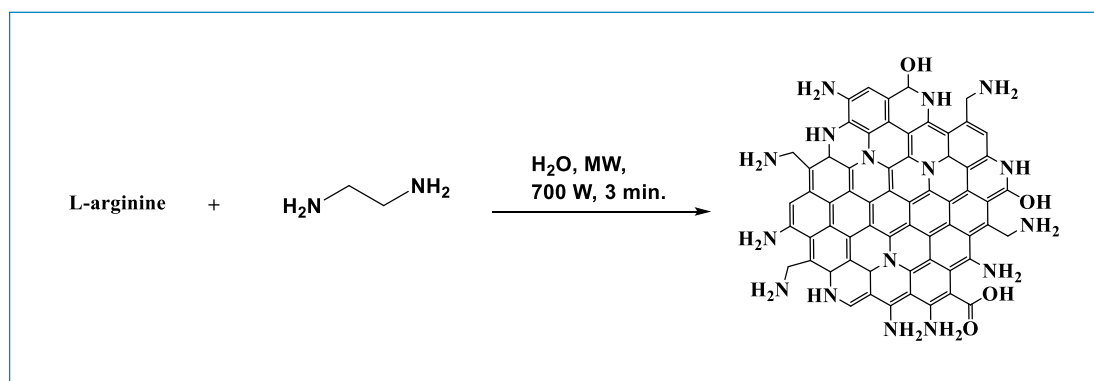


**Figure 4.1.** Synthetic route followed for the preparation of CQDs.

When the reaction was completed, CQDs were purified by dialysis. Figure 4.2b reports a typical HR-TEM image, showing the presence of NPs with an average size of  $3.07 \pm 0.6$  nm (Figure 4.2a). As shown in the high magnification micrograph of a single particle (inset of Figure 4.2b), these CQDs are crystalline with an interplanar distance of  $2.1 \text{ \AA}$ , consistent with the reported spacing in graphene<sup>[5]</sup> and (0001) graphite basal plane<sup>[4]</sup>.

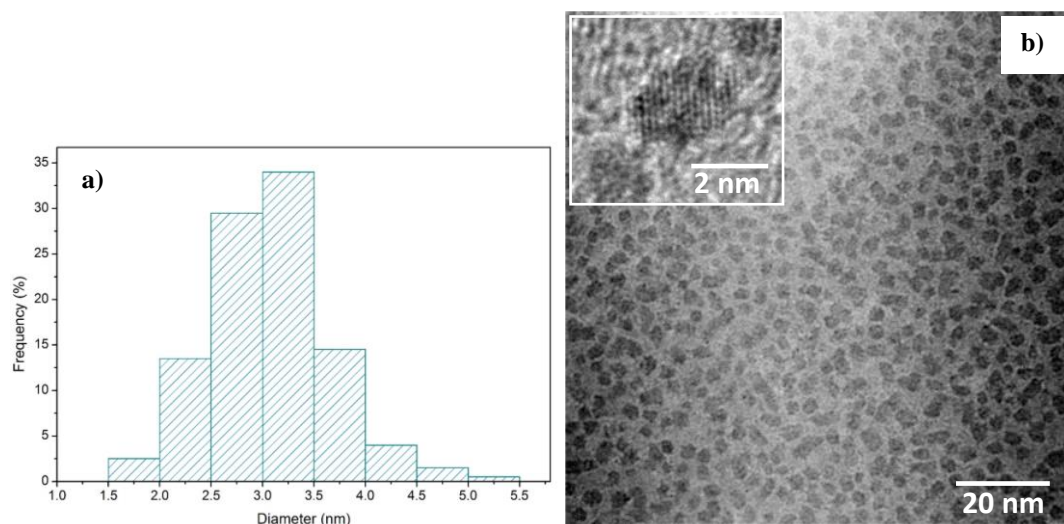


**Figure 4.2.** a) Size distribution histogram of CQDs (average size  $3.07 \pm 0.6$  nm); b) HR-TEM image of carbon dots; the inset shows a high magnification image of a single particle.

We studied the photoluminescence properties of these CQDs. In Figure 4.3a, we report the UV-vis absorption spectrum of the CQDs and in Figure 4.3b, the emission spectra obtained at different excitation wavelengths. All the spectra were acquired in ethanol. Both, in absorption and emission, CQDs show the typical features reported in literature data<sup>[1, 4, 6-8]</sup>.

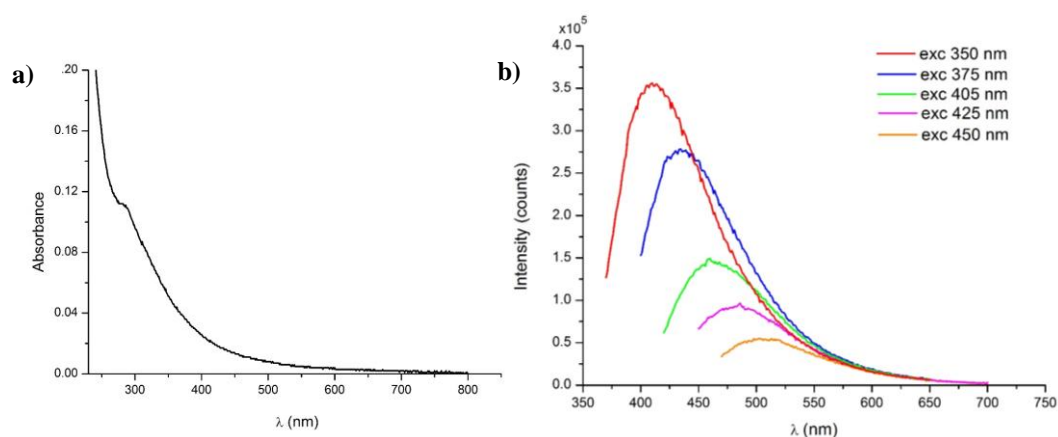


**Figure 4.3.** a) Absorption spectrum and b) emission spectra (at different excitation wavelengths reported on the top right) of CQDs in ethanol

The UV-vis spectrum in Figure 4.3a shows a broad absorption band in the range of 250 - 550 nm, with a typical quantum feature at approximately 300 nm, typical of aromatic structures.<sup>[4]</sup> The position of the emission maximum

(Figure 4.3b) shifts toward higher wavelengths when using excitation radiation of increasing wavelength. Simultaneous to the red shift, we observed a decrease of the emission intensity. More in detail, the emission maximum red-shifts from 411 to 510 nm, a total of 100 nm, when changing the excitation wavelength from 350 nm to 450 nm. By exciting at 500 nm, CQDs still show a weak emission centered at 550 nm. PLQY for CQDs in ethanol is of 7-8 % at all the excitation wavelengths. Lifetimes can be fitted with a multi-exponential decay as reported for similar NPs<sup>[9]</sup> and, in particular, with a bi-exponential decay, the two components being  $\tau_1 = 2.5$  ns (81 %) and  $\tau_2 = 7.8$  ns (19 %) ( $\lambda_{exc}$ : 375 nm;  $\lambda_{em}$ : 440 nm).

As already mentioned, there has been a strong debate in the literature whether the luminescence in CQDs comes from size or surface chemistry effects. There are reports showing that also CQDs with excitation-independent emission can be prepared<sup>[10-11]</sup>. However, it is well established<sup>[9, 12]</sup> that the presence of different emissive sites on the surface of each particle largely influences the photoluminescence properties. As extensively discussed in Chapter 1, CQDs can be considered as quasi-spherical particles or as flat nanosized graphene structures. In both cases, the surface of the material presents multifunctional surface sites that are most probably responsible for the shift in the emission wavelength when varying the excitation wavelength. In particular, the synthetic method used is known to lead to a surface rich of amino, carboxylic and hydroxyl groups, which contribute in different ways to the luminescence of the CQDs.

### 4.3 Surface modification of CQDs with cyanine 5 dye

In order to make a comparison with Si NPs, CQDs were coupled to cyanine 5 dye (Cy5-CQDs). The reaction is very similar to the one reported in Chapter 3 for Si NPs. A scheme for the synthetic route is shown in Figure 4.4.

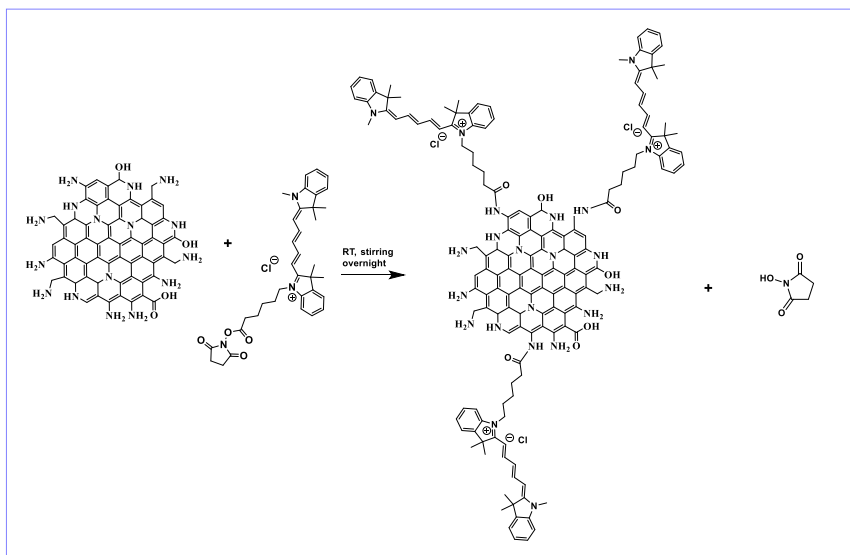


**Figure 4.4.** Synthetic route for the preparation of Cy5-CQDs

After the reaction is completed, Cy5-CQDs were purified by dialysis against water. In Figure 4.5, the absorption spectra of the free Cy 5 dye, free CQDs and Cy5-CQDs are compared. The spectrum of Cy5-CQDs presents the general absorption trend of CQDs at lower wavelengths, including the typical shoulder at 300 nm. At higher wavelengths the spectrum is dominated by the absorption bands (600 and 645 nm) typical of the dye.

In Figure 4.6, the emission spectra in ethanol of the free Cy5 dye, free CQDs and Cy5-CQDs are compared. The excitation wavelength is 350 nm, falling in a region where the most part of the absorption can be ascribed to the quantum dots rather than to the dye. Interestingly, the spectrum of the Cy5-CQDs shows both, the emission of the CQDs and of the Cy5.

More in detail, the emission peak relative to the CQDs in the Cy5-CQDs sample is red-shifted compared to the naked CQDs. The emission maximum in

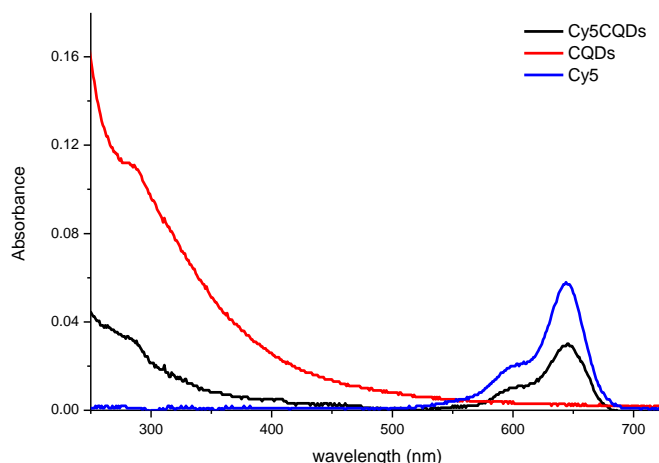


**Figure 4.5.** Absorption spectra in ethanol of free Cy5 (blue line), free CQDs (red line), Cy5-CQDs (black line)

the naked CQDs sample is centered at 410 nm (when exciting at 350 nm) while in the Cy5-CQDs the maximum is centered at 428 nm. The peak relative to Cy5 does not show any significant shift when comparing the Cy5-CQDs sample to the free dye. A similar behavior was observed also in the case of the coupling

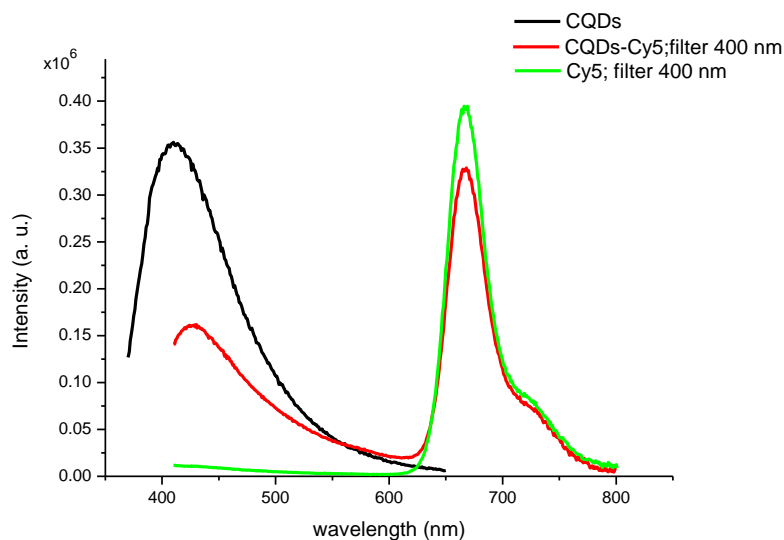


**Figure 4.6.** Emission spectra ( $\lambda_{exc}$ : 350 nm) in ethanol of naked CQDs (black line), Cy5-CQDs (red line) and free Cy5 (green line)

of the same cyanine 5 dye with Si NPs (see Chapter 3).

The PLQY were measured in ethanol. Regarding the emission window of the dye, we observe a small increase of the PLQY of the Cy5-CQDs (23 %) with

respect to the free dye (16 %) when exciting at 630 nm. The PLQY in the emission window of CQDs is instead decreasing from a value of 7 % in the naked CQDs to a value close to 1 % in the sample of Cy5-CQDs when exciting at 350 nm. This trend is different from what observed in Cy5-coupled Si NPs in which PLQY increases both, in the dye and in Si NPs emission windows. The reason for the different behavior in comparison with Si NPs is unclear. However, both systems display different properties and mechanisms responsible for photoluminescence and, although many analogies between inorganic and carbon-based NPs are reasonable, they could be oversimplifying<sup>[11]</sup>. The excited state lifetimes in ethanol of the naked CQDs, free dye and Cy5-CQDs are reported in Table 1.

In the emission window of the CQDs, the decay can be fitted with a bi-exponential function for both, the naked CQDs and Cy5-CQDs. The lifetime of the dye measured in its emission window did not change after the coupling with the CQDs. The data regarding the free components at  $\lambda_{em} = 440$  nm (for free Cy5) and at  $\lambda_{em} = 668$  nm (for naked CQDs) are missing in the table because of the very small emission of each component in the emission window characteristic of the other one.

<b>Table 1.</b> Lifetimes of the free Cy5 dye, free CQDs and Cy5-CQDs		
	<b>Lifetime (<math>\lambda_{exc} = 375</math> nm; <math>\lambda_{em} = 668</math> nm)</b>	<b>Lifetime (<math>\lambda_{exc} = 375</math> nm; <math>\lambda_{em} = 440</math> nm)</b>
<b>Cy5</b>	$\tau_1 = 0.9$ ns (100 %)	
<b>CQDs</b>		$\tau_1 = 2.7$ ns (80 %) $\tau_2 = 8.4$ ns (20 %)
<b>Cy5-CQDs</b>	$\tau_1 = 1.0$ ns (100 %)	$\tau_1 = 2.2$ ns (77 %) $\tau_2 = 8.6$ ns (23 %)

Since the emission of free CQDs is red-shifting when using increasing excitation wavelengths, it is interesting to explore the emission of the Cy5-CQDs sample at different excitation wavelengths.

The emission spectra in ethanol of Cy5-CQDs at different excitation wavelengths are reported in Figure 4.7. We observed that when increasing the excitation wavelength, the peak of CQDs is red-shifting (similarly to what happens for free CQDs), while the peak of the dye is not appreciably shifting.

We noted that the characteristic emission peaks of CQDs are always red-shifted in Cy5-CQDs in comparison to the emission peaks of the naked CQDs at the same excitation wavelength. In order to put in evidence this observation, the position of the emission maxima of the naked CQDs are marked with a dashed line in Figure 4.7. The larger red-shift of Cy5-CQDs respect to the naked CQDs indicates that the dye influences the emission characteristics of the CQDs, in line with the already discussed influence of surface effects on the photoluminescence of carbon-based nanoallotropes<sup>[1]</sup>.

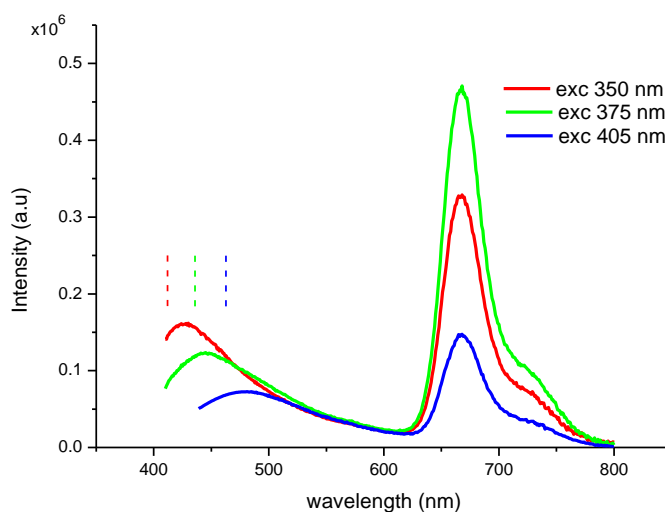


**Figure 4.7.** Emission spectra, in ethanol, of Cy5-CQDs at different excitation wavelengths

## 4.4 *In vivo* positron emission tomography of CQDs

Although CQDs were tested *in vivo* for the first time only in 2009<sup>[2]</sup>, they have been widely used in bioapplications<sup>[1, 8, 13-16]</sup>.

Recently Si NPs and some carbon-based nanomaterials, such as nanodiamonds have been compared for their properties and bioapplications<sup>[17]</sup>. They both show very good stability and very high biocompatibility in comparison to classical semiconductor quantum dots. Therefore, we found very interesting to compare in this thesis the obtained ultrasmall Si NPs and CQDs to see how their behavior *in vivo* differs. PET was performed using <sup>64</sup>Cu-labelled CQDs in the same conditions used for Si NPs and described in Chapter 3. As in the case of Si NPs, CQDs were coupled to the commercially available S-2-(4-isothiocyanatobenzyl)-1,4,7-triazacyclononane-1,4,7-triacetic acid (p-SCN-Bn-NOTA), a common ligand used for radioisotopes in PET<sup>[18]</sup>. Also in this case, the coupling happens between the isothiocyanate moiety of the ligand and the amine groups present on the surface of CQDs to form a thiourea bond in the final NPs (NOTA-CQDs) as shown in Figure 4.8.

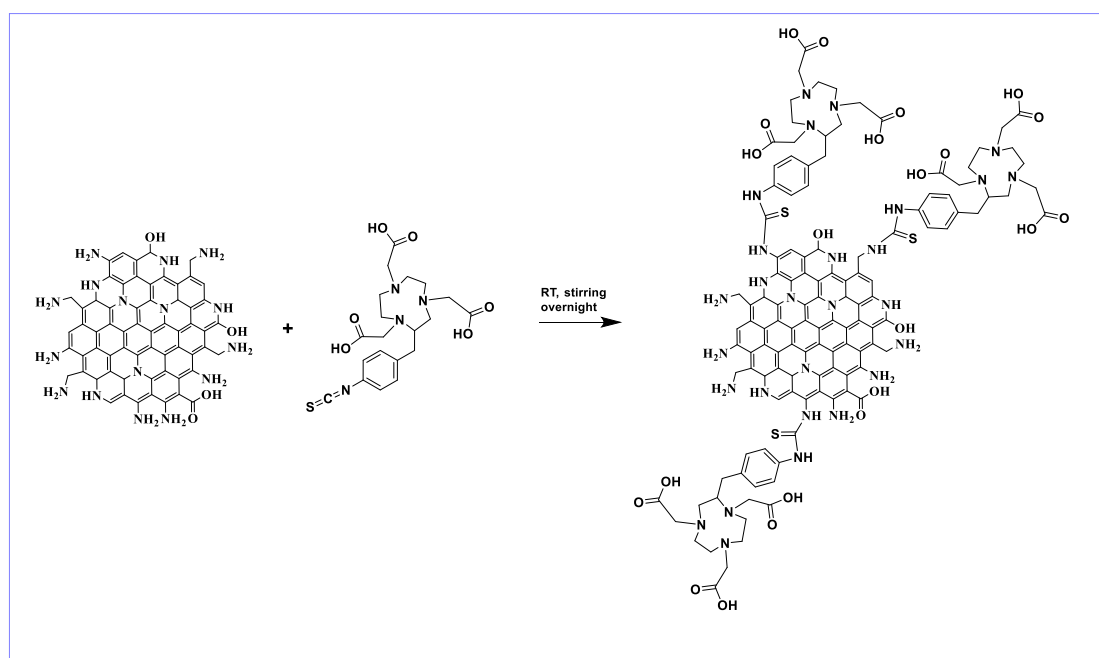


**Figure 4.8.** Reaction scheme for the coupling of CQDs with p-SCN-Bn-NOTA ligand

After the reaction is completed, NOTA-CQDs were purified from unreacted ligand by dialysis against water and afterwards, they were mixed with a [ $^{64}\text{Cu}$ ]CuCl<sub>2</sub> solution to coordinate them with the radionuclide  $^{64}\text{Cu}$  ( $^{64}\text{Cu}$ -NOTA-CQDs). Once purified,  $^{64}\text{Cu}$ -NOTA-CQDs were injected, through the tail vein, in male Wistar rats to do biodistribution studies and in female NMRI nu/nu squamous cell carcinoma (A431) tumour bearing mice to perform *in vivo* PET imaging. In Figure 4.9, PET images obtained for  $^{64}\text{Cu}$ -NOTA-CQDs at different times post-injection are showed. As can be seen, the activity of CQDs is detected mostly in the bladder at 50 minutes post-injection, but a fraction is in the gallbladder and in the intestine. The behaviour observed for CQDs is similar to the one observed for [ $^{64}\text{Cu}$ -NOTA-Si NPs] (made by microemulsion method), but the quantity of material that remains in the body and accumulates in organs is higher than in the case of Si NPs. The curve in Figure 4.9b represents the activity, expressed as percentage of injected dose, present in the bladder versus time post-injection. The curve grows in time showing that the particles are accumulating in the bladder to be subsequently, excreted. On the other hand, CQDs are accumulating more in the organism in respect to Si NPs. The curve presents a value of 40 % ID (percent of the injected dose) in the bladder at 50 minutes post-injection for CQDs, but the analogue curves for Si NPs of both kinds present a value of more than 60 % ID. Therefore, the activity of the CQDs is excreted slower than Si NPs and both are mainly cleared through renal pathway and through hepatobiliary excretion. The chemical identity of the activity excreted through hepatobiliary mechanism was not established. It could be intact CQDs but also free metal complexes deriving from catabolized CQDs. The mice used bear a tumour, in the back or right hind leg, but no accumulation of particles in the tumour site was observed as in the case of Si NPs. This could be explained with the absence of specific targeting agents on the NPs surface and with the too small size to show enhanced permeability and retention effect (EPR effect)<sup>[19-20]</sup>, as shown in Chapter 3. Our hypothesis is that the NPs we are using for this study, both Si NPs and CQDs,

possess a too small dimension to show EPR effect, so they have to be properly engineered to target cancer cells. Nevertheless, the aim in this work is to show that imaging of organs and tissues with such NPs is possible and that NPs are excreted very quickly from the body. In the future design of a multimodal imaging probe, NPs could also be functionalized with targeting agents.

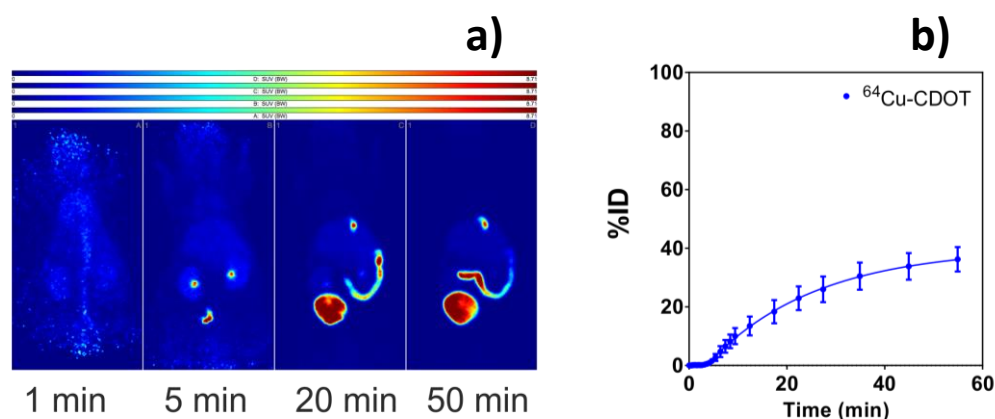


**Figure 4.9.** a) Positron emission tomography images, at different times post-injection, of NMRI nu/nu mice injected with  $^{64}\text{Cu}$ -NOTA-CQDs; b) percentage of injected dose versus time post-injection in the bladder of mice injected with  $^{64}\text{Cu}$ -NOTA-CQDs

To deeply investigate the behaviour of CQDs *in vivo*, biodistribution experiments were performed. For these studies, rats were sacrificed after certain times post injection, organs were weighed and the activity present in the organs measured. In Figure 4.10, the biodistribution experiments, reported both as percentage of injected dose (% ID) and as standardized uptake value ( $\text{SUV} = (\text{activity}/\text{weight of tissue})/(\text{injected activity}/\text{body weight})$ ) are shown.

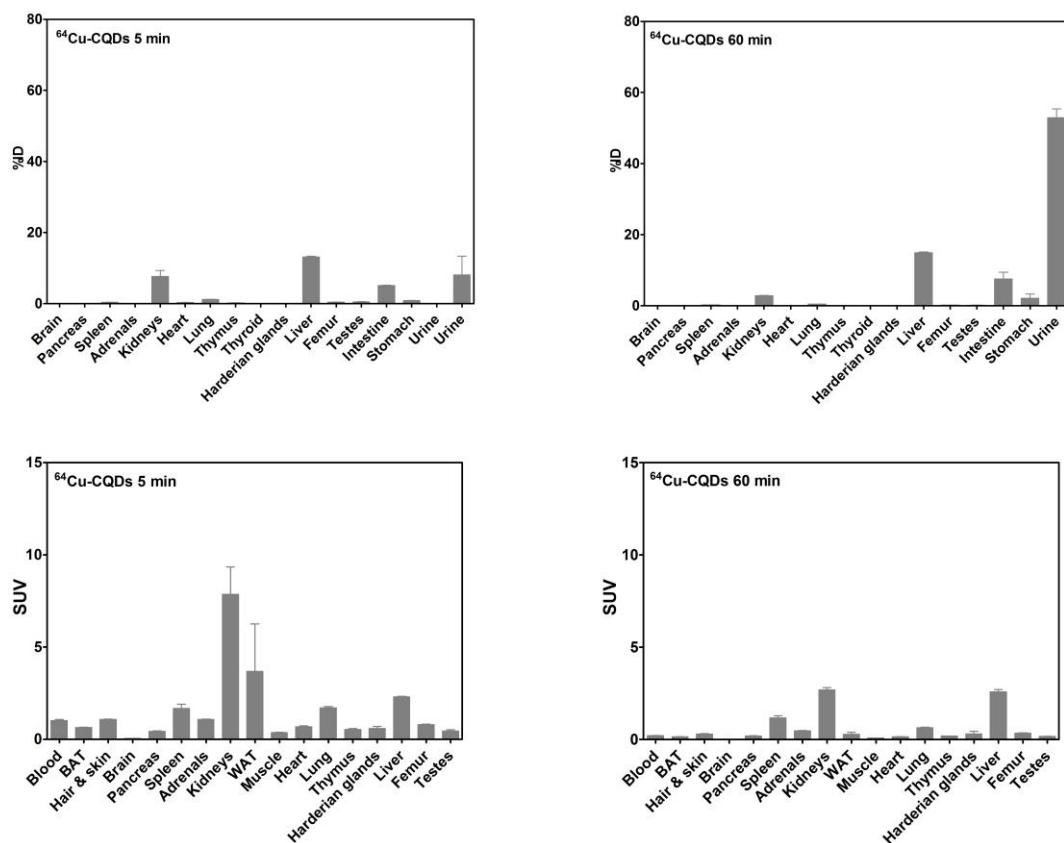


**Figure 4.10.** Biodistribution of  $^{64}\text{Cu}$ -NOTA-CQDs, expressed as % ID (upper figures) and SUV (bottom figures), at 5 and 60 minutes post-injection in male Wistar rats.

From the histograms in figure 4.10, it is evident that at 60 minutes post-injection CQDs are mainly excreted through the urine, but an appreciable quantity is still present in the liver and in the intestine. Therefore, it results very interesting to compare the two mechanisms of excretion, renal and hepatobiliary, and compare this ratio to the same ratio for Si NPs. In figure 4.11, a histogram that shows the ratios between renal and hepatobiliary excretion for CQDs and both kind of Si NPs used, is reported.

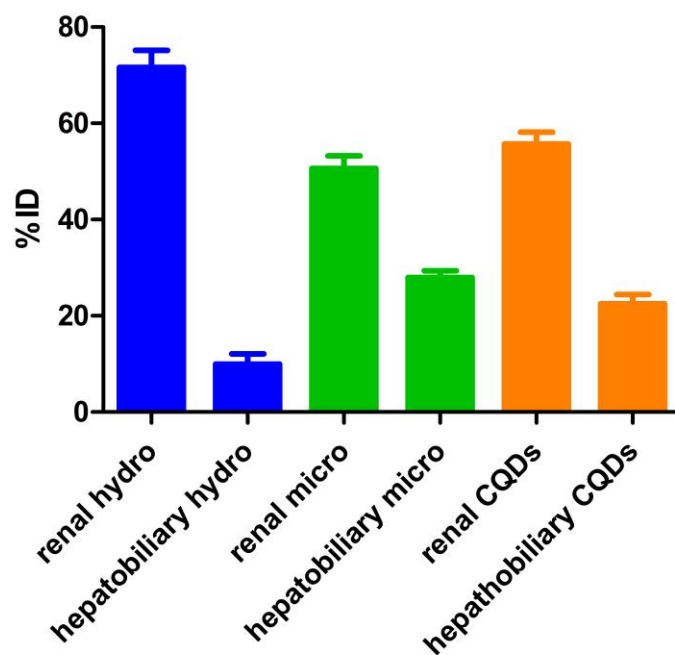


**Figure 4.11.** Histogram showing the ratio between renal and hepatobiliary mechanism of excretion for [ $^{64}\text{Cu}$ -NOTA-Si NPs (hydro)] (blue), [ $^{64}\text{Cu}$ -NOTA-Si NPs (micro)] (green) and [ $^{64}\text{Cu}$ -NOTA-CQDs] (orange)

It is evident also from this graph, that [ $^{64}\text{Cu}$ -NOTA-Si NPs (hydro)] are the most promising material among the three kinds of particles reported so far in this thesis. [ $^{64}\text{Cu}$ -NOTA-Si NPs (hydro)] are eliminated almost entirely through renal excretion, i.e. through kidneys and bladder. CQDs are also mostly eliminated through the bladder, but partially stack in the liver and the intestine as it was already shown in the biodistribution graph. CQDs are accumulating in a slighter lower percentage in the intestine compared to [ $^{64}\text{Cu}$ -NOTA-Si NPs (micro)]. On the other hand, when using CQDs some activity remains in the body in other organs, such as the spleen, as can be seen in the SUV graph at 60 minutes post-injection (Figure 4.10), while when using [ $^{64}\text{Cu}$ -NOTA-Si NPs (micro)], the activity is coming only from the kidneys (when looking at the SUV) and from the intestine (activity in intestine can be measured only in terms of % ID). In conclusion, all the ultrasml NPs studied for PET imaging in this thesis, meet the requirements<sup>[21]</sup> for future theranostics applications (size

$\leq 5.5$  nm, non-toxic components that could biodegraded into clearable components). Also if compared to CQDs, [ $^{64}\text{Cu}$ -NOTA-Si NPs (hydro)] results the best system amongst the ones used following mainly a renal clearance mechanism that is very fast. Nevertheless, CQDs have a similar behaviour to Si NPs, as expected, but follow both renal and hepatobiliary mechanism of excretion giving some accumulation in liver.

## 4.5 Conclusions

In this part of the work, ultrasmall CQDs (size  $\approx 3$  nm) were prepared, their multi-coloured emission investigated, their coupling with dyes and radiotracers performed and *in vivo* studies conducted. Due to the similar, but not identical, properties of carbon- and silicon-based materials, some comparison between these two materials in respect to surface modification with the same labels and to *in vivo* behaviour has been attempted. Cy5-CQDs display both the emission of the NPs and that one of the dye. In addition, the emission maximum pertaining to CQDs is red-shifted in the sample modified with cyanine 5 with respect to the free CQDs as it was observed also for Si NPs (Chapter 3). Finally, CQDs were labelled with the NOTA- $^{64}\text{Cu}$  complex to be used in *in vivo* PET imaging for direct comparison with Si NPs. Both experiments of imaging and biodistribution were done. The results show that CQDs have a similar, but not identical, behaviour to the one of Si NPs, especially the ones prepared by microemulsion synthesis. Indeed the majority of activity comes from the bladder after 50 minutes from injection of NPs in mice, but biodistribution studies show that CQDs follow both renal and hepatobiliary mechanism of excretion as for Si NPs made by microemulsion method. On the other hand, CQDs are excreted from the body slower than Si NPs and some accumulation in organs, such spleen and liver is observed. In conclusions, all the NPs used in this study are suitable for *in vivo* imaging, showing all of them

a fast excretion through the bladder. However, amongst the three kinds of NPs investigated, Si NPs made by hydrothermal method behave in the most ideal way being entirely excreted through renal clearance already 50 minutes after injection in the body without showing accumulation in organs. All these findings give promising expectations and important information on the design of a future multimodal probe.

## **4.6 Experimental section**

### **4.6.1 Synthesis of CQDs**

#### *Materials*

All the chemicals were purchased from Sigma-Aldrich, Fluka or Acros. Dialysis tubes were purchased from Serva (MWCO: 1 KDa; Spectra/Por® 7 dialysis tubing).

#### *Synthetic procedure*

CQDs were prepared, according to a reported method, <sup>[4]</sup> by microwave treatment of an aqueous solution of L-arginine hydrochloride (2M) and ethylenediamine (2M). 5.6 g of L-arginine hydrochloride and 1.78 mL of 1,2-ethylenediamine were dissolved in 13.3 mL of deionized water. The starting solution was processed in a common domestic microwave oven, operated at a nominal power of 700 W for 3 minutes. The reaction took place at constant pressure (1 Atm) and the temperature was not monitored. When the reaction is completed, CQDs have been purified by dialysis against water (MWCO: 1 KDa; Spectra/Por® 7 dialysis tubing). The typical reaction produces a final amount of  $\approx 1.2$  g of CQDs.

## 4.6.2 Coupling of CQDs with cyanine 5

### *Materials*

Cyanine 5 NHS ester was purchased from Lumiprobe. Dialysis tubes were purchased from Serva (MWCO: 1 KDa; Spectra/Por® 7 dialysis tubing).

### *Synthetic procedure*

Cy5-CQDs were prepared simply mixing the particles with the NHS ester of Cy5. In a typical experiment, 5.85 mg of CQDs were dispersed in 5 mL of water. Then, 50  $\mu$ L of this dispersion were added to a solution of Cy5-NHS ester in DMSO (156.7  $\mu$ g of Cy5 in 100  $\mu$ L of DMSO). The coupling has occurred at room temperature, shaking the solution for 12 hours in the dark. After reaction is completed, the sample was purified using dialysis against water (MWCO: 1 KDa; Spectra/Por® 7 dialysis tubing) for several days until the external water does not contain free dye.

## 4.6.3 Coupling of CQDs with NOTA ligand

### *Materials*

S-2-(4-Isothiocyanatobenzyl)-1,4,7-triazacyclononane-1,4,7-triacetic acid (SCN-Bn-NOTA; #B-605) was purchased from Macrocyclics.

### *Synthetic procedure*

NOTA-CQDs were prepared dispersing 1 mg of CQDs in 150  $\mu$ L of deionized water and placed in a 1.5 mL low protein binding Eppendorf-tube. A specific amount of SCN-Bn-NOTA (0.1 or 0.8  $\mu$ mol/mg - according to the used amount of nanoparticles) was dissolved in 100  $\mu$ L of deionized water and, then, added to the NPs dispersion. The final dispersion was then shaken on a thermo-mixer (Eppendorf) at 750 rpm for 16 h at 25 °C. All samples, which were used for *in vivo* experiments, have been purified by dialysis against deionized water (MWCO 500 - 1000, Spectra Por Float-A-Lyzer G2, 1 mL). Afterwards a defined aliquot was freeze-dried to obtain the final concentration of particles.

#### 4.6.4 Radiolabeling of NOTA-CQDs

The production of  $^{64}\text{Cu}$  was performed at Cyclone® 18/9 (Helmholtz-Zentrum Dresden-Rossendorf) in a  $^{64}\text{Ni}(\text{p},\text{n})^{64}\text{Cu}$  nuclear reaction with specific activities of 150–250 GBq  $\mu\text{mol}^{-1}$  Cu diluted in HCl (10 mM).<sup>[22]</sup> An aliquot of  $^{64}\text{Cu}$ ]CuCl<sub>2</sub> solution (20–100 MBq) was buffered with MES (2-(N-morpholino)ethanesulfonic acid)/NaOH-buffer (0.1 M; pH 6). Typically, a specific amount of nanoparticles, up to 10  $\mu\text{g}$ , was mixed in a 1.5 mL low protein binding Eppendorf-tube with a specific aliquot of  $^{64}\text{Cu}$ ]Cu(II)-solution (varying up to 40 MBq) and addition of MES/NaOH buffer (0.1 M; pH 6) up to a final volume in the range of 150–200  $\mu\text{L}$ . The particles have been labelled by means of mechanical shaking for 30 min at 25 °C. To check the full labeling, a 5.0  $\mu\text{L}$  aliquot of the reaction was combined with 2.0 nmol EDTA (pH 7.0) and the labeling process of the nanoparticles ( $R_f = 0$ ) was monitored by radio-TLC using ITLC-SA plates (Merck Millipore) in combination with a mobile phase of 0.9% NaCl in dH<sub>2</sub>O. As control, separate radio-TLC analysis of  $^{64}\text{Cu}$ ]Cu–EDTA ( $R_f = 0.9$ ) was performed in the same mobile phase. Evaluation of radio-TLC was carried out using a radioactivity thin layer analyser (Rita Star, Raytest).

#### 4.6.5 Animal experiments

All animal experiments were carried out according to the German regulations on animal welfare (approved by Landesdirektion Dresden, 24-9168.21-4/2004-1). Male Wistar rats (aged 7–9 weeks; Harlan Winkelmann GmbH, Borchon, Germany) and female NMRI nu/nu mice (aged 7–14 weeks; Technische Universität Dresden, Oncoray, Germany) were housed under standard conditions with free access to standard food and tap water. For PET experiments in tumor-bearing mice, about  $2 \times 10^6$  A431 cells were injected subcutaneously in the back or right hind leg of NMRI nu/nu mice according to the protocol published elsewhere.

#### **4.6.6 Biodistribution**

Two groups of four rats (5 and 60 min) were intravenously injected into a lateral tail vein with 0.5–5.0 MBq of  $^{64}\text{Cu}$ -labeled nanoparticles, which were dissolved in 0.5 mL of electrolyte solution E-153 (Serumwerk Bernburg, Germany) at pH 7.2. The specific activity ranged from 5.0 to 30 GBq/ $\mu\text{mol}$  at the time of injection. Animals were sacrificed at 5 and 60 min post injection. Blood and the major organs were collected, weighed, and counted in a Wallac WIZARD automatic  $\gamma$ -counter (PerkinElmer, Germany). The activity of the tissue samples was decay-corrected and calibrated by comparing the counts in tissue with the counts in aliquots of the injected tracer that had been measured in the  $\gamma$ -counter at the same time. The activity amount in the selected tissues and organs was expressed as percent of injected dose (% ID). The activity concentration in the biodistribution measurements were calculated as SUV ( $\text{SUV} = (\text{activity/g tissue})/(\text{injected activity/body weight})$ ) and expressed as means  $\pm$  standard deviation (mean  $\pm$  SD) for each group of four animals.

#### **4.6.7 *In vivo* small animal positron emission tomography (PET)**

Rats or mice were positioned and immobilized prone with their medial axis parallel to the axial axis of the scanners (NanoScan PET/CT, Mediso, microPET® P4, Siemens preclinical solutions). The radiotracer was administered intravenously as an infusion using a syringe pump over one minute (Harvard Apparatus, flow rate: injection volume as mL/min) through a needle catheter into a lateral tail vein. The standardized uptake values (SUV) were calculated over the ROI as the ratio of activity concentration (Bq/mL) at time  $t$  and injected dose (Bq) at the time of injection ( $t_0$ ) divided by body weight (g). For the demonstration of the increasing activity uptake, the early (midframe time 3 min p.i.) images were subtracted from the late image (midframe time 50 min p.i.).

## 4.6.8 Characterization

### *HR-TEM*

Samples for HR-TEM were prepared drop-casting an ethanolic solution of the sample on carbon coated copper grids (Quantifoil, GmbH). The analysis were performed using a FEI Titan 80-300 transmission electron microscope operated at 300 KV.

### *Photophysical characterization*

Absorption spectra were acquired using a double-beam Shimadzu UV-3600 UV-Vis-NIR spectrophotometer.

Steady-state emission spectra were recorded on a HORIBA Jobin-Yvon IBH FL-322 Fluorolog 3 spectrometer equipped with a 450 W xenon arc lamp, as the excitation source, and a TBX-4-X single-photon-counting device as the detector. Emission and excitation spectra were corrected for source intensity (lamp and grating) and emission spectral response (detector and grating) by standard correction curves.

Time-resolved measurements were performed on FluoTime 300 “Easy Tau” spectrometer (PicoQuant) equipped with subnanoseconds LDH sources powered by a PicoQuant PDL 820 variable (0.2-80 MHz) pulsed power supply. Measurements were performed using a PicoHarp TCSPC (Time-Correlated Single Photon Countings) module. The decays were fitted by means of PicoQuant FluoFit Global Fluorescence Analysis Software (PicoQuant GmbH, Germany). Lifetimes were corrected with

PLQY were measured on a Hamamatsu Quantaaurus-QY integrating sphere equipped with a 150 W CW Xenon source.

## 4.7 References:

- [1] G. Hong, S. Diao, A. L. Antaris, H. Dai, *Chemical Reviews* **2015**.
- [2] S.-T. Yang, L. Cao, P. G. Luo, F. Lu, X. Wang, H. Wang, M. J. Mezziani, Y. Liu, G. Qi, Y.-P. Sun, *Journal of the American Chemical Society* **2009**, *131*, 11308-11309.
- [3] X. Xu, R. Ray, Y. Gu, H. J. Ploehn, L. Gearheart, K. Raker, W. A. Scrivens, *Journal of the American Chemical Society* **2004**, *126*, 12736-12737.
- [4] D. Mazzier, M. Favaro, S. Agnoli, S. Silvestrini, G. Granozzi, M. Maggini, A. Moretto, *Chemical Communications* **2014**, *50*, 6592-6595.
- [5] L. Wang, Y. Wang, T. Xu, H. Liao, C. Yao, Y. Liu, Z. Li, Z. Chen, D. Pan, L. Sun, M. Wu, *Nat Commun* **2014**, *5*.
- [6] S. N. Baker, G. A. Baker, *Angewandte Chemie International Edition* **2010**, *49*, 6726-6744.
- [7] M. Bhaisare, A. Talib, M. S. Khan, S. Pandey, H.-F. Wu, *Microchim Acta* **2015**, 1-9.
- [8] Z. Fan, S. Li, F. Yuan, L. Fan, *RSC Advances* **2015**, *5*, 19773-19789.
- [9] L. Wang, S.-J. Zhu, H.-Y. Wang, S.-N. Qu, Y.-L. Zhang, J.-H. Zhang, Q.-D. Chen, H.-L. Xu, W. Han, B. Yang, H.-B. Sun, *ACS Nano* **2014**, *8*, 2541-2547.
- [10] Q. Xue, H. Huang, L. Wang, Z. Chen, M. Wu, Z. Li, D. Pan, *Nanoscale* **2013**, *5*, 12098-12103.
- [11] V. Strauss, J. T. Margraf, C. Dolle, B. Butz, T. J. Nacken, J. Walter, W. Bauer, W. Peukert, E. Spiecker, T. Clark, D. M. Guldi, *Journal of the American Chemical Society* **2014**, *136*, 17308-17316.
- [12] Y.-P. Sun, B. Zhou, Y. Lin, W. Wang, K. A. S. Fernando, P. Pathak, M. J. Mezziani, B. A. Harruff, X. Wang, H. Wang, P. G. Luo, H. Yang, M. E. Kose, B. Chen, L. M. Veca, S.-Y. Xie, *Journal of the American Chemical Society* **2006**, *128*, 7756-7757.
- [13] L. Cao, S.-T. Yang, X. Wang, P. G. Luo, J.-H. Liu, S. Sahu, Y. Liu, Y.-P. Sun, *Theranostics* **2012**, *2*, 295-301.
- [14] H. Tao, K. Yang, Z. Ma, J. Wan, Y. Zhang, Z. Kang, Z. Liu, *Small* **2012**, *8*, 281-290.
- [15] P. G. Luo, F. Yang, S.-T. Yang, S. K. Sonkar, L. Yang, J. J. Broglie, Y. Liu, Y.-P. Sun, *RSC Advances* **2014**, *4*, 10791-10807.
- [16] J. Wang, P. Zhang, C. Huang, G. Liu, K. C.-F. Leung, Y.-X. J. Wang, *Langmuir* **2015**.
- [17] M. Montalti, A. Cantelli, G. Battistelli, *Chemical Society Reviews* **2015**, *44*, 4853-4921.
- [18] J. M. Jeong, M. K. Hong, Y. S. Chang, Y.-S. Lee, Y. J. Kim, G. J. Cheon, D. S. Lee, J.-K. Chung, M. C. Lee, *Journal of Nuclear Medicine* **2008**, *49*, 830-836.
- [19] Y. Matsumura, H. Maeda, *Cancer Research* **1986**, *46*, 6387-6392.
- [20] H. Maeda, *Journal of Controlled Release* **2012**, *164*, 138-144.
- [21] H. Soo Choi, W. Liu, P. Misra, E. Tanaka, J. P. Zimmer, B. Itty Ipe, M. G. Bawendi, J. V. Frangioni, *Nat Biotech* **2007**, *25*, 1165-1170.
- [22] S. Thieme, M. Walther, H. J. Pietzsch, J. Henniger, S. Preusche, P. Mäding, J. Steinbach, *Applied Radiation and Isotopes* **2012**, *70*, 602-608.

# Chapter 5

## Preparation, surface modification and characterization of silica-coated cobalt nanoparticles

### Abstract

This Chapter deals with the preparation, characterization and surface modification of ultrasmall silica-coated cobalt nanoparticles. A synthetic method was optimized to obtain an ultrathin silica shell ( $\approx 2$  nm) which has the dual function to reduce the toxicity of the cobalt core and allow further functionalization. Nanoparticles surface was modified with amine-moieties that are suitable for subsequent couplings. Some preliminary functionalizations with model dyes were done in order to show that nanoparticles surface can be successfully modified in the perspective of a future use in bioimaging.

### 5.1 Introduction

Magnetic nanoparticles are attracting increasing interest for bioapplications<sup>[1-5]</sup>, especially for magnetic resonance imaging (MRI)<sup>[6-7]</sup>, drug delivery<sup>[8]</sup> or also in therapy thanks to hyperthermia properties<sup>[9-11]</sup>. Many efforts have been directed to study metal oxide NPs such as ultrasmall iron oxide NPs, but the literature on ultrasmall cobalt nanoparticles (Co NPs) for bioapplications is still limited and there is still large room for exploring this field. Co NPs represent another promising alternative to be used as multimodal probes, provided that some issues

regarding their toxicity and biocompatibility<sup>[12]</sup> will be solved. First of all Co NPs, as other metallic magnetic NPs, possess higher values of saturation magnetization than the ones composed of metal oxides such as ferrite or iron oxides<sup>[13]</sup>. This is a very important point because it allows to retain the same magnetic properties of oxides using smaller quantities of particles or smaller magnetic cores. In addition, as reported for other magnetic NPs<sup>[13-15]</sup>, Co NPs can switch their behaviour from ferromagnetic to superparamagnetic when they possess an ultrasmall dimension<sup>[14, 16-17]</sup>.

Synthetic methods to obtain cobalt nanoparticles have been well established and it is possible to obtain quite monodisperse Co NPs having sizes < 10 nm.

Even though cobalt has a very important role in biological systems since it is a constituent of the vitamin B and it is present in several other vitamins<sup>[18]</sup>, toxicity and instability have limited the use of cobalt nanoparticles in the past<sup>[12]</sup>.

For this reason, part of the research is focused on the surface modification of cobalt nanoparticles with a silica shell<sup>[19-22]</sup> with the aim to render them less toxic, more stable and to end up with an easier functionalizable surface. To date, there are not so many reports on ultrasmall silica-coated Co NPs (Co@SiO<sub>2</sub> NPs) with a thin silica shell. Therefore, in this part of the work, some strategies to control the growth of the silica shell on ultrasmall Co NPs have been optimized. In addition, the Co@SiO<sub>2</sub> NPs were covered with an amine-terminated layer in order to allow the further attachment of functionalities, such as dyes or biomolecules, suitable for supplying them with properties useful for multimodal imaging.

## **5.2 Preparation of cobalt nanoparticles**

### **5.2.1. Synthetic route and characterization**

Cobalt nanoparticles (size 5 to 10 nm) are prepared according to a reported method<sup>[23-25]</sup>, which is based on the thermal decomposition of Co<sub>2</sub>(CO)<sub>8</sub> in the presence of aluminium alkyl compounds (AlR<sub>3</sub>). This technique produces

long-time air-stable cobalt nanoparticles thanks to the step of controlled ("smooth") oxidation, which creates a thin cobalt oxide layer around particles preventing further oxidation. Particles size can be tuned by changing the length of the alkyl chain of the  $\text{AlR}_3$  compound or the molar ratio between  $\text{Co}_2(\text{CO})_8$  and  $\text{AlR}_3$ . The particles are, subsequently, stabilized by the addition of a surfactant, typically oleic acid and/or oleylamine. A general scheme for the synthetic route is shown in Figure 5.1.

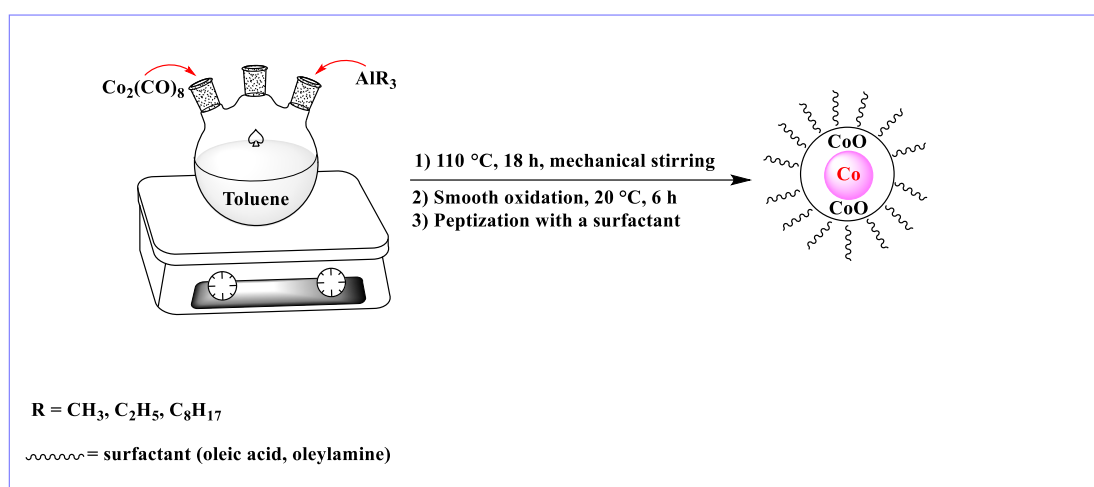


**Figure 5.1.** General scheme of the synthesis of cobalt nanoparticles

The Co NPs used in this work are in the size range 5 - 8 nm. Nanoparticles of these dimensions have been studied and characterized in the literature<sup>[23-25]</sup>. Typical HR-TEM images, at low and high magnification, of Co NPs are reported in Figure 5.2. The size distribution histogram, reported in Figure 5.3, reveals an average dimension of  $7.3 \pm 1.5$  nm.

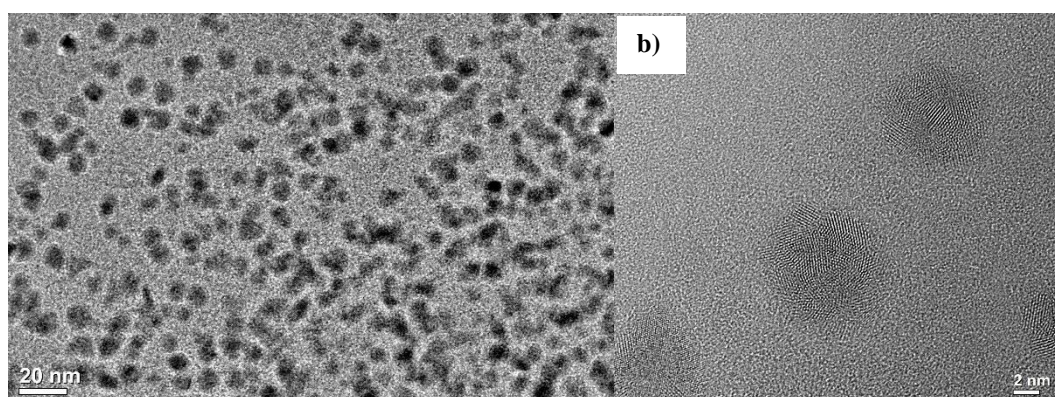


**Figure 5.2.** HR-TEM images of Co NPs; **b)** HR-TEM image at high magnification

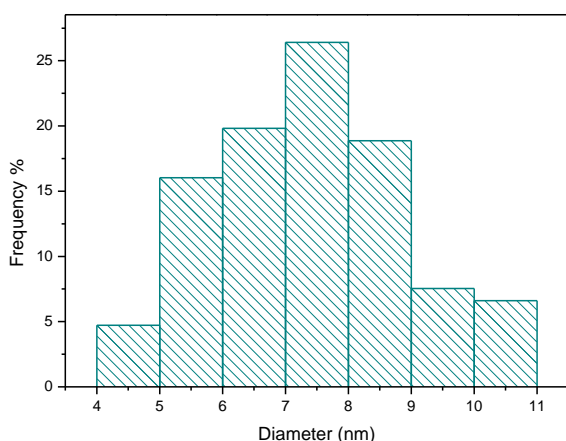


**Figure 5.3.** Size distribution histogram of Co NPs

## 5.3 Preparation of silica-coated Co NPs

### 5.3.1 Synthetic route

Silica-coated Co NPs (Co@SiO<sub>2</sub> NPs) with ultrathin silica shell were prepared with a modification of a reported method [26-27]. Co NPs previously prepared and stabilized with oleylamine and oleic acid are shaken for 2 hours in the presence of a solution of (3-Aminopropyl)triethoxysilane (APTES). In this step, the surfactant, which acts as a stabilizer, is removed and substituted with APTES. Then, a modified Stöber process<sup>[28]</sup> step was actuated reacting overnight the intermediate NPs with tetraethyl orthosilicate (TEOS) in the presence of a base, such as ammonium hydroxide. The technique we optimized for the preparation of ultrathin silica shell allows to perform the reaction at room temperature, while in the previously reported method<sup>[26-27]</sup> 100 °C are required.

The general scheme followed for the preparation of Co@SiO<sub>2</sub> NPs is showed in Figure 5.4.

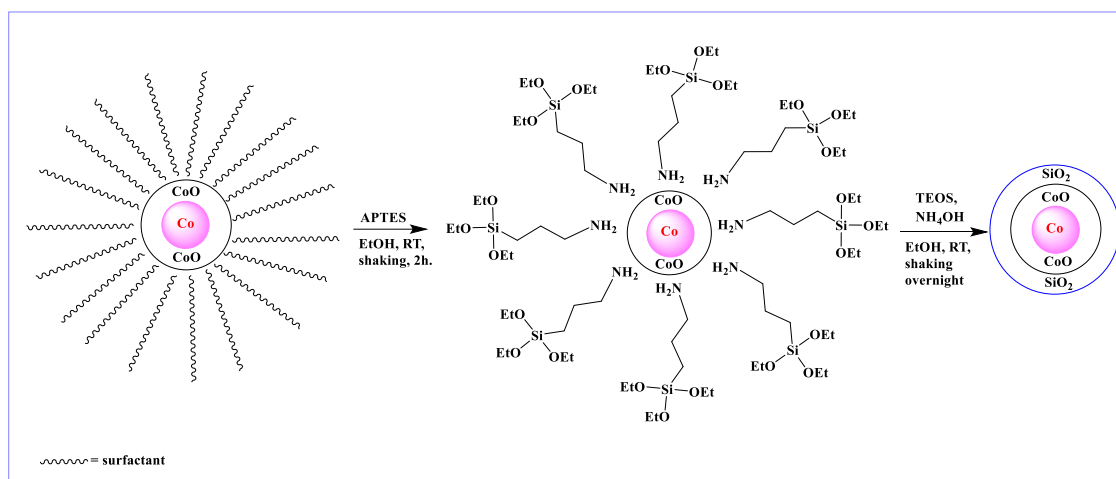


**Figure 5.4.** Synthetic route for the preparation of Co@SiO<sub>2</sub> NPs

Obtaining an ultrathin silica shell is very challenging and in most of cases, NPs encapsulated in a silica matrix rather than isolated core/shell particles were obtained. When (3-Mercaptopropyl)trimethoxysilane (SH-PTMS) has been used in place of APTES and when quantities are a little higher than a threshold value, the synthetic route leads to the formation of either separated silicon oxide NPs (Figure 5.5a) or to a silica matrix (Figure 5.5b) that encapsulates Co NPs. This can be seen also from the EDX spectrum in Figure 5.5c where the silicon peak has a very high intensity showing the presence of a too high amount of silicon oxide.

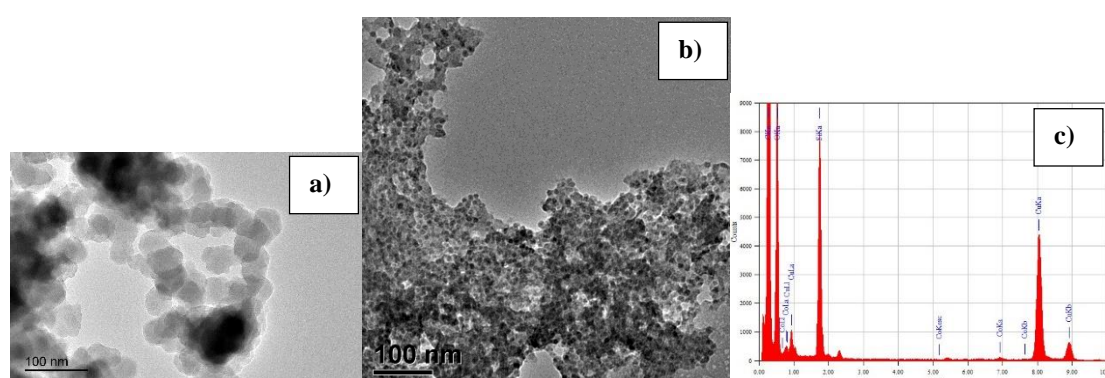


**Figure 5.5.** a) TEM image of silica NPs formed during the preparation of Co@SiO<sub>2</sub> NPs; b) TEM image of Co NPs encapsulated in a silica matrix; c) EDX spectrum showing a too high amount of silicon in the two samples

### 5.3.2 Characterization

Silica-coated Co NPs (Co@SiO<sub>2</sub> NPs) have been characterized by high resolution transmission electron microscopy (HR-TEM), energy filtering transmission electron microscopy (EFTEM), energy dispersive X-ray (EDX) analysis and X-ray photoelectron spectroscopy (XPS).

In Figure 5.6a and 5.6b, a typical HR-TEM image and the size distribution histogram for Co@SiO<sub>2</sub> NPs are shown.

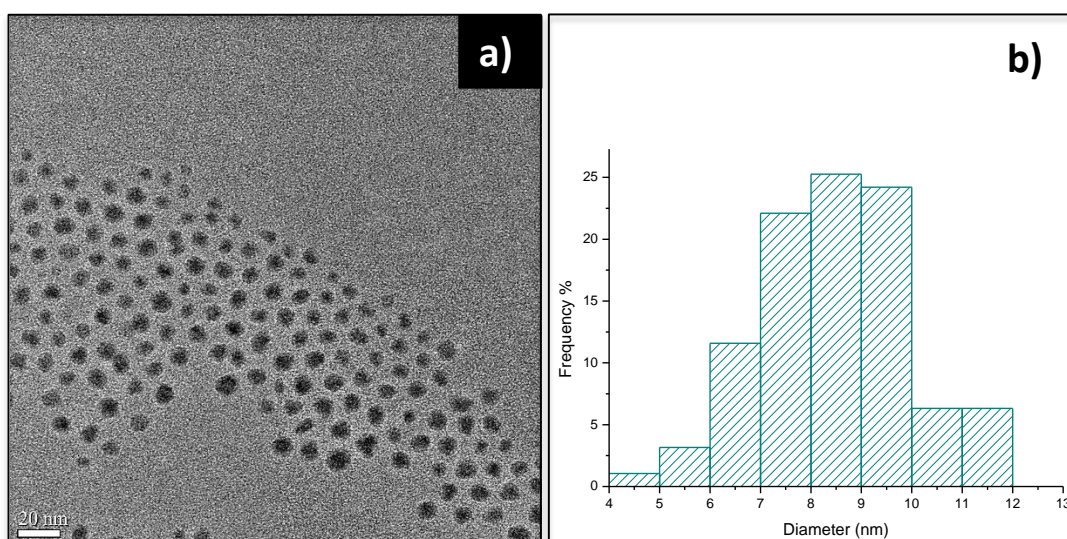


**Figure 5.6.** a) HR-TEM image of Co@SiO<sub>2</sub> NPs; b) size distribution graph (average size  $8.5 \pm 1.5$  nm) of Co@SiO<sub>2</sub> NPs

As it can be seen, the average size of NPs is  $8.5 \text{ nm} \pm 1.5 \text{ nm}$ , therefore below 10 nm even after silica coating. It must be noted, however, that this value can be affected by the difficulties in imaging the silica shell around the Co NPs, since it is ultrathin and not crystalline. Looking at the high magnification HR-TEM image, reported in Figure 5.7, the cobalt core is clearly visible and it shows a high crystallinity, similar to that observed in particles without the silica shell. Around the core, a first ultrathin shell is visible, formed by cobalt oxide originating from the synthetic route followed, which includes a smooth oxidation step at the end of the preparation aimed to stabilize the particles against further oxidation. An accurate observation reveals the presence, although with a scanty contrast, of a second thin shell that is not crystalline and can be assigned to the

silica shell. The thickness of the shell around the core, comprising both the cobalt oxide and the silica layers, can be estimated between 1 and 3 nm.

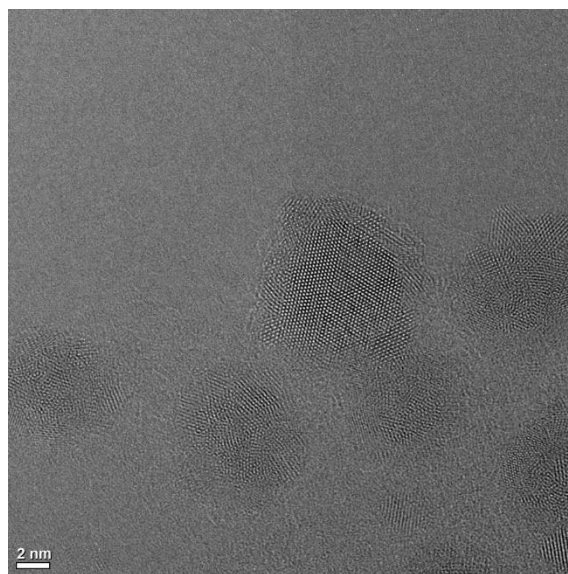


**Figure 5.7.** High magnification HR-TEM image of Co@SiO<sub>2</sub> NPs

The electron diffraction pattern measured on the same sample is reported in Figure 5.8. The pattern shows clearly the coexistence of metallic cobalt and its oxide. No diffraction signal from the silica shell is visible, indicating that, if present, it is amorphous.

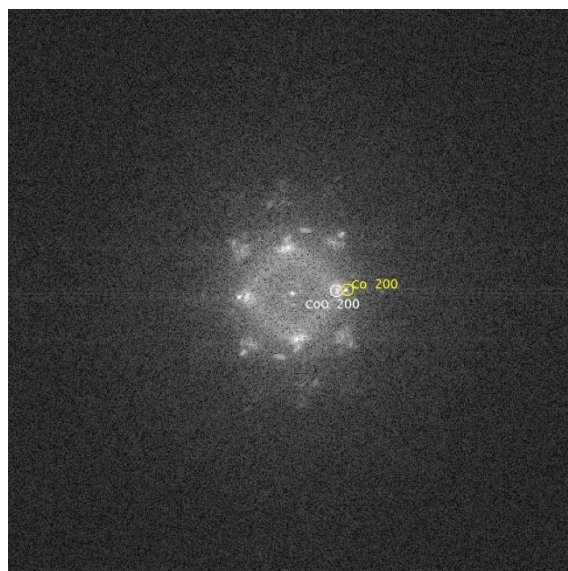


**Figure 5.8.** Electron diffraction pattern, acquired in the HR-TEM microscope, of Co@SiO<sub>2</sub> NPs

Hence, supplemental information is needed for assessing the presence of the silica shell. A first indication arises from EDX measurements, performed in the same HR-TEM microscope. As expected, Figure 5.9 shows the presence of the characteristics peaks of cobalt but also, at 1.75 keV, the  $K\alpha$  emission of silicon.

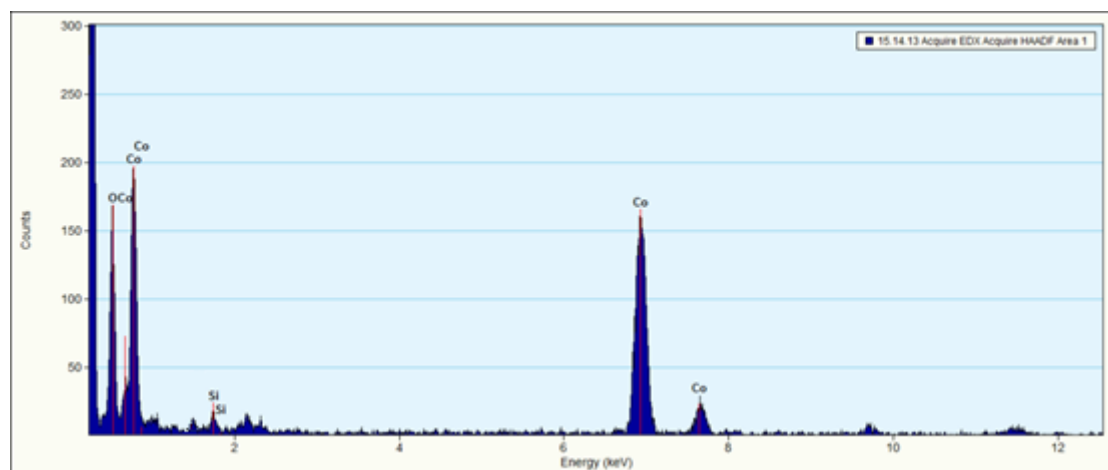


**Figure 5.9.** EDX spectrum of Co@SiO<sub>2</sub> NPs

Another evidence of the formation of the silica shell around Co NPs is given by the elemental maps obtained by energy filtering transmission electron microscopy (EFTEM). In particular, Figure 5.10a reports a conventional TEM image of the Co@SiO<sub>2</sub> NPs while the EFTEM maps of cobalt and oxygen are reported in b) and c) respectively. All the maps pertain to the same area of interest, as they are obtained from the energy loss features of the electron beam of TEM. The map in d) is the overlay of the two elemental maps, with cobalt in green and oxygen in red. The overlay confirms that the cobalt core is surrounded by a cobalt oxide skin (the region where red and green are mixed), in turn surrounded by another shell, where oxygen is not superimposed with cobalt. This is better evidenced in the zoom on a single particle shown in Figure 5.10e, from which we clearly see that the outer red region belongs to a shell and not to a continuous matrix, since several dark spaces are present in between the particles.

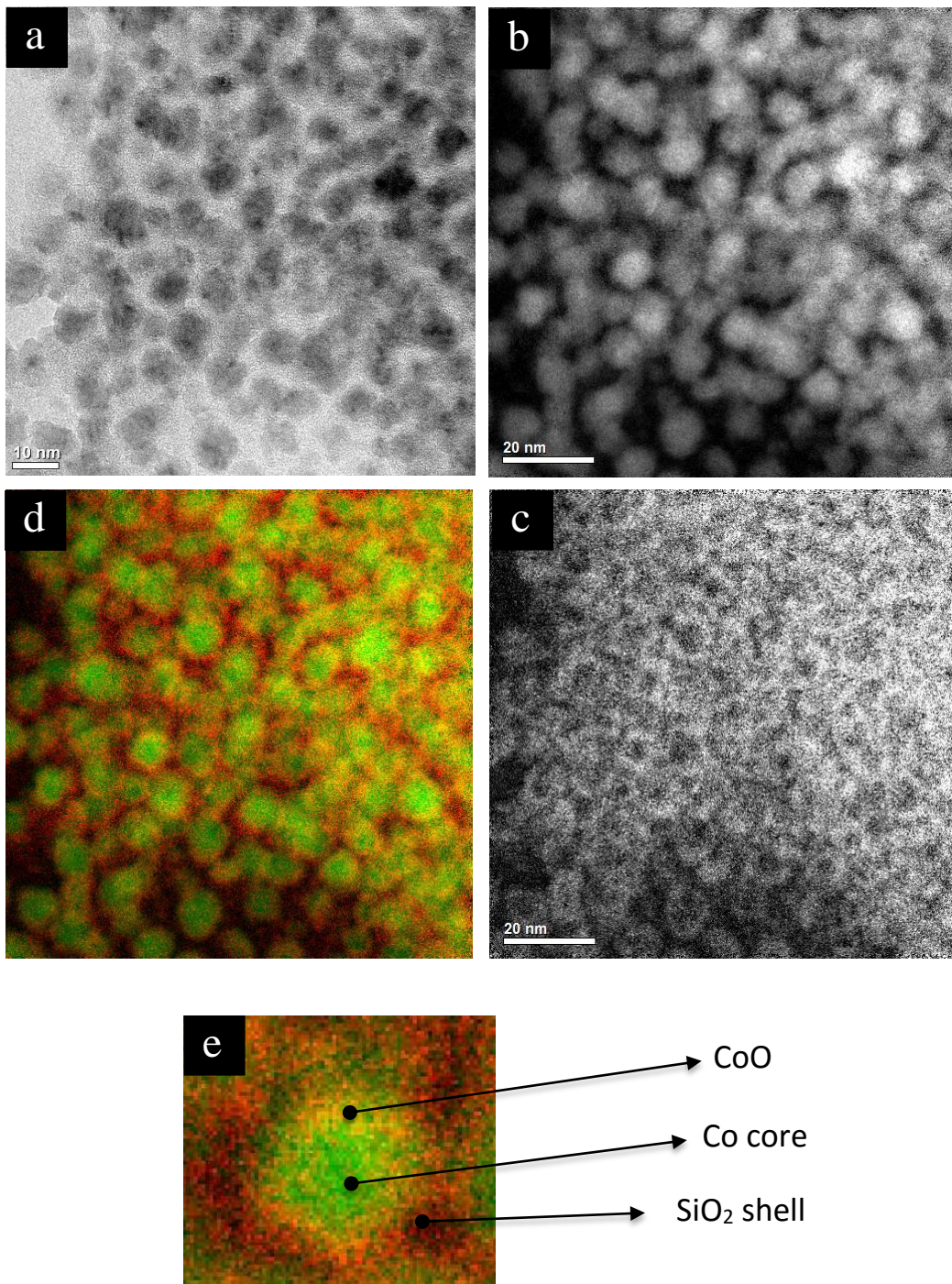


**Figure 5.10.** a) HR-TEM image of Co@SiO<sub>2</sub> NPs; EFTEM maps of (b) cobalt and (c) oxygen; d) false colour overlay of (b) cobalt and (c) oxygen; images a), b), and c) are from the same region of interest with the same field-of-view; e) overlay image zoomed on a single particle.

Further evidence of the presence of the silica shell is provided by the XPS spectra.

The survey XPS spectrum of Co@SiO<sub>2</sub> NPs, deposited onto an aluminium substrate by evaporation from a dispersion in ethanol, is reported in Figure 5.11 with the relevant peak assignments. Note that Si 2p peak overlaps with the Co 3s band so that the Si 2s peak is better suited for quantification purposes.

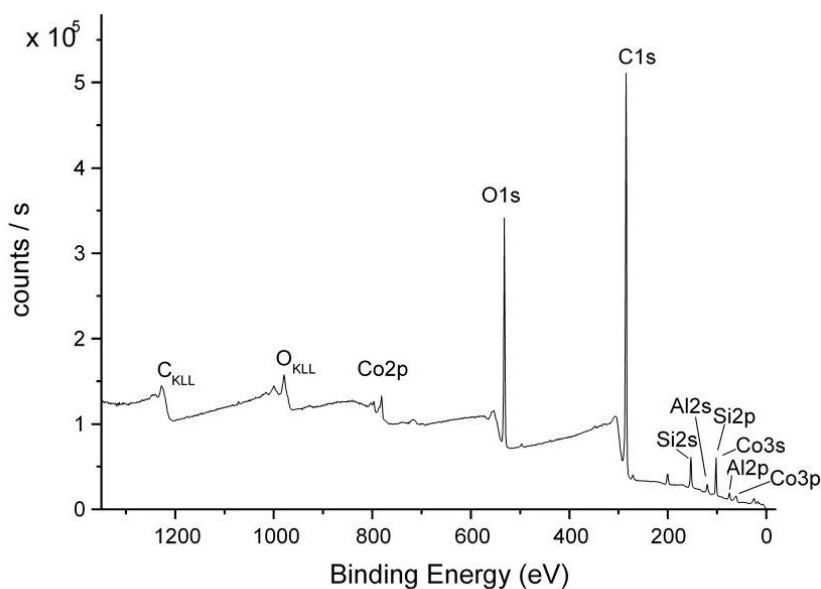


**Figure 5.11.** Survey XPS spectrum of Co@SiO<sub>2</sub> NPs, deposited on aluminium substrate. Exciting radiation Al K $\alpha$ .

The high resolution spectrum of the most characteristic peak of cobalt, i.e. Co 2p, is reported in Figure 5.12. The spectrum shows the expected complex structure of cobalt 2p, arising from the presence of the different states of oxidation of cobalt, of the spin orbit splitting and of the typical intense satellite peaks typical of cobalt. Curve resolution and assignments have been made taking into account the literature data for Co 2p chemical shifts and spin orbit splitting<sup>[29]</sup>. The general shape of the band confirms the presence of elemental and oxidized cobalt.

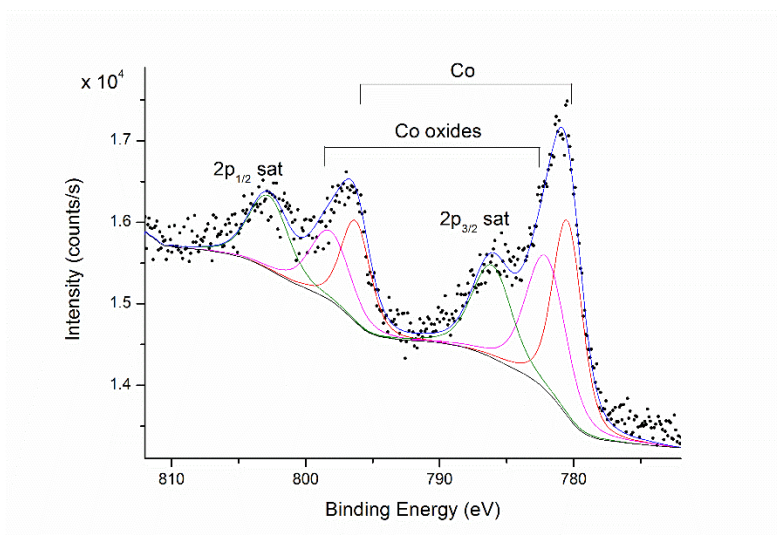
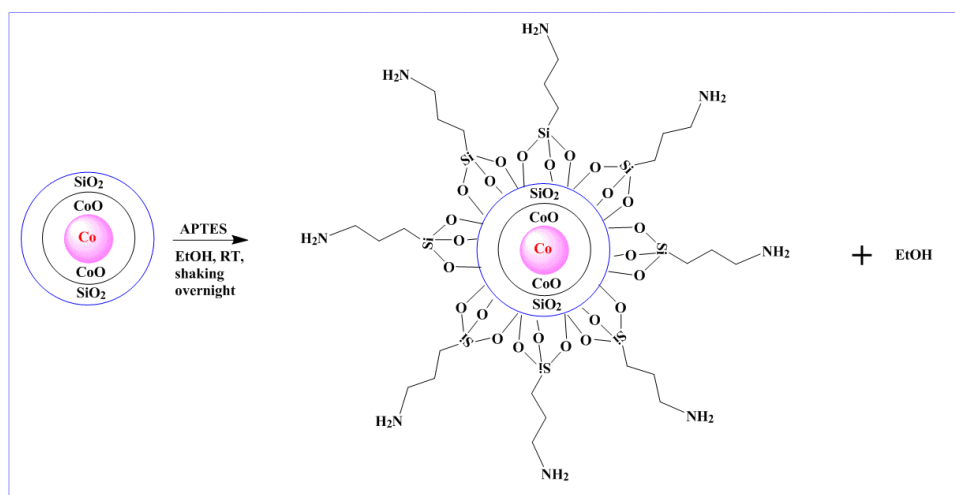


**Figure 5.12.** Co 2p region of the photoelectron spectrum of Co@SiO<sub>2</sub> NPs.

Interesting information on the composition and structure of the Co@SiO<sub>2</sub> NPs can be extracted from the intensity ratios of the peaks present in the spectrum. In particular, from the relative intensities of peaks due to Co 2p and Co 3p electrons, which have a large difference in kinetic energy (~ 705 eV and ~ 1425 eV respectively), it is possible to obtain an estimation of the thickness of an overlayer (in our case the silica shell) that attenuates the cobalt signals. The result of this estimation, explained in more details in the experimental section at the end of the Chapter, is consistent with a shell thickness of about 2 nm, in agreement with the estimations from TEM and EFTEM results.

## 5.4 Surface modification of Co@SiO<sub>2</sub> NPs with amine-moieties and dyes

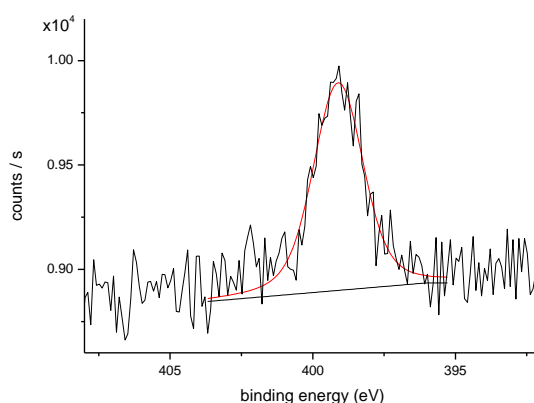
In order to perform future multimodal imaging it is necessary to functionalize the silica surface of Co@SiO<sub>2</sub> NPs. Therefore, we modified the surface with amine-moieties, by reacting Co@SiO<sub>2</sub> NPs with aminopropyltriethoxysilane (Co@SiO<sub>2</sub>-NH<sub>2</sub> NPs). The general scheme for the reaction is shown in Figure 5.13.



**Figure 5.13.** Amine functionalization of the Co@SiO<sub>2</sub> NPs

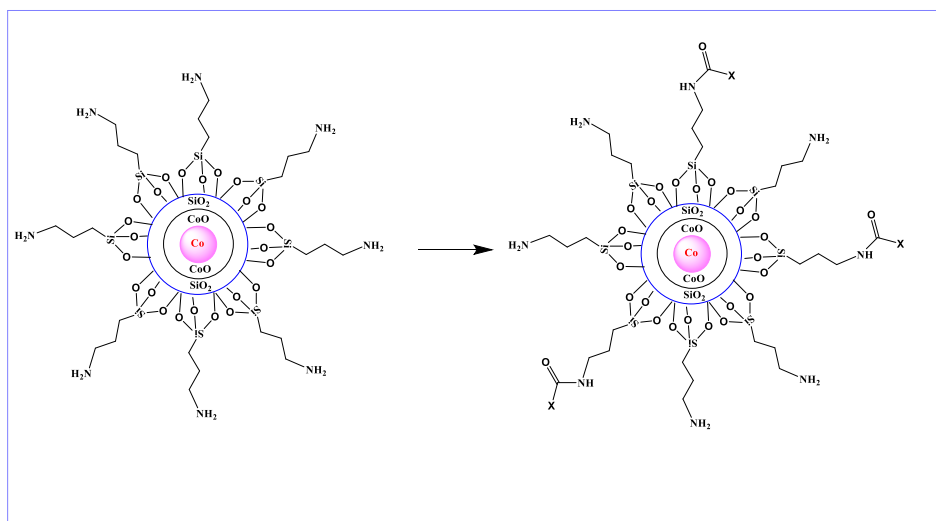
After purification by repeated centrifugation steps, Co@SiO<sub>2</sub>-NH<sub>2</sub> NPs were characterized by XPS in order to check the success of the surface functionalization and to have an estimation of the amount of amine groups present at the surface.

Figure 5.14 reports the N1s signal of the amine-functionalized sample, which is a single peak falling at a binding energy value of 399.1 eV, typical of amines. The appearance of the amine peak, not present before the functionalization step, is an indication that the functionalization took place. Also, the intensity ratio between N1s and Si1s peaks ( $\approx 0.2$ ), of the same order of magnitude of that found for the amine terminated Si NPs (Chapter 2), indicates a coverage of the silica surface not dissimilar from that of the Si NPs, and is promising in the perspective of further functionalizations.



**Figure 5.14.** XPS core-level N1s spectrum of amine functionalized CO@SiO<sub>2</sub> NPs

In order to check the feasibility of the coupling of amine-terminated Co@SiO<sub>2</sub> NPs with large molecules, in view of possible applications in multimodal imaging, we coupled the NPs with two different dyes, i.e. ATTO 655 dye and Rhodamine B. The general scheme for the reaction of Co@SiO<sub>2</sub>-NH<sub>2</sub> NPs with the dyes is shown in Figure 5.15. In the case of ATTO 655, we used the commercially available N-hydroxysuccinimide ester of the dye to create the amide bond with the amine-moieties on the surface of NPs. In the case of Rhodamine B, the amide bond is formed between the surface amine groups of the NPs and the carboxylic group of the rhodamine B, in the presence of N-hydroxysuccinimide and N-(3-Dimethylaminopropyl)-N'-ethylcarbodiimide hydrochloride (EDC).



**Figure 5.15.** Scheme for the functionalization of amine-terminated Co@SiO<sub>2</sub> NPs with the dye (X= rhodamine B or ATTO 655). For the reaction conditions, see experimental part.

The emission properties of dye-coupled Co@SiO<sub>2</sub>-NH<sub>2</sub> NPs were measured after a careful purification involving several centrifugation cycles until the supernatant did not show any detectable photoluminescence. The emission spectra, reported in Figure 5.16 show, in both cases, the typical features of the respective dyes.

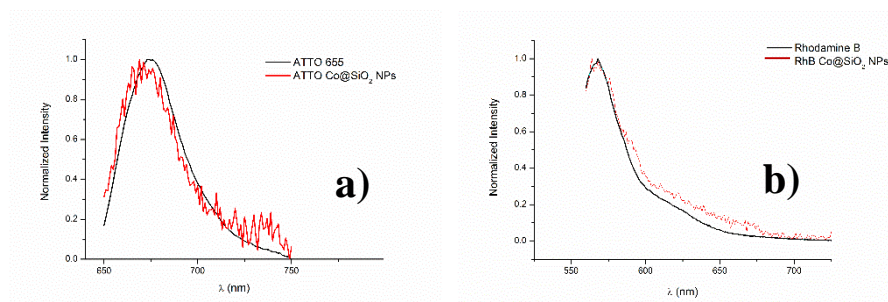


**Figure 5.16.** **a)** Emission spectra ( $\lambda_{\text{exc}} = 630$  nm) in ethanol of free ATTO 655 (black line) and ATTO-Co NPs (red line); **b)** Emission spectra ( $\lambda_{\text{exc}} = 544$  nm) in ethanol of free Rhodamine B (black line) and RhB-Co NPs (red line)

Confocal microscopy measurements, performed on ATTO-Co NPs, deposited from the solution on a glass substrate, show that the dye signal is co-localized with the NPs aggregates, as shown in Figure 5.17. The co-localization of the dye with NPs suggests that the dye is attached on the surface of NPs showing that it is possible to modify the surface of Co@SiO<sub>2</sub> in view of a future use in bioimaging.

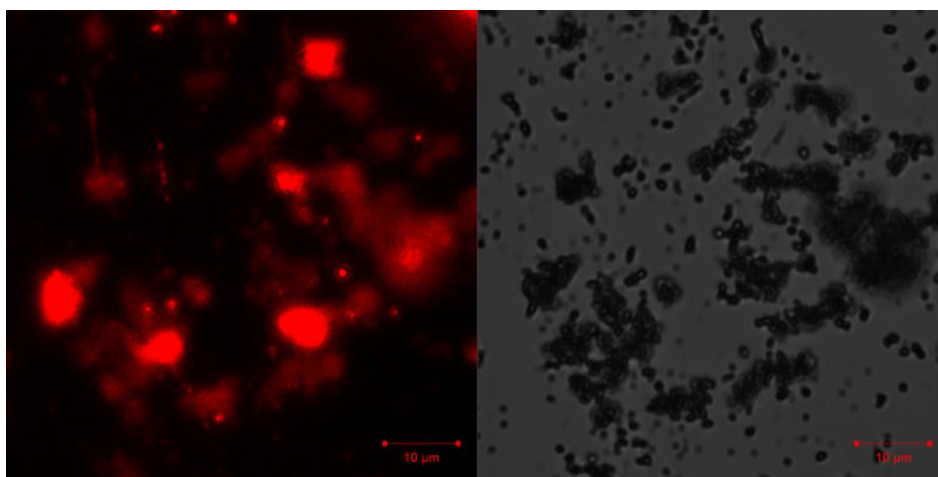


**Figure 5.17.** Confocal microscope images of ATTO-Co NPs ( $\lambda_{\text{exc}} = 630$  nm); on the right: bright field image showing NPs aggregates; on the left: detected emission ( $\lambda_{\text{exc}} = 630$  nm) of the ATTO 655 dye co-localized with NPs

## 5.5 Conclusions

Ultrasmall silica-coated cobalt NPs were prepared and characterized. TEM, EFTEM, EDX, and XPS measurements confirm the presence of an ultrathin not crystalline silica shell ( $\approx 2$  nm) around Co NPs. The surface of Co@SiO<sub>2</sub> NPs was further functionalized with amine moieties in order to render it more easily functionalizable. The functionalization with amines was confirmed by XPS. Preliminary results on couplings with model dyes, indicate the feasibility of further modification of the surface of Co@SiO<sub>2</sub>-NH<sub>2</sub> NPs with larger organic molecules, such as radiolabels for PET imaging or targeting agents for cancer cells, so prompting the SiO<sub>2</sub>-coated Co nanoparticles as potential probes in multimodal imaging.

## 5.6 Experimental section

### 5.6.1 Materials

All chemicals were purchased from Sigma-Aldrich and employed without further purification unless specified differently.

### 5.6.2 Synthesis of Co NPs

In a 500 ml three-necked flask equipped with an effective (non-magnetic!) mechanical stirrer and a reflux condenser, 17.1 g of Co<sub>2</sub>(CO)<sub>8</sub>, previously dried under argon, were dissolved in 300 ml of dry toluene. Then, either 17.6 mL of Al(C<sub>8</sub>H<sub>17</sub>)<sub>3</sub> or 3 mL of Al(C<sub>2</sub>H<sub>5</sub>)<sub>3</sub>, depending on the final NPs size desired, are added under argon flow. The mixture is stirred vigorously (400 R/min) and heated at 110 °C for 16-18 hours. As carbon monoxide evolution proceeds, the brown colour of the solution turns black confirming the formation of Co NPs. The day after, temperature is increased to 150 °C for 1 hour. Then the mixture is cooled down to 20 °C and the step of smooth oxidation is conducted. A slow stream of oxygen (4.5 Vol % O<sub>2</sub> in argon) will be slowly introduced in the

reaction mixture through a fine capillary immersed in the constantly stirred solution to form a thin layer of cobalt oxides. The reaction was kept under stirring for 6 hours. After decantation of the supernatant, the precipitated Co NPs particles were washed twice with fresh toluene. The particles are then stabilized adding 2 - 3 mL of surfactant (oleic acid, oleylamine) and heating at 60 - 70 °C for 0.5 - 2 hours.

### **5.6.3 Synthesis of Co@SiO<sub>2</sub> NPs**

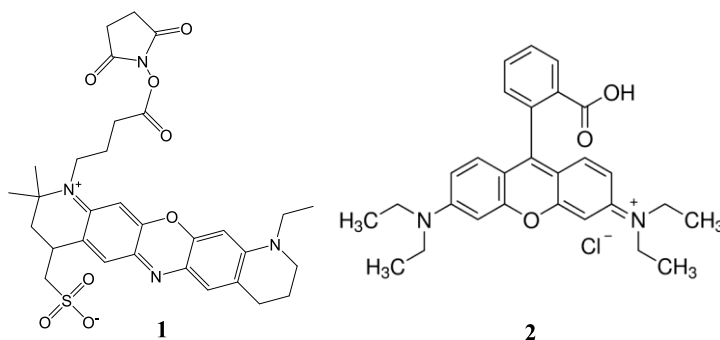
In a typical reaction, 100 µL of a solution in toluene of 5 - 7 nm cobalt nanoparticles (concentration: 6.3 mg/mL; stabilizer: oleic acid/oleylamine) were diluted in 10 mL of ethanol and mixed with 5 µL of a solution 0.04 M of (3-Aminopropyl)triethoxysilane (APTES) in ethanol. This solution was left under shaking for 2 hours. Then 5 µL of an ethanolic solution 0.04 M of tetraethyl orthosilicate (TEOS) and 5 µL of a solution 0.07 M of ammonium hydroxide in ethanol were added to the solution of cobalt nanoparticles and the mixture was left under shaking overnight. The day after, the solution was centrifuged at 5300 rpm for 30 minutes and washed with ethanol at least 3 times to obtain a final dispersion of silica coated cobalt nanoparticles in ethanol with a concentration 0.1 mg/mL.

### **5.6.4 Preparation of amine-terminated Co@SiO<sub>2</sub> NPs**

To obtain the amine-functionalization on the surface, Co@SiO<sub>2</sub> NPs were mixed with 2.5 µL of an ethanolic solution 0.04 M of (3-Aminopropyl)triethoxysilane (APTES). The mixture was left under shaking overnight. The day after, the solution was centrifuged at 5300 rpm for 30 minutes and washed with ethanol at least 3 times to obtain a final dispersion of amine-terminated Co@SiO<sub>2</sub> NPs.

### **5.6.5 Coupling of amine-terminated Co@SiO<sub>2</sub> NPs with dyes**

0.1 mg of the N-hydroxysuccinimidic ester of the ATTO 655 dye (**1**) were added to an ethanolic solution 0.1 mg/mL of amine-terminated Co@SiO<sub>2</sub> NPs. The



solution was kept in the dark and under stirring overnight. The day after, samples were centrifuged at 5300 rpm for 30 minutes and washed with ethanol until no emission was detectable in the supernatant.

In the case of rhodamine B (2), amine-terminated Co@SiO<sub>2</sub> NPs were dispersed in dimethylformamide (DMF). Then 1.4 mg of N-hydroxysuccinimide and 2.2 mg of *N*-(3-Dimethylaminopropyl)-*N'*-ethylcarbodiimide hydrochloride (EDC) were added to the NPs solution. 6 mg of rhodamine B were dissolved in 4 mL of anhydrous DMF and added to the solution of NPs. Everything was flushed with nitrogen and the well-closed reaction mixture was left under stirring overnight. The day after, samples were centrifuged at 5300 rpm for 30 minutes and washed with ethanol until no emission was detectable in the supernatant.

## 5.6.6 Characterization

### *HR-TEM*

Samples for HR-TEM, EDX and EFTEM were prepared drop-casting an ethanolic solution of the sample on carbon coated copper grids (Quantifoil, GmbH). The analysis were performed using a FEI Titan 80-300 transmission electron microscope operated at 300 KV.

### *Estimation of the thickness of the coating from XPS intensities*

The estimation was done by assuming a spherical geometry, with a cobalt core surrounded by a silica shell of constant thickness **d**. According to a literature model<sup>[30]</sup>, **d** can be estimated to be  $\approx 50\%$  of the value that one would obtain in the case of a flat cobalt sample covered with an uniform silica overlayer. In the latter case, **d** can be evaluated from the intensity ratio between two photoelectron

lines of the cobalt substrate, having a large kinetic energy (KE) difference, namely Co2p (KE ~ 705 eV) and Co3p (KE ~ 1425 eV). Indicating as  $I_1$  and  $I_2$  the two measured intensities, we can write<sup>[31]</sup>:

$$\frac{I_1}{I_2} = \frac{I_1^0 \exp[-d/(\lambda_1 \cos \theta)]}{I_2^0 \exp[-d/(\lambda_2 \cos \theta)]} \quad (1)$$

where  $I_1^0$  and  $I_2^0$  are the intensities that one would measure in absence of the overlayer (i.e, for pure cobalt),  $\lambda_1$  and  $\lambda_2$  are the inelastic mean free paths (IMFPs) of the respective photoelectrons in the silica matrix (obtained from literature<sup>[32]</sup>), and  $\theta$  is the angle between the normal to the surface and the direction of the measured electrons (in our case  $90^\circ$ ). The intensities  $I_i^0$  can be written as<sup>[31]</sup>

$$I_i^0 \propto N \sigma_i \lambda_i T(E_i)$$

where N is the atomic density of cobalt (that cancels in the intensity ratio),  $\sigma_i$  is the photoionization cross section of the i-th orbital, available from tabulated data<sup>[33]</sup>, and T(E) is the (known) transmission function of the spectrometer. By defining the "corrected intensity" of a peak as

$$I_i' = \frac{I_i}{\sigma_i \lambda_i T(E_i)},$$

eq. 1 can be rearranged to obtain:

$$\mathbf{d} = \cos \theta \frac{\lambda_1 \lambda_2}{\lambda_1 - \lambda_2} \ln \frac{I_1'}{I_2'}$$

The value of  $\mathbf{d}$  obtained in this way must then be corrected for the spherical shape according to the already mentioned model<sup>[30]</sup>.

### ***Photophysical characterization***

Steady-state emission spectra were recorded on a HORIBA Jobin-Yvon IBH FL-322 Fluorolog 3 spectrometer equipped with a 450 W xenon arc lamp, as the excitation source, and a TBX-4-X single-photon-counting device as the detector. Emission and excitation spectra were corrected for source intensity (lamp and

grating) and emission spectral response (detector and grating) by standard correction curves.

### ***Confocal microscopy***

An ethanolic dispersion of NPs was deposited, by drop-casting, on a glass substrate. The sample was then imaged on a Confocal Microscope LSM 710 using excitation laser source of 630 nm.

## **5.7 References**

- [1] T.-J. Yoon, K. N. Yu, E. Kim, J. S. Kim, B. G. Kim, S.-H. Yun, B.-H. Sohn, M.-H. Cho, J.-K. Lee, S. B. Park, *Small* **2006**, *2*, 209-215.
- [2] C. Alexiou, R. Schmid, R. Jurgons, M. Kremer, G. Wanner, C. Bergemann, E. Huenges, T. Nawroth, W. Arnold, F. Parak, *Eur Biophys J* **2006**, *35*, 446-450.
- [3] K. McNamara, S. A. M. Tofail, *Physical Chemistry Chemical Physics* **2015**.
- [4] C. Ghobril, G. Popa, A. Parat, C. Billotey, J. Taleb, P. Bonazza, S. Begin-Colin, D. Felder-Flesch, *Chemical Communications* **2013**, *49*, 9158-9160.
- [5] S. Lesieur, F. Gazeau, N. Luciani, C. Menager, C. Wilhelm, *Journal of Materials Chemistry* **2011**, *21*, 14387-14393.
- [6] L. Lartigue, P. Hugounenq, D. Alloyeau, S. P. Clarke, M. Lévy, J.-C. Bacri, R. Bazzi, D. F. Brougham, C. Wilhelm, F. Gazeau, *ACS Nano* **2012**, *6*, 10935-10949.
- [7] H. B. Na, I. C. Song, T. Hyeon, *Advanced Materials* **2009**, *21*, 2133-2148.
- [8] A. Riedinger, P. Guardia, A. Curcio, M. A. Garcia, R. Cingolani, L. Manna, T. Pellegrino, *Nano Letters* **2013**, *13*, 2399-2406.
- [9] A. Walter, C. Billotey, A. Garofalo, C. Ulhaq-Bouillet, C. Lefèvre, J. Taleb, S. Laurent, L. Vander Elst, R. N. Muller, L. Lartigue, F. Gazeau, D. Felder-Flesch, S. Begin-Colin, *Chemistry of Materials* **2014**, *26*, 5252-5264.
- [10] J. Kolosnjaj-Tabi, R. Di Corato, L. Lartigue, I. Marangon, P. Guardia, A. K. A. Silva, N. Luciani, O. Clément, P. Flaud, J. V. Singh, P. Decuzzi, T. Pellegrino, C. Wilhelm, F. Gazeau, *ACS Nano* **2014**, *8*, 4268-4283.
- [11] C. Wilhelm, F. Gazeau, *Journal of Magnetism and Magnetic Materials* **2009**, *321*, 671-674.
- [12] J. Sengupta, S. Ghosh, P. Datta, A. Gomes, A. Gomes, *Journal of Nanoscience and Nanotechnology* **2014**, *14*, 990-1006.
- [13] L.-Y. Lu, L.-N. Yu, X.-G. Xu, Y. Jiang, *Rare Met.* **2013**, *32*, 323-331.

- [14] J. P. Chen, C. M. Sorensen, K. J. Klabunde, G. C. Hadjipanayis, *Journal of Applied Physics* **1994**, *76*, 6316-6318.
- [15] C. N. R. Rao, G. U. Kulkarni, P. J. Thomas, in *Nanocrystals: Synthesis, Properties and Applications*, Springer-Verlag, **2007**, pp. 1-23.
- [16] S. N. Khanna, S. Linderoth, *Physical Review Letters* **1991**, *67*, 742-745.
- [17] L. M. Parkes, R. Hodgson, L. T. Lu, L. D. Tung, I. Robinson, D. G. Fernig, N. T. K. Thanh, *Contrast Media & Molecular Imaging* **2008**, *3*, 150-156.
- [18] M. Kobayashi, S. Shimizu, *European Journal of Biochemistry* **1999**, *261*, 1-9.
- [19] Y. Kobayashi, M. Horie, M. Konno, B. Rodríguez-González, L. M. Liz-Marzán, *The Journal of Physical Chemistry B* **2003**, *107*, 7420-7425.
- [20] N. Batail, I. Clémençon, C. Legens, A. Chaumonnot, D. Uzio, *European Journal of Inorganic Chemistry* **2013**, *2013*, 1258-1264.
- [21] V. Salgueiriño-Maceira, M. A. Correa-Duarte, M. Farle, M. A. López-Quintela, K. Sieradzki, R. Diaz, *Langmuir* **2006**, *22*, 1455-1458.
- [22] V. Salgueiriño-Maceira, M. Spasova, M. Farle, *Advanced Functional Materials* **2005**, *15*, 1036-1040.
- [23] H. Bönemann, W. Brijoux, R. Brinkmann, N. Matoussevitch, N. Waldöfner, N. Palina, H. Modrow, *Inorganica Chimica Acta* **2003**, *350*, 617-624.
- [24] H. Bönemann, W. Brijoux, R. Brinkmann, N. Matoussevitch, W. Norbert, *Vol. WO/2004/001776* Germany, **2003**.
- [25] S. Behrens, H. Bönemann, N. Matoussevitch, E. Dinjus, H. Modrow, N. Palina, M. Frerichs, V. Kempter, W. Maus-Friedrichs, A. Heinemann, M. Kammel, A. Wiedenmann, L. Pop, S. Odenbach, E. Uhlmann, N. Bayat, J. Hesselbach, J. M. Guldbakke, *Z. Phys. Chem.* **2006**, *220*, 3-40.
- [26] S. Behrens, H. Bönemann, N. Matoussevitch, A. Gorschinski, E. Dinjus, W. Habicht, J. Bolle, S. Zinoveva, N. Palina, J. Hormes, H. Modrow, S. Bahr, V. Kempter, *Journal of Physics: Condensed Matter* **2006**, *18*, S2543.
- [27] N. Matoussevitch, A. Gorschinski, W. Habicht, J. Bolle, E. Dinjus, H. Bönemann, S. Behrens, *Journal of Magnetism and Magnetic Materials* **2007**, *311*, 92-96.
- [28] W. Stöber, A. Fink, E. Bohn, *Journal of Colloid and Interface Science* **1968**, *26*, 62-69.
- [29] N. Wu, L. Fu, M. Su, M. Aslam, K. C. Wong, V. P. Dravid, *Nano Letters* **2004**, *4*, 383-386.
- [30] M. Mohai, I. Bertóti, *Surface and Interface Analysis* **2004**, *36*, 805-808.
- [31] D. Briggs (editor), *Handbook of X-ray and ultraviolet photoelectron spectroscopy* Heyden, **1977**.
- [32] S. Tanuma, C. J. Powell, D. R. Penn, *Surface and Interface Analysis* **2011**, *43*, 689-713.
- [33] J. H. Scofield, *Journal of Electron Spectroscopy and related phenomena* **1976**, *8*, 129-137.

# Chapter 6

## Instrumental techniques

### Abstract

In this Chapter, a short overview on the main techniques used during this thesis, is given. For each technique, the general features are described, while the details regarding particular experiments and measurements are reported in the experimental section of the pertinent Chapter. Commonly used spectroscopic techniques (such as UV-visible or infrared spectroscopy) are not discussed here.

### 6.1 Transmission Electron Microscopy (TEM)

Transmission electron microscopy (TEM)<sup>[1,2]</sup> is a technique capable to supply high resolution images, with resolution down to atomic scale. Therefore, it is a powerful technique for the morphological study of nanomaterials. Analogously to SEM (scanning electron microscopy), TEM technique is based on the interaction of matter with an energetic electron beam. According to the De Broglie law ( $p = h/\lambda$ ) the wavelength associated to a 10 keV electron is about 0.2 nm and it decreases by increasing the energy. For this reason, electron microscopies allow to overcome the resolution limitations of conventional optical microscopies, dictated by the diffraction limit. Actually, in electron microscopies the image resolution is dictated by other phenomena, such as electron scattering in SEM and lens limitations in TEM. Since its development in the '30s of the past century by Knoll and Ruska and the spreading of its commercial availability in the second half of the '900, TEM became an invaluable tool in materials science and in biology.

In TEM technique the energetic electron beam (typical energy in the range 80 – 400 keV) illuminates an ultra-thin sample and passes through it. Basically, an image is formed in a similar way of that of an optical microscope, but the lenses, due to the charged nature of the illuminating beam, are electromagnetic lenses. In Figure 6.1, a simplified scheme of the components of a TEM instrument is reported.

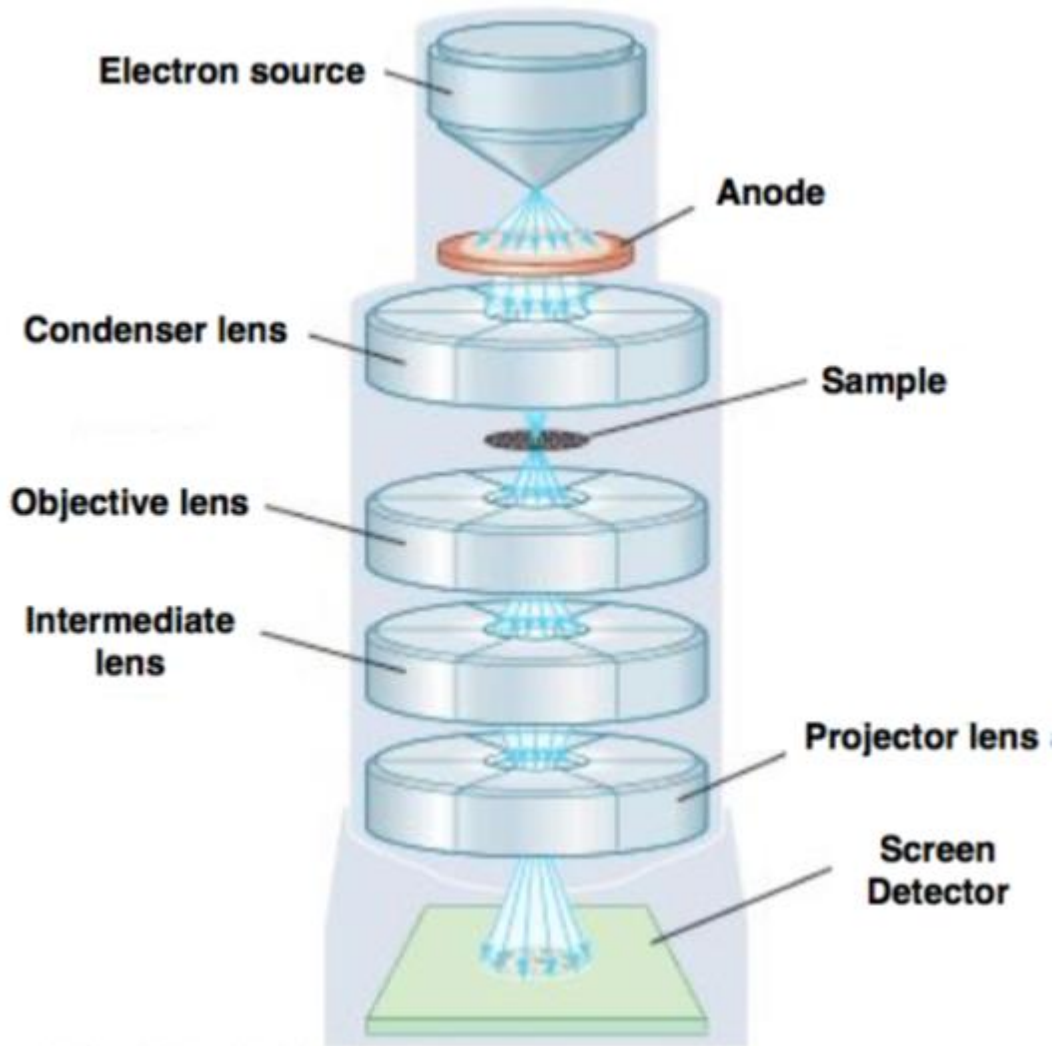


**Figure 6.1.** Schematic illustration of the basic components of an electron microscope

A typical instrument is vertically arranged. The electron source is located at the top of the column and the electron beam reaches the sample after being focused on the sample plane through the condenser lens. Right after the sample, the object lens generates the intermediate image which is then magnified by the

intermediate lens and projected on the plane of a position-sensitive detector by the projection lens. The system is maintained under high vacuum conditions in order to prevent the scattering of electrons. Electrons encountering no objects do not suffer deviations, but when passing through a solid sample, part of them are diffracted either by elastic or inelastic processes. The images of the elastically diffracted and non-diffracted electrons are recombined on the plane of the detector, and the contrast is due to the scattering properties of the different parts of the sample. For example, inclusions containing heavy elements in a light-element matrix will be imaged as darker areas in a more brilliant field (bright field image). It is also possible, by manipulating a suitable diaphragm, to allow only the diffracted electron to reach the detector, thus obtaining a "dark field" image in order to evidence particular features in the sample.

TEM technique provides also important crystallographic information thanks to the possibility of recording electron diffraction images, which are interpreted in a similar way of the standard X-ray diffraction patterns, according to the Bragg's law. Moreover, the interaction processes occurring between the electron beam and the sample can be exploited for obtaining additional important information on the sample. As sketched in Figure 6.2, EFTEM images and EDX spectra can be obtained. Both techniques are based on processes involving inelastic interactions between the sample and the electron beam. The two techniques will be outlined briefly in the following sections.

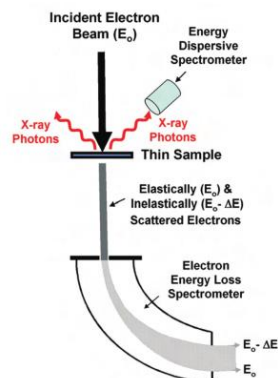


**Figure 6.2.** Scheme outlining the exploitation of inelastic scattering events for sample characterization

## 6.2 Energy-Filtered Transmission Electron Microscopy

Energy-Filtered Transmission Electron Microscopy (EFTEM)<sup>[3]</sup> is based on the energy loss features of the inelastically scattered electrons in the TEM instrument. An electron energy loss spectrum (EELS) reports the intensity of inelastically scattered electrons as a function of the energy difference with the elastic ("zero loss") peak. In an EELS spectrum several features appear. In the higher energy loss regime ( $> 40$  eV) steps or edges appear in the spectrum, at an energy loss value corresponding to the ionization of inner shell electrons of the elements present in the sample (ionization edge). The ionization edge reflects the atomic structure of the element and it is useful for elemental analysis. Figure 6.3 shows a scheme of an energy loss spectrum. The ionization edges of the inner core electrons are low intensity features over a large background due to other energy loss mechanisms, such as plasmon losses. In order to quickly acquire elemental maps, EFTEM technique makes use of energy filters for obtaining intensity maps by using energy windows selected in the pre-edge (1,2 in Figure 6.3) and post-edge regions (3 in Figure 6.3) that are subsequently computationally combined in order to take into account the background.

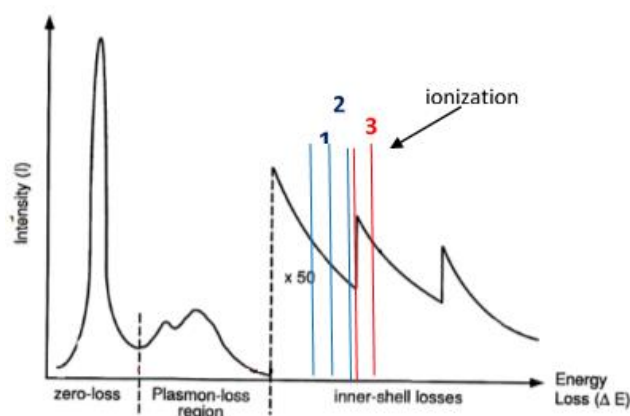


**Figure 6.3.** Illustration of the main features of an energy loss spectrum with indication of the energy windows used (three windows method) for obtaining elemental maps in EFTEM

### **6.3 Energy dispersive X-ray spectroscopy**

The technique,<sup>[4]</sup> referred as energy dispersive X-ray spectroscopy (EDS, EDX or EDA), is commonly coupled with electron microscopies, either SEM or TEM. It is used for the quantitative determination of the composition of materials in the desired area.

EDS is based on the X-rays fluorescence caused by the relaxation of core holes generated by electron-induced ionization of the inner shells of the elements. When the core hole is created, an electron from the outer shells will fill the core vacancy, with a simultaneous emission of an X-ray photon. The energy of the emitted X-ray radiation depends on energy difference between the two involved orbitals in the atom, so each element can be identified from the characteristic peaks in the EDS spectrum. EDS can be exploited in a spatially resolved way, by synchronizing the EDS data with a SEM or TEM image.

Due to the competition between X-ray fluorescence and Auger emission pathways for the relaxation of the core-hole, EDS is more sensitive for heavy elements. In practice, only elements heavier than Beryllium can be detected.

### **6.4 Emission and excitation spectroscopy<sup>[5]</sup>**

As it could be seen in this thesis, it is very interesting to investigate the photoluminescence properties of nanomaterials. In order to do this, a common spectrofluorimeter can be used to acquire both emission and excitation spectra. In Figure 6.4, the schematic setup of a spectrofluorimeter is shown. In brief, it is composed by an excitation source (in this thesis a 450 W xenon arc lamp), a dual grating monochromator through which the light passes to be directed to a

reference detector and to the sample. Emission of the sample is collected at  $90^\circ$  with respect to the incident excitation light. After, the light passes through a second monochromator to reach the detector that usually is equipped with a photomultiplier tube to amplify the signal received. The spectra are corrected for source intensity (lamp and excitation grating) and for detector spectral response and emission grating by standard correction curves (emission monochromator and Photomultiplier, PM).

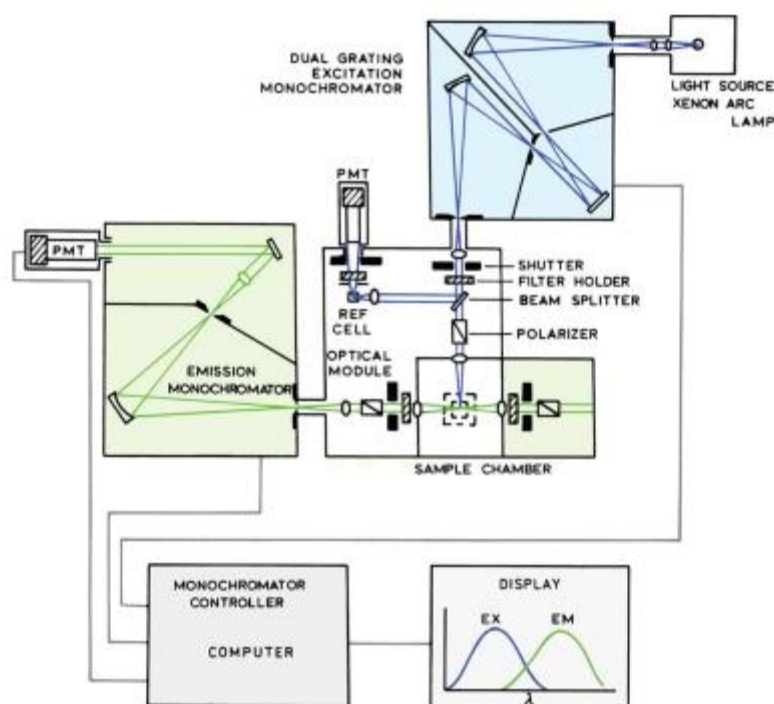


**Figure 6.4.** Schematic setup of a fluorimeter

### 6.4.1 Integrating sphere

Absolute photoluminescence quantum yields (PLQY) were measured using an integrating sphere (IS). This instrument is based on a hollow spherical cavity internally coated with a reflective material. The sample is positioned inside the IS. When the excitation light reaches it, the sample emits and the light is scattered and reflected, by the inner coating of the sphere, in all directions. In this way the effects of the original direction of the light are minimized.

A schematic setup for this instrument is shown in Figure 6.5.

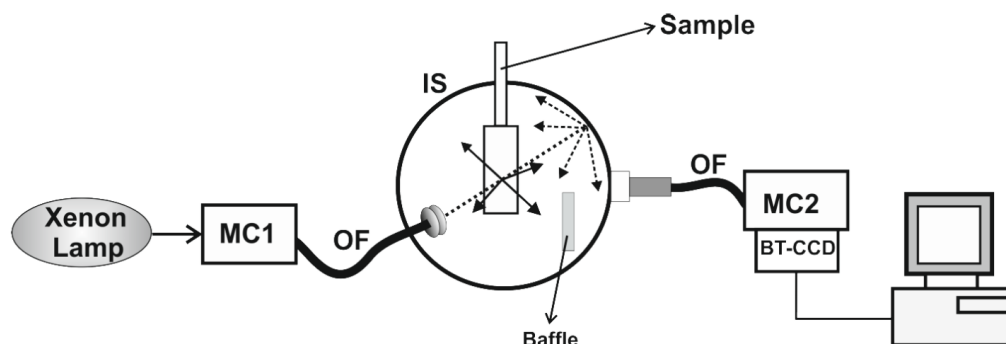


**Figure 6.5.** Schematic setup of an integrating sphere (MC = monochromator; OF = optical fiber, BT-CCD = back thinned CCD)

In the general setup, the light coming from a xenon lamp is monochromatized at the selected wavelength and it arrives to the sphere through an optical fiber (OF). The sample is positioned inside the IS and the light, emitted by it, is collected by a detector, after passing through another optical fibre and a monochromator (MC2). The measurement for the reference (solvent in a quartz tube) is acquired in the same conditions used for the sample. Then the sample in the same solvent used for the reference is also measured. The software corrects the quantum yields for the reference to give the values of absolute PLQY according to the equation in Figure 6.6.

$$\Phi = \frac{N_{emission}}{N_{absorption}} = \frac{\int \frac{\lambda}{hc} \{I_{em}^S(\lambda) - I_{em}^R(\lambda)\} d\lambda}{\int \frac{\lambda}{hc} \{I_{ex}^R(\lambda) - I_{ex}^S(\lambda)\} d\lambda}$$

**Figure 6.6.** Equation used by the software to calculate the PLQY.

PLQY represents the ratio between the number of photons absorbed by the sample ( $N_{absorption}$ ), and the number of photons emitted by the sample ( $N_{emission}$ ). In Figure 6.6  $I_{em}$  stands for intensity of the emission and  $I_{ex}$  for intensity of the

excitation light, S and R stands for sample and reference respectively,  $h$  is the Planck's constant and  $c$  is the speed of light.

## 6.4.2 Lifetime measurements

To measure the excited state lifetime, a spectrofluorimeter equipped with a pulsed excitation source (typically a laser or a flash lamp) and a time-correlated single-photon counting (TCSPC) module is used. In Figure 6.7, the general setup it is shown.

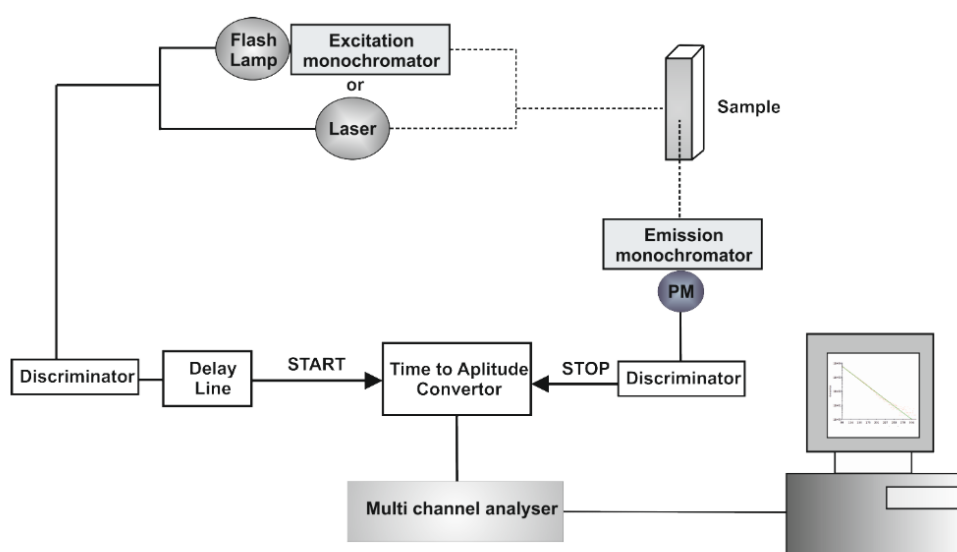


**Figure 6.7.** General setup for the measurements of lifetimes

The sample is excited with a pulsed excitation source. Each pulse of the excitation source generates an electrical signal that represents the START input of the TAC (time-to amplitude converter). The sample excited from the pulse of the excitation source will emit. Every time a photon is emitted, the detector translates it in an electrical signal that represents the STOP signal for the TAC. The final voltage measured by the TAC is proportional to the time passed between the START and the STOP signals and it is recorded as a histogram in which the x-axis represents the time passed between the START and the STOP signals and the y-axis represents the number of photons emitted during this time. The final form of the graph is a decay that can be fitted giving the values of

excited state lifetime and the relative contributions of each components (for multi-exponential decays).

## 6.5 X-ray photoelectron spectroscopy

X-ray Photoelectron Spectroscopy (XPS) is a well-established technique for the study of solid surfaces<sup>[6,7]</sup>. Following the suggestion of its founder, K. Siegbahn, the technique is often referred to as Electron Spectroscopy for Chemical Analysis (ESCA), so outlining the analytical potentialities that, actually, make XPS one of the most important tools for investigating the chemical composition of solid surfaces. A deep description of the theoretical and experimental details of this spectroscopy is out of the scope of this work. To this aim, several reviews and handbooks are available. Here the discussion will be limited to some of the main features of the technique, in connection to the kind of information obtained for this thesis work.

In XPS the material is irradiated with soft X-rays that cause emission of electrons ("photoelectrons") from the material. Photoelectrons originating from depths close to the sample surface can escape without inelastic scattering. For a conducting sample, their kinetic energy KE is given by:

$$KE = h\nu - BE - \phi$$

where  $h\nu$  is the energy of the exciting X-ray photon, BE is the electron binding energy relative to the Fermi level of the sample and  $\phi$  is the work function.

In a XPS spectrometer, photoelectrons emitted are energy analyzed and the output is a spectrum of electron counts *vs* kinetic energy. On the basis of the above equation, the x-axis can be converted in BE so that the energy of the peaks can be regarded as the energy (with opposite sign) of the orbital from which the photoelectrons originate (Koopman's approximation). So, from a XPS spectrum we obtain information on the orbitals of the atoms present in the material and hence an immediate qualitative elemental information. Actually from a simple survey spectrum it is possible to identify any element of the periodic table (excluding hydrogen and helium, due to the very low photoionization cross

section) virtually without any spectral interference. Indeed, even in the case of overlap of the peaks of certain electrons of two different elements, it is possible to discriminate among the possibilities by looking for the expected positions of the other peaks. Additional chemical information can be extracted by other features present in the spectra such as Auger peaks and energy loss features.

XPS supplies information on the chemical state of the elements detected, since BE of the core level electrons is influenced by the chemical environment, and this is reflected in a "chemical shift" of BEs that can be roughly related to oxidation state or to the charge density on the selected atom. Extensive compilations and databases of chemical shifts are, helping in the identification of the species present in the sample. Often the chemical shift is not enough for resolving among different chemical states, and curve resolution procedures are necessary. Modern instrumentation is provided with software for curve resolution, but several independent programs are available for such purpose.

XPS is a surface technique since the useful information is brought by the electrons that did not suffer inelastic scattering events: for this reason the electrons originating from deeper layers have an increasingly lower probability to escape from the surface without inelastic scattering.

In the case of an overlayer A of uniform thickness  $d$  over a homogeneous material B, the thickness intensities  $I_A$  and  $I_B$  of photoelectron peaks characteristic of the two layers can be evaluated as follows:

$$I_A = I_A^\infty [1 - \exp(-\frac{d}{\lambda_{AA} \cos \theta})] ; \quad I_B = I_B^0 \exp(-\frac{d}{\lambda_{BA} \cos \theta})$$

where  $I_A^\infty$  is the intensity of pure A of infinite thickness;  $I_B^0$  is the thickness of B in the absence of the overlayer;  $\lambda_{AA}$  and  $\lambda_{BA}$  are the IMFPs of electrons of A and B in the material of the overlay A.

A quantitative evaluation of surface composition can be obtained from the peak intensities. Indeed the intensity  $I_{j,A}$  of a photoelectron peak originating from the  $j$ -th orbital of the atom A is proportional to the photoemission cross section  $\sigma_{i,A}$  to the atomic density  $n_A$  of the atom A and to the inelastic mean free  $\lambda_A$  that, in

turn, depends on the kinetic energy  $KE_j$  of the considered photoelectron. Moreover, the instrument transmission function  $T(KE)$  must be considered.

In practice we can write:

$$I_{j,A} = k \sigma_{i,A} n_A (KE_j)^\alpha$$

where  $k$  is a proportionality factor (depending, within the same experiment, on constant instrumental factors) that cancels out when considering intensity ratios and  $\alpha$  is a parameter that includes the dependence on  $KE$  of both the IMFP and the transmission function, and is characteristic for the particular instrument used. Since all the quantities present in the above, with the exclusion of  $n_A$ , are known quantities (either from measurements or from theoretical calculations), the above equation can be used for calculating the atomic ratios present within the sampled depth.

## 6.6 Positron emission tomography

Positron emission tomography (PET) imaging<sup>[8]</sup> can be performed only if the detected animal contains a radiotracer. In this thesis,  $^{64}\text{Cu}$  was used. This radioisotope is often used in nuclear medicine because it has a half-time of 12 hours and it decays, by positron emission to  $^{64}\text{Ni}$ . In Figure 6.8 a general scheme for the positron emission process is shown.

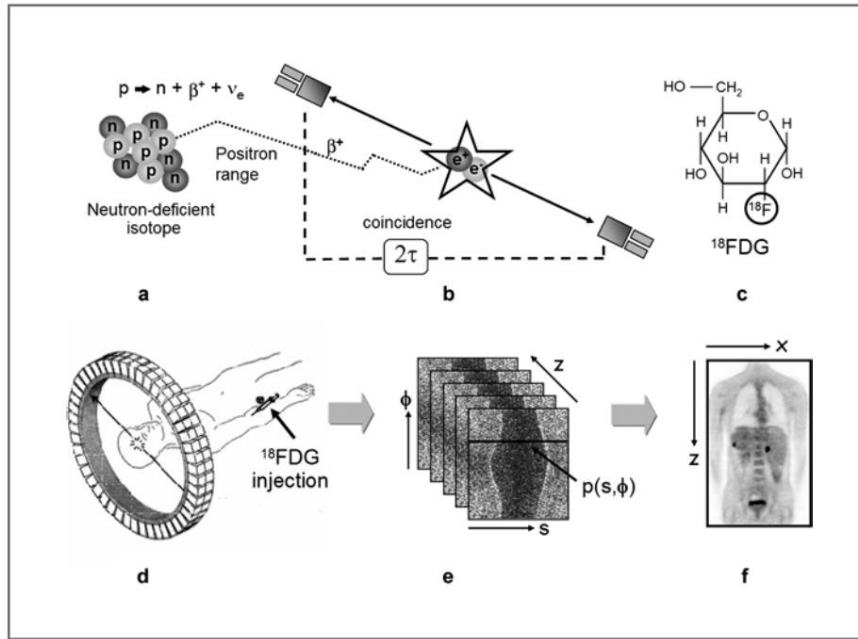


**Figure 6.8.** General setup of a PET scanner.

Positron emitters are neutron-deficient species. Therefore, they reach stability transforming a proton ( $p$ ) into a neutron ( $n$ ). During this process, a positive electron, also known as positron ( $\beta^+$ ), is emitted. The specific energy of the positron emitted depends on the radioisotope used. The positron emitted loses energy until it annihilates with an electron. This event produces two  $\gamma$ -photons with the same energies and which are emitted in opposite directions. These photons are detected in coincidence. The simultaneous detection of the two photons is the crucial characteristic of PET technique. From the position in which the emission of the two photons took place, it is possible to understand in which part of the body they were emitted giving the opportunity to study physiological processes by following the pathway of suitable tracers injected in the body.

## 6.7 References:

- [1] J. J. Bozzola, L. D. Russell, *Electron microscopy: principles and techniques for biologists*, Jones & Bartlett Learning, **1999**.

- [2] D. B. Williams, C. B. Carter, *The Transmission Electron Microscope* Springer, **1996**.
- [3] R. Egerton, in *Transmission Electron Energy Loss Spectrometry in Materials Science* (Eds.: M. M. Disko, C. C. Ahn, B. Fultz), TMS Warrendale, **1992**, p. 29.
- [4] D. C. Joy, A. D. Romig, J. I. Goldstein, *Principles of Analytical Electron Microscopy*, Plenum Press, **1986**.
- [5] J. R. Lakowicz, *Principles of Fluorescence Spectroscopy*, Springer, **2006**.
- [6] D. Briggs (editor), M. P. Seah (editor), *Practical Surface Analysis*, Wiley, **1990**.
- [7] J. C. Vickerman (editor), I. S. Gilmore (editor), *Surface Analysis-The Principal Techniques*, Wiley, **2009**.
- [8] P. E. Valk, D. Delbeke, D. L. Bailey, D. W. Townsend, M. N. Maisey, *Positron Emission Tomography Clinical Practice*, Springer, **2006**.



# Summary

The aim of this thesis, titled "Design, synthesis and functionalization of ultrasmall nanoparticles for bioimaging" is the synthesis, characterization, functionalization and *in vitro* and *in vivo* investigation of different kinds of ultrasmall (< 5 nm) nanoparticles. The work focuses on silicon nanoparticles (Si NPs), carbon dots (CQDs) and silica-coated cobalt NPs (Co@SiO<sub>2</sub> NPs), which exhibit luminescence or magnetic properties and can be functionalized through covalent bonds. This renders these systems very attractive for *in vivo* multimodal imaging, which requires the stable anchoring of multiple functionalities (e.g. labels and targeting agents) on a single nano-sized platform. The thesis is organized in six chapters.

**Chapter 1**, after a brief introduction to nanoparticles and their applications in medicine, discusses the problems connected with accumulation of NPs in organs and the requirements that nanomaterials should meet for *in vivo* imaging. In this context, the current applications of the emerging field of ultrasmall NPs are illustrated, with particular attention to the perspectives in multimodal imaging. The second part of the Chapter gives an overview of the state-of-art on properties, methods of preparation, functionalization, *in vitro* and *in vivo* applications of ultrasmall Si NPs, CQDs and Co NPs.

**Chapter 2** focuses on the still challenging preparation of ultrasmall Si NPs and on their characterization from the morphological, compositional and photophysical point of view. Two synthetic strategies, microemulsion and hydrothermal synthesis, were optimized for obtaining amine-terminated NPs that were characterized by HR-TEM, EDX, ATR-FTIR, XPS, and photophysical measurements. Both methods allowed to obtain crystalline ultrasmall Si NPs (Figure S1) with narrow size distribution and an average size of  $2.5 \pm 0.6$  nm and  $4.3 \pm 1.3$  nm, respectively, by microemulsion and hydrothermal approach. All the obtained Si NPs feature blue emission under UV irradiation (Figure S1). In both cases, the maximum of the photoluminescence (PL) is excitation-

dependent, with a red shift at increasing wavelength. These tunable PL properties are more pronounced in the 2.5 nm Si NPs prepared by microemulsion method. On a several months timescale, the microemulsion-prepared NPs show more stable PL than the hydrothermal ones. In addition, the microemulsion synthesis leads to NPs with lower surface oxide content. On the other hand, the hydrothermal method allows to prepare, with an easier synthesis and much less purification efforts, larger quantities of slightly bigger NPs (4.3 nm) that contain a higher amount of silicon oxide but display higher PL quantum yields (13 %), although their emission is less stable in time.

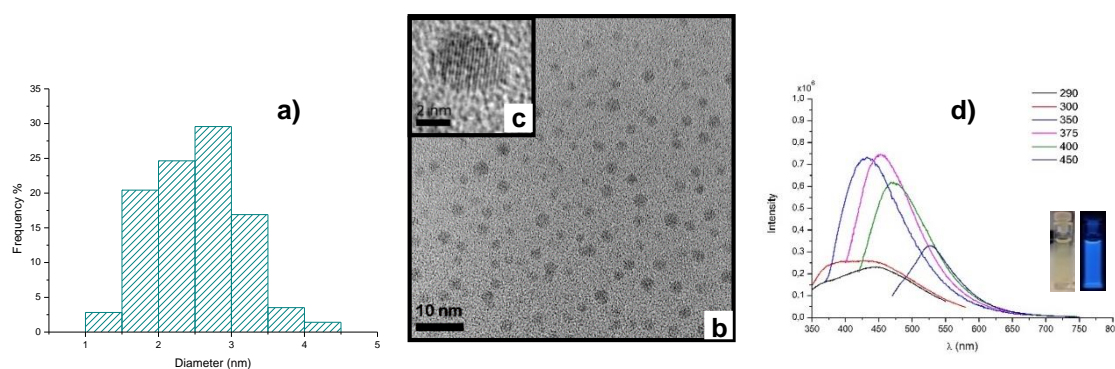


**Figure S1.** Main characteristics of amine-terminated Si NPs obtained by microemulsion technique: **a)** Size distribution graph (average size  $2.5 \pm 0.6$  nm); **b), c)** HR-TEM images, in **c)** the crystal fringes of silicon are clearly visible; **d)** Emission spectra at various excitation wavelengths in ethanol (the excitation wavelengths, in nm, are reported on the top right); inset: pictures of the solution under ambient illumination (left) and under UV irradiation (right)

**Chapter 3** deals with the further surface modification of Si NPs with functional molecules, such as dyes (cyanine, Cy5) or radiotracers ( $^{64}\text{Cu}$ -NOTA complex) suitable for *in vivo* optical or positron emission tomography (PET) imaging. *In vitro* tests in A549 cell lines (Figure S2a) assessed a low toxicity of both types of amine terminated NPs, with better performances of the hydrothermal NPs at higher concentrations (up to 1 mg/mL). The Cy5-functionalized NPs display low cytotoxicity and penetrate cells *via* an energy-dependent mechanism such as endocytosis. In *in vivo* experiments, either optical imaging with the red emitting Cy5-Si NPs (Figure S2c) or positron emission tomography (exploiting the  $^{64}\text{Cu}$ -

NOTA-Si NPs), show that the functionalized Si NPs are readily excreted through the bladder (50 minutes post-injection in mice). However, *in vivo* PET imaging (Figure S2b) and biodistribution experiments show significant differences between the hydrothermal- and microemulsion-prepared Si NPs coupled with the  $^{64}\text{Cu}$  complex. In particular, while microemulsion-prepared NPs feature some accumulation in the intestine, hydrothermal NPs behave in an ideal way being completely excreted through renal pathway. The latter result demonstrates the feasibility of the application of ultrasmall Si NPs in *in vivo* PET imaging. The result is very promising because the only existing report on *in vivo* PET imaging with ultrasmall Si NPs, differently prepared, shows that they accumulate in the liver.

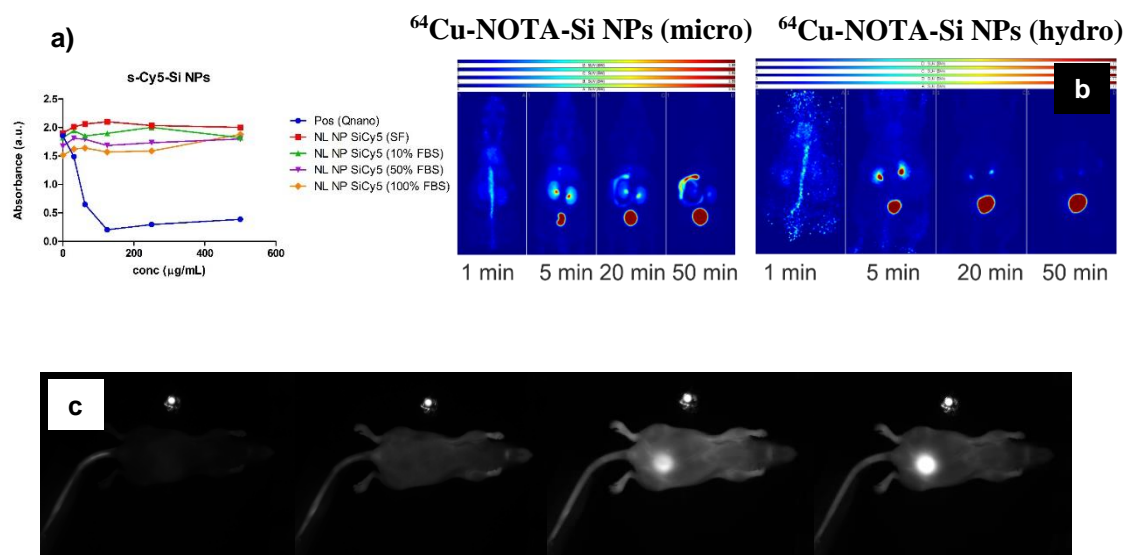


**Figure S2 a)** MTS assay after 24 hours incubation in A549 cell lines of sulfo-cyanine 5-modified silicon nanoparticles (s-Cy5-Si NPs) in cell culture medium at increasing amounts (SF = serum free) of fetal bovine serum (FBS); Pos (Qnano) are the positive control toxic NPs; **b)** PET images at different times post-injection of NMRI nu/nu mice injected with Si NPs made by microemulsion (top left) or hydrothermal (top right) method; **c)** Optical images of NMRI nu/nu mice at 0, 5, 20, 50 minutes post-injection of s-Cy5-Si NPs; the bright spot on the top is a solution of s-Cy5-Si NPs with the same concentration of the solution injected.

**Chapter 4** is dedicated to the preparation, characterization, surface functionalization and *in vivo* experiments of carbon dots (CQDs) with the aim to compare the *in vivo* behavior of such material to Si NPs. 3 nm sized CQDs, displaying multi-coloured emission that red-shifts at increasing excitation wavelengths, were coupled with Cy-5 or with  $^{64}\text{Cu}$ -NOTA complex. *In vivo* PET imaging of  $^{64}\text{Cu}$ -labelled CQDs (Figure S3) performed in the same conditions used for Si NPs, show that CQDs, analogously to Si NPs, are excreted through the bladder at 50 minutes post-injection. However, part of them, in contrast to Si NPs, stack in the liver and in the intestine. Biodistribution experiments show that CQDs are excreted through both renal and hepatobiliary elimination mechanisms, similar to microemulsion NPs.

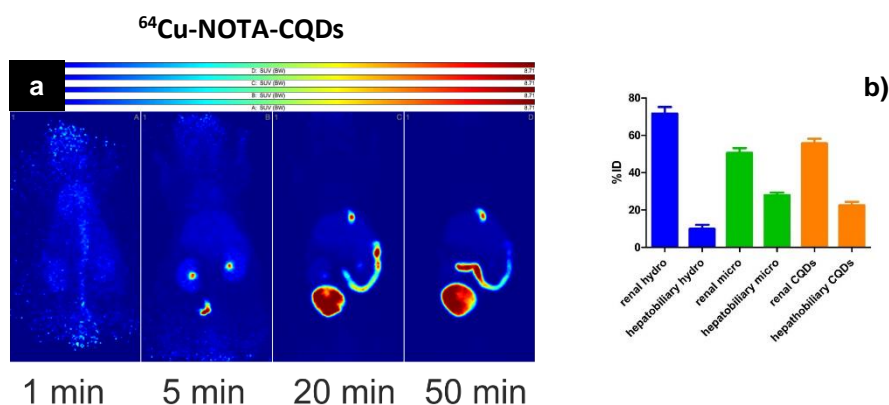


**Figure S3.** **a)** Positron emission tomography images, at different times post-injection, of NMRI nu/nu mice injected with  $^{64}\text{Cu}$ -NOTA-CQDs; **b)** Histogram showing the comparison between the ratio renal/hepatobiliary mechanisms of excretion for  $^{64}\text{Cu}$ -NOTA-Si NPs, prepared by hydrothermal (hydro) or microemulsion (micro), and for  $^{64}\text{Cu}$ -NOTA-CQDs

Finally, **Chapter 5** deals with the preparation and characterization of  $\text{Co}@\text{SiO}_2$  NPs with total average diameter < 10 nm. Cobalt NPs (Co NPs) are attractive for *in vivo* applications because of the high saturation magnetization, which could allow the introduction in the body of a smaller amount of NPs compared to magnetic oxide NPs. The silica coating should have the dual function of isolating the toxic cobalt core from the biological environment and allowing an easy covalent functionalization of the NPs. A synthetic method was optimized for

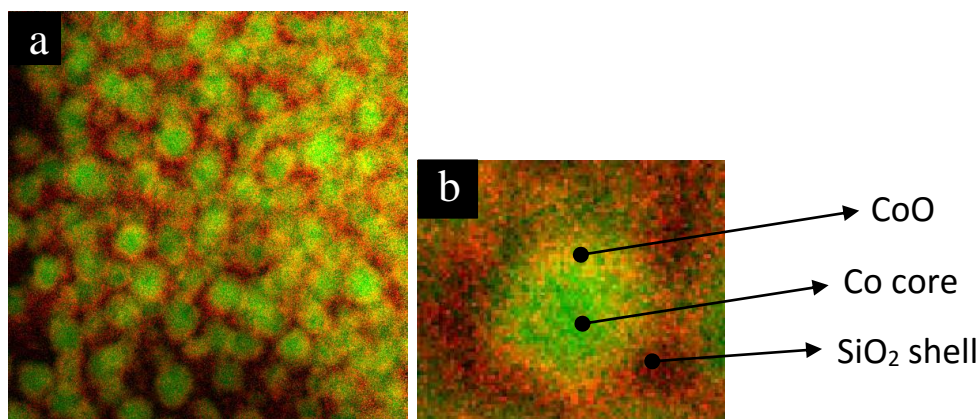


**Figure S4.** EFTEM maps of cobalt and oxygen (green: cobalt; red: oxygen); **a**) false colour overlay of cobalt and oxygen maps; **b**) overlay image zoomed on a single particle.

obtaining an ultrathin silica shell ( $\approx 2$  nm) avoiding the formation of a continuous matrix (Figure S4). Particles were, then, functionalized with amine moieties, that can be subsequently used for further functionalization. Co@SiO<sub>2</sub> NPs were characterized by means of TEM, EFTEM, EDX and XPS measurements. XPS data and preliminary couplings with model dyes confirm the presence of amine-moieties, suggesting the possibility to functionalize the surface in the perspective of a possible future use in bioimaging.

Finally, **Chapter 6** gives a short overview on the basic principles of the main instrumental techniques used during the thesis work.

In conclusion, this thesis shows that ultrasmall NPs, such as Si NPs, CQDs and Co@SiO<sub>2</sub> NPs can be prepared, characterized and functionalized through stable covalent bonds with dyes or radiotracers to study the *in vitro* and *in vivo* behavior. NPs present the properties expected and, when tested *in vitro*, they showed very low cytotoxicity. Promising *in vivo* results have been obtained since both Si NPs and CQDs were excreted from the body in short times (50 minutes). In addition, Si NPs, made by hydrothermal method, gave the best result since they showed a very good behavior in *in vivo* PET imaging, being completely excreted after 50 minutes from injection in the body and showing no accumulation in organs. Finally, Co@SiO<sub>2</sub> NPs were successfully prepared and

surface functionalized, and couplings with dyes indicate the availability of the amine moieties for possible further couplings.

This work was supported by the Helmholtz Association on Virtual Institute “Functional nanomaterials for multimodality cancer imaging” (Nano-Tracking, Agreement Number VH-VI-421).

The work was done between the University of Strasbourg and in particular, the Institute de Science et d’Ingénierie Supramoléculaires (ISIS, Strasbourg), and the Karlsruhe Institute of Technology (KIT, Karlsruhe). Both institutes are acknowledged for the hospitality and the use of instrumentation and facilities.

The WWU University of Muenster is also acknowledged for the hospitality during the first year of work.

The work described was done in cooperation with: the group of Dr. Holger Stephan at the Helmholtz-Zentrum Dresden-Rossendorf (HZDR), Dresden; the group of Prof. Kenneth A. Dawson at the University College of Dublin (UCD), Dublin; the group of Prof. Michele Maggini at the University of Padova.

## ACKNOWLEDGEMENTS

My list of acknowledgements is very long since I had the luck to meet many people, during my PhD pathway, from whom I learnt a lot about science, research and life. I started my PhD in Muenster, Germany, to continue it in Strasbourg, France and, as my PhD story, also my acknowledgements will move a little bit around Europe.

Firstly, I want to acknowledge my supervisor, Prof. Luisa De Cola, who gave me the great opportunity to carry on a PhD abroad in her amazing group. Thank you for all the things you taught me about research and all the interesting and always illuminating discussions we had. Also, thank you for the opportunity to work on a big project that gave me the opportunity to meet many people, learn many new things and travel a lot.

I want to thank our collaborators and, in particular, Dr. Holger Stephan, Dr. Ralf Bergmann and Sebastian Hunoldt from HZDR in Dresden; Prof. Kenneth A. Dawson and Dr. Louise Rocks from the UCD in Dublin; Prof. Michele Maggini and Dr. Simone Silvestrini from the University of Padova; Dr. Katerina Dohnalova and Bart van Dam from the Van der Waals-Zeeman Instituut in Amsterdam. A special thank also to Dr. Christian Kuebel and Dr. Di Wang from KIT in Karlsruhe. The financial support by Nano-tracking project (for details, page 162) is gratefully acknowledged.

Coming back to Strasbourg, I want to thank the entire De Cola group. It was very productive to study in this group, I learnt a lot and I have now many very good friends. I learnt how beautiful is to work in cooperation with people from all over the world. Thank you Eko for all the help, for giving me many advices and for many interesting discussions we had. Thank you very much Amparo (Amparito) for helping a lot during these years, especially in the last period, and for having shared with me many interesting scientific (and not) discussions; you are a good friend and I learnt a lot from you. Thank you Angélique, it was great to have the opportunity to discuss with an expert of silicon nanoparticles, thanks for all the help you gave me. Thank you Ingrid (for me simply Ingriduzza) to have helped a lot in the hard days of the writing process, to have driven me in the “bio-world experiments” and to be such an explosive and full of care friend! Thank you Damiano for all the help and for having given me many enlightening suggestions, discussing with you have been always very interesting and stimulating. Thank you Nina for teaching me many things on cobalt nanoparticles! Thank you very much Veronika (ehi girl!) because in you I found not only a great fume-hood mate and a very helpful scientist, but also a very good friend; in Italian, we say that who finds a friend, finds a treasure, so now I am rich! Longhi (Elenù) thank you so much for all your support and for being always an example of fight for our targets and for your deep honesty; I had a great time with you! Thank you Laura (daje)! You have given me always good advices and you always made me laugh whatever my mood was; thanks for the beautiful time spent together! Thank you Leana, you have been a

good friend, being always there in the moments of need; thanks for all the help and advices and also for the beautiful movies seen together.

Now I will move to the fantastic PhD students' crew! Thanks to all of you for having shared the joys and the difficulties of the PhD pathway. Thank you Youssef, you are one of the kindest persons I have ever met; thanks for all the help in science, but also in many other things (French lessons, bureaucracy, French translations), you made me feeling at home in France! Thank you Federica (Fede) for having been always there to help. We did so many things together, thank you for having always showed me passion and joy in everything. Thank you Chien-Wei and Dedy for having shared interesting discussions on science and on our PhD life. Thank you very much Aliprandi (Prandus!) for all the interesting discussions we had and for have shared the PhD pathway, I have learnt a lot from you; in the end, you were not a so bad neighbour! Thank you Ricardo for all the laughs and funny moments and for the help with everything that a foreigner may need in France! Thank you Pengkun, even though I will not rest in peace for the moment, I appreciate a lot your wisdom. Thank you mein Freund Stephan for all the discussions about science (and not); I found always inspiration after speaking with you. Thanks a lot also to John, Loic, Serena, Hiroki, Frank, Etienne and all the others for all the time spent together. Finally thank you Claire and Ines for solving all the bureaucratic and technical problems! You make always a great job! I want to thank also some people that spent only a limited period in the group, but left some stardust here. Thank you so much Beatrice (Bea), Giacomo (Jack), Valentina (Vale), Bertucci (Bertu)! It has been great to meet all of you! Bea, thanks for being one of the greatest friend I could have, you are special! Jack, you are a brilliant person, please never change, thank you for everything! Vale, you represent the spirit of "my Sicily", you are a great girl, thanks for your friendship! Finally, thanks to all the people who would be too long to list here, but who make my PhD pathway awesome.

Thanks to all my friends around the world Marie, Chiara, Cinzia, Karina, Kritee, Claudia, Nushaba and all the others.

At last, but not least, thanks to my family for all the support, trust and strength that showed me. Thanks to nonna Agata for showing how to be strong and sweet at the same time and for being always proud of me. Thanks to somebody that cannot be here anymore, but who will be always in my heart (your little stories will always make me smile). Thanks to Salvo and Daniela to be the best brother and sister that I could have ever desired. Despite the physical distance, you have been always there with your wisdom, support, love and many laughs. Finally thanks to those two persons without whom all my work would have not existed: my mother and my father. You have always trusted in me and in my work despite the distance. You gave me love and support all the times that I needed showing me what a real family is.

# Design, synthesis and functionalization of ultrasmall nanoparticles for bioimaging

## Résumé

Cette thèse est centrée sur la synthèse, la caractérisation, la fonctionnalisation et les études *in vitro* et *in vivo* de différents types de nanoparticules (NPs) de très petite taille (NPs de silicium ; « carbon dots » ; NPs de cobalt couvertes de silice) qui présentent une luminescence ou des propriétés magnétiques et qui peuvent être fonctionnalisées par des liaisons covalentes. Tous les systèmes étudiés sont très intéressants pour l'imagerie multimodale *in vivo*, ce qui nécessite l'ancrage stable de fonctionnalités multiples sur une seule plate-forme nanométrique. Dans cette perspective, les NPs ont été fonctionnalisées avec des groupements amine et, puis, couplées avec des colorants ou des marqueurs radioactifs afin d'effectuer, *in vivo*, de l'imagerie optique ou de tomographie d'émission des positrons. Lorsqu'elles sont étudiées *in vitro*, les NPs ont présenté une cytotoxicité très faible. Les expériences *in vivo* ont donné des résultats très prometteurs puisque les NPs ont été excrétées par le corps en très peu de temps, principalement par un mécanisme de clairance rénale, avec une faible accumulation dans les organes.

Mots-clés : nanoparticules ultrapetites ; bioimagerie ; biocompatibilité ; photoluminescence

## Résumé en anglais

This thesis focuses on the synthesis, characterization, functionalization and *in vitro* and *in vivo* investigation of different kinds of ultrasmall nanoparticles (silicon nanoparticles: Si NPs; carbon dots: CQDs; silica-coated cobalt NPs: Co@SiO<sub>2</sub> NPs) which exhibit luminescence or magnetic properties and can be functionalized through covalent bonds. All the systems studied are very attractive for *in vivo* multimodal imaging, which requires the stable anchoring of multiple functionalities on a single nano-sized platform. In this perspective, nanoparticles were functionalized with amine-moieties and, subsequently, coupled with dyes or radiolabels in order to perform *in vivo* optical or positron emission tomography imaging. When tested *in vitro*, ultrasmall nanoparticles showed very low cytotoxicity. *In vivo* experiments gave very promising results since nanoparticles were excreted from the body in short times, mainly through a renal clearance mechanism, with low accumulation in organs.

Keywords: ultrasmall nanoparticles; bioimaging; biocompatibility; photoluminescence